The Structural and Compositional Basis for the Transparency and Physical Properties of the *Skogsbergia lerneri* Carapace

A thesis submitted to Cardiff University for the degree of Doctor of Philosophy

March 2020

Benjamin Martin Rumney

Structural Biophysics Group

School of Optometry and Vision Science

Cardiff University

Supervisors:

Professor Keith Meek

Dr Julie Albon

Dr Philip Lewis

Acknowledgements

I would like to firstly thank all of my supervisors for helping me through a thesis with such a unique subject compared to the norm. I would like to thank Professor Keith Meek for supporting me beyond the required level both in and out of the PhD. I would like to thank Dr Julie Albon for being a constant source of help and support throughout the three and half years of the project. I would like to thank Dr Phil Lewis for his help in all things EM-based and his advice through seemingly endless microscope issues.

I would like to thank all my friends for their support and for suffering with me effectively going radio silent for the final year of my PhD, as well as all the new friends I have made at Cardiff. All the chats and socials we had amongst both the postgrads and the biophysics group as a whole were a constant and welcome support. I especially want to thank my parents, Martin and Louise Rumney and my sister Abi, who have supported me both emotionally and practically throughout the entire project as they have throughout all my life.

I would also like to thank Dr Siân Morgan for all her assistance throughout the ostracod project as well as all our trips to and from Diamond, as well as everyone in the Biophysics team for always being friendly and happy to help with anything. I would also like to thank Nick White for his enormous help and advice with all things non-linear.I would like to thank Professor Andrew Parker for his help on both the project as a whole, his specific advice on ostracods and his assistance with locating the ostracod populations that were used in this thesis. I would like to thank both Professor Andrew Parker and Dr Tegwen Malik for their assistance in capturing and transporting the ostracods to Cardiff from Florida. I'm especially grateful after hearing about some of the horror stories they came back with! I would also like to thank Tegwen for all her help with maintaining the ostracod tanks, without which the ostracods would not have thrived as well as they did.

Finally I would like to thank DSTL for their funding of this project, allowing me to be able to carry out this PhD in the first place and giving me the opportunity to be able to present my work at numerous speciailsed conferences.

Table of Contents

Table of Figures

List of Tables

Abbreviation List

ACC – Amorphous Calcium Carbonate

ACP – Amorphous Calcium Phosphate

ANOVA – Analysis of Variance

BMMA – Butyl:methyl methacrylate

BSE – Backscattered Electrons

$CaCO_3$ – Calcium Carbonate

CL – Calcified Layer

EDS – Energy-dispersive X-ray spectroscopy

EM – Electron Microscopy

Endo - Endocuticle

Epi – Epicuticle

EXAFS – Extended X-ray Absorption Fine Structure

Exo – Exocuticle

GFP – Green Fluorescent Protein

HMDS – Hexamethyldisilazane

HRM – Harmonic Rejection Mirror

OCT – Optimal Cutting Temperature compound

PBS – Phosphate Buffered Saline

PIPES - Piperazine-N,N'-bis(2-ethanesulfonic acid)

RI – Refractive Index

ROI – Region of Interest

SBFSEM – Serial Block Face Scanning Electron Microscopy

SEM – Scanning Electron Microscopy

SHG – Second Harmonic Generation

TEM – Transmission Electron Microscopy

TPEF – Two Photon Excited Fluorescence

WAXS – Wide-angle X-ray Scattering

XAFS – X-ray Absorption Fine Structure

XANES – X-ray Absorption Near Edge Structure

XAS – X-ray Absorption Spectroscopy

XRF – X-ray Fluorescence

Abstract

Background: *Skogsbergia lerneri* (Kornicker, 1958) is a species of ostracod which, like all crustaceans, has a protective exoskeleton (or carapace). As well as being used for a protective function, the *S. lerneri* carapace is also transparent. Understanding how the carapace is transparent while retaining its protective function was the primary aim of this thesis.

Results: Ultrastructural analysis showed that the carapace consisted of an epicuticle, exocuticle and an endocuticle split into a calcified, crystalline endocuticle and a laminated endocuticle. Numerous structural adaptations were seen to minimise refractive index changes at the layer intersections. These layers developed along with growth of the ostracod, maintaining similar proportions throughout. Microstructural analysis identified a chitin based second harmonic generated signal from the carapace. Pixel analysis of this signal showed a consistent level of chitin expression (~60-80% of the total carapace) throughout all the developmental stages except instar 4, which showed a lower level of expression. Elemental analysis showed that the calcified, crystalline layer comprised mainly calcium, oxygen and magnesium, leading to the assumption that the structures were calcium carbonate. X-ray absorption near edge structure analysis revealed that the calcium carbonate consisted of entirely amorphous calcium carbonate in the early to middle stages of development and a mix of amorphous and aragonite in the later stages. Unlike most crustaceans, calcite was not seen in any carapaces. Optical testing showed a consistent refractive index across all stages (1.401-1.406) leading to a mean 99.94% transmission of light at the carapace surface in seawater. Spectrophotometric results showed that light transmission increased at longer wavelengths in the younger samples but maintained a consistent level by the adult stage.

Conclusions: Through the various structural adaptations of the carapace, in combination with the rare calcium carbonate polymorph distribution and its overall thinness, the *S. lerneri* is able to maintain its transparency without sacrificing many of its physical properties.

Chapter One

Introduction

1. Introduction

Ostracods, Ostracoda, or ostracodes are a class of crustaceans well known in the field of palaeontology due to their numerous fossil records, being the most common arthropod recorded, with thousands of species discovered. While a substantial amount of research has been focussed on the study of their fossils, living ostracod species have huge potential as well, especially the order *Myodocopida* (Fig. 1.1 (Lindholm and Hobæk 2014). A particular interest is seen in the *Cypridinidae* family, which comes from the impressive characteristic of its carapace being transparent while also potentially maintaining the durable physical characteristics expected of a typical crustacean carapace. While multiple species in the *Cypridinidae* family contain transparent windows in the carapace, the species *Skogsbergia lerneri* (Kornicker 1958) has a uniform transparency across its entire carapace (Kornicker 1958).

Due to these physical features, *Skogsbergia lerneri* was chosen for this study, to investigate further how the carapace architecture (composition and design) contributes to its physical properties, as well as, how these characteristics change through the ostracod's developmental stages to the final adult structure.

1.1 *Skogsbergia lerneri*

1.1.1 Habitats

Skogsbergia lerneri are found along the eastern coast of the American continents from Florida to the top of Brazil and the Caribbean islands as can be seen in figure 1.2 (Kesling 1951a; Kornicker 1958; System 1999; Board 2017). For this thesis, *Skogsbergia lerneri* were collected off the east of the Florida Keys in the open ocean.

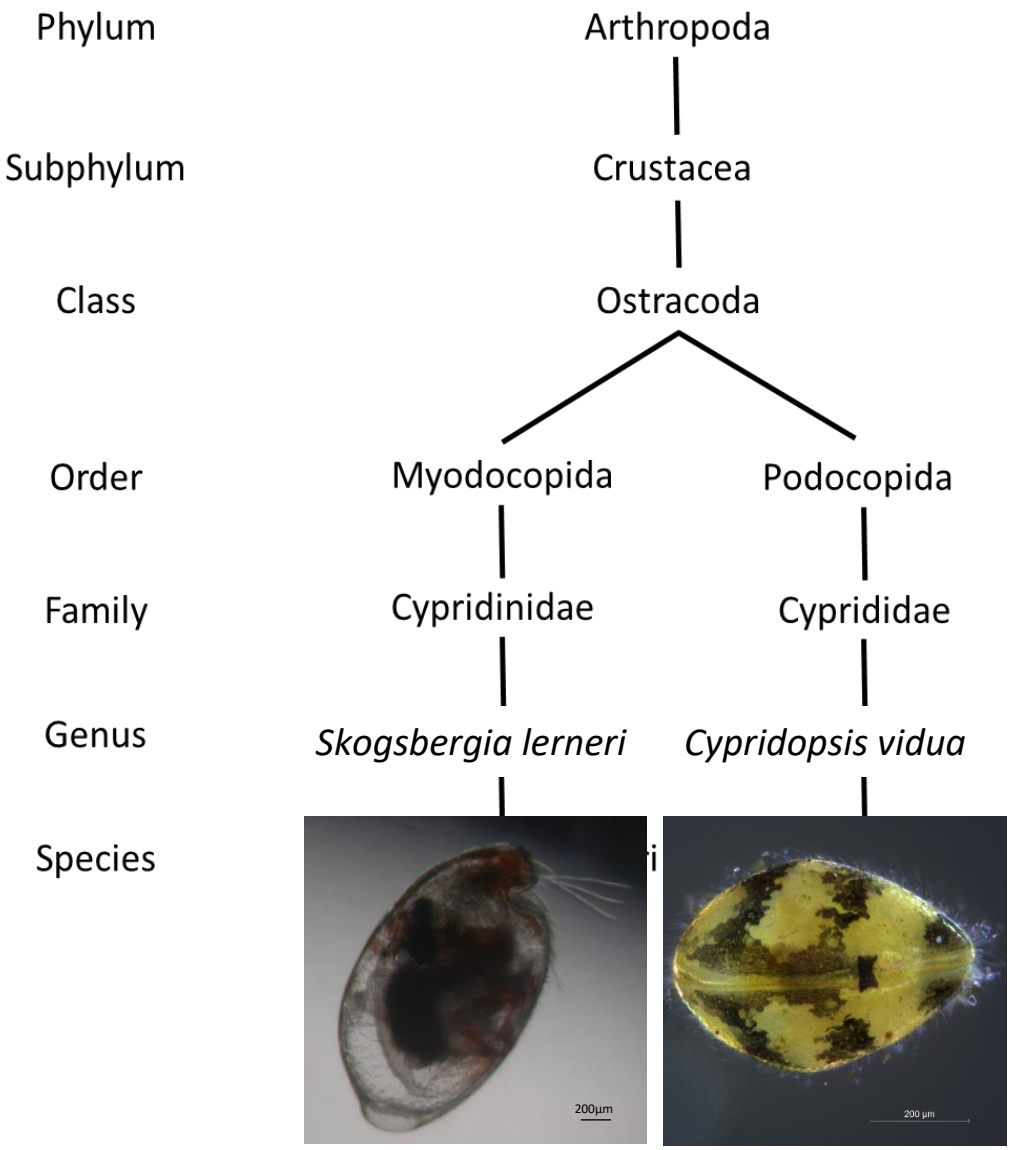

Figure 1.1: A simplified phylogenetic tree showing the taxonomy of the *S. lerneri* compared to the ostracod *Cypridopsis vidua* (O.F. Müller, 1776) of the order *Podocopida*. The image of *C. vidua* is attributed to Lindholm and Hobæk under creative commons CC 4.0.

Skogsbergia lerneri is a benthic species that can be found in the open oceans between 1-130m deep (Kornicker *et al*. 2002). As a benthic species, *S. lerneri* spends the majority of its time on the ocean floor, although unlike some ostracods, they are capable of swimming short distances (Thorp and Covich 2010). When not out for food they live within the sand or sediment of the ocean floor where they can burrow or build small nests to allow them to maintain optimal environmental conditions

(Williams *et al*. 2015). *S. lerneri* is by nature a scavenger, feeding off of meroplanktonic species but will also eat dead fish or shrimp (Cohen 1983).

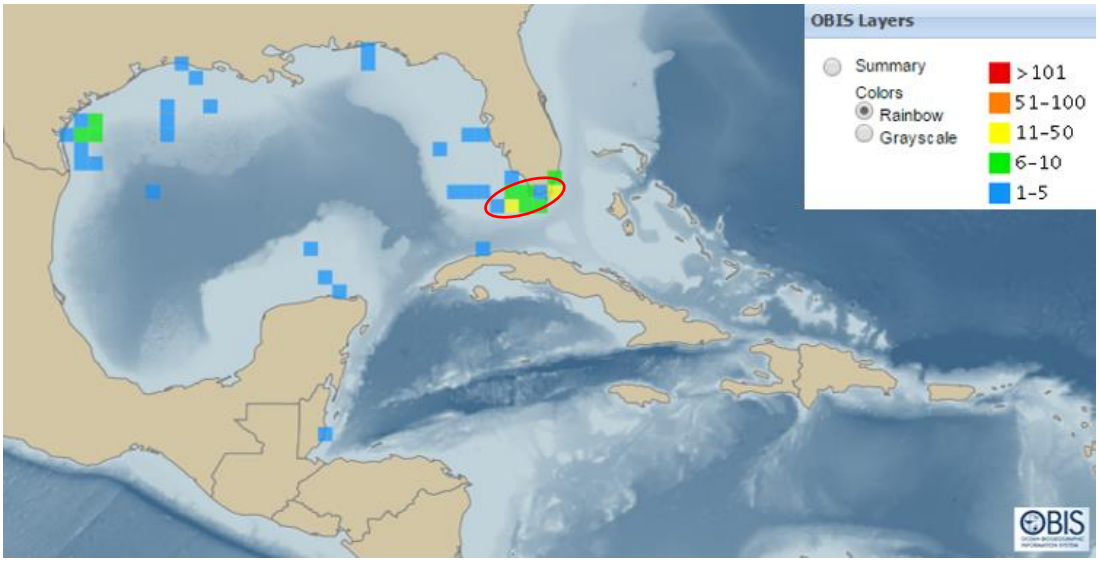

Figure 1.2: Map of reported locations of *Skogsbergia lerneri.* Colours indicative of the number of recorded cases of the species in that area. The red circle identifies locations of sample collection in this study. Distribution map generated by the Ocean Biogeographic information system (Bouligand 1972; System 1999).

1.1.2 Physical Features

All ostracods share the same distinctive features, the body is entirely enclosed within a 'bivalved' carapace. The soft body of the ostracod is placed inside two halves of a circular or oval shell, each half being called a valve and being held together at the superior end of ostracod in the hinge region (see figure 1.3). This bivalve carapace can close tightly to form a protective internal environment in the case of damaging external factors such as the presence of pollutants or oxygen toxicity (Williams *et al*. 2015). The ostracod can also open its valves to allow its appendages and large limb (known as a furca) to protrude for moving and eating.

S. lerneri follow the standard physical features of myodocopid ostracods, which vary between 1-3mm in size and are usually very calcified (Holmes and Chivas 2002). Adult females possess a carapace around 2mm long whereas adult males grow up 1.7mm in length (Cohen 1983). While no previous testing had been done on the calcium content of the *S. lerneri* prior to this thesis (to the knowledge of this author), the carapace seemed to exhibit all the physical characteristics of a calcified material. The carapace, like all ostracods, is formed by two lateral folds of the epidermis known as duplicatures, see figure 1.3b. The outer duplicature being the calcified external layer commonly thought of as the carapace. The space between the two layers has been

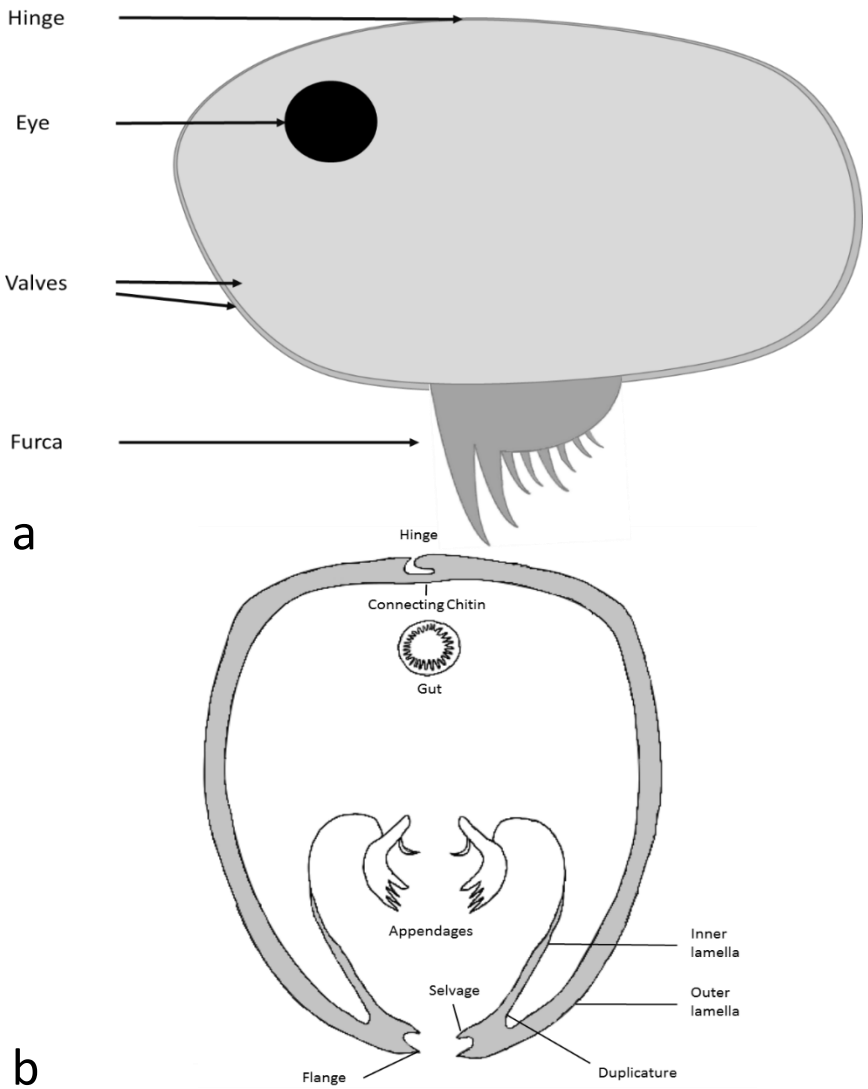

Figure 1.3: A basic diagram of an adult ostracod showing a **a)** lateral view and **b)** transverse cross-section adapted from (Bate and East 1972). For the sake of simplicity, the valves have not been drawn transparent and the main internal body has not been shown. The size and number of the claws on the furca varies depending on instar and sex.

known to house various organs and can act as a region of metabolism for certain physiological functions of some ostracods (Holmes and Chivas 2002; Yamada 2007b). The general structure of the external duplicature of the ostracod carapace in the Cypridacean family shows the carapace to be a structure comprising an outer epicuticle, an exocuticle and an endocuticle (Bate and East 1972) with a supporting epidermal cellular layer. A more detailed description of the structure of the carapace will be provided later.

S. lerneri are different from the majority of ostracod species, firstly they have the uniform transparency of the carapace instead of possessing a transparent eye window like most ostracods in the Myodocopida order (Parker *et al*. 2018). Secondly, the entire order has evolved a pair of lateral compound eyes seemingly independently of other arthropods (Oakley and Cunningham 2002; Oakley and Huber 2004) and so have a more highly developed visual system than other ostracods. *S. lerneri* shows evidence of containing multiple opsin genes or gene duplicates, although their function is somewhat unknown as there has been partial evidence towards a lack of colour vision in *S. lerneri* (Huvard 1993; Oakley and Huber 2004). Other given suggestions could be range fractionation, the process where different levels of stimuli lead to varying signal intensities, the locating of opsins in extraocular photoreceptors or the selective expression of subsets of opsins leading to differences in visual response (Oakley and Huber 2004). This surprisingly well-developed vision system may have a beneficial synergistic relationship with its transparent carapace by allowing a greater field of vision.

1.1.3 Life Cycle

Like all ostracods, *S. lerneri* grows in specific stages of a set size and development, called instars, with instars separated by moults in a process known as ecdysis, where the old carapace is shed and a new one is grown underneath. At certain ages, the ostracod will moult its old valve and grow into a new, larger one, this will also come with other developments such as more claws on its main appendage, the furca, and more/larger limbs. *S. lerneri* has five intermediate instars between the egg and the

final adult stage, totalling 7 stages of development as seen in figure 1.4. In the later stages of development *i.e*. instar 5 and adult, there can be a significant variation in carapace size between individuals. Due to this, care must be taken to not only identify the instar via carapace size but alongside other factors such as shape and furca development. The time taken to progress from initial egg to full adult is between 65-93 days (Cohen 1983).

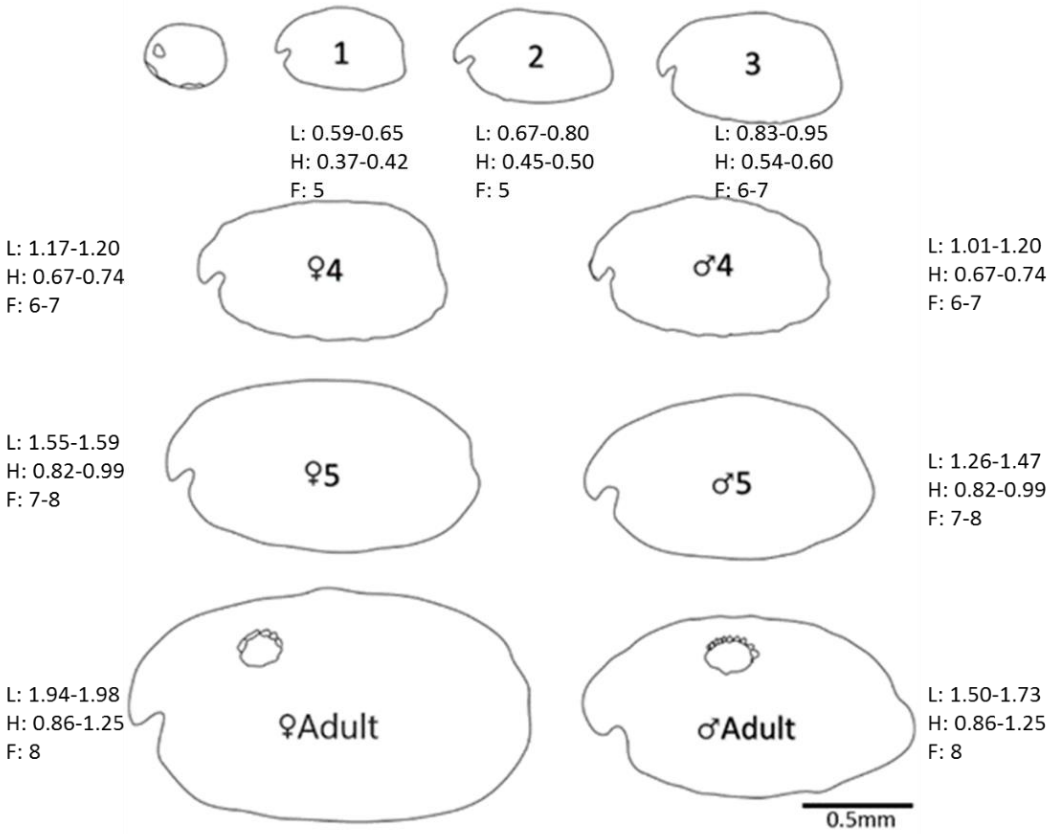

Figure 1.4: A diagram of *S. lerneri* ostracod shape and size throughout their lifespan adapted from Anne Cohen's paper (Cohen 1983). Before instar 4 there are no identifiable sexual dimorphisms between the animals so they are shown as the same for both. L:length; H:height, both in mm. F denotes the number of the claws on their furca.

1.2 General Crustacean Integument Architecture and its relationship to Ostracods

1.2.1 Composition

1.2.1.1 Organic

The most important organic component of the carapace, when studying the properties and structure of the carapace, is chitin. Chitin is a polymer consisting of 80-90% N-acetyl-d-glucosamine and 10-20% glucosamine attached by β-(1,4)-glycosidic linkage (Hackman and Goldberg 1974; Das *et al*. 2016) and is the building block from which the carapace is generated. 18-25 of these chitin crystals arrange into anti-parallel chains know as α-chitin (Minke and Blackwell 1978), which is the only form found within crustaceans (Stevenson 1985). These chains of chitin are enclosed in a protein matrix of a primary repeating protein and various 'satellite' proteins (Rudall and Kenchington 1973); this is called a nano- or microfibril. The total chitin volume fraction in a single fibril has been revealed to be 0.17 (17%) (Nikolov *et al*. 2011). Proteins are non-covalently connected to the chitin although covalent bonding has been hypothesised, with the most likely non-covalent bonding being hydrogen bonding (Rudall and Kenchington 1973; Hackman 1987). A helical arrangement of 6 proteins per turn around the chitin centre has been suggested (Hackman 1987). Unfortunately little is known about the local composition of these proteins surrounding the chitin or if there are any species to species variability between them (Fabritius *et al*. 2016b). Water is also an essential component of this construction and it is predicted that without it the protein matrix would dry out, become too stiff and cause the cuticle to become too brittle (Neville 1969). Polyphenols and a small number of lipids are also present as secondary components (Vincent and Wegst 2004). Polyphenols are important in the protective properties of the carapace, the oxidation of phenols is involved in the cross-linking of proteins, in a process known as tanning or scleroisation (Pryor 1940). This process leads to a much higher stability of the proteins and overall hardening of the cuticle.

Other proteins are found within the carapace outside of the ones involved in chitin formation, and a wide diversity has been discovered in the proportion of their intermolecular bonding. In the crayfish, *Orconectes sanborni* (Faxon, 1884), the proportion of all bonding of proteins within the cuticle could be broken down into 53% covalently bound, 26% non-covalently bound and 21% unbound (Stevenson 1985). A commonly seen protein within the exoskeleton is resilin, and resilin or resilin-like proteins have been seen in crustaceans from copepods (Kannupandi 1976) to crabs (Welinder *et al*. 1976). Resilin is an important factor when determining the physical properties of a carapace, as it maintains extremely high elastic efficiency with only 3% of applied energy lost as heat (Stevenson 1985). It is also used to store kinetic energy and increase flexibility in various limbs and joints of athropods. Resilin is also extremely suitable for optical materials, as it is both transparent and amorphous (Michels et al. 2016).

Lipids have also been found within the crustacean carapace (Stevenson 1985), cholesterol has been found in the prawn *Penaeus japonicus*, Spence Bate, 1888 at a mean concentration of 4.67mg/g (Kanazawa *et al*. 1976). One of the main functions of these lipids is the waterproofing of the exoskeleton (Bursell 1955), lipids, as well as proteins and calcium salts are the main constituents of the outermost layer of the cuticle, the epicuticle (Stevenson 1985) which forms the initial layer of protection.

1.2.1.2 Inorganic

Mineralisation and calcification are difficult processes to categorise as many crustaceans have varying mineralisation levels both to adapt to their environment and dependant on what is available. For example, animals that exist in seawater usually have a much higher proportion of magnesium content due to its availability. The marine *Tylos europaeus* Arcangeli, 1938 showed a 0.1 magnesium/calcium ratio in comparison to a much lower ratio in the cave-dwelling *Titanethes albus* (C.Koch, 1841) (Hild *et al*. 2009; Fabritius *et al*. 2016b). This relationship has been

quantitatively demonstrated in magnesium and other trace elements found in the carapace such as strontium (Holmes and Chivas 2002).

The benefit of a harder cuticle is balanced by the significant energy costs of incorporating minerals, especially the rarer ones (Hild *et al*. 2009). Flexibility needs to be considered as well, the higher the inclusion of mineralisation, the harder and less flexible the cuticle will be (Hild *et al*. 2009) which will affect delicate moving parts. The *Myodocopid* ostracod exists in seawater and possess a carapace that is a continuous shell, except for the hinge connecting the two valves. Therefore it most likely maintains a higher level of magnesium-containing calcite crystal lattices, as it does not require any flexibility and has an easier access to magnesium from its marine environment. However, this may be offset by a general lowering in the level of calcification/mineralisation to maintain transparency.

Calcium is the most commonly occurring mineral in the exoskeleton, although it exists in multiple forms. Calcite is located within the exocuticle, but is constrained to a thinner outer layer and is not homogenously present, whereas the majority of the exocuticle and the entire endocuticle contain amorphous calcium carbonate (ACC) exclusively (Al-Sawalmih *et al*. 2008). It is speculated that, due to its presence exclusively in the outermost exocuticle layer, the function of calcite is a protective one of impact and wear resistance.

From a structural categorisation, four major mineral morphologies have been listed (Fabritius *et al*. 2016b), on the microfibril level they are found either as small spherical particles (20-50nm) that form around the microfibril (Fabritius *et al*. 2009) or as solid tubes completely enclosing the microfibril (Ruangchai *et al*. 2013). Whereas on the chitin-protein fibre level, minerals are found as either tubes enclosing the macrofibrils or as large mineral blocks surrounding irregularly shaped clumps of microfibrils (Seidl *et al*. 2011). Small amounts of magnesium and significant amounts of potassium have been found in the carapace which both influence calcium carbonate polymorph formation (Fabritius *et al*. 2016b). Potassium has been shown to stabilise ACC, which due to its low stability tends to crystallise into more stable compounds (Addadi *et al*. 2003; Al-Sawalmih *et al*. 2008), and helps the animal control the production of calcite (Reddy 1977). Although it should be noted that

experimental evidence has indicated that high concentrations of potassium are not necessary for ACC formation or stabilisation and multiple compounds are also suitable (Habraken *et al*. 2015). Magnesium has been shown to increase the elastic constraints of magnesium containing calcite crystals when added in the most stable conformation and has a beneficial effect on the stiffening impact of the cuticle's mechanical properties (Fabritius *et al*. 2016b).

The interplay of various elements on calcite and its structure is a very important aspect of the cuticle's hardness, calcite as a pure mineral is soft and extremely brittle and even when optimised still breaks easily (Huber *et al*. 2015). Yet when strengthened correctly calcite becomes strong enough to be an essential component of crustacean armour and the teeth of many animals such as sea urchins, which constantly graze the sea bed (Goetz *et al*. 2014). A couple of different structures have been predicted to prevent the fragility seen in pure calcite and are dependent on the level of calcite (Huber *et al*. 2015). The first, found under lower calcite concentrations, contains a high number of fibrils and a subsequent large interface between the inorganic calcite and organic phase. This is predicted to both increase stability and reduce crack propagation, which allows for longer crystalline domain slopes (Huber *et al*. 2015). The second, with a higher calcite level, have less but thicker fibres, which, due to the smaller organic/inorganic interface requires shorter crystalline domains and creates for a larger surface area and higher stability by making the calcite domain borders more irregular (Huber *et al*. 2015). However, between these changes in the calcite domains, the fibres running through them stay unchanged and remain a permanent fixture of the mechanical properties of the cuticle.

There has been evidence to suggest that crustaceans have an element of control over the crystallisation of the amorphous calcium carbonate into calcite, leading to varying organisations and microstructures, unlike other biological forms of calcium carbonate tissue (Seidl *et al*. 2012; Huber *et al*. 2015). This control has been predicted to be related to function and behaviour, including a response to predators (Seidl *et al*. 2012).

1.2.2 Architecture

Structures within all crustaceans follow the same general classification, the main difference being the location or proportion of various structures. The lowest level of the structural hierarchy is identical between all species, the chitin crystal formation, and a degree of similarity remains until the highest levels where it becomes highly differentiated even between very close species (Ruangchai *et al*. 2013; Alagboso *et al*. 2014; Fabritius *et al*. 2016b).

The basic carapace structure comprises four layers (Stevenson 1985): a thin outer layer devoid of chitin known as the epicuticle; a dense laminar layering of chitin known as the exocuticle; a less dense laminar layering known as the endocuticle (both exo- and endocuticle together are known as the procuticle) and the epidermal cells connected to a basal membrane (Fig 1.5). The boundaries between these layers are not generally smooth and distinct borders, for example, the proximal epicuticle layer and exocuticle border is erratic with multiple extensions. This is predicted to strengthen the connection between the two layers to prevent delamination (Fabritius *et al*. 2016b).

Throughout every layer, penetrating through the epidermis to the epicuticle, are pore canals, which form pore openings at the carapace surface. The ostracods maintain three different types: simple pores with extruding sensory hairs (known as setae or sensilla); sieve pores also containing setae and exocrine pores that transport minerals required for moulting (Maddocks 1990; Holmes and Chivas 2002). These pore canals have numerous structural functions as well as the primary one stated that will be described later.

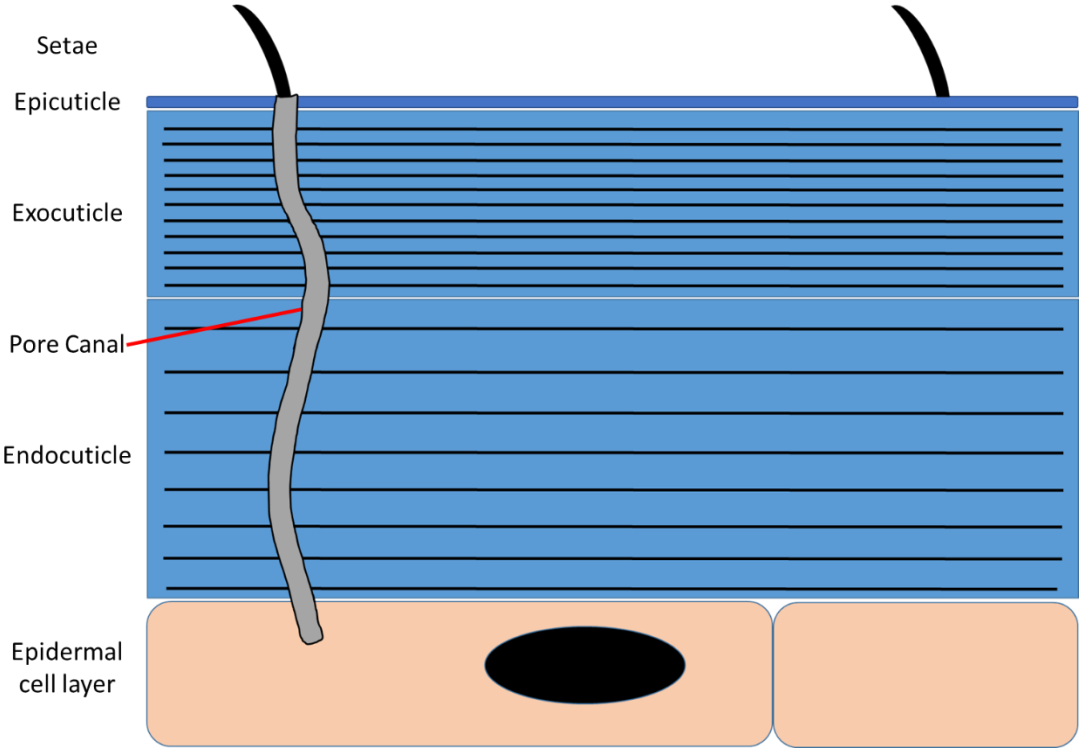

Figure 1.5: A diagram of a basic crustacean carapace structure. The black lines represent chitin lamellae with the exocuticle being smaller but more densely packed with lamellae and the endocuticle being the reverse. To simplify the full pore canal is shown, however the pore canal twists throughout the carapace creating a spiral like structure so the entirety of the canal would not be able to be seen in 2D cross section.

1.2.2.1 Epicuticle

The epicuticle is different from the other main parts of the cuticle, as it does not contain chitin within it. This layer is further split up into at least two layers, an outer thin membrane and an inner, thicker layer. In some crustaceans such as fiddler crabs, there are six distinct layers (Green and Neff 1972). Across the surface of the epicuticle, spines projecting from the surface through the exocuticle are found, these numerous extensions that project down into the exocuticle vary in size depending on the organism (Fabritius *et al*. 2016b). In the crab *Cancer pagurus,* Linnaeus, 1758 vertical canals were only found within these spines and the base layer, and these canals were the only area where mineralisation occurs within the epicuticle (Hegdahl *et al*. 1977b). The form of calcification is unique in the epicuticle as a consequence of it forming in crystalline plaques which rest against each other (Neville 1975; Stevenson 1985). It is interesting to note that the thickness and level of

mineralisation of the epicuticle vary drastically at different areas on the same organism, which has been theorised to be due to an adaptation to various mechanical strains (Ruangchai *et al*. 2013).

As one might expect, smaller creatures have thinner layers. In a similarly sized ostracod to *S. lerneri* (as opposed to crustaceans generally), *Cypridopsis vidua* (Müller, 1776), the thickness varies between 4nm – 29nm towards the selvage, although *C. vidua* is around 0.66mm long and so about half the size of *S. lerneri* (Bate and East 1972). Other ostracods have shown epicuticles ranging anywhere from 9 to 50nm thick, depending on the organism (Seidl *et al*. 2011; Fabritius *et al*. 2016b). Recently research has been carried out on the ultrastructure of *Euphilomedes japonica* (Mueller, 1890) and others of the same subclass as *S. lerneri* (myodocopa), which showed three distinct layers to the epicuticle, comprising of a thin outer layer, a thick middle and an electron-dense inner layer, that total around 1µm in thickness (Yamada 2019).

1.2.2.2 Exocuticle

Sometimes referred to as the primary procuticle, the exocuticle consists of densely packed fibrous laminae parallel to the surface that roughly make up a constant 25% of the depth of the integument (Hegdahl *et al*. 1977a). While most of the fibrils run parallel to the surface, some run vertical or obliquely as connectors (Stevenson 1985).

These microfibrils appear to connect to each other within a bundle known as a macrofibril which have diameters ranging from 25-300nm with the microfibrils, having a range between 1.8-6.5nm (Neville 1969; Stevenson 1985; Raabe *et al*. 2005a). The macrofibrils are arranged in laminae showing a specific helicoidal arrangement. Due to the importance of this formation to both the structure and the physical properties of the overall carapace, this will be described in more detail in its own section. A small subset of crustaceans do not contain these macrofibrils and the larger order structures are created purely from microfibrils (Fabritius *et al*. 2016b).

In some crustaceans, for example, the holocarid *Squilla desmarestii,* Risso, 1816 the laminar sheets are separated with a non-chitinous membrane, however, this has only been seen in certain holocarid and copepod species and so far not in ostracods (Dennell 1978). Calcification is highest within the exocuticle (Neville 1975) where calcite, vaterite and hydroxyapatite crystals occupy the space between the chitin microfibrils. The proportion of calcification varies greatly and in general the larger number of calcite crystals the less protein. Crustaceans have a higher level of calcification compared to insects due to the need to withstand the hydrostatic pressure, except in pelagic species due to their need to float (Neville 1975; Stevenson 1985).

The border between the exocuticle and the lower endocuticle is difficult to differentiate without TEM imaging, which reveals the exocuticle to be rougher and to contain larger interconnecting, branching pore canals (Fabritius *et al*. 2016b). The exocuticle also maintains the property of being stronger and stiffer than the endocuticle due to a higher fibre fraction (Cheng *et al*. 2008). For example, in the claw of the *Homarus americanus*, H. Milne Edwards, 1837 via nano-indentation, a distinct decrease in hardness was found between both the layers with a mean 450MPa found in the exocuticle and 282 MPa in the endocuticle (Sachs *et al*. 2006).

In some ostracods, the exocuticle can be subdivided into an outer, electron-dense layer considered to be strengthened by tanning and an inner non-tanned layer (Bate and East 1972). In *C. vidua* the layer varied between 0.054µm and 0.158µm, again dependent on the location (Bate and East 1972).

1.2.2.3 Endocuticle

This endocuticle is also known as the secondary procuticle or the post-ecdysial procuticle, as it is the portion secreted after the moult (Stevenson 1985). It is similar to the exocuticle in most crustaceans in that it is made up of fibrous laminae running parallel to the surface and they make up the bulk of the cuticle (Vincent and Wegst 2004). However, there are notable differences, the most obvious being that the

layers are much less densely packed together. This is due to the planes of fibres in the endocuticle being much thicker and creating a coarser matrix structure, for example in the *Homarus americanus*, each endocuticle stack of fibres was just under four times thicker (Raabe *et al*. 2005b).

Secondly, the layer is split into two separate layers, an outer calcified principal layer and a thin, uncalcified membranous layer (Drach and Tchernigovtzeff 1969), although this second layer is not found in all crustaceans (Fabritius *et al*. 2016b). Amorphous calcium phosphate is found throughout the endocuticle and is concentrated within areas that undergo higher mechanical stress (Ruangchai *et al*. 2013). Pore canals are found to be smaller with much less branching compared to the exocuticle layer (Fabritius *et al*. 2016b). These canals are elliptical and the inner walls show no structurally differentiated lining (Hegdahl *et al*. 1977c).

As with the epicuticle/exocuticle interface, the border between the exocuticle and endocuticle does not cleanly separate the two layers. In the crab *Cancer pagurus,* bulbiform extensions from the endocuticle protrude into the exocuticle (Hegdahl *et al*. 1977c) reinforcing the connection between the layers.

While the previously mentioned endocuticle has the basic structure of that in crustaceans, ostracods differ slightly. Instead of a layer composed of less densely stacked chitin lamellae (Vincent and Wegst 2004), the apical portion of the endocuticle takes on a completely different formation in ostracods. Here it forms a much more open structure with slender chitin fibres creating a matrix containing large crystalline granules of calcium carbonate ($CaCo_3$) (Bate and East 1972) as can be seen in figure 1.6. In one study the mean size of these crystals was found to be around 2µm (Jorgensen 1970), they also showed no preferred crystallographic orientation when studied via X-ray diffraction (Travis 1963) and are bonded externally and internally by chitinous layers (Rosenfeld 1979). Looking at the research more specific to the Myodocopid family, a scanning electron microscopy (SEM) study examined cross-sections of various myodocopid ostracod shells (Sohn 1988). This study identified five primary components that can form the structure of the endocuticle which are: laminate (as seen in the generic crustacean architecture), columnar, fine granular, coarse granular and homogeneous. There has also been

some discussion about whether the coarse granular layer can be distinguished into two separate types depending upon the size of the inner electron-dense core (Rosenfeld 1979). Individual species can have anything from one to a combination of four of these components (however never all five) depending upon whether they were pelagic or benthic. *Vargula hilgendorfii,* Mueller, 1890 a benthic ostracod much like *Skogsbergia lerneri*, was assessed to contain laminate, coarse granular,

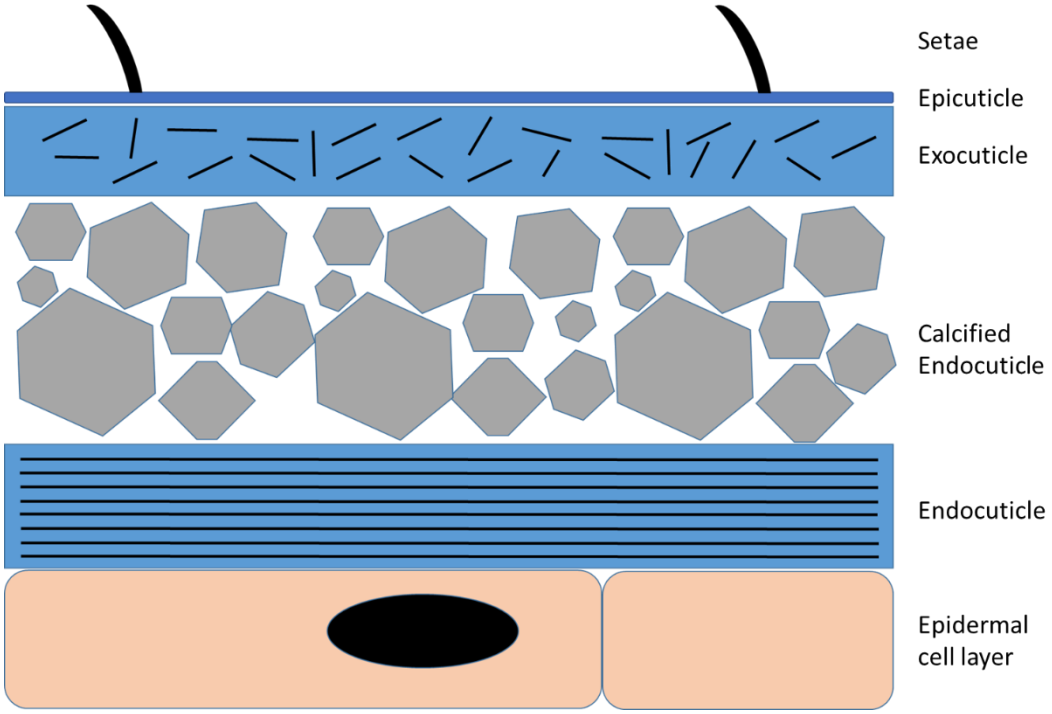

Figure 1.6: A diagram of a basic ostracod carapace structure. The black lines represent chitin lamellae with the exocuticle being smaller but more densely packed with lamellae and the endocuticle being the reverse. The calcified endocuticle can be seen to be composed of $CaCO_3$ crystals with no preferred orientation.

homogeneous components, with some discussion about a fourth, columnar component. The most prominent and common of these components is the laminate which consists of multiple thin layers of chitin stacked on top of each other. A secondary component was also found in *Vargula hilgendorfii*, multiple crystalline nodules made from calcite (Sohn 1969), however, these were found to be more prominent in preserved specimens and so may be inflated due to the preservation method rather than natural morphology. It was also noted in this study that there is little difference between juveniles and adults except for larger, less defined grains in the coarse granular component (Sohn 1988).

1.2.2.4 Epidermal Cell Layer

Occasionally known as the hypodermis, the epidermis is a single layer of cells, overlying a basement membrane. This makes up the lowest level of the integument that shows evidence of intense secretory activity and controls the secretion of the other layers (Stevenson 1985; Mrak *et al*. 2015), including to some degree the morphological patterning of chitin lamella as well as their formation (Whitten 1969; Rudall and Kenchington 1973). The epidermis also reabsorbs calcium from previous layers just before moulting to preserve mineral storage (Glotzner and Ziegler 2000). Consequent specialisations are a larger surface area through both greater exposure and folding, an increase in the abundance and volume of mitochondria and a complex collection of channels and interstitial dilations known as the interstitial network, although the first two alter depending on the current moulting stage (Ziegler 1997). There is also an important structural function for the epidermis which is to connect with the muscle cells underneath the integument via microtubules attaching to hemidesmosomes at the epidermal cells' apex that, in turn, connect to a muscle attachment fibre (Caveney 1969).

1.3 Physical Properties of Crustacean Carapaces

Crustacean carapaces are well known for being a tough yet lightweight protective material. It is no surprise that studies have investigated the specifics of their mechanical properties and the feasibility of synthetically creating or artificially mimicking them.

Most of the research done in this field around crustacean carapaces is based on the mechanical or physical strength of the substance as a durable or protective material. As such certain points have to be taken into account when understanding data given from an engineering, especially a tribological, perspective. Mainly when testing hierarchically structured materials that are subject to mechanical loads it is necessary to identify what specific property is being studied (Raabe *et al*. 2005b). There exists

no specific metric unit for wear damage and instead, it can be categorised into a combination of other fundamental properties such as hardness, elastic modulus or fracture toughness (Amini and Miserez 2013).

It is important to keep in mind what area of the exoskeleton is being tested. Different parts will have different strengths depending on their function (Amini and Miserez 2013), the hardness of the claw in crabs is 3-4 times harder than the walking legs (Chen *et al*. 2008). This is due to the required flexibility needed of legs, which is lost if the exoskeleton becomes too mineralised and stiff.

1.3.1 Hierarchical Design

Raabe (Raabe *et al*. 2005a) summarised the structural hierarchy of the procuticle into six distinct levels (see figure 1.7), the smallest being the arrangement of antiparallel chains of chitin, known as α-chitin (Carlstrom 1957). The strong crystallographic texture is rare even in man-made materials and was not expected from previous studies (Kesling 1951b; Jorgensen 1970; Bouligand 1972; Rudall and Kenchington 1973; Gharagozlouvanginneken and Bouligand 1975; Kumar 2000). These α-chitin chains form long narrow units covered by proteins, known as microfibrils and these, in turn, form the third distinct level called a macrofibril (described in section 1.2.2.2 above). The fibril forms a systematically woven and branched laminae containing various proteins and biominerals (Raabe *et al*. 2005a). These laminae are then stacked into planes maintaining a helicoidal or 'twisted plywood' arrangement (Raabe *et al*. 2005b). This arrangement allows for a much more even distribution of force throughout the carapace, causing the forces to be spread horizontally at each plane, rather than passing completely vertically down the structure. The sixth and final level is the stacking of the helicoidal formations and the inclusion of pore canals (Nikolov *et al*. 2010; Nikolov *et al*. 2011). See Figure 1.7 of a diagram for the hierarchical breakdown. Helicoidal or twisted plywood arrangement was proposed in arthropod cuticle by (Bouligand 1972), the fibril layers seen in the exo-and endocuticle have a specific layering where each layer is rotated from the one below it through a small angle at an axis perpendicular to the planes.

Most fibrils run in parallel with the lamella, however, a smaller proportion of fibrils run perpendicular or obliquely to the others. The combination of the different orientations leads to the illusion of parabolic patterns in oblique sections of cuticles (Cheng *et al*. 2008). Later studies have redefined this formation into a 'twisted plywood' or sometimes 'Bouligand' pattern and found that the interconnected pore canal fibres running through the planes bend around cavities in a 'twisted ribbon' structure in the cuticle to form a 'honeycomb' structure (Cheng *et al*. 2008). It is important to note that while at imaging at certain cutting angles and in older literature it may seem like there is a parabolic pattern in these interconnected fibrils as well as the laminar layers, this is just an illusion caused by the helicoidal pattern. It has been shown that one of the main differences between the endo and exo-cuticle layers is the degree of the rotation. In the lobster cuticle, the exocuticle showed a much shorter pitch of rotation of 10µm compared to the 30µm from the endocuticle (Nikolov *et al*. 2010).

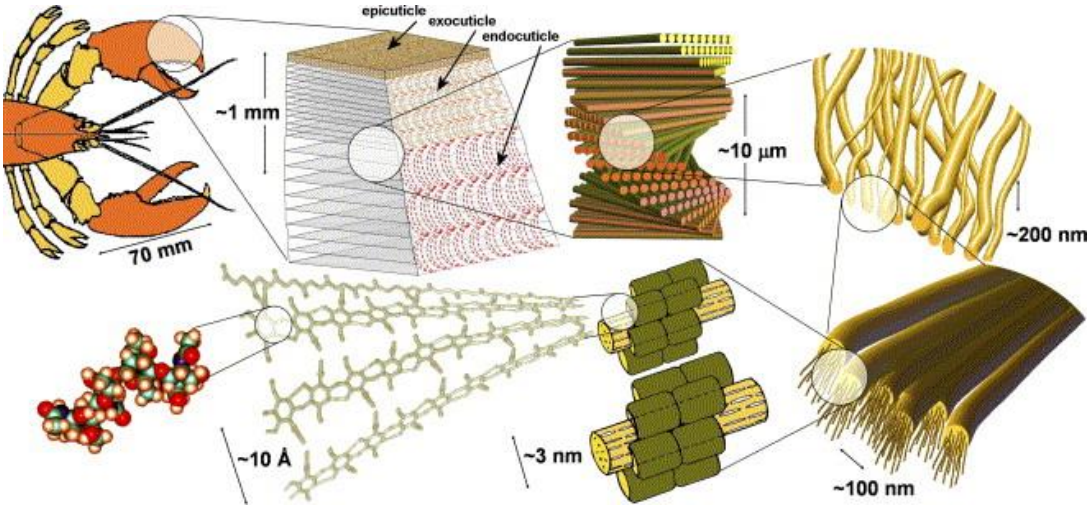

Figure 1.7: Hierarchical structural formations of the crustacean cuticle, starting from the entire carapace and ending with the specific chitin crystal. Image taken with permission from (Raabe *et al*. 2005b)

This twisted plywood stacking has been speculated to create enhanced resistance to crack propagation and deflecting compared to a smooth stacking orientation (Raabe *et al*. 2005a). As well as crack resistance, this formation directly affects the hardness

and stiffness which can be seen on experiments between the exo- and endocuticle. The main difference between the two layers structurally is the density and number of these twisted plywood planes. A microindentation experiment (Raabe *et al*. 2005b) showed a transition of nearly one order of magnitude in hardness between the layers, with the exocuticle, with the mean 3.7 factor increase in stacking density being the harder. However, is it also important to state that this increase in hardness does not match the increase in stacking density one to one and there is plenty of potential for other factors to have an effect. There is also a steady increase in exocuticle hardness as it gets closer to the endocuticle to the point its hardness is doubled from the most basal values 50µm from the exocuticle/endocuticle transition.

Pore canal fibres are essential in maintaining high interlaminar shear strength and shear stiffness in a layer composite structure such as the carapace. This is accomplished by absorbing energy through the stretching and friction of transverse fibres, which can help prevent delamination (Cheng *et al*. 2008). Chen *et al* describe a 'Hole-pin' joining structure that seems to be a pore canal and pore fibre with chitin fibres surrounding the whole continuously to form a pattern known as a 'fibre-round-hole' distribution. This specific pattern leads to any crack in the area near the hole causing a change in its propagation orientation from moving towards the hole to actually avoiding it. Comparison of man-made made materials with this specific pattern to one without showed a much greater maximum pull-out force (Chen *et al*. 2014).

The progression from a single, crystalline chitin to the overall honeycomb structure can be defined as different hierarchical orders and they have a synergistic effect between themselves. It has been observed that the specific characteristics of the structures at the lower hierarchies (*i.e*. α-chitin) contribute significantly to their macroscopic properties, while the shortcomings of the intrinsic properties of these lower hierarchy biomaterials are corrected by the superstructures at the upper hierarchies (*i.e*. twisted plywood structures) (Nikolov *et al*. 2010).

NIkolov *et al*. studied the effect of hierarchies by analysing two main mechanics (Nikolov *et al*. 2010; Nikolov *et al*. 2011). Firstly, NIkolov showed the anisotropy ratio

is compensated throughout the hierarchies by strongly decreasing from 4.25 in the chitin crystal (119 GPa axially to 28GPa transversally) to 1.25 in the honeycomb structure. The anisotrophy ratio is defined as the ratio between a physical property (in this case the elastic modulus) in different dimensional axes (*i.e.* the axial axis compared to the transverse axis). Secondly Nikolov showed large deviations of up to 20% in structure at lower hierarchies had no serious effects on the macrostructure. This was put down to the soft protein wrapping of the chitin nanocrystals and the twisted plywood structure, negating the structural changes. As such the overall properties of the crustacean cuticle are highly robust to large variation and frequency of any component except on the higher levels of the hierarchical order.

The specific hierarchical structure of the carapace leads to a near-optimal use of the stiffness of the individual components available. In fact, the cuticle showed all mechanical properties approaching close to the theoretical upper bound of mechanical behaviour (Nikolov *et al*. 2011).

1.3.2. Heat Resistance

Chitin is shown to be very heat resistant for biological material, degradation was not shown to occur until 270^{o}C and this chitin was not completely removed from the *H. americanus* carapace until around 500-600^{o}C. Most importantly from a structural point of view, major decomposition was not confirmed until 370^{o}C, only showing gradual change before this point (Romano *et al*. 2007). In the centre of the sample, the structure was well preserved although individual fibres were rough and broken. The areas nearer the surface still displayed a very well developed honeycomb structure but the walls were not compact and former fibrillar structures were no longer visible (Romano *et al*. 2007). The overall lack of influence the heat treatments had on the overall structure holds a positive implication to the physical resistance of the cuticle at high temperatures. It should be noted that while there seems to be minimal structural change, it is not known how these changes would affect transparency.

1.3.3 Hardness

Hardness is defined as the resistance of a material to localized, permanent deformation (Chua *et al*. 2017). A study by Amini and Miserez modelled the hardness of crustacean exoskeletons amongst multiple biological materials, based upon controlled depth-sensing indentation experiments and found at the hardest point it can range from 0.5– 5 GPa hardness when tested against yielding at a blunt contact (Amini and Miserez 2013). It also showed good resistance to cracking, having the greatest abrasion resistance response out of all the moderately mineralised materials. A moderately mineralised material being defined in this study as below 75% mineral content by volume, with crustacean exoskeletons containing approximately 40% mineralisation (Romano *et al*. 2007). When testing pressure under contact with a sharp object, crustacean exoskeletons showed evidence for yielding well before any cracking occurred. In the crab species *Cancer pagurus*, a distinct structural architecture is seen where the exocuticle is invaded by highly mineralised bulges from the endocuticle, in which the regular plywood-like layers rotated vertically (Fabritius *et al*. 2012; Fabritius *et al*. 2016b). This alternation of hard bulges and the calcite-containing exocuticle provide a high level of protection against predators due to its ability to disperse compressive loads. The bulge containing vertical layers act as pillars and transfers the compressive load to the lower regions of the endocuticle, which due to their horizontal arrangement, can dissipate the energy in a much more widespread and stable horizontal fashion (Fabritius *et al*. 2012).

It is not known where the ostracod carapace would lie on a scale of function compared to hardness. We can hypothesise that as it has no moving parts, excluding the hinge at the back, it will not need to sacrifice protection for mobility but as the carapace is not expected to undergo near constant assault, like a claw, it probably will not be as hard as its potential maximum. However, predicting levels of localised hardness through the carapace would only be in comparison to other parts of the ostracod and not against other crustaceans so might be seen as somewhat of a moot

point. There is also a high likelihood that due to specific structural prerequisites needed to retain transparency, the hardness may be reduced by some level.

1.3.4 Hydration

Hydration is also a critical parameter that influences the mechanical response of biological tissue. Hydration has been shown to lower the hardness and modulus of the tissue but increase the fracture toughness and cause a shift towards yielding, rather than cracking, dominated damage (Amini and Miserez 2013) when modelled on previous predicted wear map resistances (Zok and Miserez 2007). It has been speculated that the natural hydration of a crustacean exoskeleton significantly minimises the embrittling effect of the inorganic salt components (Hepburn *et al*. 1975). In crab exoskeletons the mean toughness value under compression pressure, predicted from the Vickers hardness value, of wet samples was 8.3 ± 1.5 MPa compared to the dry value of 1.6 ± 0.5 MPa and the yield strength was almost doubled when tested on wet tissue (Chen *et al*. 2008). Water also affected the fracture surface of the previously tested samples with the dry samples having a flat surface while wet samples have an irregular appearance due to bundle pull out (Chen *et al*. 2008), which could be caused by stronger bonding between microstructures.

Nacre or 'mother of pearl' can be seen in some aspects as a more extreme version of a crustacean exoskeleton where the calcium carbonate goes from a moderate component of the structure in a crystallised form to being the predominant aspect with chitin reduced to being a 'mortar' (Stempfle and Brendle 2006). Water has been shown to increase both the ductility and toughness of nacre at the cost of a slight reduction in tensile strength of roughly 18%, in contrast, the increase in toughness is nearly tenfold (Jackson *et al*. 1988). Toughness in this study was being measured in three different ways: a single-edged, notched tensile unstable fracture and both stable and unstable single-edged, notched three-point bending fractures. This change is predicted to be due to the water plasticising the organic matrix resulting in

a tendency for de-bonding to occur around the crack tip at the point of fracture (Jackson *et al*. 1988).

Transparency is also affected by hydration and this has been seen within other biological material. The cornea shows a decreased level of transparency with increased hydration due to an increased amount of light scattering (Zucker 1966).

1.3.5 Elastic Modulus

Elastic modulus is defined by the resistance of a material to elastic deformation (a self-reversing change) (Ashby and Jones 2012). The elastic modulus represents the tensile elasticity or more specifically the tendency of an object to deform along an axis when opposing forces are applied along that axis and in this field of study is mainly defined by the Young modulus. The mean elasticity in the main parts of the cuticle remained fairly consistent, the elastic modulus for example, generated via tensile testing in the z-direction of a sheep crab, was 511 ± 79 MPa for mean samples of a fraction of the cuticle containing both exo- and endocuticle. A purely endocuticle reading gave 536 ± 87 MPa , with the carapace having an overall tensile strength of 518 ± 72 MPa wet and 764 ± 83 MPa dry (Chen *et al*. 2008). However, when discussing the entire cuticle structure, like all physical properties it changes depending on where on the crustacean is being tested, another study comparing entire cuticle sections at different areas of the crustacean revealed a Young modulus of between 4-12 GPa against blunt contact (Amini and Miserez 2013).

The compressive modulus of the same samples (Chen et al. 2008) was shown to be higher than the tensile modulus, providing higher values in both strength and stiffness. The overall compressive modulus of the carapace was 634 ± 63 MPa wet and 1.07 ± 0.1 GPa dry, showing an approximately 40% increase compared to the tensile measurements. The difference was much greater in dry samples, with the compressive modules showing a 4.4 times increase from the tensile value of 12.9 ± 1.7 MPa to 57 ± 10 MPa. As the majority of the force applied to a crustacean carapace

is likely to be compressive in nature (i.e. collisions), a higher compressive modulus is a very important attribute to maintain.

1.3.6 Fracture Toughness

Fracture toughness is described as the ability of a material containing a crack to resist fracture (Chua *et al*. 2017). Fracture toughness is created primarily through the structure of various gradients, as these gradients lead to stress redistribution away from the point of contact and can be either smooth or sharp. Smooth gradients such as microstructural gradients, for example, changes in layer thickness (Amini and Miserez 2013) can be seen in the lamellae of the crustacean cuticle or porosity gradients (Chen *et al*. 2008) and are adaptations towards wear and tear abrasion that are seen in crustacean exoskeleton. These adaptations lead to stress redistribution beneath the point of contact and improves tolerance against contact yielding as well as minimising crack propagation (Suresh 2001).

Crack propagation resistance or fracture toughness is further enforced by sharp gradients such as organic to inorganic interfaces, or regions with abrupt variations in mineral content as seen in the crustacean integument. This resistance has been proven via mathematical modelling (He and Hutchinson 1989) (Amini and Miserez 2013) and through multiple biological examples including human teeth which have a toughness similar to that of glass yet remain incredibly resilient regardless of numerous cracks by utilising mechanisms such as this one (Chai *et al*. 2009).

The direction of impact plays an important role in how the integument reacts to fractures, Chen *et al*. (2008) showed that the structure was much more resistant to pressure from the z-axis direction *i.e*. perpendicular to the surface. The tensile strength of dry endocuticle samples in the x-y direction was found to be 12.9 MPa which was around 50% less than what was seen in the z-direction at 19.8MPa (Chen *et al*. 2008). Both this tensile strength and fracture toughness increase has been hypothesised to be due to the pore canal tubules running throughout the integument layers. Imaging showed a high density of pore canal tubules ruptured in tension and

it was proposed that the tubules act as a ductile component which helps stitch the more brittle bundles together. When pressure is applied to separate the chitin bundles leads to a stretching of the tubules before an eventual failure if enough pressure is applied and this helps provide additional toughness to the entire network (Chen *et al*. 2008). While the tubules have this positive effect on fracture toughness, they have an overall reduction in the structural strength and only exist due to mineralisation requirements. To compound this problem, due to the intensive requirements of mineralisation, canal openings make up 30% of the area of the cuticle (Nikolov *et al*. 2011). To combat this the formation of the macrostructure of regular honeycombs with thick walls guarantees the greatest possible in-plane stiffness (Nikolov *et al*. 2010). The specific geometry of this structure ensures the canal pore area is just large enough to both ensure optimal cuticle stiffness and maximal fluid transport capacity for mineralisation.

1.3.7 Transparency

The suitable comparison when looking at a transparent, protective cuticle in-depth seems to be the cuticle covering the cornea of the isopods *Ligia oceanica* (Linnaeus, 1767) and *Sphaeroma serratum* (J.C. Fabricius, 1787) (Alagboso *et al*. 2014), as they need to maintain the strength of an exoskeleton while also being transparent.

Numerous structural adaptations have been undertaken, including specialised epicuticular extensions in *L. oceanica*. These extensions are comparatively longer and regularly spaced, with the dimensions of the extensions and the distances between them below the wavelength of light (Alagboso *et al*. 2014). The spaces in between contain calcite and so it has been predicted the extensions reduce the steep change in refractive index between the epicuticle and a subjacent layer of calcite (Fabritius *et al*. 2016b) which helps the antireflective nature required. It is not difficult to imagine parallels between this and the transparent carapace of *Skogsbergia lerneri*.

S. serratum maintains a lack of pore canals in the central region of the cornea (Alagboso *et al*. 2014; Fabritius *et al*. 2016b) due to the size of the cross-section of

the pore canals being within the wavelength of visible light which would cause scattering. Where canals cannot be avoided, they are restricted to the interommatidial regions. It is more difficult to draw parallels to the transparent *S. lerneri* when considering pore canal reduction as, due to the importance of these canals, they cannot be completely removed or significantly reduced over the entire carapace instead of just a small area. Possible explanations could be smaller, more numerous pores that are smaller than the wavelength of light, more spread out pores that are far enough apart to not cause any significant visual problems or a lack of pores in the carapace directly over the eyes. Calcite found in the exocuticle was also shown to be thinner than outside of the cornea, which is suggested to perhaps be due to the birefringence property of calcite that, if too thick, could lead to a blurring of light (Fabritius *et al*. 2016b).

Compositional differences have been observed as well, most crustacean carapaces contain carotenoids however they are known to pigment the general cuticle and are absent in the corneal cuticle of *L. oceanica* and *S. serratum* (Alagboso *et al*. 2014). Therefore, it is likely that the *Skogsbergia lerneri* carapace will not contain any carotenoids.

To understand the role of this transparency, an understanding of the context of this transparency within the wider marine environment is needed. The most important questions of transparency are its purpose within the organism and whether transparency is a requirement for a particular organism or it is generated as an ancestral adaptation. Transparency is an adaptation employed by multiple animals in the ocean (Cronin 2016) as traditional camouflage is not very effective. This can be attributed to two main factors; the lack of environmental cover to camouflage in the open ocean and the additional vertical angles to be observed from (as compared to most terrestrial animals). The consequence is that organisms need two separate camouflages to deal with observation from both above and below. Unique camouflage techniques have been ultilised by some animals, such as the reflective sides of fish (Denton 1970) or bioluminescent counterillumination (Claes et al. 2014) to prevent being backlit from below. However both of these have issues that prevent

such adaptations being effective always, such as the movement of the animal or specialised adaptations of predators (Cronin 2016).

Initially transparency could be deemed an adaptation developed by a particular species with this attribute; the phylogenetic distribution of transparency is diverse, uneven and highly influenced by the environment (Johnsen 2001). However several factors complicate this issue when it comes to *S. lerneri*. First, is the concept that any organism small enough will be transparent. The interactions of light is covered in chapter 6 but to simplify: the thinner a material is, the less light interacts with it and so the closer the material will be to transparent, as understood by the Beer-Lambert law modified for solids (Fox 2010). As such, organisms that are small enough will be transparent inherently, rather than due to a specific adaptation caused by environmental pressure. *S. lerneri* could fall into this category due to the small size of the animal and the thinness of the carapace overall.

Another potential issue is the phylogenetic link between *S. lerneri* and other ostracods. A closely related ostracod from the same subfamily, *Photeros annecohenae* (Torres and Morin, 2007) is bioluminescent (Gerrish and Morin 2008). As such *P. annecohenae* would posses a transparent carapace to utilise this bioluminescence regardless of any protective benefit. Therefore a transparent carapace may have nothing to do with the survival of *S. lerneri* and instead could be an ancestral attribute that the *S. lerneri* has not had a need to change. Due to these factors there is a possibility that the *S. lerneri* carapace may not be specifically adaptated for camouflage or that there even are structural or compositional features within the carapace at all. Therefore, transparency outside of the eye window is merely inherent.

1.4 Aims and Hypothesis

1.4.1 Overall Hypothesis

S. lerneri will possess an ultrastructure and composition, different to that of similar, non-transparent ostracods, that allows it to maintain carapace transparency and retain the mechanical properties of similar, non-transparent crustacean carapaces of similar size.

1.4.2 Overall Aim

To analyse the structure and composition of the *S. lerneri* carapace, to further our understanding of their contribution to the physical properties (transparency and strength) of the carapace.

1.4.3 Hypothesis 1

The ultrastructure will have a resemblance to other ostracod species, however specific differences in the structure will be seen to allow for the observed transparency. Changes seen during development will follow that of other ostracods.

1.4.4 Aim 1

To determine the ultrastructure of the *S. lerneri* carapace architecture and if it alters through the ostracod's developmental stages.

1.4.5 Hypothesis 2

A signal specific to chitin, will be derived from non-linear microscopy signals, and will enable analysis of chitin expression to be performed in the ostracod carapace, showing higher levels of chitin expression at later developmental stages.

1.4.6 Aim 2

To develop a non-invasive imaging technique to examine chitin expression and distribution throughout the *S. lerneri* carapace.

1.4.7 Hypothesis 3

Elemental composition and polymorphs of calcium carbonate, together with their distribution, will share a similarity with the standard crustacean carapace but with a unique composition in order to maintain *S. lerneri* carapace strength and transparency. However, the composition will be modified as the ostracod develops.

1.4.8 Aim 3

To analyse the elemental composition of the *S. lerneri* carapace and how it changes throughout the ostracod's developmental stages

1.4.9 Hypothesis 4

The *S. lerneri* carapace will have optical properties similar to that of other biologically transparent materials across the visible spectrum, but will maintain mechanical properties consistent with the carapaces of crustaceans similar in size.

1.4.10 Aim 4

To evaluate the physical properties, optical and mechanical, of the carapace.

Chapter Two

Methodology

2. Methodology

2.1 Aquaculture

2.1.1 Licensing for the Acquiring and Transportation of Samples

For collection off the east coast of the Florida Keys (Keys Marine Laboratory) and transport of ostracods (*Skogsbergia lerneri)* into the UK, several permits were required. These were: special activity licenses (SAL-16-1796-SR and SAL-19-1796-SR); Florida Keys National Marine Sanctuary permits (FKNMS-2016-116 and FKNMS-2018-116); a Fish Health Inspectorate authorised aquaculture production business certificate (following an inspection in the US via an authorised veterinarian) and a general import authorisation license. *S. lerneri* were identified via their size (capture nets porosity allowed *S. lerneri* only to enter), the location of their habitats and general features as stated by Cohen (Cohen 1983). Collection, identification and transportation of ostracods were carried out personally by Lifescaped Ltd.

2.1.2 Transfer of Ostracods from Deliveries to Aquaculture Tanks

During shipment (Airsupply, Slough) by air into the UK, and to Cardiff, the ostracods were contained within sealed bags containing their natural seawater within insulated boxes that were fitted with an air pump to ensure survival during transport.

Before adding the new ostracods to the aquaculture tanks (described below) in Cardiff, the ostracods were acclimatised to the tank conditions. The ostracod-containing sealed bags were placed in the tank for 45 minutes to bring the new ostracods to the correct temperature (25˚C). The bags were then opened to release the ostracods with Florida seawater into an 18-litre bucket, to which a slow transfer of aquaculture tank water was added to fill the bucket with a ratio of 1:2 Florida seawater:tank water. Hot water was added to excess water from Florida and disposed of via lab sinks, to prevent its contamination of the general UK water systems. Water transfer was performed through a drip tube, starting very slowly and

increasing throughout the transfer to prevent shock. Once the bucket was full, the traps were released and ostracods were added into the tank safely using smaller, 2-litre buckets.

2.1.3 Maintenance of Aquaculture

After the new ostracods were added, water changes were carried out using artificial seawater using Pro-Reef Sea Salt (Tropic Marin, Wartenberg, Germany, CAT: 10551), created at a salinity of 35 parts salt mixture per 1000. Testing was carried out daily for several days until ammonia and nitrate/nitrite levels were optimal.

The Cardiff, ostracod aquaculture was in custom-built specialised tanks (see Fig 2.1), which enabled the ostracods to breed. The aquaculture ecosystem (*i.e*. near-identical to their natural habitat) was maintained with salt water (mentioned above). Additionally, to maintain optimal conditions, tank water was tested twice weekly for pH levels, salinity, temperature (Table 1). The concentrations of ammonia, nitrite and nitrate were also tested twice weekly via NH_4^+/NH_3 and NO_2/NO_3 test kits from Tropic Marin (Wartenberg, Germany, CAT: 28270 and 28260 respectively). The water in the

Figure 2.1: The two ostracod aquaculture tanks used for housing the ostracods throughout the project. Each tank was split into smaller separate containers to allow for easy locating of the ostracods.

tank was renewed by 18-54 litres a week, with the larger volume water changes being performed when tank water conditions were not optimal.

Ostracods were fed twice a week with fish (Tropical Marine Centre, Gamma Slice, frozen Whole fish, CAT: 8474), the remains of which were removed several hours after introduction to prevent the build-up of ammonia, nitrate and nitrite to damaging levels.

Parameter	Optimum level
Salinity	35 (ppt)
pH	pH 7-8
Ammonia	0.02-0.05mg/L
Nitrate	0.5-1mg/L
Nitrite	0-0.02mg/L
Temperature	25-26^{o}C

Table 2.1: The optimal conditions for *S. lerneri* ostracods within the aquaculture tank. Note that ppt represents parts per thousand.

2.2 Dissection

2.2.1 Development of dissection protocol

Ostracods were removed from the aquaculture tank and anaesthetised in ice-cold water for 5 minutes, before being transferred and sacrificed in 30% ethanol. Initially, ostracods were placed in 4% paraformaldehyde to fix the animal immediately after death. However, this led to an embrittling of the carapace with cracking during the dissection process which would damage the samples. Instead, fixation was performed after the dissection process had been completed.

The ostracod was placed on a slide and immersed in a small amount of PBS which in combination with the 30% ethanol relaxed the muscles for easier dissection (Namiotko *et al*. 2011; Martens and Horne 2016). The ostracod was securely

supported from the back at the hinge by an insect pin (attached to a long wooden handle) or a microdissection needle and a razor blade or scalpel was inserted into the front opening, between the 2 valves, of the ostracod near the furca. The blade was

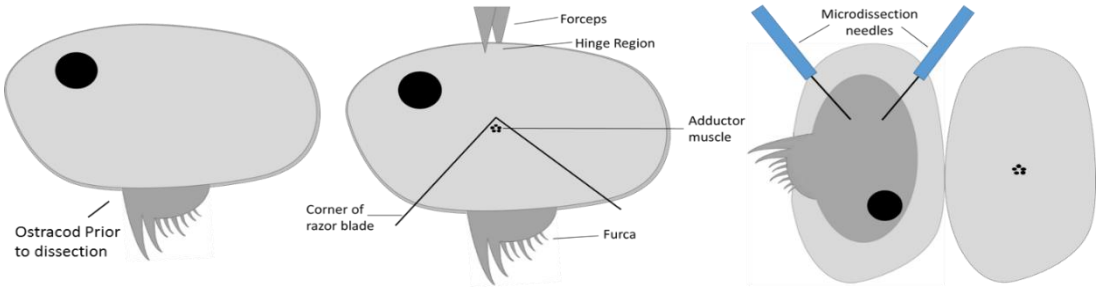

Figure 2.2: A diagram detailing the process of ostracod dissection. Once the body has been removed the carapace is checked to make sure there were no remaining pieces of tissue.

then pushed up following the curve of the shell to sever the adductor muscles, which when carried out on both sides allowed for easy, clean removal of the body tissues. The dissection technique can be seen in figure 2.2.

2.2.2 Dissection Axes

Across all experiments, any transverse sections taken, were selected from a distance of one-third of the length from the anterior of the carapace (being defined as the end

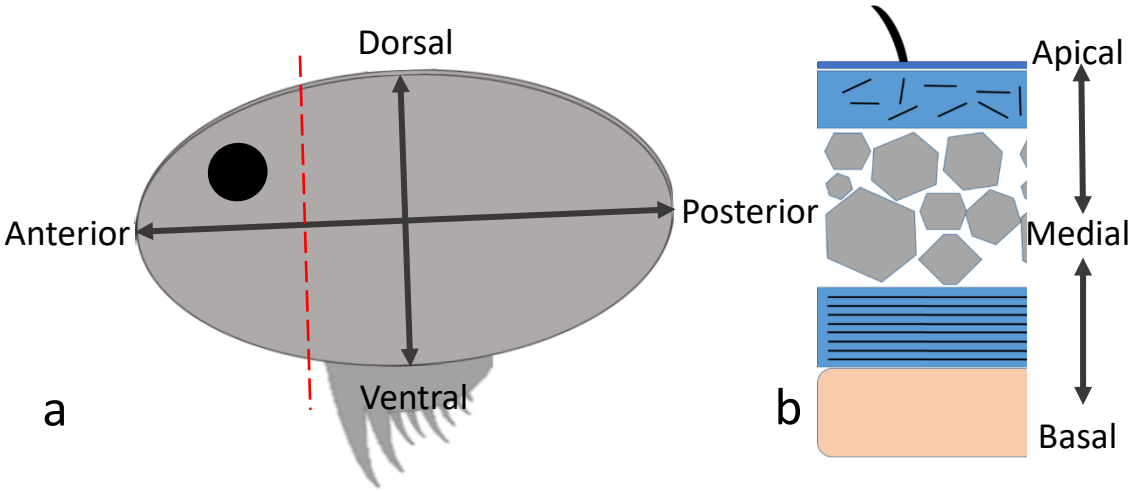

Figure 2.3: The anatomical axes stated for **a)** the ostracod and **b)** the cross-section of the carapace, as a reference for the TEM imaging. The red dotted line indicates where dissection takes place for transverse cross-section images.

nearest the eyes and mouth). This was to ensure that data were recorded consistently from a similar position in all samples. Throughout the thesis all directional axes will refer to the directions seen in figure 2.3.

2.3 Electron Microscopy

2.3.1 Transmission Electron Microscopy (TEM)

Single valves from each sample were fixed in modified Karnovsky fixative (2% paraformaldehyde, 2.5% glutaraldehyde (Karnovsky 1965)) in 0.1M sodium cacodylate buffer for 2-3 hours at pH 7.2-7.4 at room temperature and then washed in the same buffer. Samples were then immersed with 1% osmium tetroxide (TAAB, Berkshire, UK, CAT: O015/1)/1.5% potassium ferricyanide (Thermo Fisher Scientific, Waltham, USA, CAT: 10414583) and place on the rotator for one hour. Next, the tissue was immersed in heated (60^{o}C) 1% thiohydrocarbozide (Sigma Aldrich, St. Louis, USA, CAT:88535-25G) for 20 minutes, 1% osmium tetroxide for one hour, 1% uranyl acetate (aqueous) overnight and finally Walton's lead aspartate (Walton 1979) for one hour at 60^{o}C. Samples were rinsed in distilled water 3 times for 10 minutes in between every step and care was taken to remove as much liquid as possible at each step to prevent overstaining. The tissue was then serially dehydrated through 70%, 90%, 100%, 100% ethanol for 15 minutes each, before further dehydration in acetone/ethanol (1:1), 100% acetone, 100% acetone again for 15 minutes each.

The resin, Durcupan (Sigma Aldrich, St. Louis, USA, CAT:44610), was made up at a concentration of 22.8ml of component A, 20ml of B, 0.6ml of C and 0.2ml of D. A, B and a conical flask was pre-warmed in the oven at 50^{o}C for 5-10 minutes. Resin infiltration was started by keeping the samples in acetone/Durcupan (1:1) for 2 hours. The samples were transferred to acetone/Durcupan (1:3) for two hours and then pure Durcupan resin overnight with the vial tops off. Durcupan was renewed twice over 6 hours, and then samples were individually embedded into moulds and placed into an oven at 60^{o}C for a minimum of 24 hours.

Once fully hardened, sample blocks were trimmed down to a small trapezoid with a razor blade around the sample to remove excess resin. The trapezoid shape minimises compression of the resin during the cutting process. They were then

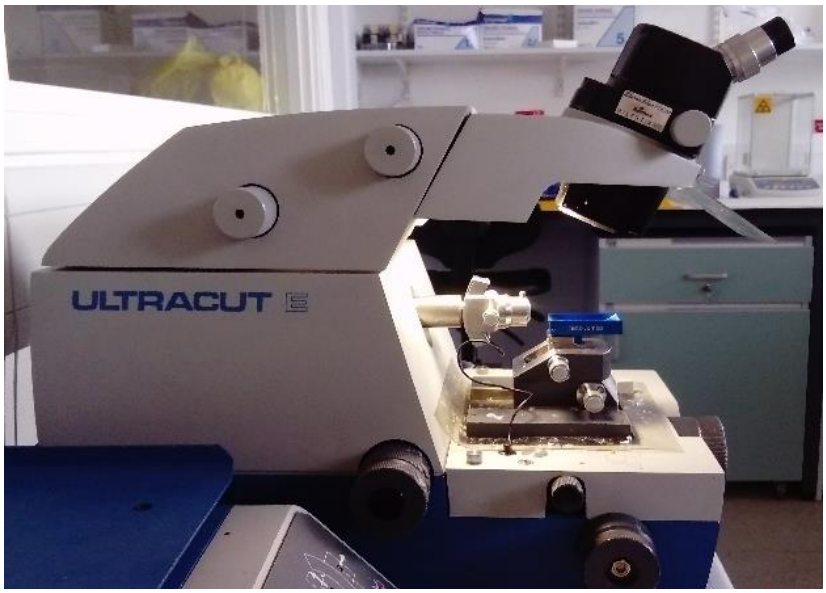

Figure 2.4: The Ultracut E ultramicrotome with an 8mm diamond knife with microscope attachment.

'polished' by cutting the block with a glass knife on a Leica EM UC7 ultramicrotome (Reichert-Jung Ultracut E) to create a smooth surface, seen in figure 2.4. A glass knife was created by using a glasscutter (Leica EMKMR2). Then 100nm ultrathin sections, identifiable by their golden sheen, were cut from each block using the ultramicrotome and an 8mm diamond knife (Diatome, Midau, Switzerland, CAT:DH4580) set at a 45° angle. Sections were collected on G300hex copper grids (Taab, Berkshire, UK, CAT:GC060/C), dried on filter paper in a Petri dish and stored ready for TEM.

Initial optimisation of the protocol tried both a marine optimised version of the fixative piperazine-N,N'-bis(2-ethanesulfonic acid) (PIPES) (Baur and Stacey 1977) and filtered water from the aquaculture tank to help prevent damage through osmosis. Unfortunately, the PIPES fixative did not prevent cellular breakdown and the filtered tank water did not produce as optimal a result as the Karnovsky fixative.

Additionally, since the same sample blocks were required for subsequent SBFSEM, en bloc staining (described above) with uranyl acetate and lead aspartate before sectioning was determined to be optimal, over grid staining for all imaging. This

substantially reduced preparation time for the TEM sections and maintained near-identical conditions for both TEM and SBFSEM. TEM was carried out first, as the relatively few sections taken would prevent any major change in carapace depth between the techniques. This meant the same samples could be used, both to increase sample number and allow for sample comparison between the two techniques. It also prevented the potential loss of samples that can be caused by the precipitation of lead during on grid staining.

TEM was carried out using a Jeol 1010 microscope using an accelerating voltage of 80kV. Electron microscope images were collected on a Gatan Orius 1000 CCD TEM camera. Images were taken at a 1 second exposure time with a beam current of 68µA at 1.5k, 4k and 10k magnifications using Gatan digital micrograph software.

2.3.2 Serial Block Face Scanning Electron Microscopy

Following block sectioning for TEM, the sample blocks were cut to create a smaller surface area for SBFSEM (see figure 2.5). Sample blocks were cut into a square shape to prevent debris build-up within the ultramicrotome that could obstruct the images.

Following trimming the modified block was chopped off with a razor blade, superglued onto a sample pin (Leica, UK, CAT:16701950), and cemented with silver epoxy resin (Agar, Stansted, UK, CAT:AGG3349) (figure 2.6).

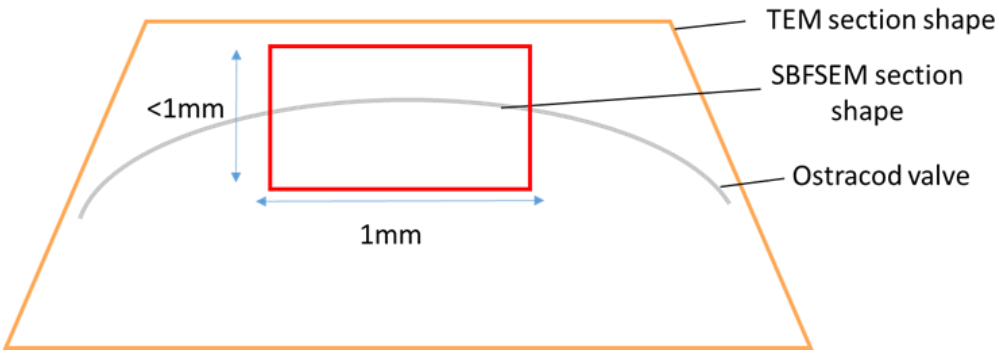

Figure 2.5: The size and shape of the different resin blocks as compared to the sample embedded in the resin. The SBFSEM sections were 1mm width maximum and 1mm in height maximum, whereas the TEM sections encompassed the sample in its entirety.

The sample was then gold-coated at 7nm thickness and placed into the Zeiss Sigma VP FEG 3view Scanning Electron Microscope using Gatan Digital Microscopy software

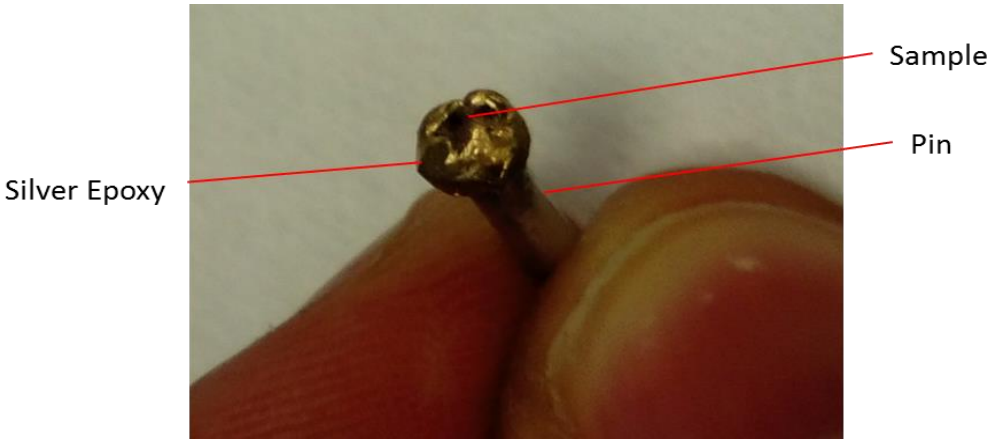

Figure 2.6: The cut off, trimmed resin block, attached to the sample pin via the silver epoxy

(Gatan, ver 3.3.2), as seen in figure 2.7. The voltage and vacuum were set at between 2-3 KeV and 26-31 Pa respectively. Due to the semi-vacuum conditions of the microscope chamber, these conditions were altered to create optimal conditions

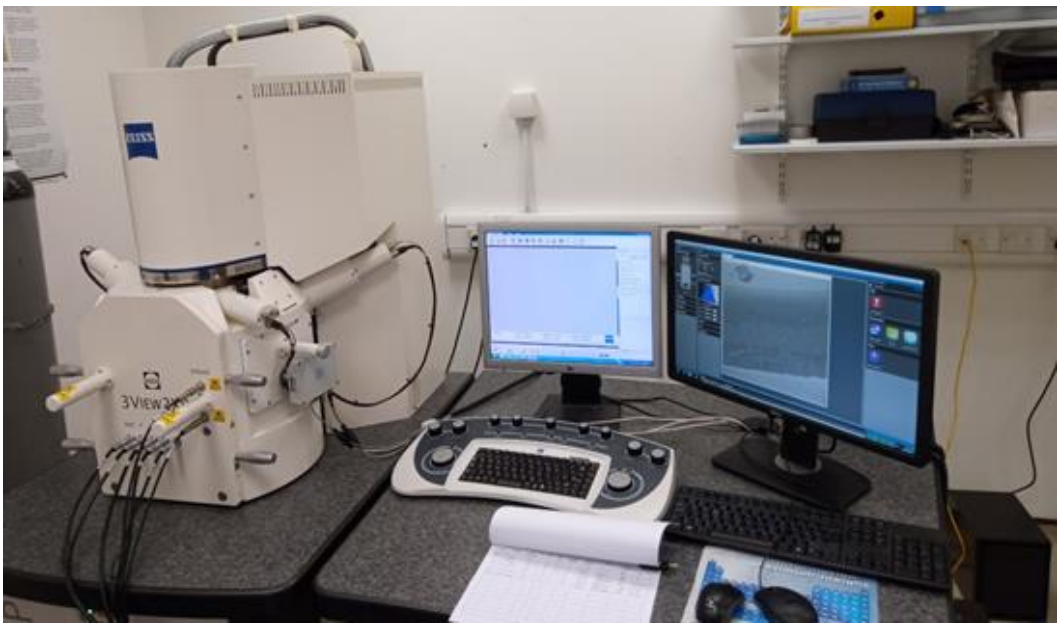

Figure 2.7: The SEM and attached computers processing a sample. The original chamber of the SEM has been replaced with the 3view system as can be seen in the bottom left of the image.

without damaging the samples. Images were taken at 4Kx4K with a resolution of 7.5nm per pixel and a pixel dwell time of 8µs. SBFSEM images were acquired from the block face, using the Gatan 3view 2XP system. Serial slice images were acquired

automatically following successive 50nm thick cuts by the 3view micro-ultramicrotome. Approximately 1000 serial images per tissue block were taken and imported into the 3D modelling software, Amira version 6.0.1. The images were then resampled to provide a reduced resolution suitable for 3D modelling.

2.3.3 Amira Software

Images generated from SBFSEM were imported into Amira as tifs and were resampled from their original input resolution (4096x4096x468) to a lower resolution (1024x1024x468) for better clarity and processing. For models generated by automatic thresholding a 'volren' object was created and the colourmap minimum and maximum values were adjusted for best visualisation.

For manually created models Amira was switched into 'Segmentation' mode and the resampled tif images were selected for tracing. Labels were created for each wanted material and position and shape of each was then manually traced. The trace was repeated for each image slice and the number of image slices was dependent on how many were needed to properly recreate the structure (normally 50-100). Amira was then swapped back into 'Project' mode and the 'generate surface' object created, once the correct label was selected the 'surface view' object was created.

All videos were created within Amira's animation and rendering properties within the 'Animation' tab. Videos were exported as .avi formats.

2.3.4 Scanning Electron Microscopy

Samples were fixed in Karnovsky fixative for two hours and placed in 0.1M Na cacodylate buffer. Afterwards, samples were washed thrice in distilled water before being dehydrated. Samples were serially dehydrated through ethanol in steps of 70%, 90%, 100% and 100% again for 30 minutes each. Further dehydration was carried out via the addition of hexamethyldisilazane (HMDS), (Thermo Fisher

Scientific, Waltham, USA, CAT: 11492108), firstly in a 1:1 concentration with 100% ethanol for 30 minutes and then in 100% HMDS for another 30 minutes. Samples were then placed in a desiccator in the fume hood, topped up with HMDS and left until all liquid had fully evaporated. The vial lids were removed to assist dehydration, however, parafilm was placed over the opening and holes created in the film with scissors. This was to prevent extremely rapid evaporation of the HMDS, which can cause damage to the sample. Samples were placed on adhesive Liet discs and then coated with 9nm of gold to prevent electron charging.

2.4 Non-linear microscopy Sample Preparation

Non-linear analysis was carried out for the purpose of determining if chitin within the samples generated non-linear signals (second order) that could be used to examine the distribution of chitin within the carapace.

2.4.1 Cryosectioning

Initially, cryosections of ostracod valves at all instars were to be used for non-linear microscopy. Tinfoil holders were created with a circular base around 2cm wide and 4cm long and were then filled with OCT. Isopentane was cooled in liquid nitrogen, then samples were then snap-frozen in the isopentane and then placed into the OCT in the sample holder, which was placed into the isopentane until frozen. Blocks were stored at -80^{o}C. Sections were cut from the frozen OCT samples with the use of the Leica CM3050S cryostat (see figure 2.8) at a thickness of 30µm with a cutting temperature of -21^{o}C. Sections were placed onto Superfrost Plus slides, coverslipped in PBS and sealed with nail varnish.

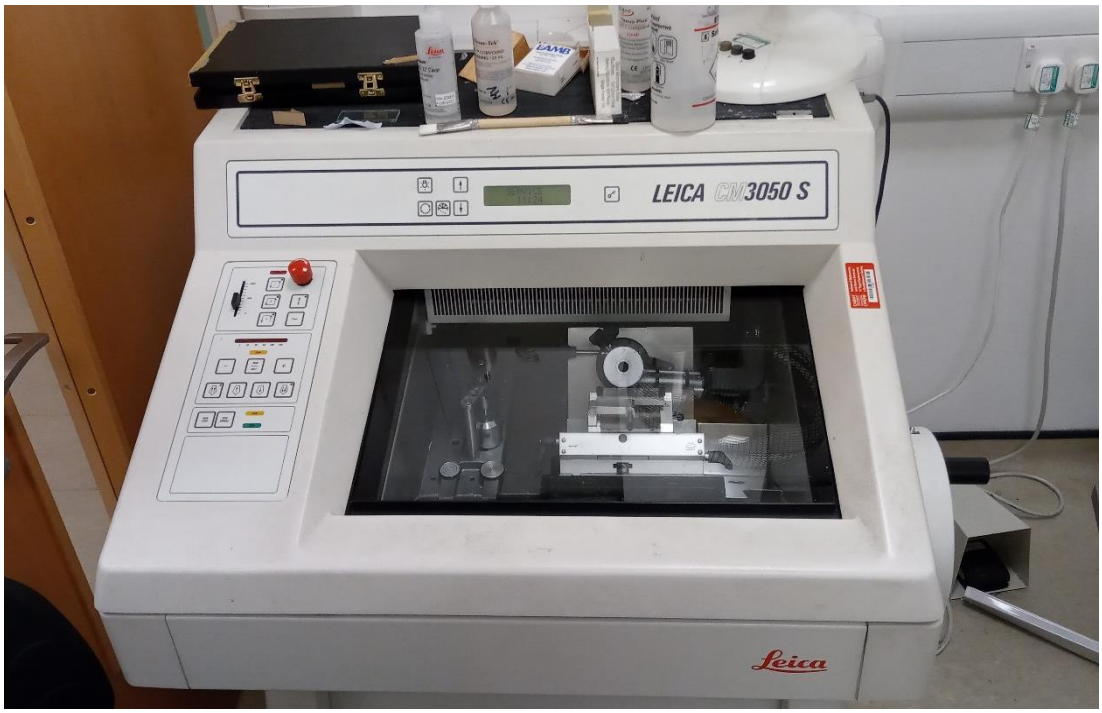

Figure 2.8: The Leica CM3050S cryostat while not in use, the internal temperature of the chamber is kept to above -20°C to prevent the OCT from melting.

Unfortunately, samples embedded in optimal cutting temperature (OCT) compound did not produce sections with good morphology; the samples were found to smear instead of cutting cleanly. This was believed to be due to the difference in hardness between the sample and the frozen OCT.

2.4.2 Butyl:methyl methacrylate (BMMA)

2.4.2.1 BMMA Resin Creation

BMMA is a plastic resin that was chosen as an embedding media to replace OCT for production of sections prior to non-linear microscopy.

BMMA was created by mixing butyl methacrylate and methyl methacrylate (Sigma Aldrich Corp., St. Louis, MO, USA, CAT: 235865 and M55909 respectively) at a ratio of 1:4 for 30 minutes. The hardness of the resin could be increased by increasing the

proportion of the methyl to butyl methacrylate. Dithiothreitol (Sigma Aldrich, CAT:10708984001), a reducing agent, was added to the mixture to a final concentration of 5mM. Benzoin ethyl ether (Sigma Aldrich, CAT:172006), a photo-inhibitor, was added to provide 0.3% total volume. The BMMA solution was degassed with inert N_2 gas for 30 minutes to prevent polymerisation due to excess oxygen. The final BMMA solution was kept at -20^{o}C to prevent premature polymerisation from heat and ambient light.

2.4.2.2 Sample preparation

Valves were embedded in BMMA resin according to the embedding protocol previously reported (Parfitt *et al*. 2012). In brief, samples were fixed with 2% paraformaldehyde in PBS, pH 7 for 24 hours, then embedded in low melting point 3% agarose (ThermoFisher Scientific, CAT:R0801). The agarose had been heated at a temperature above 67^{o}C, maintained above that temperature in a beaker of hot water and degassed with a vacuum pump to remove bubbles. Once embedded in the agarose, the samples were arranged into the preferred orientation to allow transverse cross-sections to be cut and were cooled on an ice block to below 25^{o}C to set the gel. The samples were then cut out of the gel with a biopsy punch and placed into individual capsules. They were serially dehydrated through increasing concentrations of ethanol at 50%, 70%, 90%, 100%, 100% at 30-minute intervals and then infiltrated with increasing concentrations of ethanol:BMMA solutions; 2:1, 1:1, 1:2 for a minimum of 3 hours per step. Finally, the samples were placed in fresh 100% BMMA and polymerised under UV light at 4^{o}C overnight. Blocks were stored at room temperature until sectioning.

Chitin flakes were for testing were acquired from Sigma-Aldrich (St. Louis, USA, CAT:C9213) and were coverslipped in air for analysis.

2.4.2.3 Sectioning

Samples were serially sectioned at 2µm thickness using the Ultracut E ultramicrotome equipped with an 8mm diamond knife with microscope slide attachment. Serial sections were placed in ribbons onto poly-L-lysine-coated slides (Thermo Scientific, CAT:10219280) and then left to adhere on a 70^{o}C hotplate for a minimum of two hours.

2.4.2.4 BMMA removal

If required for imaging, the BMMA resin was removed from the sections by immersion in acetone for 10-30 minutes. Initially, deplasticising was performed for 10 minutes, but the longest duration showed a greater removal of BMMA. Sections were then rehydrated through a series of ethanol concentrations at 90%, 70%, 35%, 10 minutes each, and finally rinsed in PBS for 10 minutes. Slides were then coverslipped in PBS and sealed with nail varnish.

2.4.3 Equipment and software

A pulsed femtosecond Ti:Sapphire Chameleon laser (Coherent) was used for excitation of samples over a range of 700nm-1050nm. This was because chitin-derived maximum intensity signals were suggested to be emitted around 450-460nm for SHG and 520nm for TPEF based on 2 previous studies (Gualda et al. 2007; Reinhardt et al. 2017). In cases where wavelengths lower than 700nm were to be excluded, a 690+ nm beam splitter was used. The Two Photon Excited Fluorescence (TPEF) and Second Harmonic Generation (SHG) emission filters were set at 505/119nm and 400/12nm respectively. All forward propagated signals were detected by a NDD.2 (non-descanned) detector (Zeiss, Oberkochen, Germany) and all back-propagated signals were collected either by a BiG.2 (Zeiss) or an internal Gallium Arsenide Phosphide (GaAsP) (Zeiss) detectors.

Images were captured as single images and montages in 2D. A Zeiss Axio Examiner Z.1 captured images and Zen 2.3 (black) (ver.14.0.0.201) (Zeiss, Oberkochen, Germany) was used to collate and analyse all images. All calibration and scale bars were provided in software by Zen (ver.14.0.0.201). Images were taken with a resolution of 512x512 pixels and an image size of 212.55x212.55µm with a pinhole size of 601 Airy units. 20x 0.8 NA air and 40x 1.3 NA oil immersion objective lenses were used throughout these experiments.

For laser power testing, a power meter (Thor labs) was fitted in place of a sample to test the energy reaching the sample. The laser wavelength was set to 800nm and the percentage was increased linearly and the mean power reading was taken.

2.5 X-ray Microtomography and Ptychography

X-ray microtomography and ptychography was carried out in order to perform 3D analysis of the ostracod carapace at high resolution, without any of the potential damage caused by sample preparation and/or sectioning needed for other techniques.

2.5.1 X-ray Microtomography

Ostracod samples were used at the Diamond Light Source synchrotron near Oxford, UK on beamline I13-2. Data were generated of both the whole ostracod and carapace valves mounted onto metal pin sample holders (CN Technical Services Ltd, Wisbech, UK) at 4x for the whole and 10x magnification for the carapace valve. A monochromatic beam was used with a pco.edge 5.5 detector and scanned through a 180-degree rotation. 4x total magnification for the whole ostracod used 0.5 second scan acquisition time, with a 12cm detector distance from the sample. 10x magnification for the carapace valves used a 0.2 acquisition time with a 22.5cm detector distance from the sample. Reconstruction of scans was carried out via a series of tomocommands in Savu (ver 0.1) and ImageJ (ver 1.5.1) before being rendered in Avizo 9 3D imaging software (ver 2019.1).

2.5.2 Ptychography

Ptychography is a method of computational imaging that uses coherent diffraction imaging to generate 3D models (Pfeiffer 2018). Multiple overlapping diffraction patterns are taken by scanning an x-ray probe over a specimen. Coherent interference patterns are processed with intensive reconstruction algorithms to generate a 3D reconstruction. After dissection, ostracod valves were frozen at -20^{o}C to prevent degradation. At Diamond, the valves were cut into a sharp point with a scalpel for better focusing. Samples were then glued to metal pins, placed in the beam for scanning (see figure 2.9) and Bragg ptychography was then carried out.

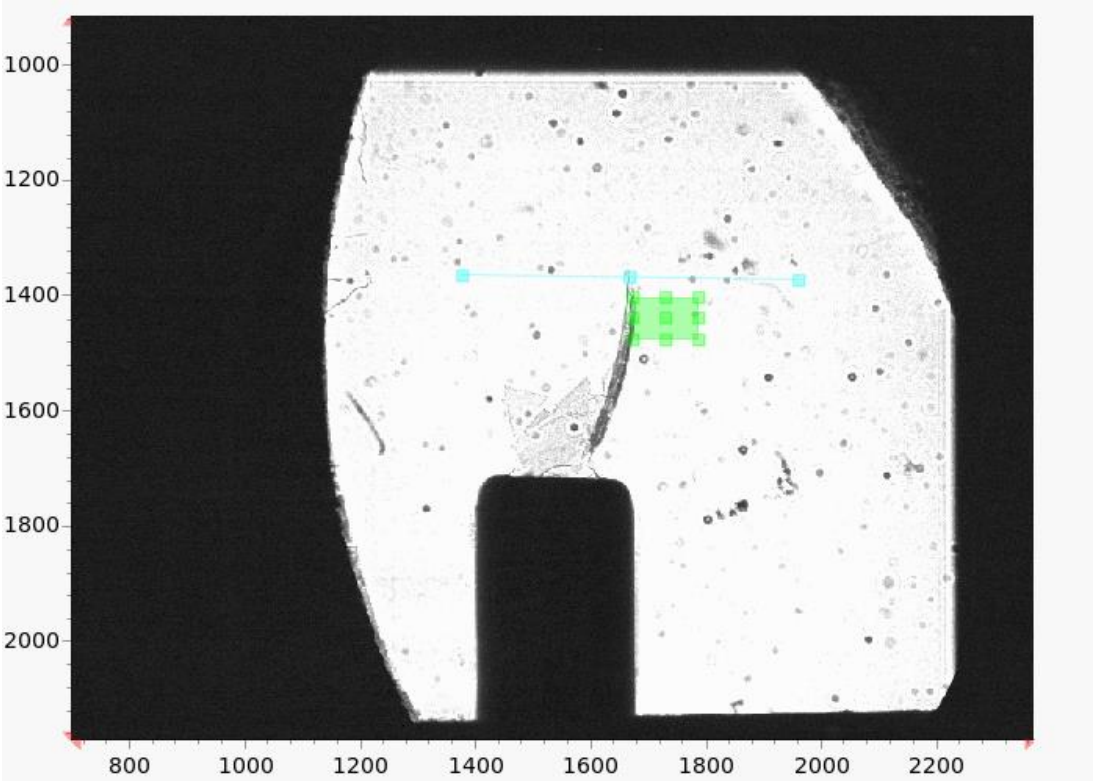

Fig 2.9: Sample attached to the pin on the I13-2 beamline. Here the entire sample can be seen, the left half of the valve has been cut away to form a point. The blue line shows the total sample rotation with the middle point being the centre of rotation that the sample should be aligned to. The green square is used for alignment of the sample with the camera, with the area of interest being centred on the top left corner of the square.

An Excalibur ODIN detector was used at a distance of 14.5 metres using a silicon monochromator (silicon 111 double crystal) as seen in figure 2.10. Experiments were carried out at 9.7KeV energy with an exposure time of 0.05 seconds with a beam size of 15µm and a wavelength of 0.1278nm. Samples were scanned to acquire 600 images through a 180-degree rotation. Images were then initially reconstructed using Tomocommand to determine the value for the centre of rotation. This value was then used in DAWN software (ver 2.5.0) to determine a more accurate centre of rotation, obtained with the most focussed image. Both Dr Silvia Cipiccia and Dr Darren Batey

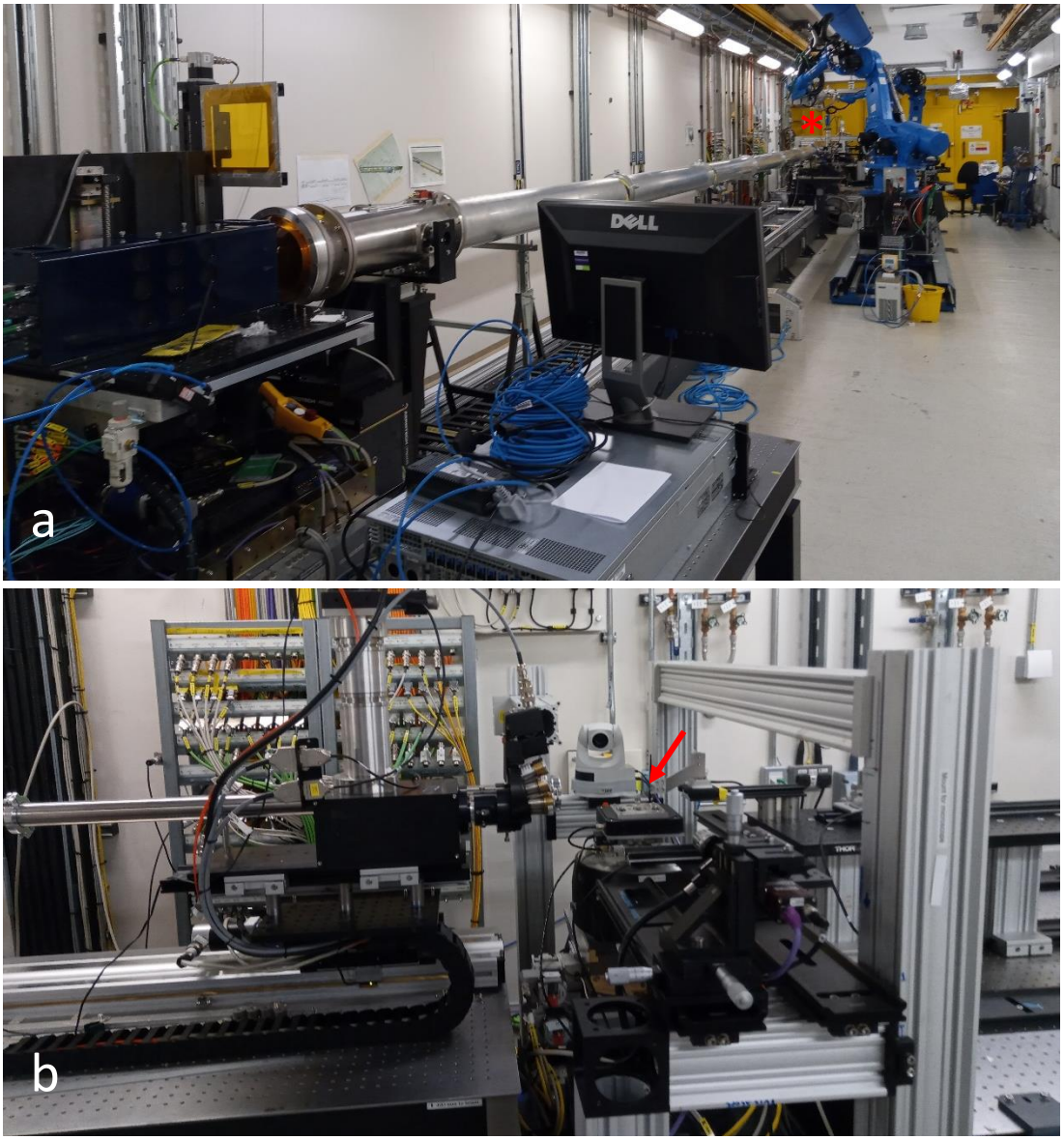

Figure 2.10: a) The beamline setup for I13-1, the ptychography station showing the beamline with the detector is at the near end of this photo. * denotes the position of the sample station, also shown in **b)** and indicated by the arrow.

generously assisted with the use of the beamline equipment and the generation of the 3D models afterwards.

2.6 Elemental Analysis

2.6.1 Energy-dispersive X-ray spectroscopy

Energy-dispersive x-ray spectroscopy (EDS) was carried out for the purpose of discovering the distribution of elements within the ostracod carapace by layer. Samples were fixed in modified Karnovsky fixative (Karnovsky 1965) in 0.1M Na cacodylate buffer ($Na(CH_3)_2AsO_2$) for 1 hour and then serially dehydrated with ethanol and HMDS as previously described for SEM protocol in Section 2.3.2. Samples were then dissected transversely so that their cross-section was visible and placed on carbon adhesive Leit discs (Agar Scientific, Stansted, UK, CAT:AGG3357N). These were then mounted on aluminium stubs (Leica, UK, CAT:16701950) and sputter coated with an 8nm layer of gold via an EM ACE 200 low vacuum coater (Leica, Wetzlar, Germany) and a Pascal 2005SD vacuum pump (Pfeiffer vacuum, Aßlar, Germany). Samples were analysed by a Tescan Maia 3 field emission gun scanning electron microscope (FEG-SEM) fitted with an $XMAX^N$ 80 energy dispersive X-ray detector (Oxford Instruments, UK) at 10.0kV using a finely polished cobalt standard. Images were acquired using the secondary electron and backscattered electron detectors. Analysis of the intensity ratios of the Kα line of carbon, oxygen, calcium, magnesium, phosphorous, silicon, sodium and fluorine generated semi-quantitative measurements of signal intensity. Values for other trace elements were also found but were not analysed.

Data analysis was carried out using Oxford Instruments Aztec software (Ver 3.3) with a map sum spectrum being generated for each element in the sample showing counts per second against energy. All data were collected from energy release generated from the K electron shell. Multiple peaks are generated for heavier elements and so the combined value of all peaks was used. Comparison of elemental signal intensity against a referential elemental standard allowed for the total amount of each

element within the sample to be calculated. The data were then mapped against the original SEM image to reveal individual elemental localisation. Dr. Tom Davies generously assisted with using the microscope for the generation of the images.

2.6.2 X-ray Fluorescence

X-ray Fluorescence (XRF) was carried out for the purpose of analysing the elmental composition across the entire carapace in order to determine the overall elemental distribution of the carapace (as apposed to in the vertical cross-section examined in EDS).

Dissected ostracod valves that were used for synchrotron analysis at the Diamond beamline I18 (Mosselmans *et al*. 2009) were frozen at -20^{o}C after dissection and during travel to prevent degradation before analysis. Some samples were briefly fixed in 4% paraformaldehyde before also being frozen to prevent embrittling and to maintain equal conditions to the others. The paired valves were separated and placed on Kapton adhesive tape.

The beamline used for x-ray fluorescence had a cryogenically cooled Si (111) monochromator. A 2µm x 2µm beam size was used on the sample with a four-channel silicon drift detector (Hitachi High-Tech Science Corporation, Tokyo, Japan) at a distance of 26mm.

XRF was carried out at both high and low energy modes. Low energy XRF was used to detect magnesium, potassium, sulphur, chloride and silicon signals and was carried out at 3keV with an exposure time of 0.05s. High energy XRF was utilised to examine calcium expression and was carried out at 4.8keV with an exposure time of 0.02s. Both high and low energy XRF studied the same samples via raster scans over an area between 0.85x0.5mm and 2.2x1.3mm with 5µm step increments.

During analysis, the samples were contained within a helium bag to both prevent unwanted interaction between the beam and the heavier oxygen, and to help reduce the dehydration of the sample over time.

PyMCA X-ray fluorescence software (ver. 5.3.1) (European Synchrotron Radiation Facility) was used to analyse the data generated from low energy XRF analysis. Data

were fitted to an active curve generated from a silicon and chlorine-based calibrant. This generated a plot of the elements against their total concentration. The data analysis was modified with an attenuator thickness of 0.003mm and a Fano factor of 0.12. Data were normalised across the samples and colour maps of individual elemental distribution were generated.

High energy XRF was processed with Diamond Synchrotron's DAWN software. Under the Mapping perspective, data were imported and processed via the XRF Elemental maps option. In this maps option, the Kα version of calcium was selected as the element chosen for analysis, this generated an elemental map of calcium distribution throughout the valve.

2.6.3 X-ray Absorption Near Edge Structure

X-ray Absorption Near Edge Structure (XANES) analysis was carried out for the purpose of identifying the species of calcium carbonate polymorphs present within the ostracod carapace. Samples were prepared as described in section 2.8.2. The XANES experiments were performed at the same station with an identical beam size and monochromator as XRF. The mechanically bent Kirkpatrick-Baez Si mirrors were used for the XANES mapping at the Ca *K*-edge to provide harmonic rejection. XANES was carried out as a series of four- or six-point line scans along the ostracod in either 300/200/150/100 µm steps, dependent on which would capture the majority of the valve. The experiment was run at 4.2keV using the silicon stripe on the harmonic rejection mirror (HRM).

Data generated from this experiment were analysed via Athena: XAS Data processing software (Demeter version 0.9.26). The values were normalised against a known calcite sample at both the upper and lower limits of the energy values. The elements examined during this experiment were light enough to need only k-edge energy spectra comparison. Through this analysis, the different polymorphs of $CaCO_3$ could be identified via comparison with previously characterised $CaCO_3$ absorption spectra (Brinza *et al*. 2013). Determination of the different polymorphs with previous

literature was aimed at four factors: the pre-edge region, the shoulder peak at around 4025eV, the number of peaks and presence of peaks in the post edge region (fig 2.11).

Dr Fred Mosselmans generously assisted with the use of the beamline equipment for XANES and XRF and helped with processing the generated data.

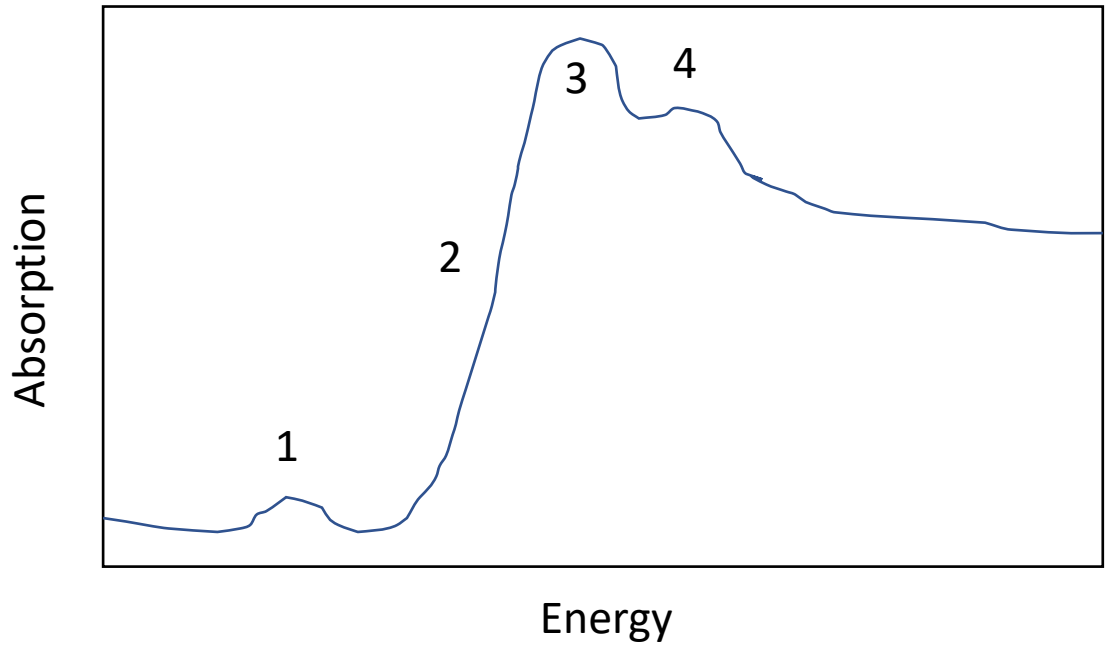

Figure 2.11: A representative XANES spectrum with the four important areas labelled. 1: the pre-edge, 2: the shoulder peak, 3: the peak and 4: the post-edge region.

2.6.4 Wide Angle X-ray Scattering

Wide Angle X-ray Scattering (WAXS) was carried out for the purpose of chitin analysis within the *S. lerneri* carapace, to determine if chitin spacing differed to previously observed spacing identified in other ostracod species, due to the carapace's transparency. Unfixed samples were held between clingfilm and placed in the sample holder to be measured. WAXS scans were carried out at 9KeV with a rhodium high resolution monochromator, used to control x-ray flux, with a 1 second exposure time. WAXS was carried out on beamline I02 at the Diamond Light Source synchrotron.

WAXS was carried out using a beam with a cross-section size of 160x60µm and a wavelength of 0.979Å, at several areas across the centre of the valve with 150µm spacings between sampling points. Powdered calcite was used as a calibrant.

Data were processed via SAXS4COLL (Abass *et al*. 2017) after being converted to TIFFs in DAWN software. The data of powdered calcite were imported for calibration with a spacing of 3.05Å, and the data missing in the detector module gaps were interpolated by the pattern centro-symmetry. The centre of the pattern was found through a SAXS4COLL centring script and the position of the chitin peaks was generated.

2.7 Summary of Structural and Compositional Techniques

A large number of seemingly similar techniques are used within this thesis, however they each have a specific purpose for their use. This difference could be the location studied or the scale at which a structure is examined for example. Table 2.2 shows a summary of each technique and the differences between them.

Goal	Technique	Target Location	Approx. Scale	Function
Ultrastructure	TEM	Cross-section of entire carapace	0.2-5µm	Identification of the layering of the carapace and all internal structures in the highest resolution possible.
	SEM	Carapace surface	1-200µm	Imagining of the carapace surface and the patterning of pore holes and setae.
	SBFSEM	The entire carapace over a ~20µm depth	2-10µm	Generation of 3D models of the carapace created at high resolution with the same samples used for TEM.
	WAXS	Chitin	~20Å	Measuring the chitin spacing within the *S.lerneri* carapace to compare against chitin within non-transparent carapaces.
	XMT	The entire carapace over a ~30µm depth	10µm	Generation of 3D models in a theoretically higher resolution than SBFSEM.
Microstructure	SHG and TPEF	Cross sections of the entire carapace	50-500µm	Identification of chitin signal from each technique and analysis of the distribution seen throughout the carapace.
Composition	XANES	Central line scan across the entire length of the carapace	N/A	Identification of $CaCO_3$ polymorphs throughout the carapace.
	XRF	Entire carapace via top down scan	~250µm	Identification of the elemental composition over the entire carapace.
	EDS	Cross section of entire carapace	10µm	Identification of elemental composition throughout the vertical layers of the carapace through analysis of transverse cross-sections.

Table 2.2: A table outlining the various structural and compositional analysis techniques used and a brief breakdown showing the differences between them by their scale, function and target location. Approx. scale was based off of the scale bars used for the images, with the exception of WAXS.

2.8 Spectroscopy

2.8.1 Refractometry

Refractive index testing was carried out with an Abbe 60 refractometer (Bellingham & Stanley, Tunbridge Wells) at room temperature (20.5^{o}C). The refractometer was first calibrated with a quartz test piece with an RI of 1.5159 using 1-Bromonapthalene as the optical suspension fluid. The equipment was then adapted for use for the *S. lerneri* valves by the use of black tape to shrink the area of sample analysis for a more accurate carapace reading. One valve from each ostracod was removed and placed in a drop of 1-Bromonapthalene before the refractive index was measured. Since, 1-bromonapthalene has been used in refractive index testing of other organic material, such as the cornea (Clark and Carney 1971), without affecting tissue properties , 1-Bromonapthalene was used on the carapace.

2.9.2 Transmittance measurements

Samples were analysed using a Hitachi U-2800 UV-VIS spectrophotometer with UV Solutions software and measured over the spectral range of visible light (400-700nm) at 2nm intervals, with a 10mm optical path length. The spectrophotometer was adapted for use by the ostracod sample holders by attaching them to the side of the cuvette holder facing the light source. The absorbance of a control slide containing only the silicone oil (SigmaAldrich, USA,317667) was first measured before being compared to the absorbance of the single valve samples. To study the proportion of incident light that was transmitted through the samples across the spectral range, the absorbance values were converted to percentage transmittance. Mean values were plotted as a function of wavelength and all readings were normalised against a suspension fluid only control. After the silicon experiments, the same methodology was carried out with 3.5% saline solutions created from the same mineral salt product used for tank water creation.

Chapter Three

Ultrastructural Analysis

3. Ultrastructure analysis

3.1 Introduction

The physical and optical properties of the crustacean carapace have been shown in chapter 1 to be heavily influenced by its specific ultrastructure (Chapter 1.3.1 and 1.3.5). The ultrastructure of the *S. lerneri* carapace is most easily and clearly seen via electron microscopy and as such, a substantial portion of this chapter's data were generated through various electron microscopy techniques. The three methods being examined are transmission electron microscopy (TEM), scanning electron microscopy (SEM) and serial block face SEM (SBFSEM). A brief outline of the principles behind each of these techniques is given below.

3.1.1 Transmission electron microscopy

TEM is the most basic form of electron microscopy and, as the name suggests, involves the transmission of electrons from the gun (incident electrons) through the sample and to the detector below (Fig 3.1). Unlike the other techniques shown here, the samples are cut into thin sections placed on grids as the electrons need to penetrate the entirety of the sample, so it must be extremely thin (around 100nm). The image is recreated through the pattern and level of absorption of the electrons as they pass through the sample. Where the electrons are absorbed by the heavier materials of the sample, no electrons can penetrate, and the lack of detection is represented by a lack of signal. While this gives the highest level of resolution, reaching up to around 0.1nm, it requires more sample preparation including multiple chemical processing steps. Nearly every step in EM tissue preparation techniques alters the sample in some way, for example the dehydration steps can substantially damage the natural structures within a tissue through tissue shrinkage (Bastacky et al. 1985). TEM, as previously mentioned, has both more intense steps and many

unique ones such as OsO_{4+} and lead staining, and so has a greater effect on the samples, including overstaining and the formation of deposits.

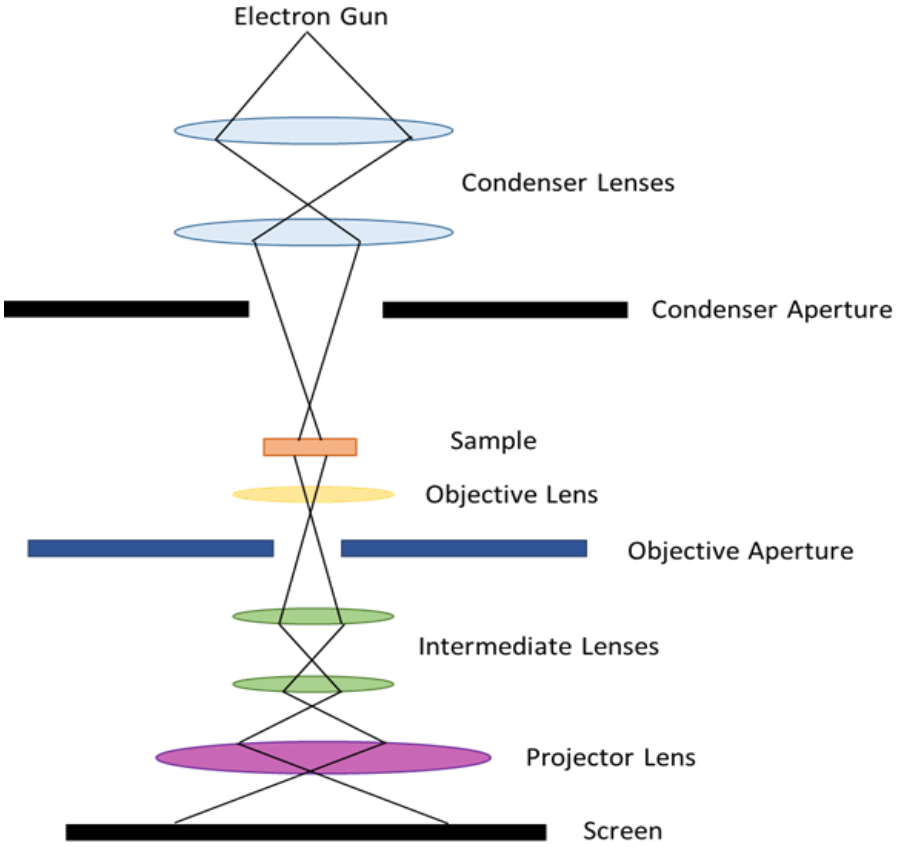

Figure 3.1: A diagram showing the internal structure of a TEM and the path of the electrons through the sample to the screen. As the name suggests, the electrons transmit through the sample. Although named as lenses, these parts are in fact electromagnets used to focus the electron beam.

3.1.2 Scanning Electron Microscopy

SEM utilises a similar form of electron microscopy but differs in how it detects the signal. Instead of detecting electrons that penetrate through sections, SEM scans across the sample and utilises a detector above the sample to measure electrons reflected off (Fig 3.2). As electrons can reflect from the sample in different directions based on its topography, a 3-dimensional image of the surface can be generated. There are several different types of electrons given off by the interaction of incident electrons with the sample. Secondary electrons are generated by being knocked out

of their atom's orbit by the incident electrons. These are lower energy, below 50eV (Joy 1991) inelastically scattered electrons and provide the best spatial information, as they are only released from within a few nm of the surface. Backscattered electrons (BSE) are incident electrons that are reflected from large atoms in the sample to exit back out of the surface and are generated from deeper in the sample. BSE are elastically scattered, meaning there is very little energy loss but a large change in direction (Zhou and Wang 2007). These electrons are used more for composition studies. Characteristic x-rays are another form of measurement generated and record the change in energy of electrons moving between orbits to identify elements; this technique is used in chapter 5 and so will be discussed later. As the samples are not measured by penetration of the electrons, very little sample preparation is required as opposed to TEM. SEM samples only require fixation and dehydration and therefore avoid the intense staining and resin infiltration steps. Just before being placed into the microscope, samples are gold coated to prevent a process known as 'charging' where static electric fields can build up and damage the

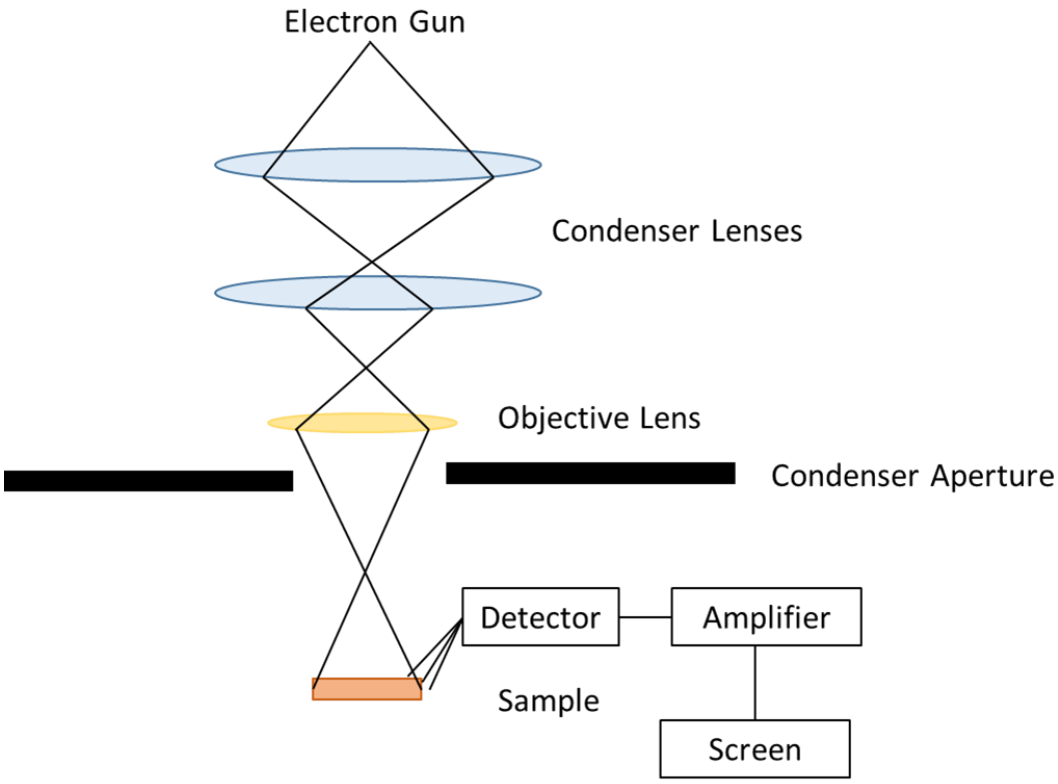

Figure 3.2: A diagram showing the internal structure of a SEM and the path of the electrons through the sample to the screen. Here the electrons do not penetrate through the sample and instead the scattered electrons are detected.

sample. Conventional SEM collects low energy secondary electrons and this allows a non-destructive method of surface imaging in a very short period (Vernon-Parry 2000). However, the resolution can only reach 2nm which is around 20 times lower than TEM's maximum.

3.1.3 Serial Block Face Scanning Electron Microscopy

SBFSEM is, as the name suggests, an offshoot of normal SEM but allows for a 3D reconstruction at more than a surface level. The process involves the use of an ultramicrotome inside of the vacuum chamber of the scanning electron microscope. The sample is cut into a flat block and an SEM image is taken of the surface, utilising the elastically back-scattered electrons from the heavy metal stains used to contrast the biological sample. These generate a 2D image of the exposed surface similar to TEM, but with lower resolution. However, within the SBFSEM, the ultramicrotome then cuts the imaged section off and another image is taken of the newly revealed sample surface. This process automatically repeats for a set number of cuts, usually between 500-1000, and a 3D reconstruction can be generated from the set of images obtained (Gluenz *et al*. 2015). Every section follows exactly from the previous, something nearly impossible and too time-consuming to do in TEM. There are examples of serial TEM being carried out (Birch-Andersen 1955; Bang and Bang 1957) and each is considered a titanic expenditure of effort to correctly maintain 3-dimensional accuracy. SBFSEM removes this extreme difficulty and requires very little additional effort to prepare as the fixation and staining process is the same as in TEM. It does however, require a significant time investment for both the cutting and imaging and the generation of the 3D reconstructions.

3.1.4 Wide Angle X-ray Scattering

WAXS is a technique that involves the use of x-rays to interact with the electrons related to atoms or molecules (for this chapter it will be molecules) within a sample and measure the periodicity of repeating electron densities. The interactions with these x-rays will generate a series of diffraction peaks (called reflection orders) at specific scattering angles (Giannini *et al*. 2016). The intensity of these peaks will be narrower and more intense from a crystal with high lattice coherence and broader and fainter from amorphous materials. The position of the innermost of these peaks depends on the spacing between the molecules (and their related electrons) in accordance with Bragg's law for:

$2dSin\Theta = n\lambda$

Where d stands for the interplanar spacing (in this case the intermolecular distance), n is the order of reflection, λ is the wavelength and 2Θ is twice the Bragg angle Θ, The relationship can be seen in fig 3.3.

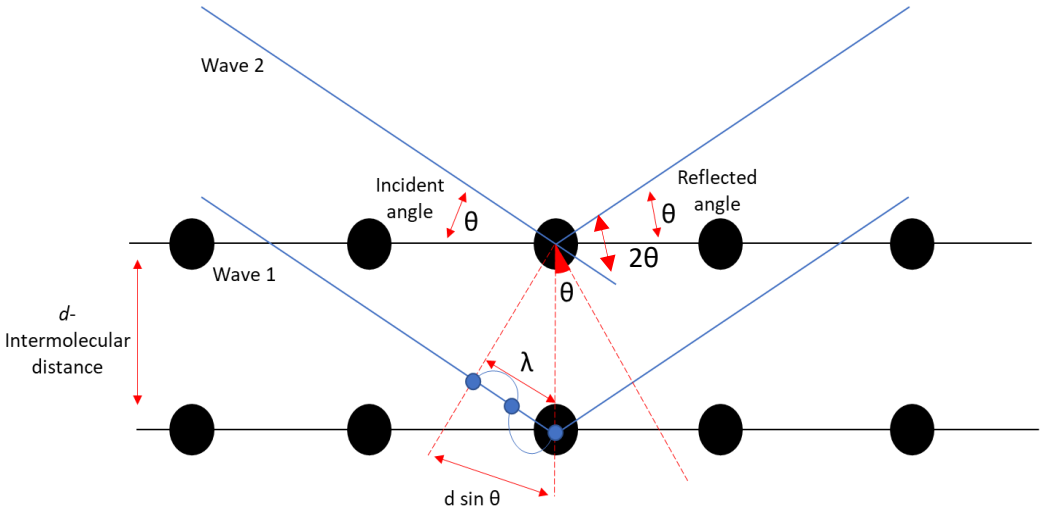

Fig 3.3: The relationship between θ, d and λ as described by Bragg's law shown between 2 intermolecular planes. The combination of the incident and reflected angle is equal to 2θ.

The scattering angle can be determined from the sample-to-detector distance and the position of the diffraction maximum on the detector (Fig 3.4). Then, using this

formula, the intermolecular distance can be calculated. The distance from the sample to the detector is not known accurately but can be found by calibrating the system using a material with a known d-spacing. As WAXS involves the analysis of scattered x-rays, as explained above, minimal (if any) extensive or invasive specimen processing is carried out. This allows the samples to be measured in-situ which is especially important for measurement-based analysis, as processing may alter the size or shape of internal components within a sample (as discussed in 3.1.1).

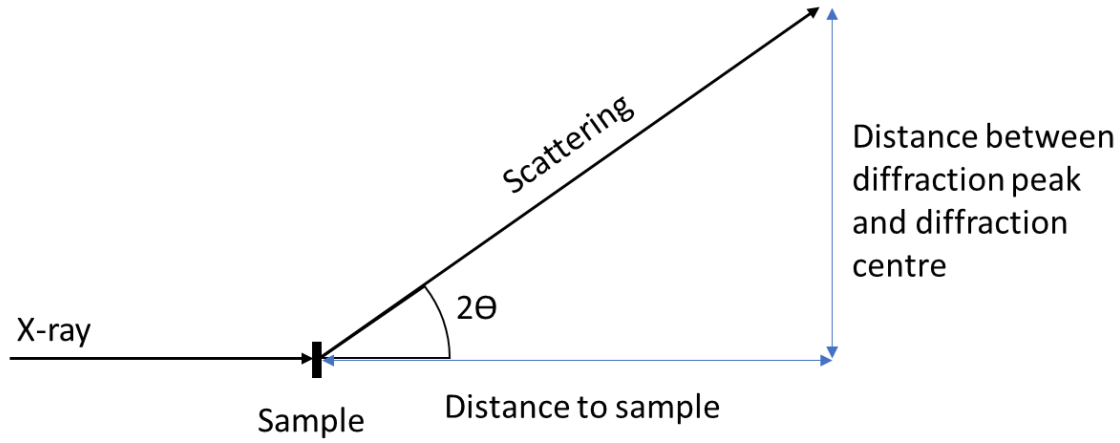

Fig 3.4: A representation of the path of the x-ray beam and how from this interaction the Θ can be calculated for use in the Bragg's law equation

3.1.5 Ptychography

Ptychography is a technique which has one major advantage over EM, its much greater penetration depth. Even advanced techniques such as SBFSEM require such small section thickness (50-100nm) to generate an accurate model, that very little of the whole sample is analysed. Ptychography is a method of computational imaging that utilises what is known as coherent diffraction imaging to generate an accurate model with a much higher sample depth penetration (Pfeiffer 2018). Effectively it measures multiple (usually hundreds or thousands) of overlapping diffraction patterns by scanning an x-ray probe over a specimen and recording this data via a detector. This overlap, in conjunction with intensive reconstruction algorithms that solve the phase of the waves that arrive at the detector, can lead to the generation

of a 3D reconstruction of the initial sample (Rodenburg and Maiden 2019). While this technique is very powerful, the reason it has only grown in popularity over the last decade or so is due to the extremely challenging computational demands of the algorithms, and so it is still somewhat of a rare technique.

3.1.6 Previous Ostracod Ultrastructure Research

Numerous studies have been carried out on ostracod carapaces, many of which were discussed in the introduction (section 1.2.2). However, it has been noted that the majority of these have been carried out on podocopan carapaces (Yamada 2019). Very few research articles describe the carapace of transparent ostracods of the myodocopidan order, to which *S. lerneri* belongs. Additionally, most research has focused on *Vargula hilgendorfii* (Sohn 1988; Abe and Vannier 1995) and has concentrated on either specific structures, such as the hinge or marginal infolds (Yamada 2007a; Yamada and Keyser 2010), or with a lack of information concerning the specific ultrastructure of the calcified outer cuticles (Okada 1982; Keyser 2005; De Deckker and Martens 2013). Detailed analysis of the ultrastructure throughout developmental stages has not been reported (Sohn 1988).

Transparent carapaces are reported to be ultrastructurally similar to that of non-transparent ostracods, although thinner (Berndt *et al*. 2019), and with a difference within the crystalline endocuticle. Previous studies on other myodocopid carapaces have shown they commonly maintain a combination of monohydrocalcite and calcite (Sohn 1969; Smith and Bate 1983), although there have been concerns about the degree of calcite formation potentially being misrepresented due to calcite formation caused by sample processing (Yamada 2019).

3.1.7 Aims and Hypothesis

Hypothesis:

The *Skogsbergia lerneri* will possess a carpace that will be structurally similar to that of others within the myodocopan subclass, and crustaceans in general, in terms of the major layers. However it will show specific differences that can be related to its transparency, as was demonstrated within chitin lamellae spacing in previous research into the transparent eye windows of the *Macrocypridina castanea* (Brady, 1987) (Parker *et al*. 2018). Structural changes will occur throughout the development of the ostracod, however they will not deviate from or substantially interfere with the expected layered structure of the carapace in order to avoid the transparency being affected.

Aims:

i. To characterise the layers and structures within the ultrastructure of the adult carapace of the *Skogsbergia lerneri* to determine the basis of its transparency.
ii. To analyse the changes in carapace ultrastructure, including layer proportions, throughout ostracods development.
iii. To generate 3D reconstructions of the carapace to confirm observations in (i) and (ii) are consistent across a 3D perspective, and to identify any additional ultrastructural differences that could be missed due to the limited viewpoint of 2D imaging.

3.2 Experimental Design

i) Characterisation of the Ultrastructure of the Adult Carapace

The ultrastructural features of the adult carapace were analysed using TEM (n=5) (chapter 2.3.1) and SEM (n=3) imaging (chapter 2.3.2). Chitin was measured with

WAXS that was carried out as three line scans of seven points each (n=3) across the in 150µm steps with a beam of cross-section size of 160x60µm using a 1-second exposure and a 0.979Å wavelength, with a detector distance of 350mm. The height and width of the crystals measured within the endocuticle section 3.3.3.3 were taken as the distance between the two farthest points of the x-axis and y-axis respectively. 3D reconstructions of the crystals were traced by hand based on SBFSEM images.

ii) Analysis of Changes within the Ultrastructure Throughout Development

Changes in carapace ultrastructure throughout development were analysed by TEM imaging at n=5 for instar 2, 3, 5 and the adult, and n=4 for instar 1 and 4 due to contamination of some samples. Ptychography was performed on the left valve of all developmental instars (n=1) at beamline 13-1 at the Diamond Light Source (chapter 2.7.2) with a beam size of 15µm and reconstruction carried out.

iii) Generation of the 3D reconstructions

SBFSEM imaging was performed for every instar (n=1), 1000 sections at 50nm thickness each were generated for each sample and reconstruction carried out with AMIRA (Chapter 2.3.3).

iv) Statistical Analysis

Every measurement value generated for each ultrastructure feature was averaged over a minimum of 3 different cut sections per n number. All comparisons of size differences between the instars were carried out via one-way ANOVA testing with Tukeys post-hoc, calculated with SPSS, showing significance at $p<0.05$. Direct comparisons between two sets of data were carried out with independent t-testing. Kolmogorov-Smirnov testing determined that all data sets were normally distributed (excluding analysis with samples sizes of 1) and so normal distribution was assumed. Kurtosis and skewness were seen to be between ±1.5 for all data sets. All data was assumed to have equal population variance due to having either equal sample sizes or similar (e.g. n=4 and n=5). All data generated from these sample populations was assumed to be done via random independent sampling as samples were chosen at

random and no emphasis was put on selecting images based on their structural characteristics.

All samples for TEM and SBFSEM were cut and sectioned one-third of the way down the carapace in the anterior-posterior axis to try and ensure that any changes would be comparable both between and within instars. This is because substantial differences in thickness are found throughout the ostracod carapace, (Bate and East 1972).

3.3 Results

3.3.1 The Adult Carapace Ultrastructure

The adult carapace of *Skogsbergia lerneri* consists of four main layers (Fig 3.5): a thin outer epicuticle, an exocuticle, a large crystalline endocuticle layer and an inner membranous endocuticle layer. The mean thickness of the carapace was 19.2±1.78µm and was proportionally comprised of 0.85% epicuticle (0.16±0.02µm), 21.98% exocuticle (4.2±0.64µm), 59.19% crystalline (11.34±0.81µm) and 19.08% endocuticle (3.66±0.88µm) as seen in figure 3.5.

All layers were significantly different from each other ($p<0.001$) except for between the exo- and endocuticle ($p=0.34$). Minimal variation was seen between the layer dimensions although the greatest amount was seen within the endocuticle, which was caused by the differing number of lamellae contained within.

Chitin can be seen within the exocuticle and the endocuticle, although it is much less dense within the exocuticle and lacks the even, lamellae patterning of the endocuticle.

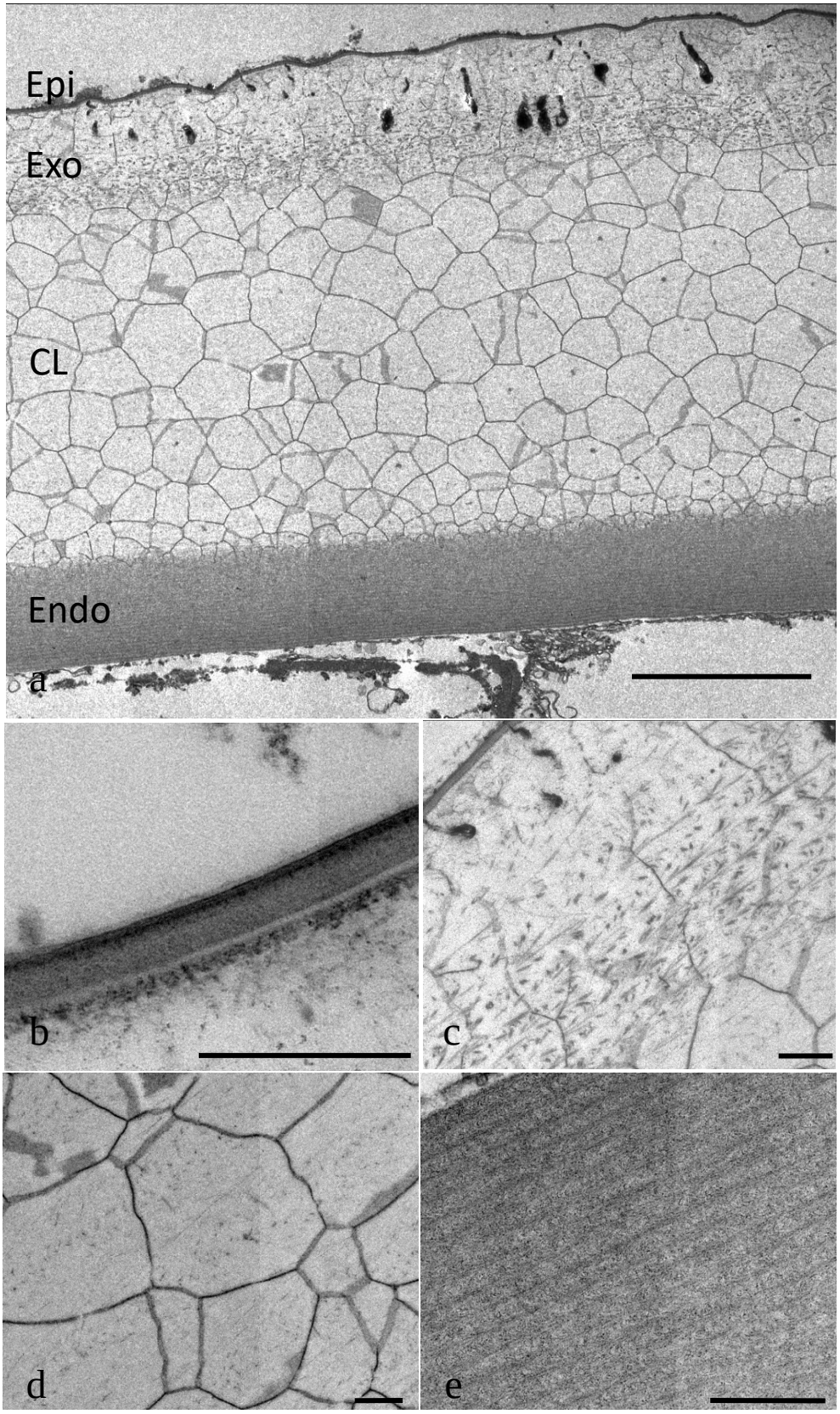

Figure 3.5: a) Cross-section of the adult *S. lerneri* carapace. The carapace is divided into four main sections the epicuticle (Epi), the exocuticle (Exo), the calcified layer (CL) and the endocuticle (Endo). Scale bar represents 5µm.**b-e** are the different sections in higher detail, **b)** the epicuticle **c)** the exocuticle **d)** the crystalline endocuticle **e)** the chitin lamellae. Scale bar represents 200nm

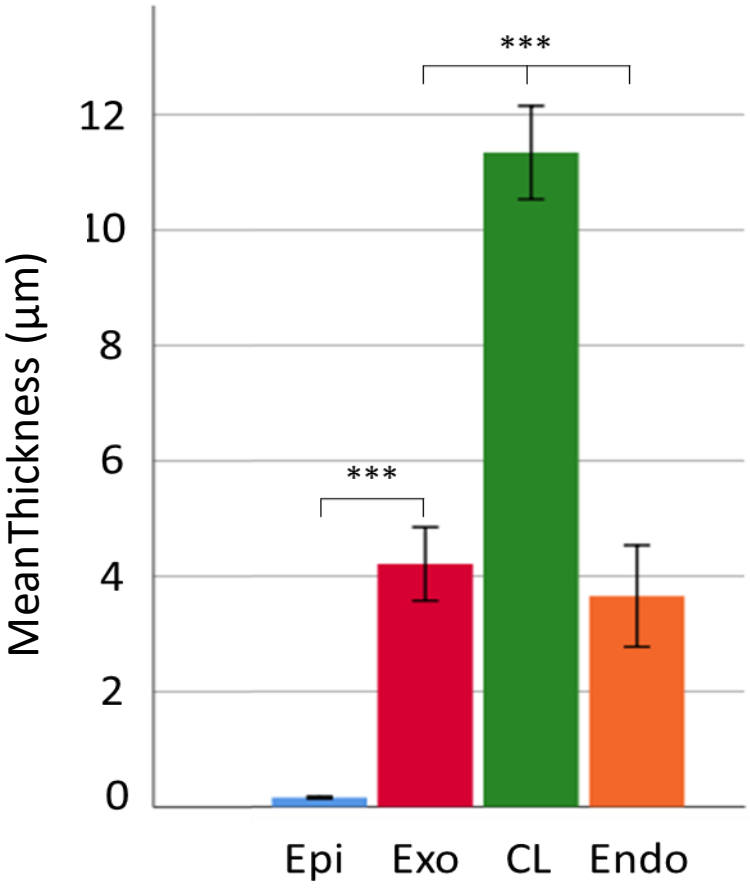

Figure 3.6: The measurements from the adult carapace in Figure 3.5 showing the thickness of each of the layers. *** represents p<0.001.

3.3.1.1 Epicuticle

The epicuticle is the outermost protective layer of the carapace and can be seen to comprise of at least 3 distinct parts, the extremely thin outer layer, the thick inner layer and the electron-dense basal layer (Fig 3.7a). It appears to lack both chitin and calcium carbonate as can be seen by the absence of distinct structures within its layers. The epicuticle showed no significant change in thickness along the entirety of the carapace cross-section and had only a couple of nanometers difference between samples (Fig 3.6). There is a very distinct separation between the epicuticle and the exocuticle, with the only disruption in the epicuticle's structure being the inclusion of pore canals (Fig 3.7b) and projections from the base of the epicuticle protruding into the exocuticle.

Pore canals were found regularly spaced throughout the entire carapace (Fig 3.7) penetrating through the epicuticle and the entire carapace into the cellular layer below. Different pore canals were seen depending upon their different roles, smaller, empty pore canals for mineral transport and much larger pore canals containing a seta for environmental awareness were seen.

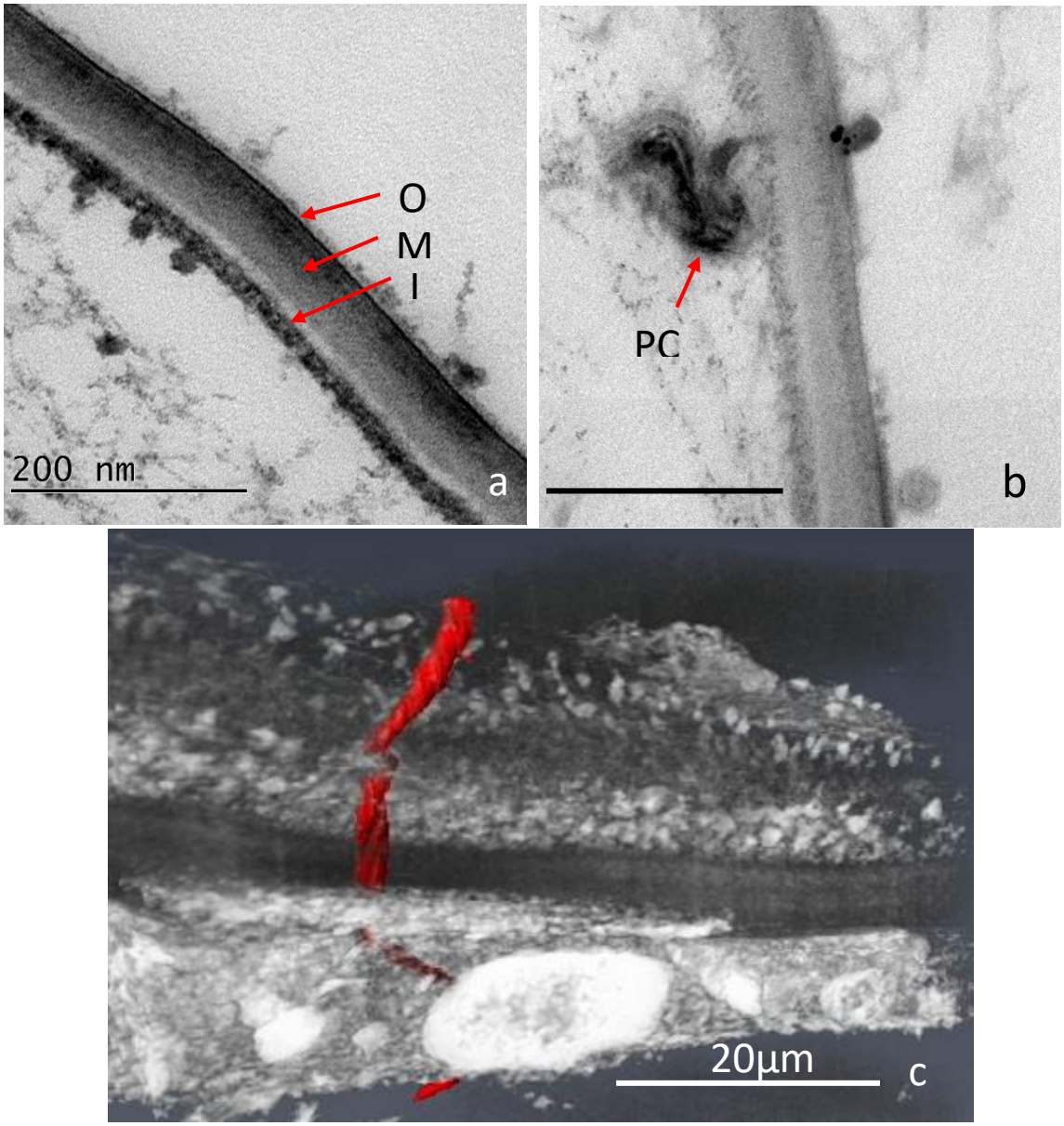

Figure 3.7: The epicuticle layer of the adult carapace at 40,000x magnification showing **a)** the 3 identifiable layers of the epicuticle and **b)** a pore canal interfacing with epicuticle. **c)** A screenshot of a highlighted pore canal travelling through the adult carapace, see the attached file for the full video. Abbreviations: O, outer; M, middle; I, Inner; PC, pore canal. Scalebar is set at 200nm for **a** and **b**, and 20µm for **c**.

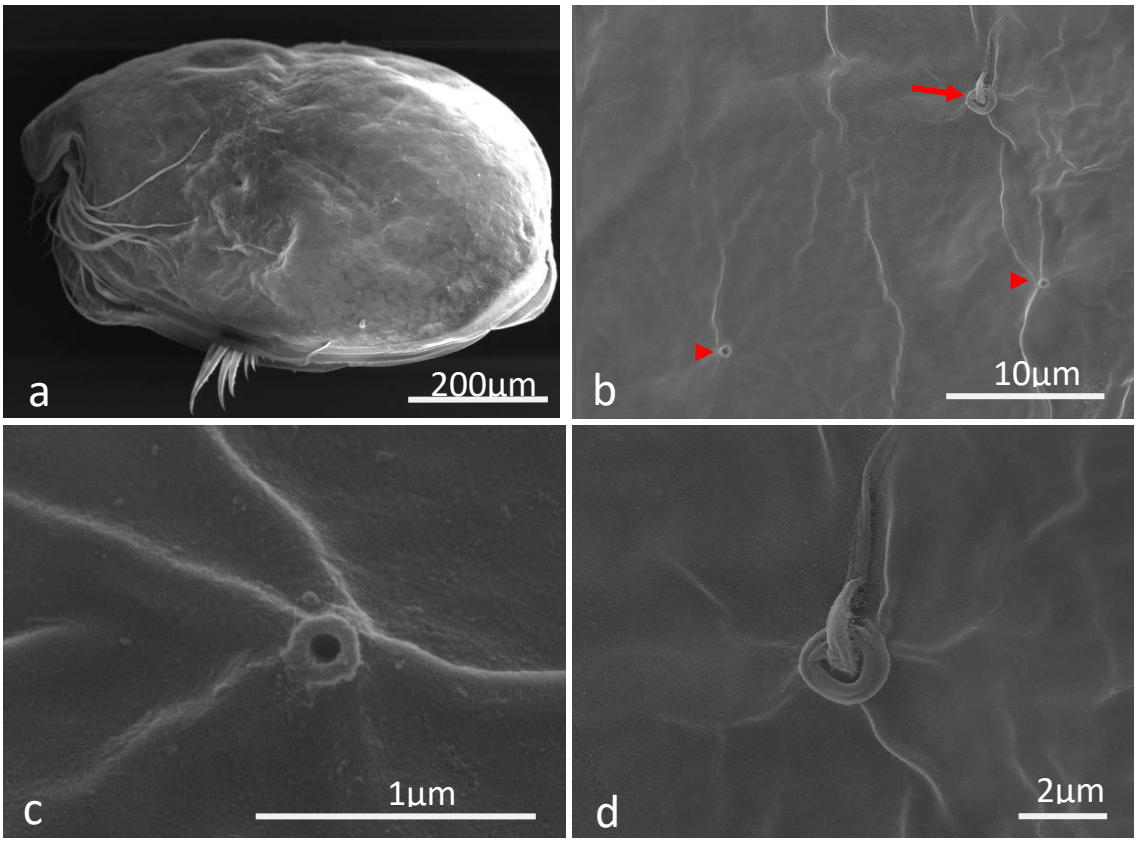

Fig 3.8: a) The external ostracod carapace under SEM at 250x magnification, this view revealed one valve of the shell. **b)** A close up of the surface reveals the two main types of pore canals on the ostracod carapace at 5000x magnification. **c)** The smaller pore hole indicated by the arrowheads in **b** are involved in secretion, and lack any identifiable features (taken at 50,000x magnification). **d)** The larger pore canal indicated by the arrow in **b** housed a seta for sensory observation (taken at 15,000x magnification).

3.3.1.2 Exocuticle

The adult exocuticle within the carapace reveals an organised if loosely packed series of chitin fibrils when compared to the endocuticle (Fig 3.9). The curved shape of many of the different fibrils, along with their varying sizes reveals the presence of a twisted plywood structure within the layer. The end of the exocuticle is hard to define, as the crystalline polyhedrons seem to overlap into the exocuticle layer preventing the creation of a distinct edge between the two and rather just a transition into the crystalline layer when the chitin fibrils stop (Fig 3.9a).

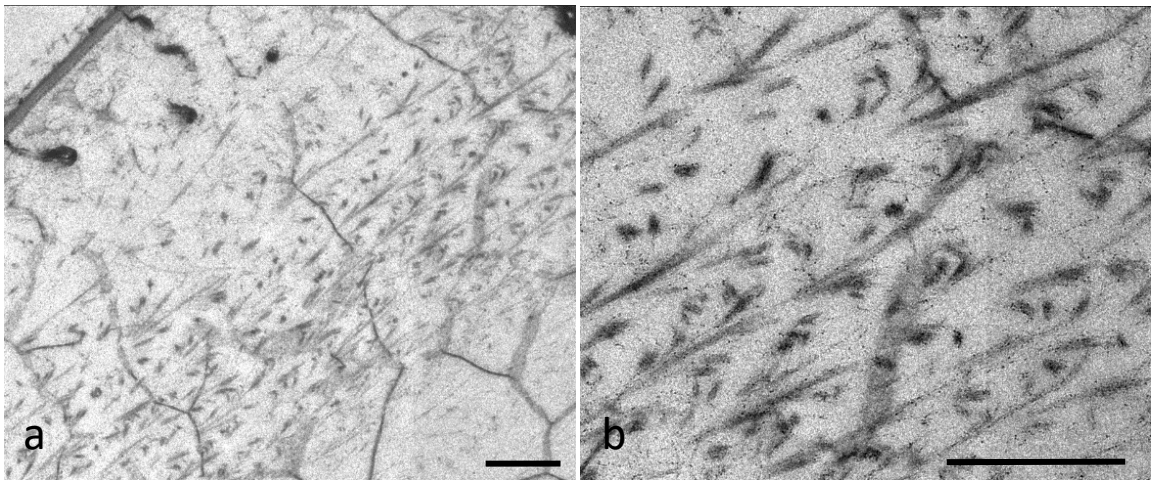

Figure 3.9: The adult exocuticle seen at **a)** 3000x magnification and **b)** 10,000x magnification. A horizontal orientation can be seen throughout the entire layer. The scale bar corresponds to 200nm.

As mentioned previously between the epicuticle and the exocuticle are numerous projections that start from the base of the epicuticle and continue throughout the exocuticle (Fig 3.10). These can be distinguished from the pore canals by their reduced size, constant appearance and the fact that they stop before the crystalline

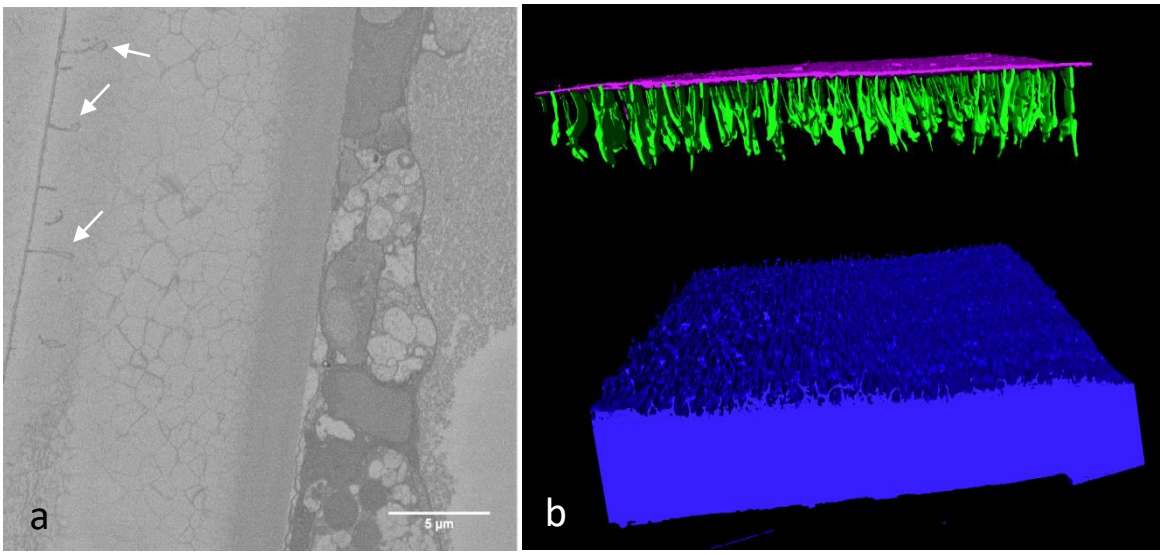

Figure 3.10: a) A representative SBFSEM image used to create a 3D reconstruction. The epicuticle projections can be clearly seen extending all the way through the exocuticle. The most prominent ones are labelled by the arrows. **b)** A 3D reconstruction of the carapace without the exocuticle chitin and crystalline layer, generated from manual tracing. Projections from the epicuticle that extend into the exocuticle are numerous and clearly visible. Pink is the epicuticle, green are the projections and blue is the chitin lamellae layer see the attached file for the full video.

layer instead of penetrating the entire carapace. While these projections may seem sparse from the 2D imaging, 3D reconstructions reveal a very dense formation (Fig 3.10b).

3.3.1.3 The Calcified/Crystalline Layer

The crystalline layer was seen to consist of polyhedrons of varying sizes (Fig 3.11) that are extremely similar in appearance to the expected calcium carbonate crystalline

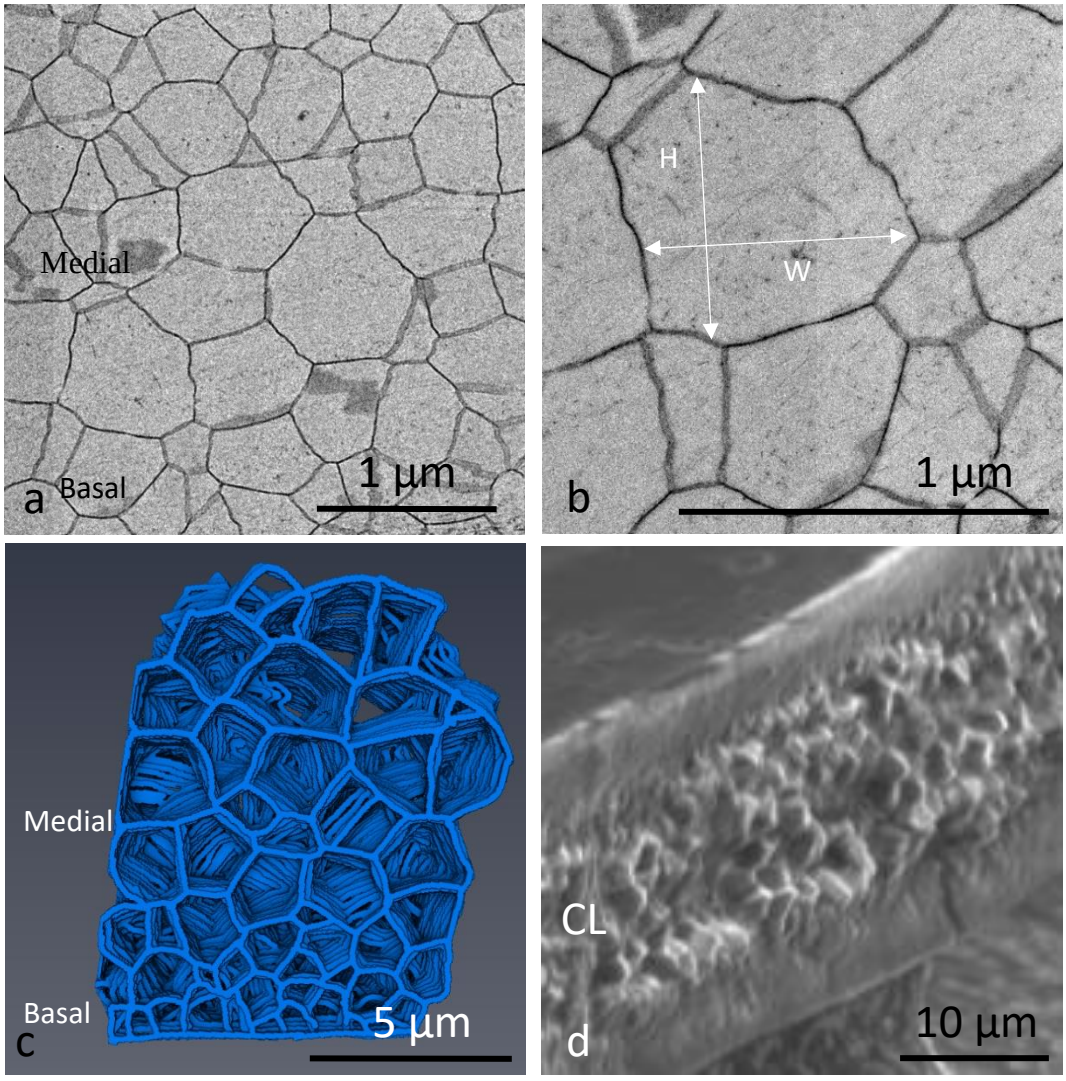

Figure 3.11: a) A TEM image of the adult crystalline layer from a single cross-section labelled with the larger medial crystals and the smaller basal crystals **b)** A 4000x magnification image of the crystals with labels showing the measurements for height (H) and width (W). **c)** A manually traced reconstruction showing the 3D structure of the adult crystalline layer with labelling for medial and basal crystals. **d)** An SEM image of the cross section of the adult carapace for better visualisation, CL = Crystalline Layer.

structures seen in other myodocopid ostracods (Yamada 2019). Chapter 5 will analyse this layer and discuss the composition of these polyhedrons in greater detail.

These polyhedrons vary widely in size and lack uniformity, however, they get smaller in diameter towards the basal end. Medial polyhedrons had a mean height of 1.07±0.3µm and a mean width of 1.02±0.34µm whereas the basal polyhedrons had a mean height of 0.34±0.1µm and width of 0.39±0.13µm. Independent t-testing from a mean of both measurements (herein referred to as the length) showed that medial polyhedrons were significantly larger than the basal crystals (p=0.002) (Fig 3.12). As well as being smaller, the polyhedrons interfacing with the endocuticle are not fully formed and seem to fuse into the chitin lamellae.

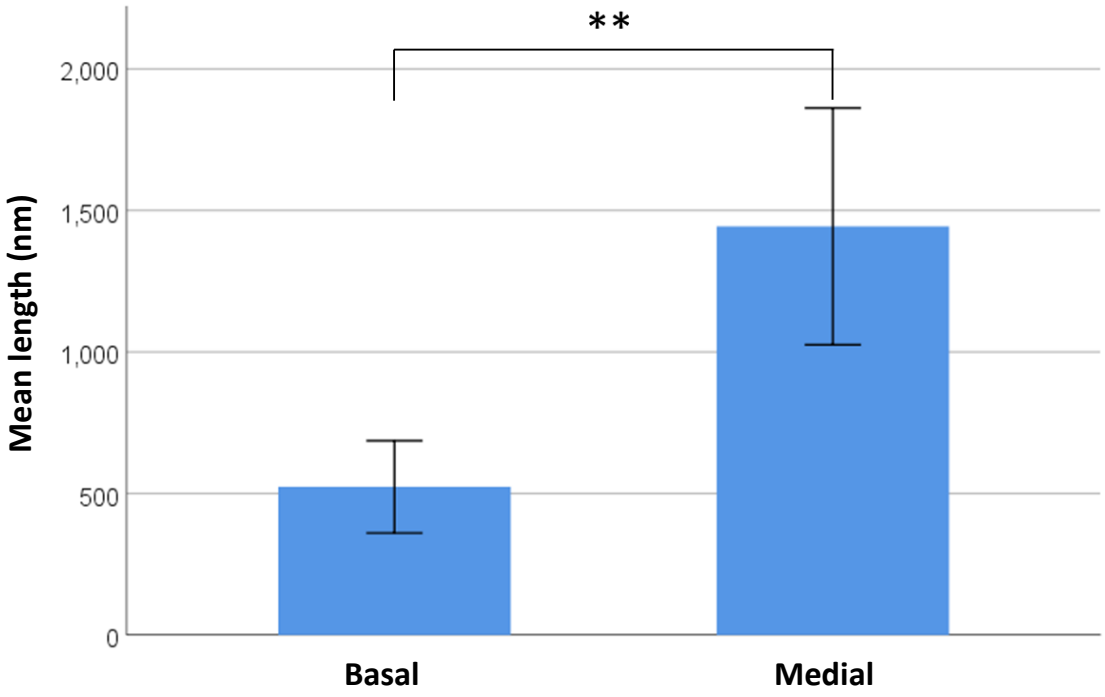

Figure 3.12: The mean length of the crystals within the adult carapace averaged between height and width measurements. The medial crystals were significantly larger than the basal ones (p=0.002). Error bars are ±SD.

3.3.1.4 Endocuticle

The endocuticle comprises organised, regularly repeating chitin lamellae (fig 3.13) that maintain their consistency throughout the entire layer. The mean thickness of each lamella was 75.9±13.7nm with a distance of 44.05±4.4nm, measured from the basal edge of one lamella to the proximal edge of the next. At higher magnifications it is seen that the chitin fibrils within the lamellae are not entirely orientated parallel

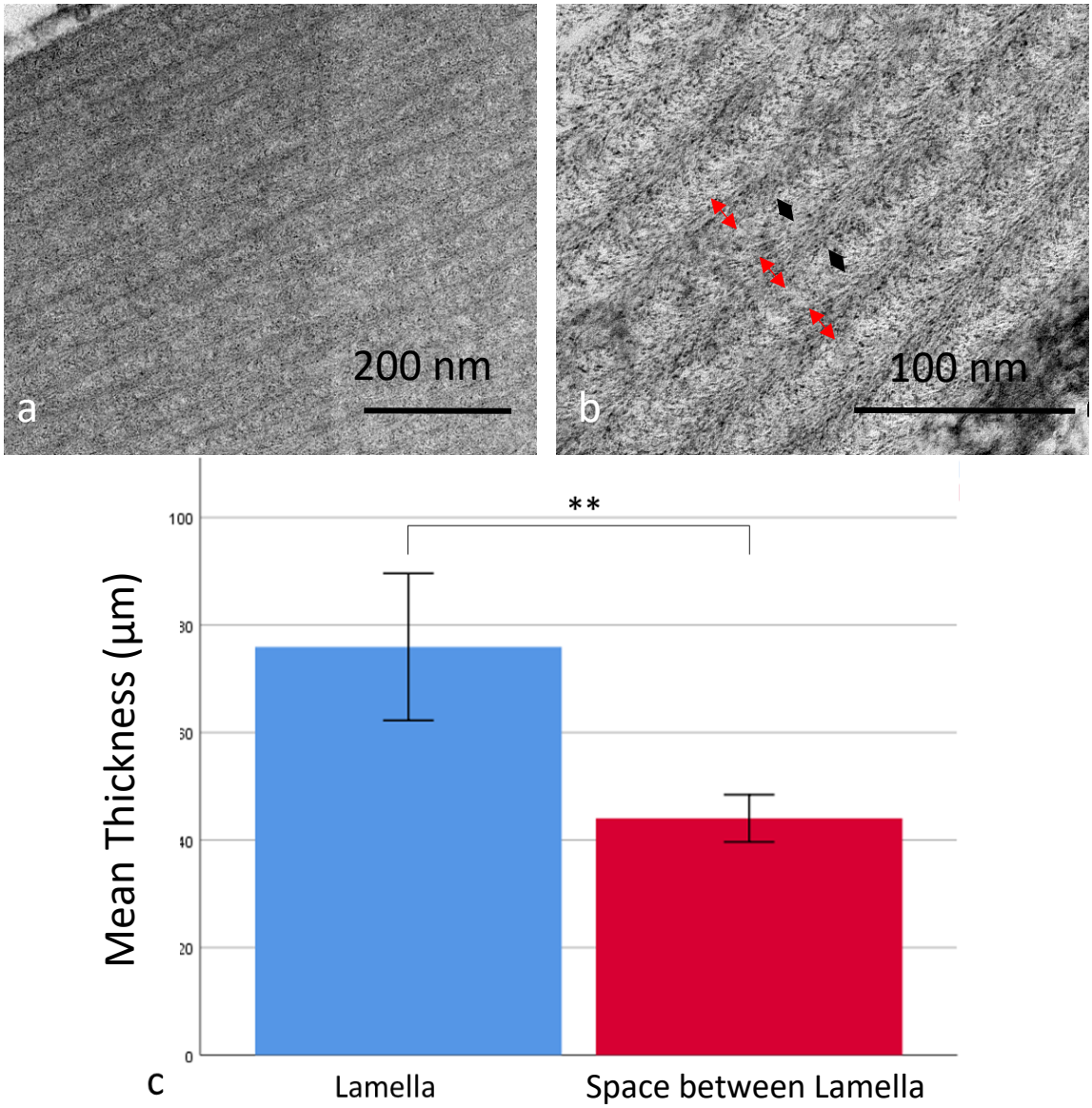

Figure 3.13: TEM imaging of the endocuticle layer seen at **a)** 4000x and **b)** 10,000x magnification. Chitin lamellae are indicated via the red double-headed arrows and the spaces in between are shown via the black double-headed arrows. **c)** The mean width of the chitin lamella and the spaces between them. ** represents p<0.01 and error bars represent ±SD.

with the lamella but branch off at the edges, implying a twisted plywood structure as in the exocuticle. The mean number of lamellae contained within the adult endocuticle was 17.6±4.6 and ranged between 12 and 24.

3.3.1.5 Chitin Spacing

WAXS was carried out on ostracod carapace samples, after being calibrated with a calcite standard. An intermolecular distance was generated for three adult samples (Fig 3.14). This gave mean intermolecular distances of 20.6±0.5Å, 20.5±0.6Å and

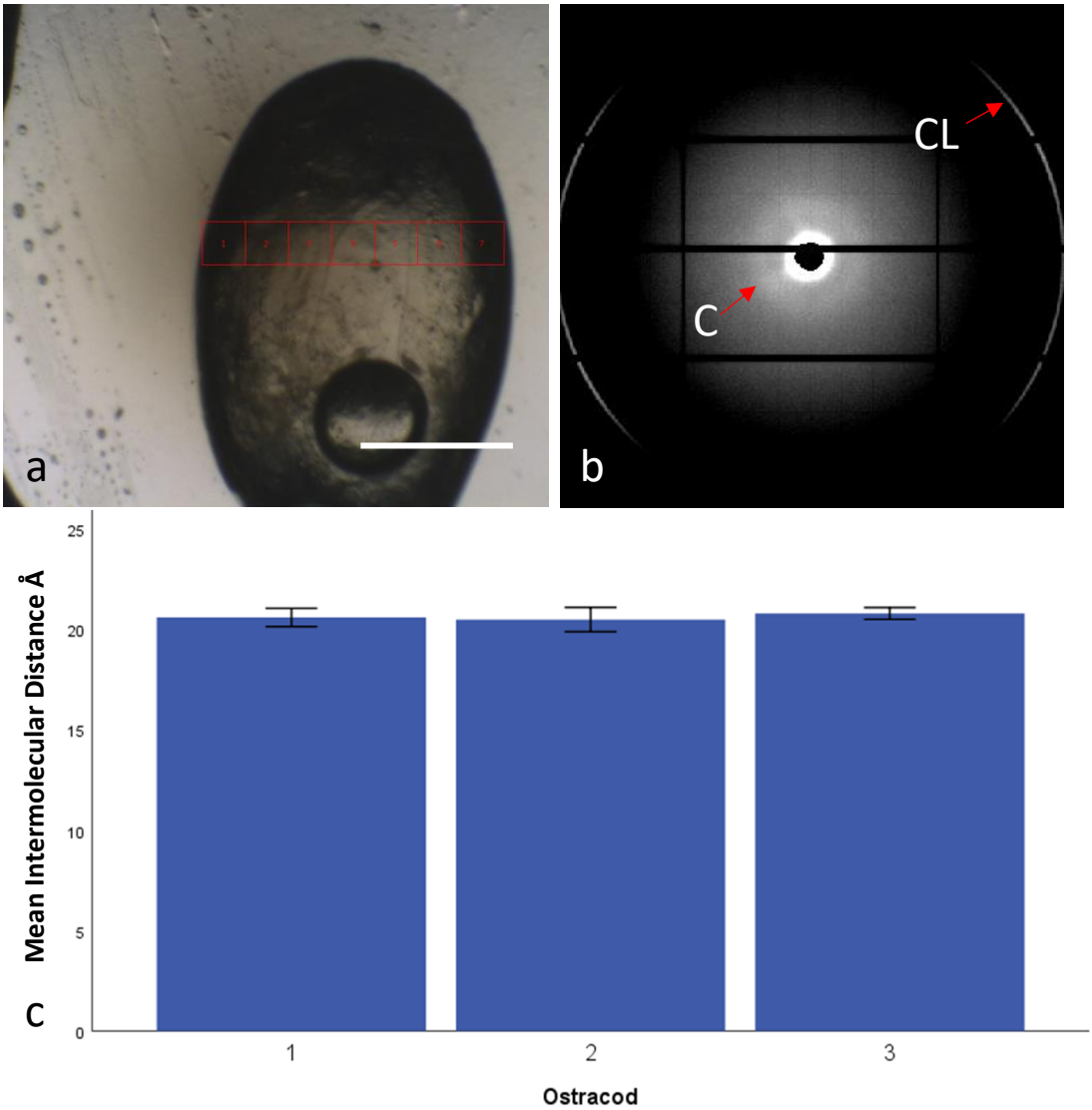

Fig 3.14: (**a**) Representative WAXS single line scan from an adult ostracod carapace, each of the red squares is a point on the scan at which an x-ray exposure was taken. (**b**) a diffraction pattern taken from a single exposure point of a line scan from **a**. diffraction pattern taken from a single exposure point of a line scan from **a**. Arrows indicate diffraction rings, C shows the chitin diffraction ring (first order), CL shows the clingfilm diffraction ring, which the samples were held in **c)** The mean intermolecular distances in the three ostracod samples. Scale bar represents 500µm and error bars are ±SD.

20.8±0.3Å, leading to a mean adult chitin molecular spacing of 20.6Å (Fig 3.14c). No significant differences were found between the intermolecular distances of chitin between any of the carapaces.

3.3.2 Changes in the Ultrastructure Throughout Development

There were significant changes in the ostracod carapace throughout its development, both in the overall size of the layers and in the layer proportion (Fig 3.15). The most noticeable change in structure was the lack of a formed crystalline layer within the instar 1 carapace. There were consistent changes in the thickness of the layers as they progress throughout development.

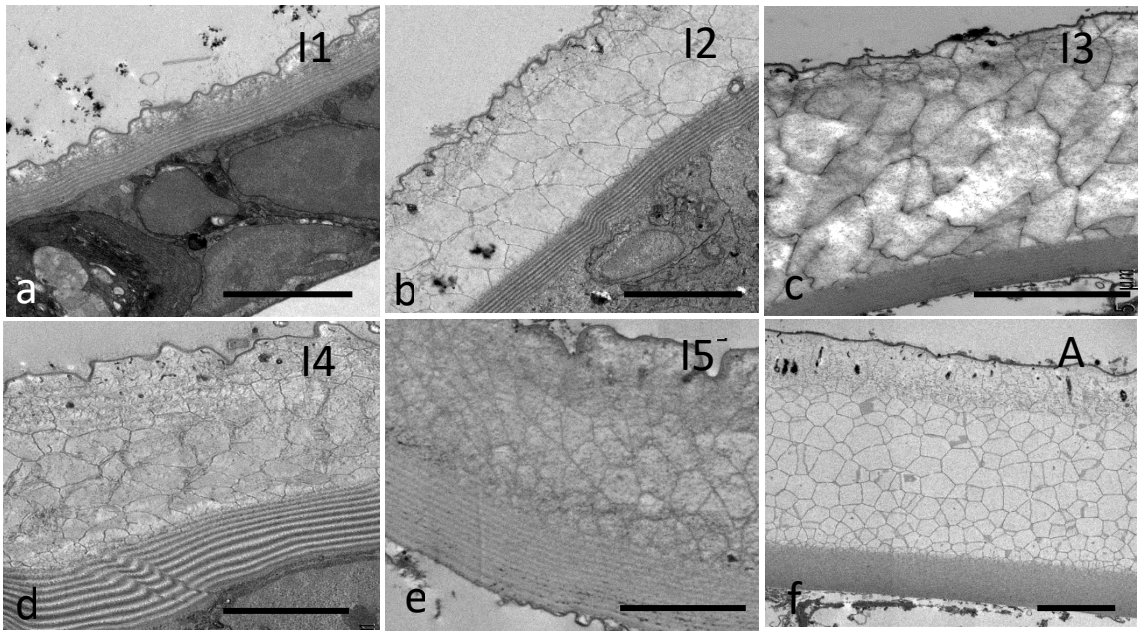

Figure 3.15: Cross sections of the carapace from each instar, **a)** instar 1, **b)** instar 2, **c)** instar 3, **d)** instar 4, **e)** instar 5 and **f)** the adult for reference. Scale bars represent 5µm.

After the ostracod's progression from an egg, the earliest form of the carapace, instar 1 was 1.5±0.24 µm thick, with a proportional breakdown of 2.21% epicuticle; 30.9% exocuticle, 24.05% underdeveloped crystalline layer and 41.8% membranous endocuticle layer (Fig 3.15). Instar 2 showed significant growth (p=0.04) to maintain a carapace with a mean thickness 6.5±1.2µm consisting of 1.25% epicuticle, 22.29% exocuticle, 52.4% crystalline endocuticle and 18.8% membranous endocuticle. Instar 3's carapace was also significantly thicker than its predecessor (p=0.03) with a mean

thickness of 10.16±1.27µm. The proportions were found to be: 1% epicuticle, 19.12% exocuticle, 59.83% crystalline endocuticle and 16.46% membranous endocuticle. There was no significant change in thickness between instar 3 and 4, instead, instar 4 showed a reduction in thickness, although there was a high standard deviation. The carapace had a thickness of 5.61±2.9 µm consisting of 1.5% epicuticle, 24.5% exocuticle, 46.27% crystalline endocuticle and 25% membranous endocuticle. The

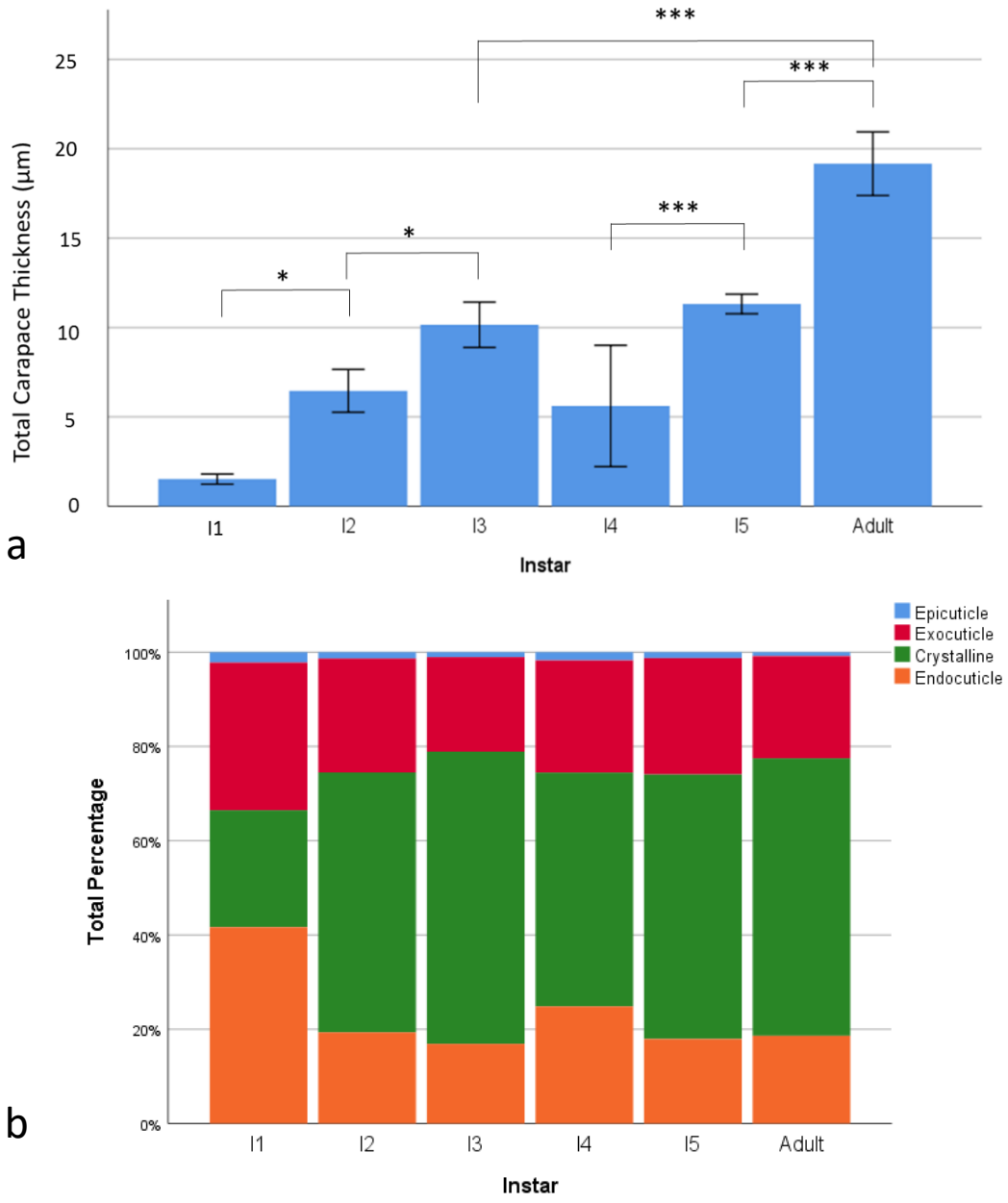

Figure 3.16: a) The mean carapace thickness at each instar. The thickness increases gradually with development with exception of I4. **b)** The percentage proportions of the layers within each instar, the largest variation is seen within the crystalline layer. * represents p>0.05 and *** is p<0.001. Error bars are ±SD.

carapace of instar 5 was significantly thicker than that of instar 4 ($p=0.001$) at 11.3±0.55 µm, although it was not significantly different from instar 3 ($p=0.9$). The proportions of the layers were: 1.24% epicuticle, 24.55% exocuticle, 55.78% crystalline endocuticle and 17.79% membranous endocuticle. Finally, the adult layer was significantly larger than all other instars ($p<0.001$) with a mean thickness of 19.16±1.78µm and, as previously mentioned, had proportions of 0.85% epicuticle, 21.98% exocuticle, 59.19% crystalline endocuticle and 19.1% membranous endocuticle. The most substantial change from these was the transition from instar 1 to 2 where the crystalline layer increased by 28.35%, whereas the organic layers (exo- and endocuticle) proportionally decreased by a combined total of 31.6%, although the actual thickness of the organic layers increased by 1.55 µm.

3.3.2.1 Epicuticle

The epicuticles of all the instars maintain the same structure as the adult, they are formed from three different layers, an outer layer, the thick middle layer and the third electron-dense inner layer (Fig 3.17). Throughout the progression of the instars, the epicuticle grows thicker (Fig 3.17g). There was a significant increase ($p=0.04$) in the thickness from instar 1 (33.6nm) to 2 (80.5nm). The mean epicuticle thickness increased to 100nm at instar 3, however, this change is not significant ($p=0.7$). The epicuticle thickness actually decreased from instar 3 to 4 by 13.4nm to 87.3nm. However decrease is not significant ($p=0.7$), and there is a substantially larger standard deviation (SD±33.8nm) than the other instars. The instar 5 epicuticle is significantly thicker ($p=0.018$) than instar 4 at 140.2 nm and the adult instar had the largest epicuticle with a mean thickness of 161.9nm; this was significantly larger than all other instars except for instar 5 ($p<0.003$).

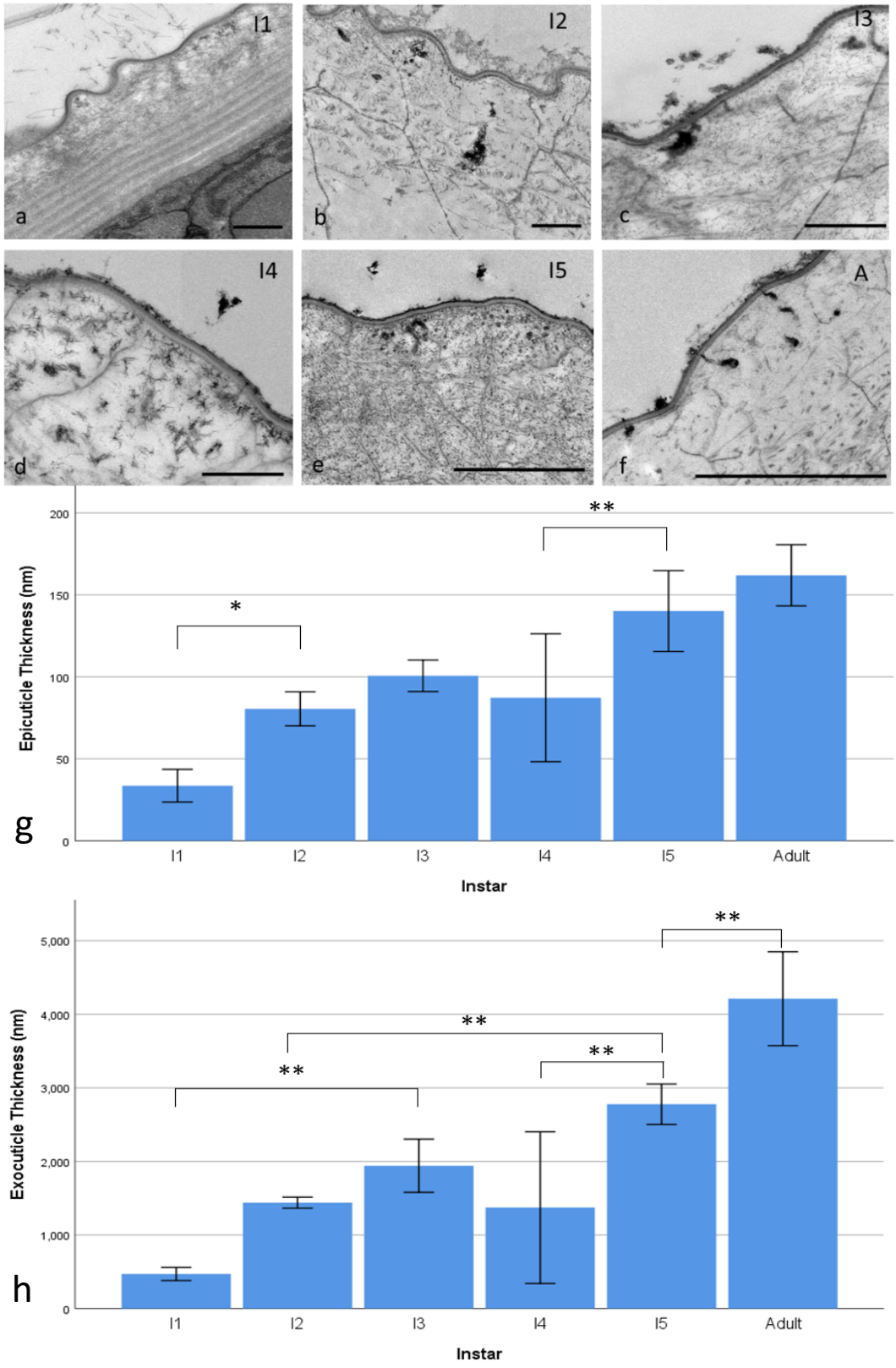

Figure 3.17: The epicuticle and exocuticle at each stage of development **a)** instar 1, **b)** Instar 2, **c)** instar 3, **d)** instar 4, **e)** instar 5 and **f)** the adult. The chitin within the exocuticle can be seen to follow a specific orientation. **g)** The thickness of the epicuticle throughout development, the thickness increased steadily throughout the instars. **h)** The thickness of the exocuticle throughout development, the thickness increases steadily throughout the instars. * represents $p<0.05$ and ** represents $p<0.01$. Scale bar is 500nm

3.3.2.2 Exocuticle

Throughout development, the instars can be seen to maintain the orientation of chitin fibrils within the exocuticle, which run parallel to the endocuticle and epicuticle (*i.e*. horizontally) across the carapace (Fig 3.17). The exocuticle significantly increased between instar 1 and 2, from 0.47µm to 1.44µm ($p=0.001$) (Fig 3.16h). Instar 3 had a mean exocuticle thickness of 1.94µm, although this was not significantly greater than instar 2 ($p=0.68$). As in the previous sections, instar 4 actually decreased in thickness to 1.37µm, however, due to the large standard deviation (0.89) this was not significant. Instar 5 was significantly thicker than instar 4 at 2.78µm ($p=0.009$) and the adult was significantly thicker than all other developmental stages with a mean thickness of 4.21µm ($p<0.005$).

3.3.2.3 Crystalline Layer

The crystalline layer was the most variable, with the largest increases in thickness throughout all of the layers. The crystalline layer of instar 1 had a mean thickness of 0.37µm which became significantly thicker ($p=0.001$) in instar 2 (3.38µm) (Fig 3.18). The crystalline layer then significantly increased again to 6.08µm ($p<0.001$) at instar 3. The instar 4 crystalline layer decreased in thickness to 2.6µm, however, unlike the previous features this decrease was significant ($p<0.0001$). This layer increased significantly to 6.3µm at instar 5 ($p<0.001$) and the adult crystalline layer is significantly thicker than every other instar with a mean thickness of 11.3µm ($p<0.0001$).

Apart from instar 1, all the development stages have the same crystal polyhedron patterning, being larger at the centre and smaller at the basal position (Fig 3.19). The sides of each polyhedron are inconsistent throughout the carapace, with some being smooth and relatively straight, whereas others are jagged and curved. The instar 1 crystals are completely different from those seen in the other instars, they lack a defined structure and the sides are uneven. There is also no identifiable distinction

between the exocuticle and the crystalline layer making it difficult to separate the two. This most likely suggests that the instar 1 crystalline layer consists of partially developed polyhedrons, which have formed by instar 2.

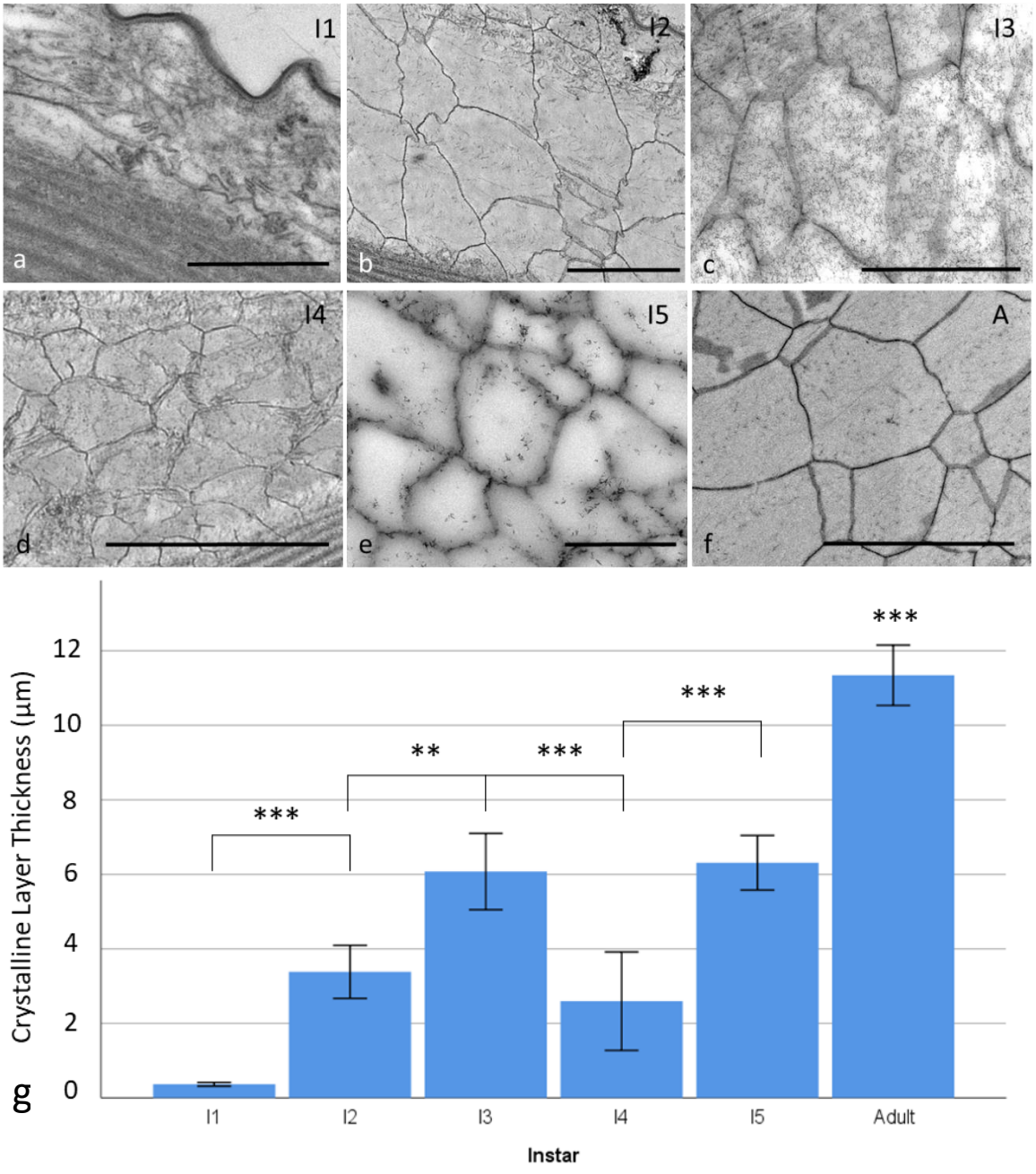

Figure 3.18: The calcified layer from each development stage (where possible) showing **a)** instar 1, which lacks fully formed crystals, **b)** instar 2, **c)** instar 3, **d)** instar 4, **e)** instar 5 and **f)** the adult. The crystals are largest in the centre and reduce in size toward the basal axis. Scale bar is 200 microns. **g)** Measurements of the calcified layer throughout development. The crystalline layer increases generally throughout development, although it decreases at instar 4. * represents $p<0.05$, ** represents $p<0.01$ and *** represents $p<0.001$.

Every instar with fully developed crystals had significantly larger medial polyhedrons and smaller basal ones, both in height and width (fig 3.19). Instar 2 had a mean basal polyhedron height of 0.46µm and width of 0.52µm, with larger medial ones 1.63µm high and 1.4µm wide (p=0.001). Instar 3 had basal polyhedrons 0.42µm in width and 0.54µm in height, the medial ones were larger with a height of 1.24µm and a width of 1.36µm (p=0.001). Instar 4 followed the same pattern as the other instars within the crystalline layer, containing basal polyhedrons with 0.53µm height and 0.56µm width as well as larger, medial polyhedrons 1.52µm high and 1.55µm wide (p=0.002). This runs against instar 4 development in previous carapace layers, where instar 4 has shown a decrease in size. Instar 5 had smaller basal polyhedrons 0.77µm high and 0.62µm wide, the medial polyhedrons were larger with a mean height of 2.01µm and width of 1.67µm (p<0.001). The adult again had smaller basal polyhedrons, 0.34µm high and 0.39µm wide, and larger medial ones, 1.07µm high and 1.02µm wide (p=0.001). While there were significant differences between the differently positioned polyhedrons in each instar, the only significant difference between polyhedrons of the same position throughout the instars, was between instar 5 and the adult. Although the crystalline layer is large in the adult, the polyhedrons were in fact smaller. The medial polyhedrons had a significantly smaller height, showing a reduction of 1.07µm (p=0.016) and the basal ones had significantly shorter widths, width a shrinkage of 0.31µm (p=0.003).

Throughout all instars (except for instar 1), no significant difference was seen between height and width in the polyhedrons within each instar. When the medial and basal crystals were averaged together the crystals were roughly equal in diameters (Fig 3.20). This is especially true for the adult crystals where the difference was only 0.05µm, this translates to a 0.03% difference between them.

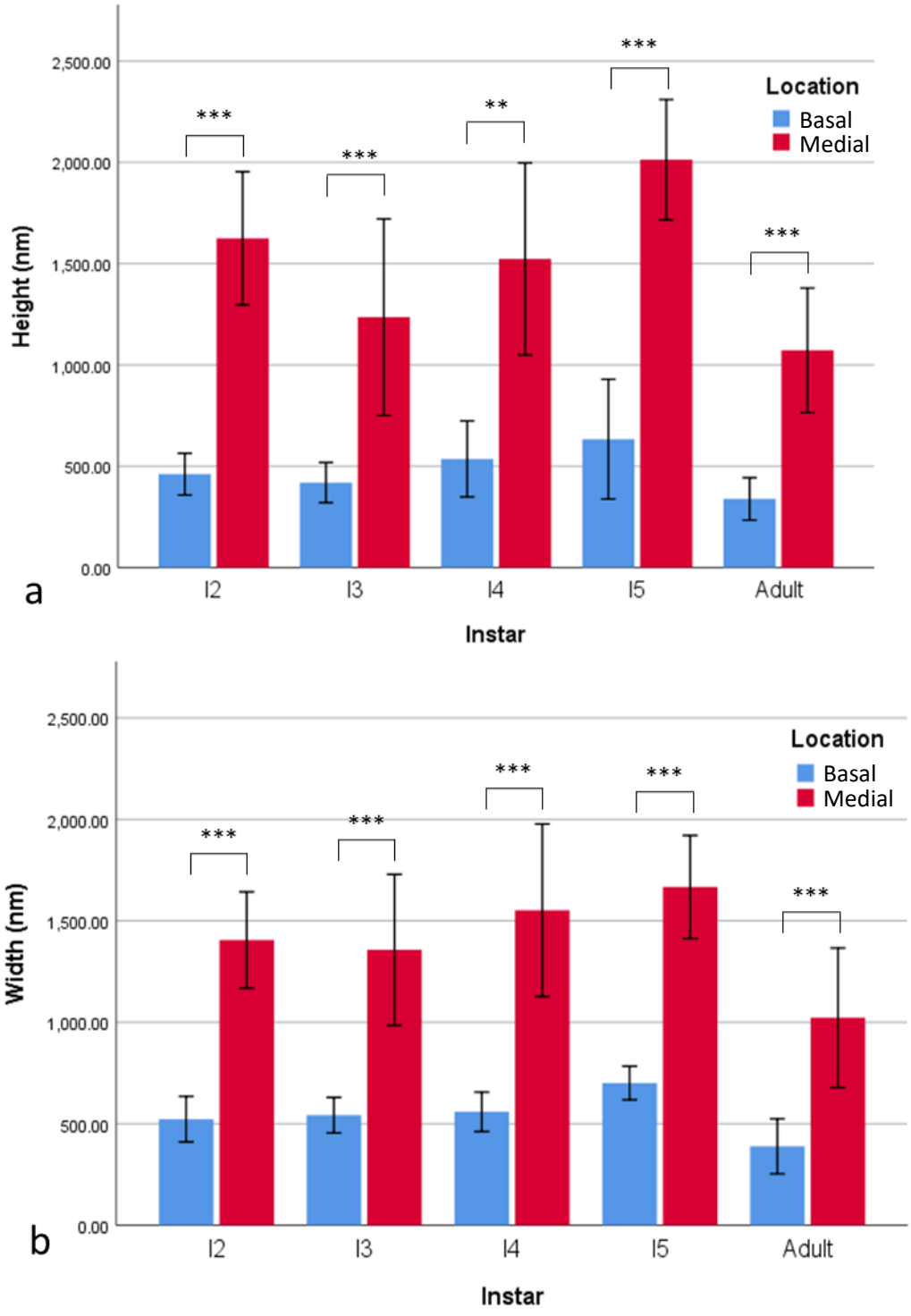

Figure 3.19: Measurements of the crystal size between the medial and basal positioned crystals displaying **a)** crystal height and **b)** width. The crystals at the basal layer were significantly smaller than those found in the medial part of the layer. ** represents $p<0.01$ and *** represents $p<0.001$.

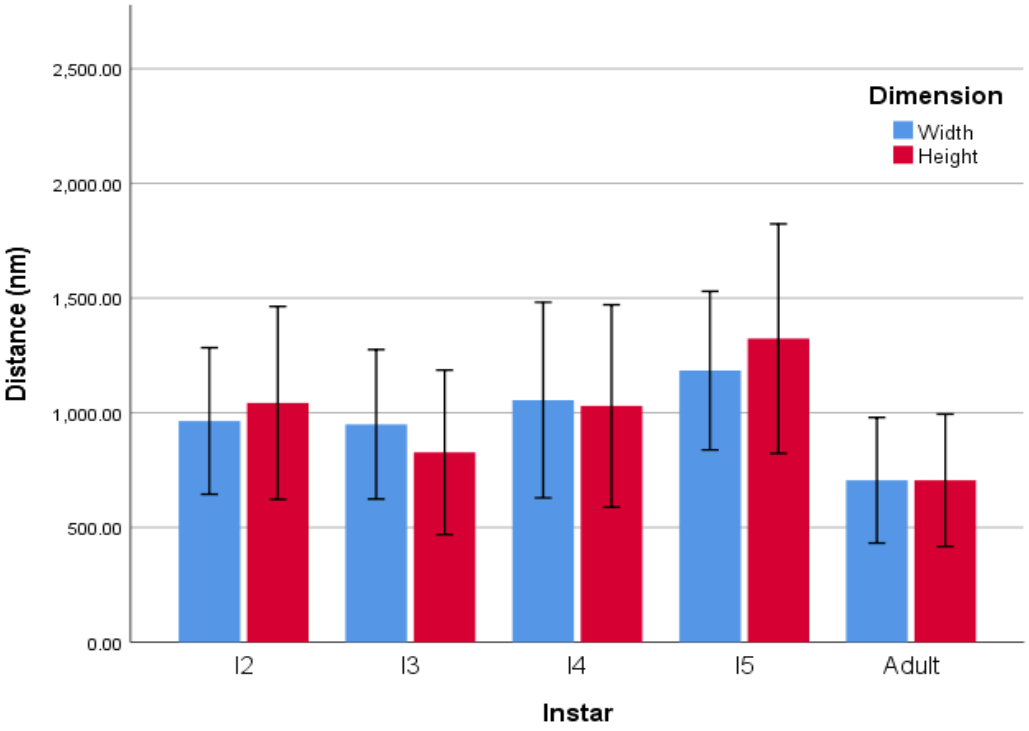

Figure 3.20: Comparison between the widths and heights of the crystals across the entire layer. No significant difference was seen between width and height at each instar. * represents $p<0.05$

3.3.2.4 Endocuticle

Throughout the instars, the endocuticle layers increased in size and number of chitin lamella, as development progressed (Fig 3.21), additionally there were some changes in the lamellae themselves. However, unlike most previous features, these changes were not in line with an increase in age and were specifically related to instar 3.

The increase in membrane endocuticle layer thickness is very gradual, with significant increases only seen between instar 1 and instars 3 and above, and the adult compared to the rest (Fig 3.21g). This is mirrored in the number of lamellae within the endocuticle, which only shows significant growth between instar 1 and 4 and above, and the adult when compared with all other instars (Fig 3.21h). Instar 1 has a mean thickness of 0.64µm and 5.4 lamellae, instar 2 has a thickness of 1.21µm with a mean of 7.7 lamellae. A significant increase in endocuticle thickness is seen at instar 3, the thickness of 1.67µm being thicker than instar 1 ($p=0.019$), however, with a

mean 8.8 lamellae, these were not significantly more numerous than instar 1 ($p=0.32$). Instar 4 had a mean thickness of 1.4µm and a mean 10 lamellae per layer ($p=0.049$), which was a significantly increased number of lamellae, compared to instar 1. Instar 5 did not have a significantly thicker layer compared to instar 4 ($p=0.8$) and had 10 lamellae, the same as instar 4. The adult endocuticle had a significantly thicker layer, at 3.66µm, and more lamellae, 17.6, than all other instars ($p<0.01$ and $p<0.001$ respectively).

The thickness of the lamellae is larger than the distance between them in every instar (Fig 3.22). Instar 1 had a mean thickness of 67.9nm with a statistically significant smaller distance of 42.36nm ($p<0.001$). Instar 2 had a thickness of 91.8nm and a smaller sized distance of 59nm ($p=0.02$) while instar 3 had a thickness of 58.8nm and a smaller distance of 33.2 ($p=0.003$). Instar 4 had a thickness of 71.2nm and smaller distance of 51nm ($p=0.049$). I5 had the largest endocuticle dimensions with a lamella thickness of 95.87nm and a significantly smaller distance of 63.6nm ($p=0.009$). The adult had a mean lamella thickness of 73.4nm and a smaller distance of 45.7nm ($p=0.006$).

There were very few differences between the dimensions of each lamella between each instar. The lamella thickness of instar 3 was significantly thinner than that of instar 5 ($p=0.013$) and instar 2 ($p=0.3$) lamella and the distance between the lamellae was significantly shorter than in instar 5 ($p=0.009$). With the exception of these comparisons, there were no other significant differences between any of the lamella or their spacing throughout the developmental stages.

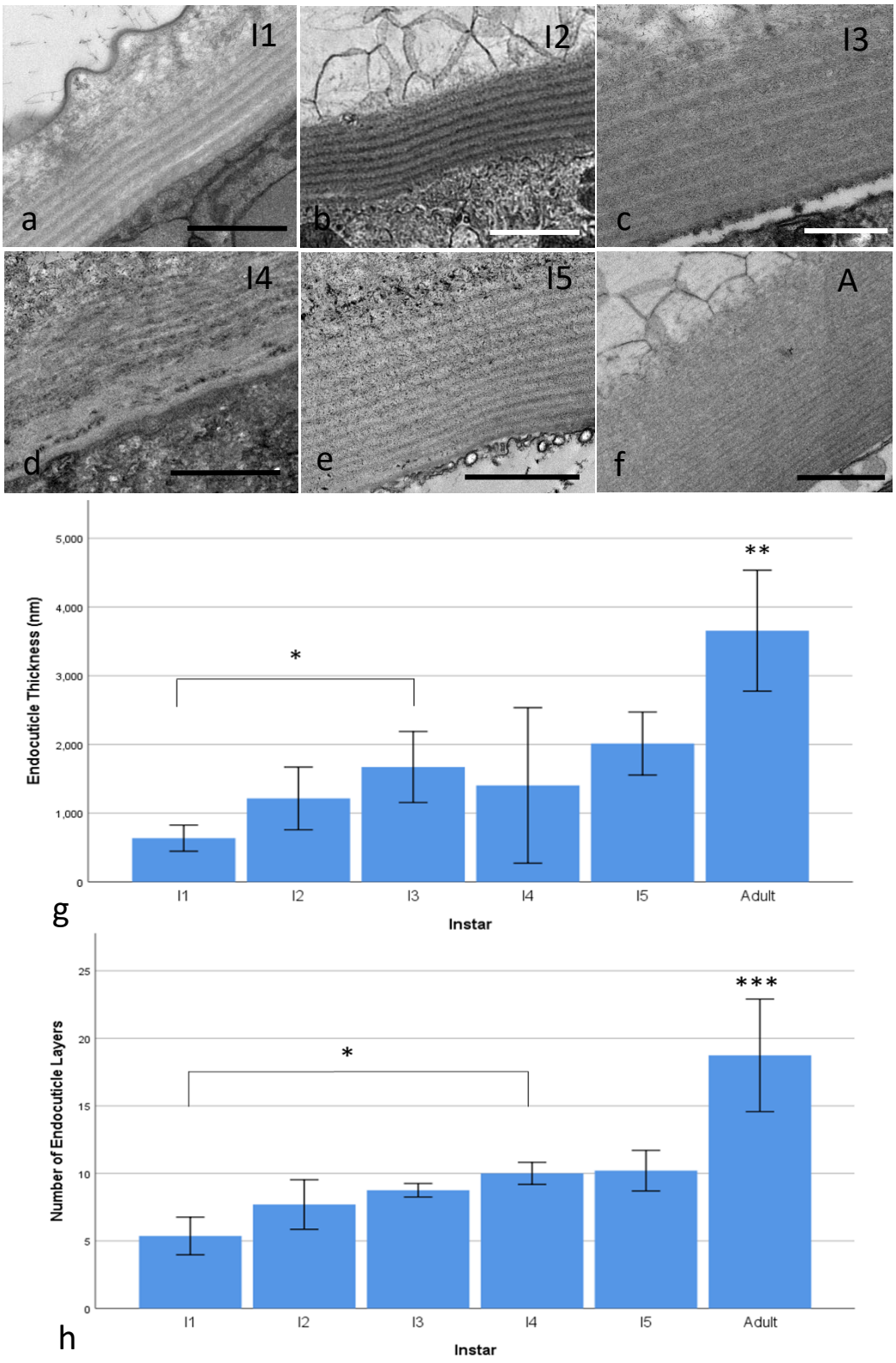

Figure 3.21: The endocuticle layer from **a)** instar 1, **b)** instar 2, **c)** instar 3, **d)** instar 4, **e)** instar 5 and **f)** the adult. Individual chitin lamellae can be seen within each layer. **g)** The thickness of the endocuticle layer throughout development. **h)** Comparison between the number of lamellae within the endocuticle throughout development. In both **g+h** the endocuticle increases gradually with a sharp increase in the adult. Scale bars are 1µm.* represents $p<0.05$, ** represents $p<0.01$ and *** represents $p<0.001$.

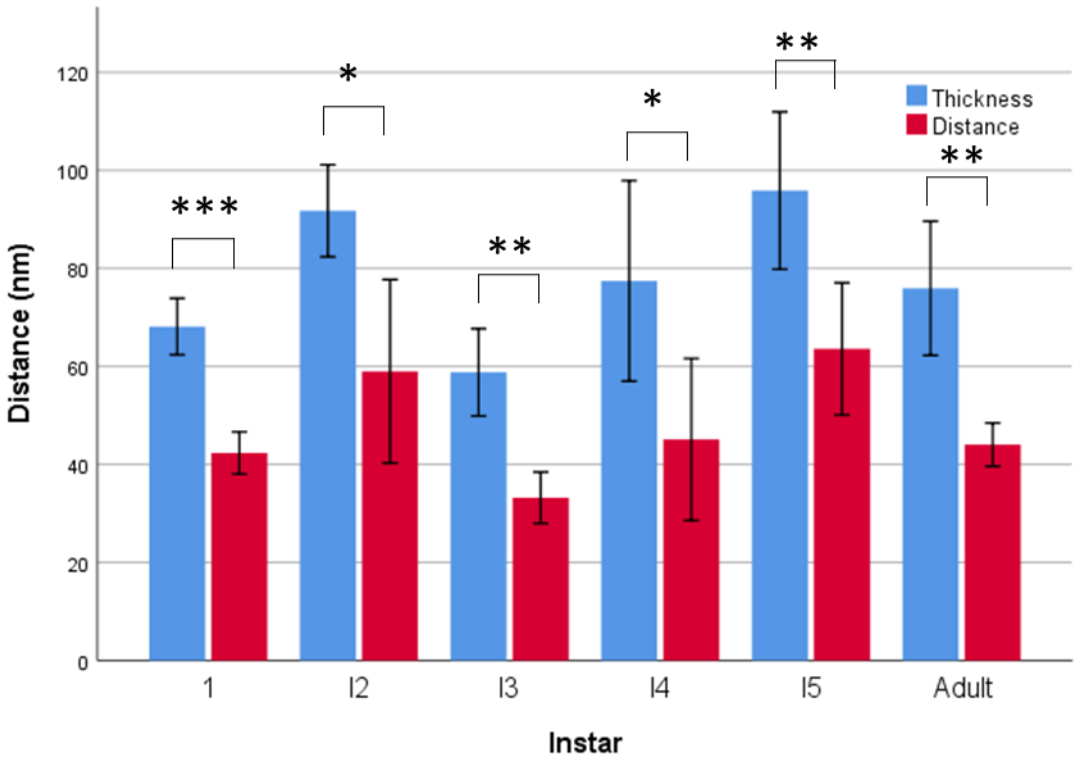

Figure 3.22: Comparison between the thickness and spacing distance between the lamellae. All lamellae except for those in instar 4 were significantly thicker than the difference between them.* represents p<0.05, ** represents p<0.01 and *** represents <0.001. Error bars are ±2 SE

3.3.3 3D Reconstruction of the Carapaces throughout the Instars

Using SBFSEM, the carapace was examined in three dimensions to confirm changes observed in the 2D TEM micrographs and determine if any additional changes unobservable from 2D sections are present. In the 3D model generated from the adult carapace (Fig 3.23), it was noted that the proportion of the layers did not drastically alter along the length (100µm in this model) of the carapace scanned. The edges of each layer were clearly distinct, smooth and uninterrupted, with each layer remaining parallel and a constant distance with each other, suggesting that any cross-sectional view through the carapace would provide a good representation of its structure. Apparent gaps, within the endocuticle, were a result of incorrect thresholding due to uneven staining that affected the contrast. As seen previously (Fig 3.10), the epicuticle projections had similar density throughout the carapace. Additionally, two pore canals were identified. While there were not enough pore

canals to make accurate predictions for the spacing between them, their sparseness was observed, and that they penetrated through the carapace.

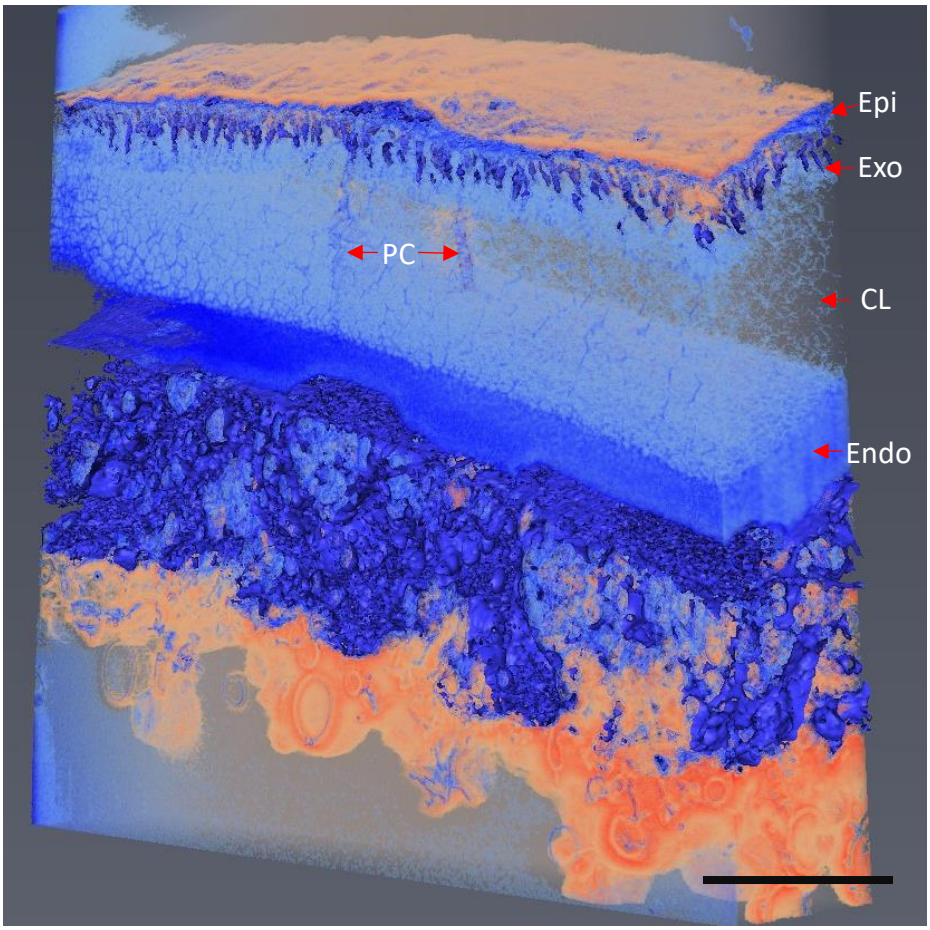

Figure 3.23: 3D volume render of an adult carapace generated from 1000 SBFSEM slices. The crystal layer was made more transparent so the pore canals can be seen. Abbreviations: Epi, Epicuticle; Exo, Exocuticle; CL, Crystalline Layer; Endo, Endocuticle; PC, Pore Canal. Scale bar is 10µm.

3D reconstructions of carapace sub-volumes were made for each instar (Fig 3.24) to see if there were differences in carapace structure between developmental stages. It was determined that overall carapace structure in these 3D visualisations was consistent with that observed in TEM micrographs. As with the adult sample, the borders between the layers were even, smooth and uninterrupted.

The 3D models enabled detailed investigation/analysis of specific layers, in isolation of the rest of the carapace (Fig 3.25). Individual features such as the crystalline endocuticle can be manually traced to study the structure in greater detail. The 3D reconstructions confirmed that the crystals are not tubes that carry on throughout the entire carapace, but that they tapered off in the z-axis and new polyhedrons

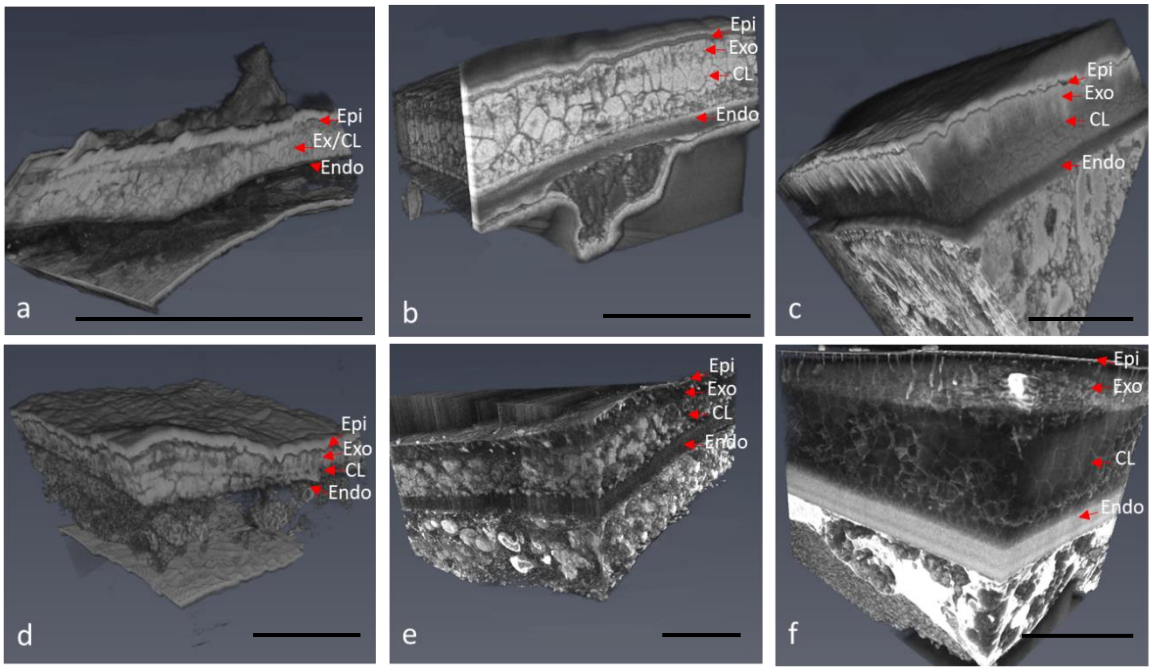

Figure 3.24: 3D volume renders of each instar **a)** instar 1, **b)** instar 2, **c)** instar 3, **d)** instar 4, **e)** instar 5 and **f)** the adult. Abbreviations: Exo, Exocuticle; Exo, Exocuticle; CL, Crystalline Layer; Endo, Endocuticle. See attached videos for 3D reconstructions. Scale bars are 10µm.

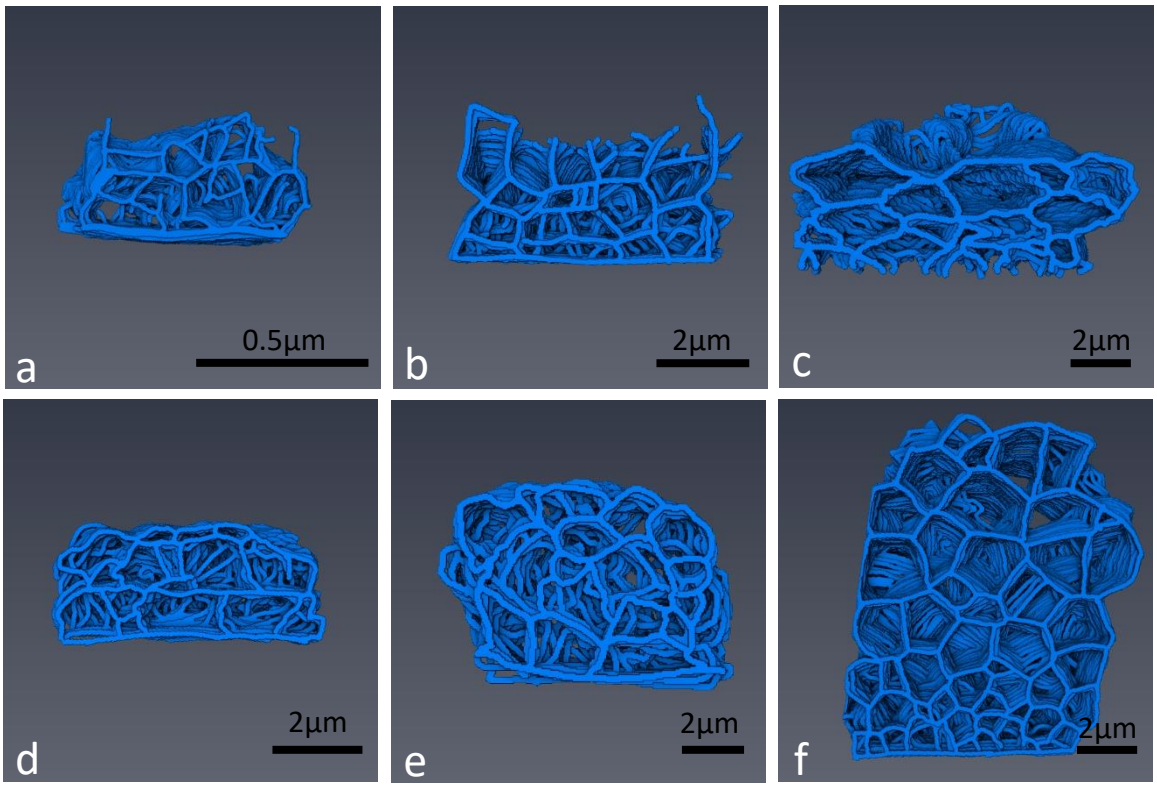

Figure 3.25: Traced 3D models of a transverse section of the crystalline endocuticle layer for each developmental stage showing, **a)** instar 1, **b)** instar 2, **c)** instar 3, **d)** instar 4, **e)** instar 5 and **f)** the adult. Scale bars represent 0.5µm for instar 1 and 2µm for all other developmental stages

started. Examining the depth of the polyhedrons can provide a better understanding

of how these polyhedrons fit together within the endocuticle. It was determined that the polyhedrons were randomly unorganised and of variable size, whichever directional axis it is viewed from, consistent with that observed in 2D TEM micrographs (Figs 3.25 and 3.26).

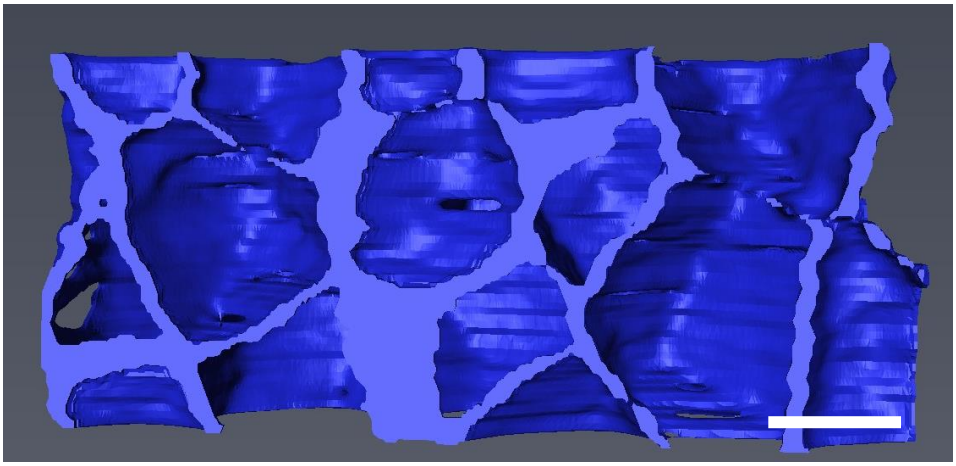

Figure 3.26: Reconstruction of the adult crystalline endocuticle, showing a horizontal cross section. The shape of the polyhedrons can be seen to be as disorganised and variable as in the transverse plane. Scale bar represents 500nm.

3.3.4 Analysis via Ptychography

Synchrotron x-ray ptychography provided several issues, as it was difficult to prevent movement within the sample during scanning. More significant vibrations were seen for instars 2, 3 and the adult which prevented the reconstruction of any usable data for these stages. 3D reconstructions were able to be generated for instars 1, 4 and 5, although these lacked contrast and therefore prevented distinction between the different layers and detailed analysis of the internal ultrastructure of the carapace. However, carapace thickness was analysed in Instar 1, 4 and 5 (Fig 3.27). Unlike the previous EM analysis, these reconstructions included the epidermal cells below the endocuticle and showed a combined mean thickness of 7.6±0.51µm for instar 1, which was significantly increased to 8.6±0.4µm ($p=0.03$) for the instar 4 carapaces, and 12.15±0.75µm at instar 5 ($p<0.001$).

Variation in the thickness was measured along the anterior-posterior axis (length) and the dorsal-ventral axis of the carapace. This dorsal-ventral axis is in relation to the entire ostracod, however as the sample was only comprised of the valve, the sample was placed on its side and so appears to be the width in Fig 3.26, instead of the height. The change in thickness along the anterior-posterior axis was greater than that along the dorsal-ventral as in table 3.1. The deviation along the dorsal-ventral axis was 0.9% from the central thickness of 7.66µm for instar 1, 1.88% from the central thickness of 8.69µm for instar 4 and 6.2% from the central thickness of 11.78µm for instar 5. The variation along the anterior-posterior axis was 12.19% for instar 1, 13.78% for instar 4 and 8.99% for instar 5.

a

Anterior-posterior	Instar 1	Instar 4	Instar 5
Anterior	6.77µm	8.01µm	11.65µm
Centre	7.54µm	9.33µm	11.46µm
Posterior	8.52µm	8.4µm	13.33µm

b

Dorsal-Ventral	Instar 1	Instar 4	Instar 5
Dorsal	7.66µm	8.56µm	11.6µm
Centre	7.66µm	8.69µm	11.78µm
Ventral	7.52µm	8.5 µm	13.06µm

Table 3.1: The thickness of each carapace measured from the images taken to form the 3D reconstructions in **a)** the anterior-posterior axis and **b)** the dorsal-ventral axis.

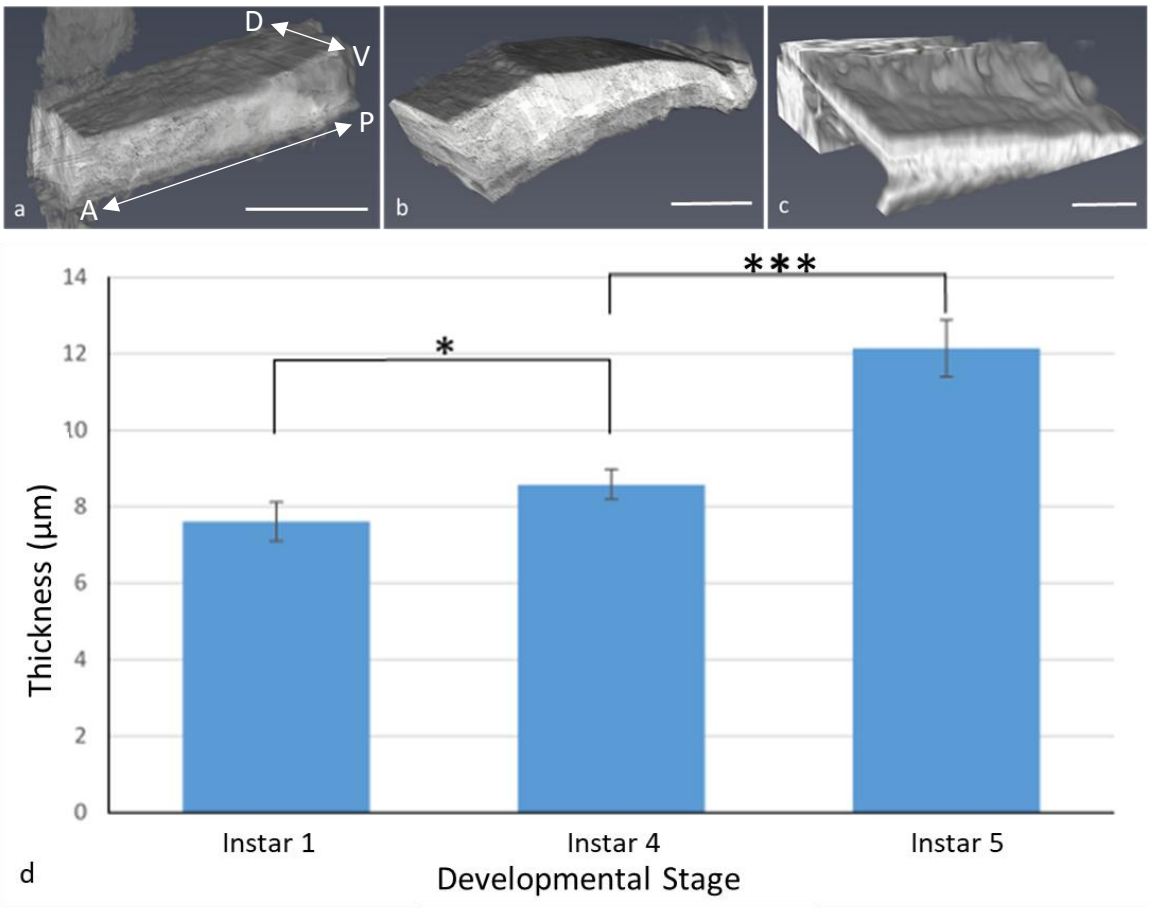

Figure 3.27: 3D reconstructions for the ptychography-derived data of **a)** instar 1, **b)** instar 4 and **c)** instar 5 carapaces. **d)** Carapace thickness increased throughout the instars. Scale bars represent 10µm, * represents p<0.05 and *** represents p<0.001. Abbreviations: A: anterior, P: Posterior, D: Dorsal, V: Ventral

3.4 Discussion

This study was the first to monitor the growth of the internal structures of the carapace in a myodocopid ostracod and is the first to investigate ultrastructural development in detail in an ostracod, as well as the first to subject crustaceans to the aforementioned techniques for investigations. While changes in ostracod instars have been analysed, these are measurements recorded from a surface view, either SEM or observations by eye (Kesling 1951a; Cohen 1983; Yumoto 1994) or are focused on the changes in the overall size of the ostracod body (Gerrish and Morin 2008; Pereira *et al*. 2017).

The ostracod carapace increased in thickness as it progressed through the instars until reaching a maximum thickness in the adult. It is interesting to note that this increase in thickness was not proportional to the increase in the size of the carapace. The maximum increase in carapace length over the ostracod's lifespan was from 0.59mm to 1.98mm (Cohen 1983), an increase of 3.36 times, whereas the mean increase of thickness found in this work was from 1.5µm to 19.16µm, a 12.7 times increase. Therefore it seems that this increase in thickness is not just to maintain a proportional relationship with the carapace as it grows but perhaps to create a more protective valve as the animal gets older. Mineral uptake may increase with age, resulting in a thicker calcified layer, as seen with *S. lerneri* in these results. This would make the increase in thickness a natural result of ageing, rather than a specific adaption. Another potential reason is purely a structural one, an increase in the area of the carapace may require more than a proportional response in thickness to maintain structural integrity. This change in thickness is similar to that seen in other ostracods, for example, analysis of the same part of the carapace in *Xestoleberis Hanaii* Ishizaki, 1968 from the order podocopia, showed a thickness increase from 2.3µm at instar 2 to 16.5µm at the adult stage (Yumoto 1994). Unfortunately, this author made no measurements on instar 1, however judging by the change in thickness of the other instars, the estimated thickness of the instar 1 would create a similar change in proportions to that found here.

The epicuticle increased in thickness over the ostracod's lifetime by roughly a factor of five, however, the structure of the epicuticle remained consistent throughout all the instars. The epicuticle ultrastructure was comparable with other myodocopid ostracods, such as *E. japonica*, in which the carapace is also divided into the same three distinct layers (Yamada 2019). While structurally similar, a substantial size difference in the thickness was seen, the adult *E. japonica* was approximately between 1 and 1.5mm long with an epicuticle thickness of 1µm (Yamada 2019). The *S. lerneri* adult was larger, at a maximum of 2mm in length (Cohen 1983) but with an epicuticle thickness of 161.9nm. This six-fold size difference between the two epicuticles may be linked to the required transparency of *S. lerneri*. *E. japonica* is smaller and lives around the same sea level and water conditions, which would

suggest the need for an equal, if not thinner epicuticle. However, *E. japonica* is not transparent and so needs to make no compromises to the thickness of the overall carapace. It is important to note that, as has been discussed previously, any material that is thin enough will be transparent, and 1µm is a very thin layer. An increase of less than a micron would not have a substantial effect on transparency, so it is unlikely that *S. lerneri* would have evolved such a thin epicuticle purely for transparency.

Thinner ostracod carapaces have also been seen, for example, in the adult *Cypridopsis vidua* which is only 0.6mm in length (Roca *et al*. 1993) but has an epicuticle thickness of 29nm (Bate and East 1972). This raises the question of why the epicuticle of *S. lerneri* is not proportionally even thinner to more easily maintain transparency. There are several potential reasons for this. *C. vidua* is a freshwater species, so will experience less punishing conditions and depths than a marine-based species such as *S. lerneri,* and this could allow it to maintain a thinner, less protective epicuticle than would be otherwise needed. Secondly, *C. vidua* is not from the myodocopid order of ostracods and so significant genetic differences may well be involved that could not be modified by environmental influences. Finally, there could be the possibility that this thickness is the optimal size for *S. lerneri*, it is thin enough to maintain transparency but thick enough to provide the maximal protection. There would be no reason to have a thinner epicuticle if the lower energy cost is offset by the higher risk of permanent damage.

The two chitin-based layers, the exocuticle and the laminated chitin endocuticle share a similar level of progression throughout the developmental stages. They both substantially increase in thickness as the instars progress, the epicuticle increased by a factor of 9 from 0.47µm at instar 1 to 4.21µm in the adult, and the endocuticle increased by a factor of 6 from 0.64µm to 3.66µm. It is interesting that, while these are large increases, they are actually both lower than the total thickness increase between the instars, which increases by a factor of 12.7, so their relative thicknesses both proportionally decrease. This is mainly due to the severe reduction of the crystalline endocuticle within the instar 1 carapace (24% total carapace compared to 59% in the adult), giving the exocuticle and endocuticle larger proportions by its

absence (30.9% and 41.8% respectively). When comparing instar 2 onwards, the two chitin layers together increase at a similar rate to the total thickness, the total proportion of the carapace staying between 22-24.5% for the exocuticle and 16.5-25% for the endocuticle.

The exocuticle consists of chitin fibrils organised in a much looser pattern than within the endocuticle, which is composed of numerous, regularly spaced chitin lamellae. Both layers showed a chitin orientation parallel to the surface of the valve, as seen in other ostracod carapaces such *as C.* vidua (Bate and East 1972). The chitin in both layers showed patterning representative of a typical crustacean twisted plywood structure (Bouligand 1972). The apparently differently sized fibrils in the exocuticle and the curved appearance of the fibrils within each endocuticle lamella, are instead all identical chitin fibrils but being viewed at different rotations. Twisted plywood structures are, as was mentioned in chapter 1, extremely effective at diffuse force distribution and so the *S. lerneri* carapace will possess the characteristic hardness and toughness of a crustacean carapace.

The chitin organisation within the *S. lerneri* carapace is very similar to that seen within most ostracods (Bate and East 1972; Smith and Bate 1983). The greatest similarity is seen in ostracods within the same order, myodocopida, specifically *Vargula hilgendorfii, Cypridina noctiluca* Kajiyama, 1912 and *Euphilomedes japonica* (Yamada 2019). However, the myodocopid *Halocypris infzata* Dana, 1849 shows a much lower level of parallel organisation in the chitin in the exocuticle (Smith and Bate 1983). The total thickness of the layers in the adult *S. lerneri* is consistent, or slightly thinner than that of the non-transparent *E. japonica*, which had an exocuticle varying between 2-5µm and an endocuticle around 5µm (Yamada 2019). Importantly they are also similar to the transparent *V. hilgendorfii* examined in the same paper which appears to maintain an exocuticle between 4-5µm and endocuticle around 3µm. Even though these layers are roughly equal between the two transparent myodocopid ostracods, *V. hilgendorfii* is much larger than *S. lerneri*, being up to 3.4mm long (Abe and Vannier 1995). The thickness of these layers may then be the maximum thickness possible, whilst maintaining transparency, as this formation leaves *V. hilgendorfii* with a much thinner carapace proportional to its size.

Within the *S. lerneri*, the lamellae do not follow the same proportional growth of the larger layers and show almost no significant changes between the instars. The only exceptions to this involved instar 3, whose lamellae were significantly thinner than both instar 2 and 5, and had an inter-lamella distance smaller than instar 5. The lack of any size differences elsewhere implies that this is not a developmental change and it is instead instar 3 specific. This change is immediately reverted with no lasting impact carrying on to any other instars. The changes in ostracod size from instar 2 to 3 and from instar 3 to 4 were not substantially different than the change between any of the other developmental stages (Cohen 1983), which leads to the belief that the I3 carapaces used were not truly representative. Intensive EM processing can damage samples, however, this seemed not to have occurred for any of the other samples. The most likely reason is that several of the instar 3 carapaces were caught close to post-moult, which would not be recognisable to the naked eye. In other myodocopids studied these chitin lamellae only develop post-moult (Yamada 2019) and it would seem likely that they may be thinner while being developed. The significant difference seen in every instar between their inter-lamella distance and their lamella thickness implies that the formation of this layer is a highly regulated, with a greater degree of order than is apparent in the other layers. This is further reinforced by the fact that this inter-lamella distance grows and shrinks alongside the lamella thickness such that the distance is always between 56.5-66.5% of the thickness of the lamella, again showing a high level of regulation.

What can be compared to other myodocopid carapaces, is the number of chitin lamellae seen in the carapace and *V. hilgendorfii* is comparable at points during its development (Yamada 2019). From TEM sections presented in this article, there can be seen to be roughly 20 chitin lamellae, organised and spaced in a similar pattern. The number of lamellae has previously been linked to the level of calcification and the weight of the carapace (Voss-Foucart and Jeuniaux 1978) so a large number of lamellae may just be indicative of a high level of calcification. Potentially the similarity seen between *S. lerneri* and *V. hilgendorfii* may purely be due to their (comparatively) closer taxonomy. In contrast, the podocopid ostracod *Bicornucythere bisanensis* Okubo, 1975 maintains only a very thin membrane layer (Okada 1982) although it

still shows significant calcification. This layer of the carapace appears to be a substantial proportion of most myodocopid crustaceans (Sohn 1988), although unfortunately no specific measurements or lamellae counts have been recorded.

The crystalline endocuticle seen between the two organic layers is formed from polyhedrons likely to consist of calcium carbonate polymorphs (Kesling 1951a; Jorgensen 1970; Rosenfeld 1979). Again the structure is very similar to that seen in general myodocopid ultrastructure (Yamada 2019) where the polyhedrons shrank in size, the more basal they were. This change was substantial at all stages of development, it was a reduction of roughly a third at all instars no matter how large the layer became. The polyhedrons also never significantly changed size throughout the ostracod's lifespan, except for the adult, in which they decreased in size compared to I5. This meant thicker layers consisted of more polyhedrons rather than larger ones, which could suggest an imposed limit to the polyhedron size, as this requires the creation of more of the biological matrix and so is more energy-intensive to create. Instar 1 did not have a properly developed crystalline layer, which is almost certainly due to the ostracod not having access to enough of the various minerals or available energy in the egg. No significant difference was seen between the height and the width of these polyhedrons, leading to structures with no preferred morphological orientation. While this is consistent with other myodocopida examined (including the non-transparent ones), it is at odds with some podocopian carapaces. *B. bisanensis* possess "grains" slightly wider than those seen in the *S. lerneri*, at 2µm wide but only 0.3µm thick (Okada 1982), leading to a much more brick-like structure. Other podocopian species had "crystal units" of no preferred morphological orientation that decreased towards the basal end but were much larger (Jorgensen 1970). These crystal units ranged from 6µm to 0.5µm near the chitin lamellae. This implies that if there is an imposed limit on the size of the polyhedrons within *S. lerneri*, it may be restricted to the myodocopian order. The minimum size of 0.5µm at the most basal end of the layer is similar to the minimum size of that within *S. lerneri*, 0.52µm. The polyhedrons of *V. hilgendorfii*, appear to be made of amorphous calcium carbonate or monohydrocalcite, instead of the usually expected calcite (Yamada 2019). This reduced size and change in the composition

may also be due to the depth at which the ostracod lives. Yamada suggests because *V. hilgendorfii* is nekto-benthic and would spend more time away from the ocean floor than benthic species, this would explain the lighter carapace, with pelagic species being even lighter by showing very little mineralisation, if any. The carapace of the benthic *S. lerneri* (Kornicker *et al*. 2002) seems to reaffirm this idea showing a thicker carapace than that of *V. hilgendorfii* and an equal, if not higher, level of mineralisation.

Changes in the crystalline endocuticle due to the fixation steps within EM processing is an issue which has been raised in the literature (Sohn 1969,1988; Yamada 2019). The concern is that amorphous calcium carbonate or monohydrocalcite is altered into much more distinct grains/polyhedrons of probable calcite. An example of this is shown by Yamada (2019) who showed the comparison in *V. hilgendorfii*. This would suggest that although the well-defined crystals in *S. lerneri* could imply a significant proportion of calcite within the composition, it may just be amorphous calcium carbonate. This is of special interest as the non-fixed carapace was transparent and the fixed was opaque and it is likely this processing plays a role in this loss of transparency. None of the EM carried out in this chapter was done without fixation so it is difficult to know how *S. lerneri* would be affected, however due to the ultrastructural similarities to *V. hilgendorfii,* it is likely to be similar. It is important to note that not all grains generated like this are due to this fixation effect, (Smith and Bate 1983) showed grains of calcite different from those generated by this fixation. Also, the imaging of the non-fixed *V. hilgendorfii* was from SEM, so it is difficult to get an exact representation of the ultrastructure. It should be kept in mind however when considering transparency, that the sharp, flat edges of the polyhedrons may be an artefact and much smoother borders may exist in the living creature reducing light reflections at the interface.

The ptychography work was a pilot study to determine if this technique could be used for the first time to analyse ultrastructure in this small and lightweight material. While specimen preparation, experimental and data analysis protocols were successfully established, there were still issues relating to micro-vibrations shaking the carapace and causing issues with contrast within the sample. This prevented the outcome of 3D reconstructions at the nanometre scale and limited the reliability of the exact thicknesses of the carapaces. However, comparisons between the samples are still valid and showed that variation in carapace thickness was not always proportionate to the developmental stage. The thickness along the length of the instar 5 carapaces showed lower variation than either instar 1 or 4, with instar 4 having the highest. Changes along the width were more consistent with what would be expected, with both the instar 1 and 4 having very little fluctuation in thickness and the adult having the highest. Additional work will be carried out to remove as many of the issues created by sample vibration as possible, through modifications to the reconstruction algorithms. This work has been started, however, it is incomplete and not in a publishable state (Fig 3.28). If modifications to the algorithms does not

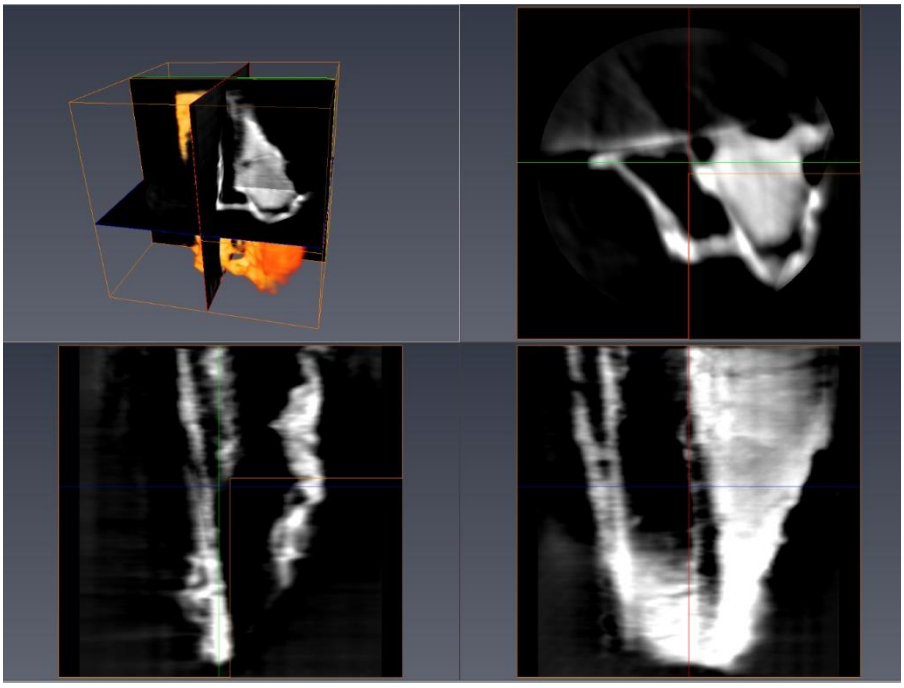

Fig 3.28: 2D slices from ptychographic reconstructions. Additional processing was performed to reduce issues caused by sample vibrations. A much higher level of detail can be seen from the ultrastructure.

improve the images then alternate sample preparation can be prepared. Samples could potentially be embedded within a resin or agarose that does not absorb x-rays. This would prevent any movement of the samples whatsoever but will require further beam-time sessions at the synchrotron.

The difference in the variation is also interesting to analyse, with a higher overall variance seen across the length instead of the width. This could be due to the fact that the selected area of the carapace chosen to analyse was a third of the way down the carapace at the central width. Because of the curved nature of the carapace, the structure is flatter near the centre and more curved towards the edges. Therefore the curvature would be greater in the anterior-posterior axis (as it is further from the centre of this axis) than the dorsal-ventral axis (which is closer to its centre). This increase in curvature could lead to a larger variance by the thinning and thickening of the carapace which helps create this curved structure.

No previous studies have employed WAXS analysis on ostracods from the sub-order myodocopina or on the chitin of ostracods maintaining a transparent carapace to this author's knowledge. The WAXS analysis in the present study was carried out to measure the spacing of the chitin molecules and to confirm it was in line with previous crustacean studies which showed the chitin orthorhombic unit with dimensions of a= 4.74 Å, b= 18.86 Å and c= 10.32Å, within the lobster cuticle (Minke and Blackwell 1978). The mean distance seen from the apparent chitin within the *S. lerneri* was 20.6Å, which would set it closest to the distance seen in the b axis at 18.86 Å. This is not caused by processing altering the shape, as tests on the effects of dehydration and deproteinisation have shown minimal changes to the chitin crystal's dimensions (Serrano *et al*. 2016). Previous WAXS analysis of chitin within the ostracod carapace showed much stronger results for the c axis (Parker *et al*. 2018). The reason why the b-axis is so much more prominent in the *S. lerneri* is most likely a practical one, this ostracod is much smaller than the one used in Parker's paper and the analysis was only focused on the eye window. Here the WAXS was carried out across the body and the smaller size of the carapace meant that while the centre of the valve was flat to the beam, a large amount of the sample would have been at an angle due to the curvature. As the chitin is highly organised within the carapace, this

change in the angle of incidence would lead to a different axis being measured. The *Macrocypridina castanea* (Parker *et al*. 2018) also showed changes in chitin spacing around the eye window believed to be to help transparency, and this may be why *S. lerneri* showed a change in overall chitin spacing compared to previous literature.

Skogsbergia lerneri is an ostracod that possesses a transparent carapace. There are many different mechanisms to achieve transparency and individual, less effective mechanisms could be combined to achieve greater effects. The simplest way to achieve transparency is through a material's thickness, as according to the linear attenuation coefficient within the Beer-Lambert for solid light (Swinehart 1962), the thinner the material the lower the effect of scattering/absorption. Therefore, if any given material is thin enough it can become transparent. Thus, maintaining a thin carapace makes it significantly easier for the *S. lerneri* carapace to retain its transparency. Another simple way for a material to be transparent is for all its components to have the same refractive index (RI) (Maurice 1957). While it is very doubtful that every layer of the *S. lerneri* carapace has the same RI, instances can be seen of structures having been organised to modify a sharp RI change into a smoother one, which would create less scattering (Born and Wolf 1980). For example, the projections coming down from the epicuticle, the lack of a distinct exocuticle-crystalline endocuticle border and the size reduction of polyhedrons close to the chitin lamellae, all point to the presence of a gradient between adjacent layers that could minimise any RI changes.

The other potential mechanism of transparency is based around the concept of destructive interference of light, similar to what is seen in the human cornea. Within the cornea an organised tightly packed pseudolattice of collagen fibrils are distributed in such a way that all the light scattered from the fibrils interferes destructively to prevent scatter in every direction except forwards (Knupp *et al*. 2009). To accomplish this the distance between adjacent collagen fibrils must be similar, and less than half the incoming light's wavelengths. A recent study into transparency within the ostracod *Macrocypridina castanea*'s carapace showed that a lamellae distance of between 125 and 150nm gave optical transmission of above 90% between 350nm and 675nm, as well as 900nm upwards (Parker *et al*. 2018). As

the distance between lamellae in *S. lerneri* averages to 47.9nm, significantly shorter than half the wavelength of any visible light and the adjacent lamellae are similar in size, it seems probable that this same mechanism would also be in effect. However, the important difference between *M. castanea* and *S Lerneri* is that *M. castanea* is composed of chitin lamellae for over half its entire carapace, whereas these lamellae only comprise 19% in the adult *S. lerneri*. As such, the effect these lamellae can have on overall transparency is reduced. The solution is most likely a combination of all these factors: a thin carapace overall means scattering and absorption are less impactful; the smooth change between RI gradients minimises the scattering that still happens and the transparency mechanism of the chitin lamellae means they do not increase scattering further.

Chapter Four

Microstructural Analysis

4. Microstructural Analysis

4.1 Introduction

4.1.1 The Importance of the Carapace and Chitin

The carapace is essential for the protection of the crustacean it encompasses. Chitin is essential to the overall strength of the carapace, and as such is found in specific structures throughout most of the tissue (see section 3.3.1). These include ordered hierarchical structures which contribute to the physical properties of the carapace. The abundance and level of organisation of these chitin containing structures within the carapace make chitin a potential target for nonlinear imaging. What is especially promising, is that chitin has endogenous fluorescence and there is compelling evidence that chitin has the properties required for emission of second harmonic generation (SHG) signals (*i.e*. it is non-centrosymmetric) (Rabasovic *et al*. 2015). Using chitin as a target for non-linear microscopy has not been carried out within ostracods and establishment of a successful technique allows for a new method for the measurement of chitin distribution within a carapace.

The aim of this chapter was to develop a method to acquire a chitin-derived signal within the ostracod carapace using non-linear imaging in order to provide an overall evaluation of its contribution to ostracod carapace structure. This will provide specific component identification (chitin) to analyse chitin distribution throughout the carapace, as opposed to the small volume viewed using electron microscopy.

4.1.2 Nonlinear Optics

Nonlinear microscopy is an imaging technique involving the use of nonlinear optics, where the effects of the presence of light on the optical properties of a material system do not react with a linear response, as commonly seen with conventional microscopy. The response from the sample material is dependent on the strength of the optical field in a nonlinear manner (Boyd 2008). This response varies depending

on which order of nonlinearity is utilised. The experiments used in this chapter are only investigating second-order optics, and so the other orders will not be discussed (Campagnola *et al*. 1999; Boyd 2008).

As well as by order, nonlinear microscopy can be divided into whether the light is coherent or incoherent in relation to signal phase and power. Incoherent microscopy produces signals with a random phase and a power proportional to the concentration of radiating molecules. Coherent microscopy however, produces signals with a precise and predictable phase, determined by a range of factors and a power proportional to the concentration of radiating molecules squared (Mertz 2004). The experiments performed in this chapter use both coherent (SHG) and incoherent (TPEF) signalling.

Nonlinear microscopy has been used for biological research for the last few decades (Campagnola and Loew 2003; Oheim *et al*. 2006; Campagnola and Dong 2011) as the process holds numerous advantages over other forms of light microscopy. One such reason is a significant reduction of any phototoxicity or photobleaching that is seen in microscopy utilising linear fluorescence methods (Campagnola and Dong 2011). This is especially true in SHG, as the signal arises from induced polarisation rather than absorption. The ability to identify specific materials or tissue without the need for artificial tags such as green fluorescent protein (GFP) or dyes is another important benefit. Other reasons include the generation of better optical contrast due to the longer near infra-red wavelengths and deeper imaging of tissue less permeable by conventional light microscopy wavelengths (Oheim *et al*. 2006; Rabasovic *et al*. 2015). Studying structures at a much larger scale than what has been observed at the ultrastructural level (Chapter 3), may allow for the identification of potential larger structural formations previously not observable., This is especially valuable along the carapace (*i.e*. a direction parallel to the surface) as ultrastructural analysis was mainly focused on layer formation through the carapace.

4.1.3 Two-photon-excited-Fluorescence

Two-photon-excited fluorescence, unlike SHG, is based upon nonlinear absorbance rather than scattering, with the near-instantaneous absorbance (a time window of 10^{-18}s) of two low-energy photons that combined have enough energy to excite the fluorophore. This required level of energy needs to approximately match the energy difference between the normal ground state (S_0) and the excited state (S_2) (Fig 4.1). This combination of photons in normal light conditions is extremely unlikely requiring high light intensities to be observable (Göppert-Mayer 1931) typically a photon density of 10^{20}-10^{30} photons/cm^2 (Oheim *et al*. 2006). After the absorption event has occurred, the molecule undergoes a radiation-less loss of energy through internal conversion to the state S_1 (Fig 4.1). While it is possible from this state to undergo phosphorescence (Oheim *et al*. 2006), it is rare and so only fluorescence will be discussed here. Once S_1 is reached, molecules will return to the ground state, most molecules will do so without emitting a photon and instead, the energy is converted or transferred away from the molecule. Some molecules, however, will emit a photon when returning to the ground state, this photon will have lower energy than the combined total previously absorbed by the fluorophore due to the energy loss during the conversion from S_2 to S_1. Due to the lower energy, the photon will have a longer wavelength, and this reduced energy and increased wavelength is known as the Stokes' shift. The nonlinear, second-order nature of this mechanism and so the requirement for two photons, means that the emitted fluorescence will depend upon the intensity (number of photons per time unit and cm^2) squared. This proportional relationship between the emission and square of the excitation is limited by a depletion in fluorophore ground states, known as saturation (Mertz 2004).

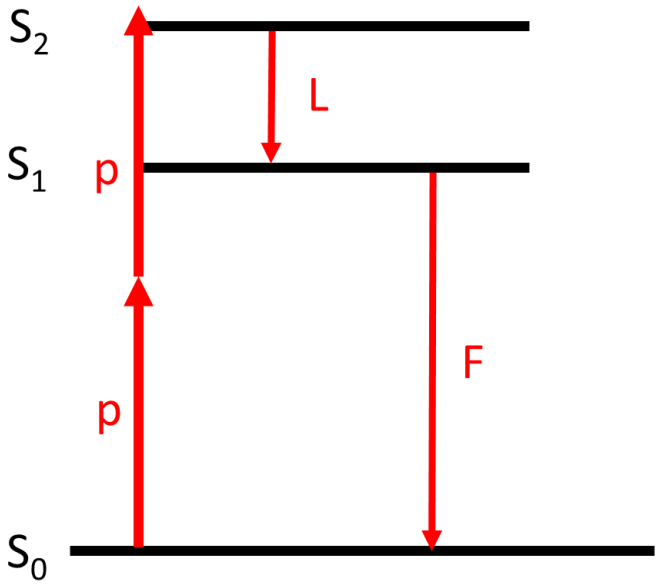

Figure 4.1. A simplified diagram of TPEF excitation in relation to fluorescence based on the Jablonski diagram. S_0 shows the ground state of the fluorophore, S_1 is the activated fluorescent state and S_2 is the temporary higher energy state. L shows the radiation-less energy loss, p shows the photons, which combined give enough energy to reach the higher energy level. F shows the energy loss to the base state from which some fluorophores will release photons. (Campagnola *et al*. 1999).

4.1.4 Second Harmonic Generation

Second Harmonic Generation is based upon the process of an induced nonlinear polarisation where two excitation photons interact with a material that emits a photon in a coherent wave at exactly twice the incident frequency and half the wavelength (Fig 4.2) (Campagnola *et al*. 1999). Unlike the nonlinear absorption mechanism TPEF follows, SHG is based on nonlinear scattering. There is no loss of energy due to the formation of an excited state, and so the emitted energy can maintain its coherency (Reinhardt *et al*. 2017). Critically, SHG can only occur in a material with a non-centrosymmetric structure such as birefringent crystals or specific biological structures *e.g*. collagen fibrils (Campagnola *et al*. 1999).

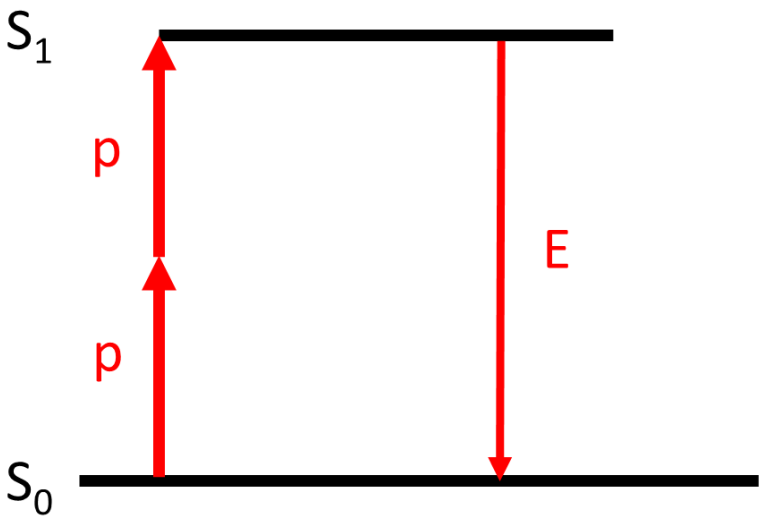

Figure 4.2: A simplified diagram of SHG scattering based on the Jablonski diagram. S_0 shows the ground state of the fluorophore, S_1 is the activated fluorescent state. p shows the photons, which combined give enough energy to reach the higher energy level. E shows the energy loss to the base state from which will release photons. Figure modified from Campagnola *et al* (Campagnola *et al*. 1999).

4.1.5 SHG and TPEF analysis on arthropod carapaces

Previous chitin analysis has found SHG signals derived from the carapace of other arthropods, specifically two cave-dwelling insect species (Rabasovic *et al*. 2015). These species do have some similarity to *S. lerneri* in that they have a thin chitin-based carapace which is also depigmented. SHG signals have not been identified in crustaceans. However, there exist numerous differences in the exoskeleton between different crustaceans; from structural layout to mineral composition and such differences between crustaceans and insects are even larger (Willis 1999). There has also been a reported difficulty in replicating these published results as a second study could not detect an SHG signal following 840nm excitation, although it was in the cuticle of a bedbug, *Cimex lectularius* Linnaeus, 1758 (Reinhardt *et al*. 2017).

TPEF analysis has been somewhat more successful, with both of the aforementioned studies identifying a TPEF signal from chitin (Rabasovic *et al*. 2015; Reinhardt *et al*. 2017), which was also observed in another study; nonlinear analysis of various cells within *Drosophila* (Chien *et al*. 2011). The main issue with TPEF analysis of the

ostracod carapace is identifying the source from which the signal is emitted (Reinhardt *et al*. 2017). Unlike SHG, a purely chitin response, it is proposed that resilin and potentially oxidated melanin, also contribute to the TPEF signal (Andersen 1964; Reinhardt *et al*. 2017).

4.2 Experimental Design

4.2.1 Hypothesis

A chitin-derived SHG and/or TPEF signals can be identified from within the ostracod carapace and will enable the characterisation of the distribution of chitin within different ostracod instars.

4.2.2 Aims and Objectives

Overall Aim: To identify non-linear chitin-specific signals within the carapce for each stage of the ostracod's development in order to visualise chitin distribution and quantify chitin content.

To achieve this a number of objectives will be pursued:

i) Determine optimal parameters (excitation and emission wavelengths) for derivation of chitin nonlinear signals using a positive control sample, namely chitin flakes.

ii) Using parameters determined in (i), identify nonlinear signals emitted from ostracod carapaces.

iii) Determine a laser power that generates optimal signal response without sample damage

iv) Optimise the chitin-derived nonlinear signal parameters in the carapace:

- Determination of optimal excitation wavelength
- Determination of optimal emission wavelength

v) Further identification of non-linear signal

vi) Determine differences in nonlinear signals and chitin expression through ostracod developmental stages.

4.2.3 Method development

i) *Determination of a nonlinear signal generated from a pure chitin positive control sample*

Before the investigation of the generation of nonlinear signals within the ostracod samples, it was necessary to confirm that there were clear, recognisable SHG and TPEF signals generated from crustacean chitin. As there has been confusion over the presence of a consistent signal (Reinhardt *et al*. 2017). Therefore practical grade purity, coarse chitin flakes (section 2.4.2.2) were mounted in air under a coverslip and excited at 920nm using 20% total laser power. Emission spectra were acquired over 398-698nm, through 3nm slit widths.

ii) *Determination of a nonlinear signal in ostracod samples*

Samples, in triplicate, were excited at 800nm as lower excitation wavelengths have greater signal response (Rabasovic *et al*. 2015) and forward-scattered SHG signals were collected by a NDD.2 detector (described in 2.4.3) with a 400/12nm filter, whilst back-scattered TPEF signals were collected with a BiG.2 with a 505/119nm filter.

iii) *Determination of optimal laser power to generate an optimal signal response without sample damage*

Since nonlinear signals have been generated from chitin using 800nm excitation wavelengths previously (Rabasovic *et al*. 2015), 800nm was set as the lower limit.

Laser power was tested at excitation wavelengths of 800nm, 840nm, 900nm and 1000nm to cover the potential range of wavelengths for future experiments.

Laser powers were tested in triplicate samples and included 5, 10, 15 and 20%, with exposure times ranging from 3-30 minutes, dependent on sample damage at time of imaging. Initial imaging started at 20x, however the majority was carried out at 40x for the highest generation of signal and the greatest level of damage.

iv) Identification and optimisation of nonlinear signals

a. Determination of optimal excitation parameters for nonlinear imaging of ostracod carapace chitin:

An excitation spectral scan was carried out to try and identify optimal excitation parameters for both TPEF and SHG signals. The samples were subjected to an excitation wavelength range of 700 to 1000nm, with an emission wavelength filter of 400nm/12 for the forward-propagated SHG, 505nm/119 for the back-propagated TPEF. Additionally, a 690+ beam splitter was used to filter out signals above 690nm. To record the correct results for all samples it is important to maintain a consistent level of energy at every wavelength. Changes in the wavelength will cause an associated change in laser power, with longer wavelengths having lower energy photons. Therefore, for all experiments involving multiple excitation wavelengths, the laser power had to be calibrated with the excitation wavelength to produce equal energy. This prevents shorter wavelengths incorrectly showing a higher emission signal due to the greater amount of energy used. A macro based on the calibration table (table 4.1) was modified from a pre-existing energy calibration calculation used for excitation analysis and the proportional change between each set laser power was used throughout these experiments.

Excitation Wavelength (nm)	Laser Power (%)	Excitation Wavelength (nm)	Laser Power (%)
840	2.8	960	15.1
850	3.2	970	18.1
860	3.6	980	20.9
870	4	990	24.3
880	4.4	1000	28.9
890	4.8	1010	35.9
900	5.8	1020	42.4
910	7.2	1030	49.2
920	8.6	1040	58
930	9.8	1050	73.5
940	11	1060	100
950	12.9		

Table 4.1: Laser power levels at increasing excitation wavelengths for maintenance of constant energy levels to sample. The calibration was based on starting from 840nm and the increase in laser power is nonlinear, with the later wavelengths requiring a substantial increase in power percentage.

b) Determination of optimal emission parameters for nonlinear imaging of chitin:

Ostracod samples were cut into sections, both with and without BMMA resin were subjected to nonlinear microscopy to ascertain whether BMMA resin interfered with chitin signal generation. Firstly, samples with BMMA resin were analysed. To determine optimal excitation, emission wavelengths and power usage, a series of 6 spectral emission scans (using 10nm emission slit widths) were performed over a range of excitation wavelengths from 840nm to 990nm, increasing in 30nm intervals. The emission signals over 690nm were excluded from the internal detector by an internal 690+ filter. All emission spectral scanning was performed with a pixel dwell time of 8.24µs with line averaging of 16.

Since SHG signals could not be detected within triplicate BMMA embedded ostracod samples, an additional optimisation step was needed to remove BMMA resin *i.e*. 'deplasticising' sections.

c) Removal of BMMA resin

To confirm whether an SHG signal could be seen within ostracod sections following BMMA resin removal (see section 2.5.4 from chapter 2 for deplasticising procedure), a series of emission spectral scans were carried out on deplasticised samples. Spectral imaging was performed using the parameters described above in section b).

v) Further Identification of Second-Order Signal via Powermeter measurement

Powermeter readings were taken multiple times per minute and after a minimum of 10 minutes, values were averaged to a mean per percentage laser power. To generate a value for laser power that considered changes in the laser power caused by constant use, the values were taken again after the machine had been in near-constant use for 5 hours running different experiments. The two sets of data were compared and a mean of the two values was taken to account for the changes seen.

To reinforce that the signal coming from the samples is truly a second order signal, the rate of reaction can be calculated. Plotting the log-log plots of the power interacting with the sample against the singal emitting from the sample will give a line equation with the gradient being representative of the order of the reaction. SHG imaging of rat tail tendon collagen was used as a positive control to confirm that a second-order relationship was seen, due to its strong second-order signal. Next, the same was performed for the adult ostracod carapaces for comparison. Images of rat tail tendon, a positive control for a collagen-derived SHG signal and the *S. lerneri* carapace were generated at 2%, 4% and 6% laser power and log signal against log power plots created for both.

vi) Nonlinear imaging of different ostracod developmental stages

All sample (n=5 per developmental stage) BMMA sections were deplasticised and mounted in PBS. Spectral imaging was performed at an 840nm excitation wavelength at 10% total power throughout an emission wavelength range of 400nm to 600nm, with a 10nm slit.

a) Comparison of chitin-derived emission spectra

The shape of each emission spectrum curve (containing both SHG and TPEF signal data) was normalised to the peak signal value, so that the highest peak of each curve was set to 100. Then intra-instar spectra and inter-instar spectra were compared using Kruskal-Wallis, followed by analysis with Dunn's test, using a Bonferroni corrected significance level. Since, significant differences were observed, Kruskal-Wallis analysis was repeated on data derived from the SHG (420-450nm) or TPEF (483-583nm) parts of each spectrum to determine which curves were consistent.

b) Analysis of chitin contribution to carapace through developmental stages

Lambda stacks acquired were converted into binary images in Image J; to quantify SHG pixels (*i.e*. white pixels) derived from chitin as a percentage of total pixels within the carapace. To do this three region of interests (ROI) were selected to encompass the full width of each carapace (n=5 per developmental stage).

Using the measure tool. Each image selected was the 430nm (which was both close to the centre of SHG peaks seen and the theoretical truest SHG signal of 420nm) emission image taken from the emission lambda stack/montage so that only chitin derived SHG signals were quantified.

vii) Statistical Assumptions

For the powermeter reading, log-log plot testing and pixel analysis, a normal distribution was assumed following Kolmogorov-Smirnov testing. Kurtosis and skewness were seen to be between ±1.5 for all data sets.

Kolmogorov-Smirnov testing showed non-normal distribution for the spectrum data, therefore non-normal distribution was assumed and Kruskal-Wallis analysis and Dunn's test were used.

All data generated from these sample populations was assumed to be done via random independent sampling as samples were chosen at random from their groups and no emphasis was put on selecting images based on their structural features or non-linear properties. Equal variance between the populations was also assumed due to equally sized testing groups.

4.3 Results

4.3.1 Determination of a nonlinear signal generated from a pure chitin positive control

Excitation of chitin flakes at 920nm, using 20% total laser power, generated nonlinear signals over the emission range 398 - 695nm. The SHG signal (Fig 4.3a) was identified as a sharp peak at an emission wavelength of 460nm (*i.e*. at half the original excitation wavelength). The TPEF signal derived from chitin flakes (Fig 4.3b) was represented by a broad peak within the emission spectrum, ranging from 480 to 670nm, with a peak around 536nm.

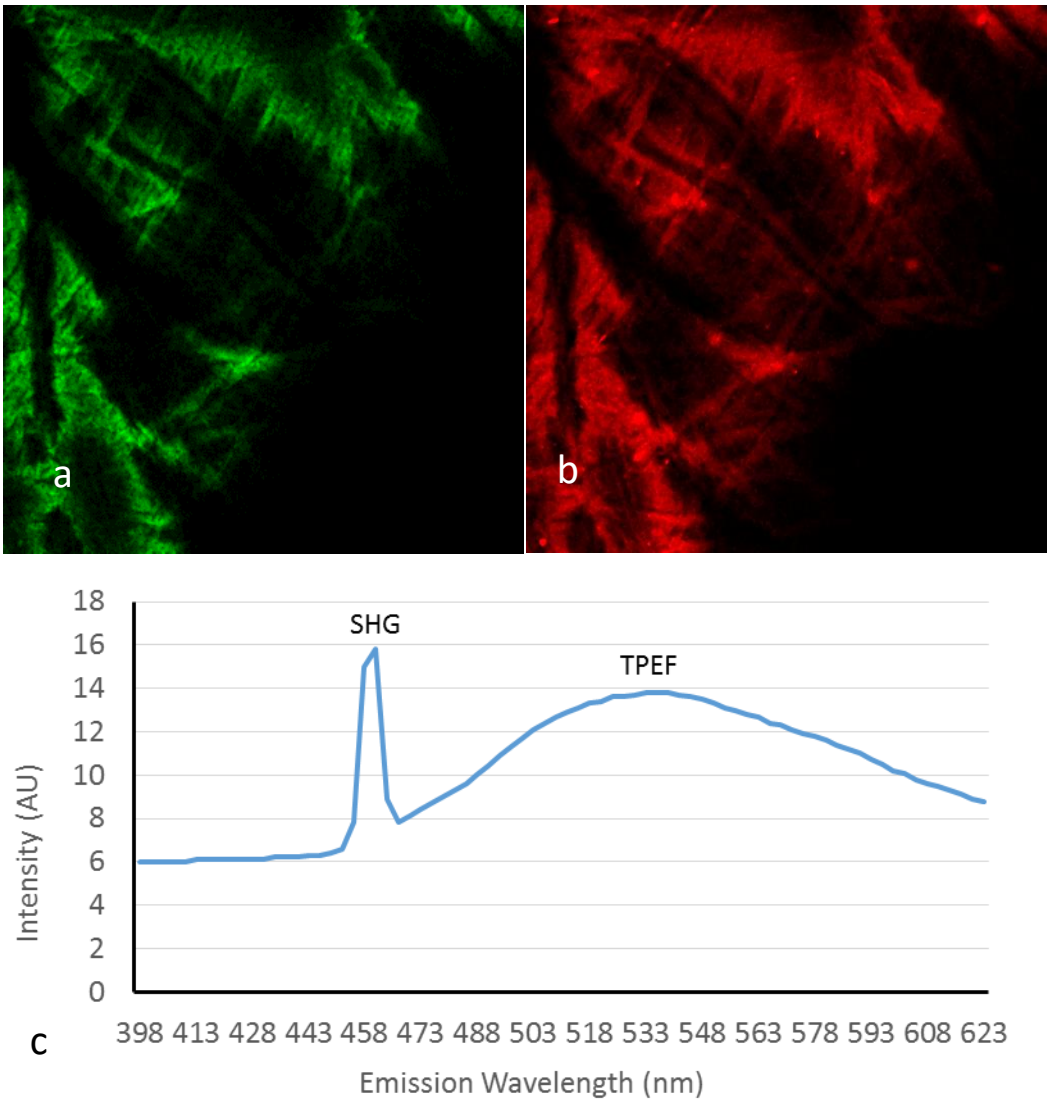

Figure 4.3: Nonlinear signals emitted from purified chitin flakes. Purified chitin excited at 920nm generated a **a)** SHG signal (emission wavelength: 455 - 465nm) and a **b)** TPEF signal (emission wavelength: 480 – 670nm) with **c)** the emission spectrum denoting the positions of the SHG and TPEF signals.

4.3.2 Determination of a nonlinear signal in ostracod samples

Nonlinear signals, forward-scattered SHG and TPEF, were emitted from the ostracod carapace (Fig 4.4). The forward scattered signal was present throughout the entire valve (Fig 4.4a). This widespread signal was consistent with chitin's ubiquitous dispersal throughout the carapace (as discussed in chapter 1). TPEF was derived from specific structures, including a central supporting structure throughout the valve and

the attachment of an additional limb (Fig 4.4b). TPEF distribution differed from that of SHG signals, as it was observed throughout the valve.

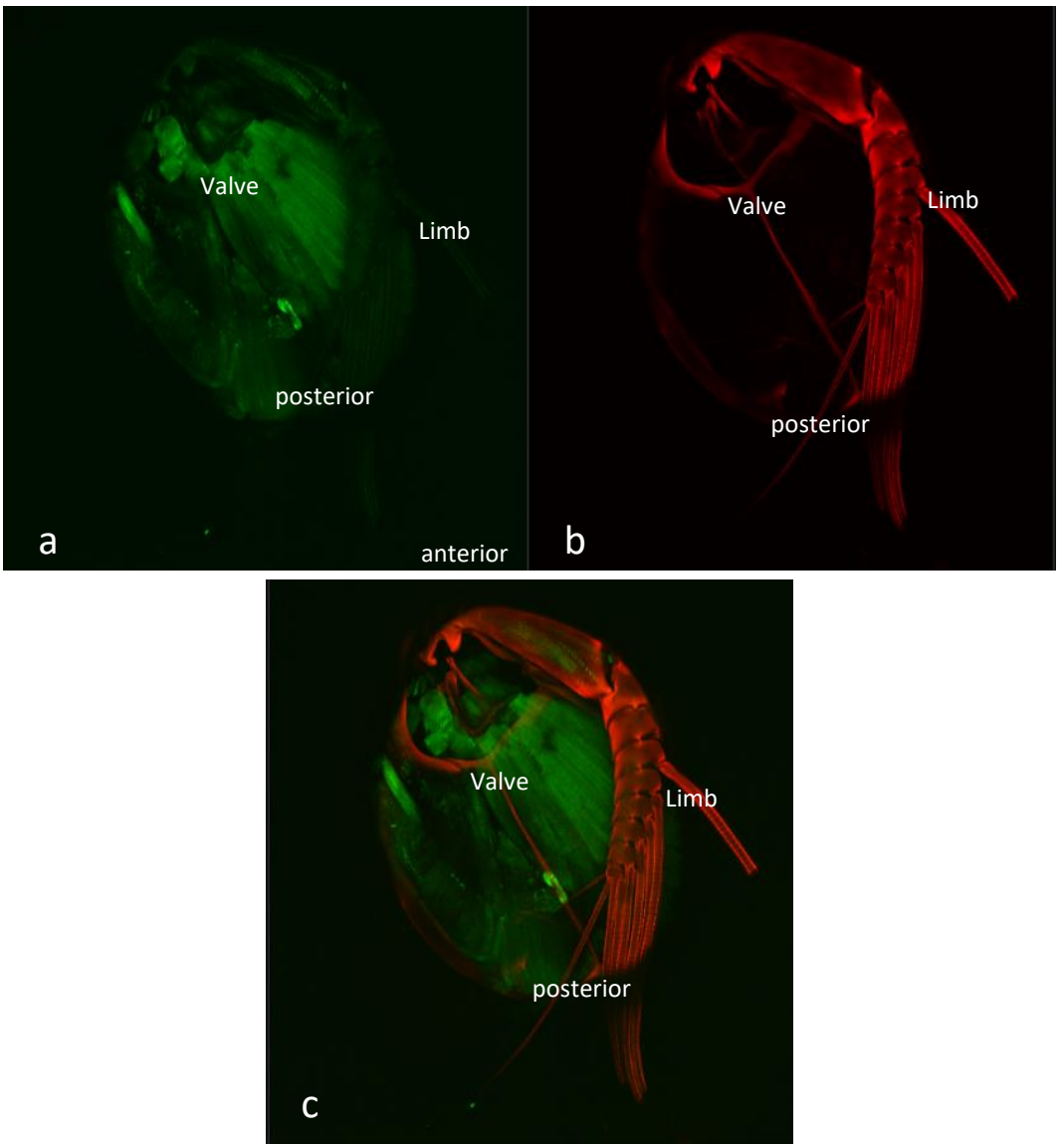

Figure 4.4: Maximum intensity projection of nonlinear signals emitted from an ostracod valve. **a)** Forward scattered signal collected at SHG's predicted emission wavelength, 394-406nm; pseudo-coloured green **b)** Back scattered signal collected at a range within TPEF's predicted emission wavelength, 445.5-564.5nm and pseudo-coloured red. **c)** An overlap of both images shows that two distinct signals are emitted from the sample.

4.3.3 Determination of laser power for optimal signal response without sample damage

Before further nonlinear microscopy of the ostracod samples was undertaken, determination of the optimal laser power was performed, to assess optimal signal production, without causing damage to the sample from the beam energy.

In BMMA-sections of *S. lerneri* at 800nm excitation, no sample damage was seen when the applied laser power was at 5%, 10% and 15% for 30 minutes. Mild damage was evidenced as the creation of a small bubble following three minutes at 20% laser power (Fig 4.5b). Significant damage was identified at nine-minutes with the generation of multiple bubbles taking up a significant portion of the image, as seen in figure 4.5c. 15% was deemed the maximum safe power level to ensure negligible sample damage in BMMA sections at 800nm.

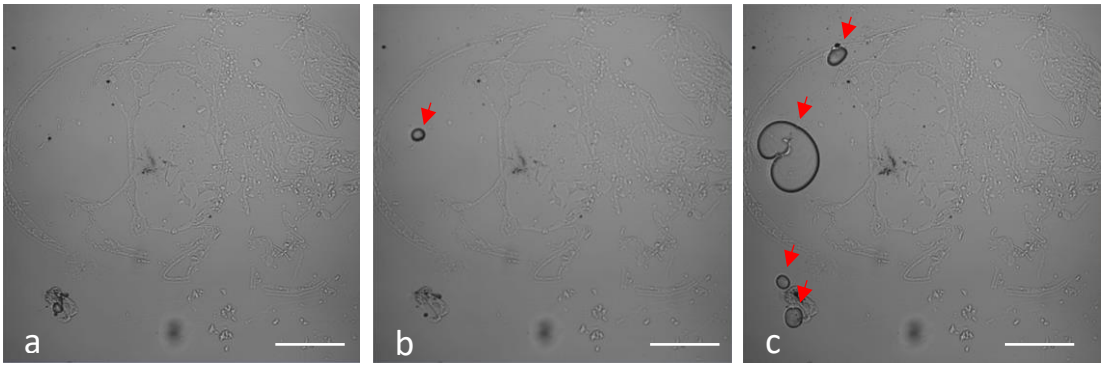

Figure 4.5: The effect of 20% laser power on samples in BMMA sections at 800nm at 20x 0.8NA, Phase contrast images acquired **a)** pre-laser exposure, **b)** post 3-minutes laser exposure indicating early damage and **c)** major sample damage observed at 9 minutes. Examples of sample damage are denoted by red arrows. Scale bars are 500µm.

The effect of laser power over exposure times was also tested in tissue sections following removal of BMMA. Analysing laser damage, using a 40x objective lens, no damage was identified following excitation at 840nm with laser powers below 40% for thirty minutes exposure. At 40% laser power, the damage was seen after three minutes with a small amount of disintegration around the edges of the carapace. Extreme damage followed at about four-minute exposure with significant portions of

the sample destroyed (seen in Fig 4.6a-c). 20% laser power was deemed the optimal power level to use at 840nm in deplasticised tissue sections.

At 900nm excitation, in deplasticised tissue sections, sample damage was negligible up to 30% laser power, with mild damage at eleven minutes exposure and moderate damage after thirty minutes (Fig 4.6d-f). 25% laser power was deemed the optimal power level for 900nm excitation. At the 1000nm excitation wavelength, as the overall laser energy is substantially reduced, mild damage was observed only after 30 minutes exposure of 100% laser power (Fig 4.6g-i). Therefore 90% laser power was determined to be the optimal power level for 1000nm. While this power optimisation experiment did not test any longer wavelengths, it would be safe to assume any experiments carried out at a wavelength significantly longer than 1000nm could be safely carried out at 100% laser power

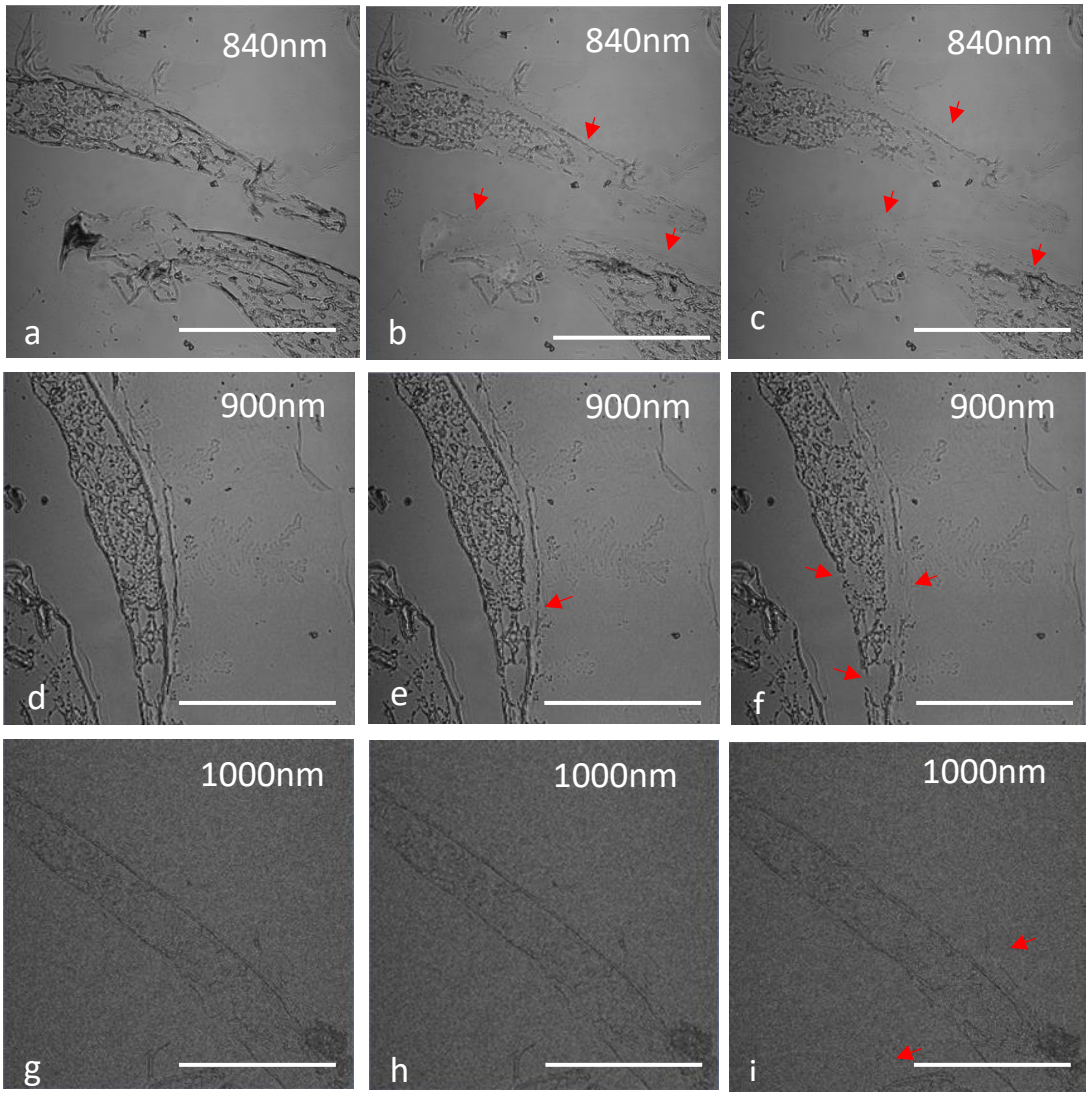

Figure 4.6: The effect of laser power on deplasticised, damaged tissue sections at various excitation wavelengths. Examples of damage are shown via red arrows. Phase contrast images acquired following excitation **(a-c)** at 840nm using 40% laser power, (**d-f)** at 900nm using 30% and (**g-h)** at 1000nm using 100% **a)** Initial pre-laser image **b)** post 3 minute laser exposure indicating early damage **c)** major sample damage observed at 4 minutes. **d)** Initial pre-laser image. **e)** post 11 minute exposure showing initial damage. **f)** End of test at 30 minutes showing damage to the sample. **g)** Initial pre-laser image **h)** post 15 minutes showing no damage had been caused to the sample, **i)** End of test at 30 minutes where mild damage can be seen. Scalebars were 100µm.

4.3.4 Identification of nonlinear signal from BMMA embedded samples and optimisation of nonlinear parameters

A strong TPEF signal was emitted from 445-565nm in the BMMA embedded carapace tissue sections following 840nm excitation (Fig 4.7). However, the signal within the SHG wavelength range, emitted at half the excitation wavelength, was not produced from the chitin-rich carapace.

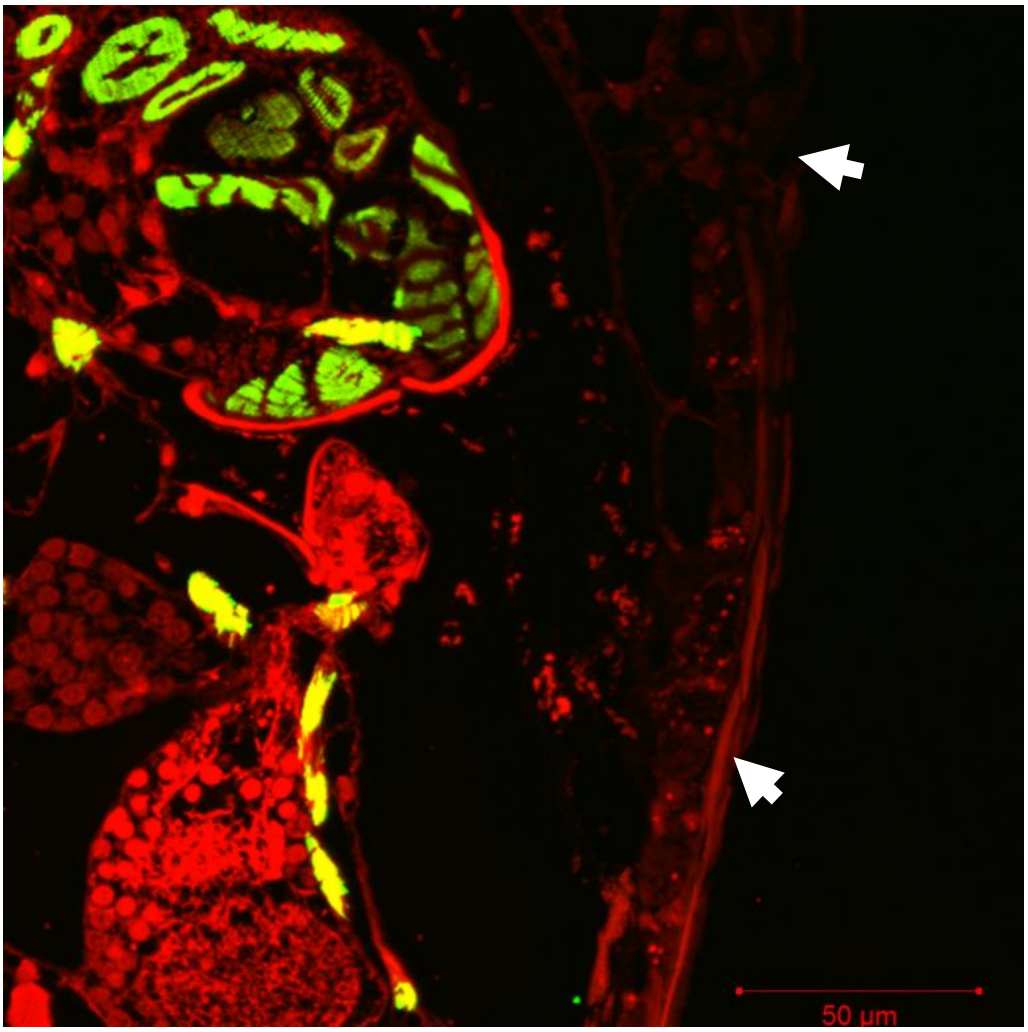

Figure 4.7: Maximum intensity projection of nonlinear signals derived from an ostracod BMMA section. Red: TPEF wavelength. Green: SHG. Arrowheads mark the carapace.

4.3.5 Determination of optimal excitation and emission wavelengths

An excitation spectral scan (excitation wavelength range between 700 and 1000nm, emission wavelengths: 394-406nm) was carried out to identify both nonlinear signals and the optimal excitation wavelength. Excitation lambda stack montages (Fig 4.8) showed a strong signal between 700nm and 810nm, before gradually decreasing. This was indicative of a TPEF signal response, which had a characteristic broad peak.

Based on the excitation lambda montage, an SHG signal could not be interpreted. The characteristic strong signal with a narrow range centred at half the excitation wavelength was not identified. To determine if an SHG signal underlied the TPEF signals, a series of emission spectra at constant excitation wavelengths were

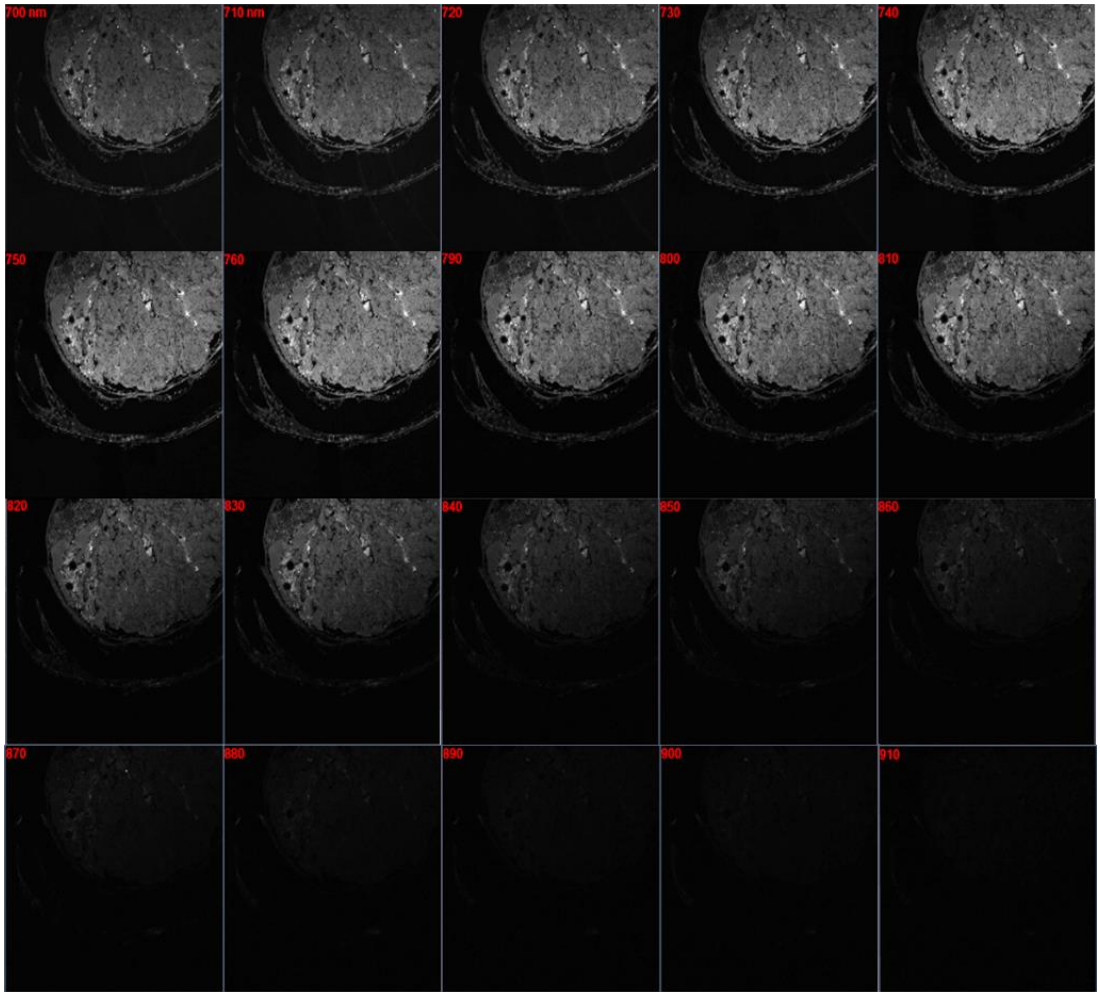

Figure 4.8: Excitation lamda stack of ostracod sections in BMMA over 700nm and 900nm, in 10nm steps. The strong signal between 700nm and 810nm, before slowly decreasing is indicative of a TPEF signal response.

undertaken in an attempt to separate any SHG peak from the broad TPEF signal. Results identified a strong signal, with a broad peak, consistent with that of TPEF in all excitation ranges (Fig 4.9, Fig 4.10). However, no second peak, indicative of an SHG signal was observed at the half excitation wavelength. Signals acquired after excitation at 870nm and 900nm were of a much higher intensity than that of the others.

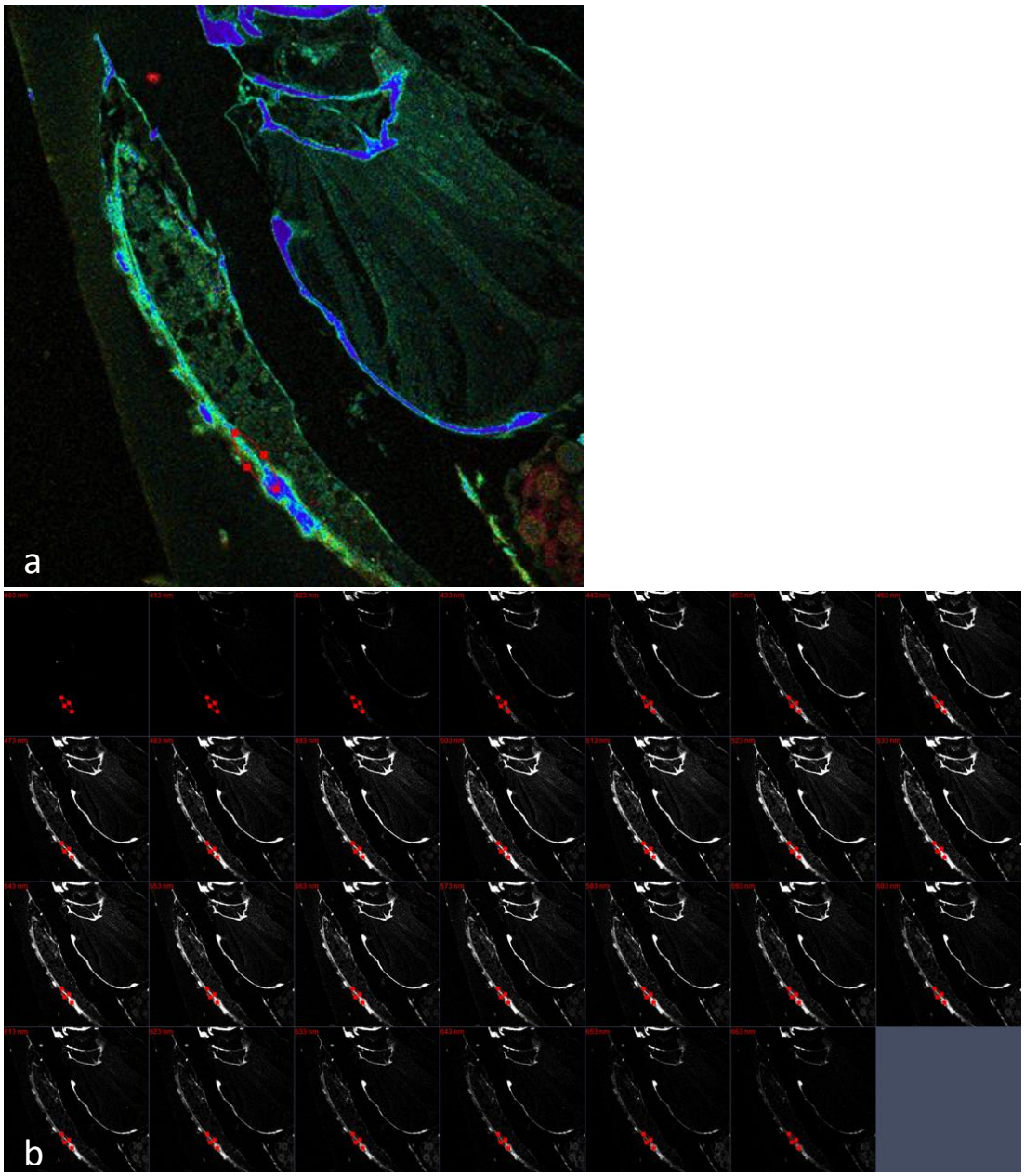

Figure 4.9: a) Emission lambda stack, 403 - 663 nm, following excitation at 840nmin BMMA embedded ostracod sections. **b)** Montage of emission lambda stack images, at 10nm increments. Pixel intensity values were extracted from the regions of interest, denoted by red circles.

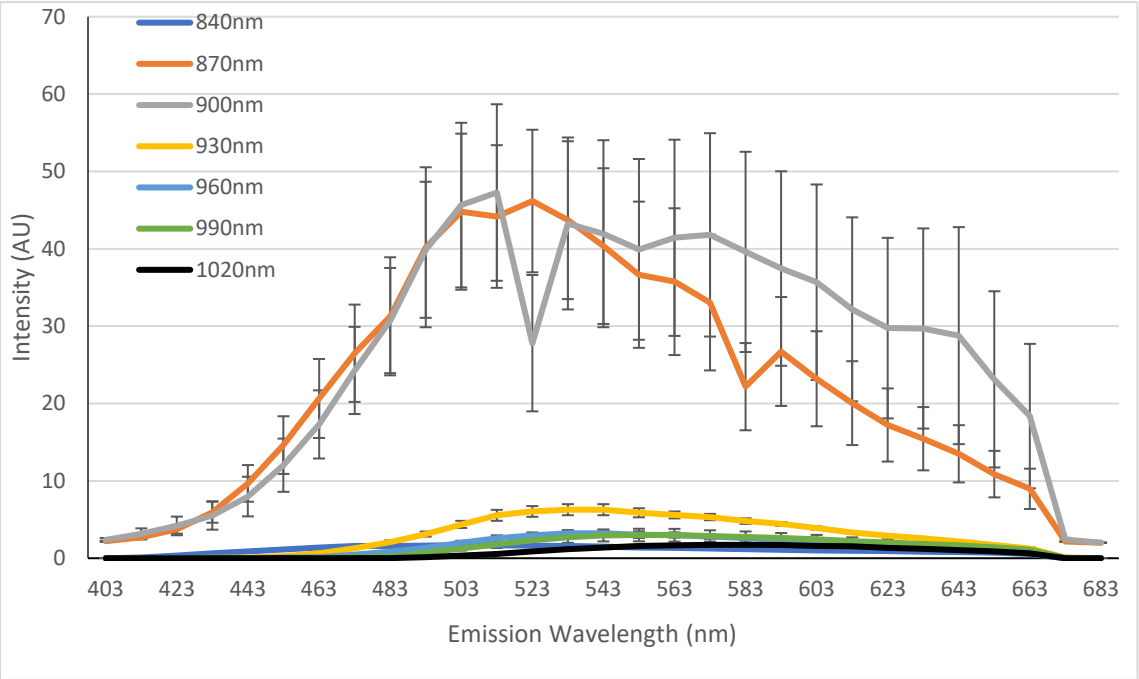

Fig 4.10: Relative intensity of emission spectra from ostracod BMMA sections at different excitation wavelengths, between 840nm and 1020nm. All emission spectra show a TPEF curve, with 870nm and 900nm having a significantly increased signal, but no SHG peaks. Error bars shown are ±SE.

4.3.6 Identification of nonlinear signals within deplasticised ostracod sections

To determine whether an SHG signal was masked by the presence of BMMA resin, emission spectra were repeated (see section 4.45) in deplasticised ostracod tissue sections (*i.e*. BMMA resin removed). A TPEF signal was easily identified, similar to that in BMMA- sections, in all excitation wavelength ranges. However, unlike the BMMA embedded samples, when emission spectral intensities derived from ROIs within the ostracod carapace were taken (Fig 4.11), a secondary peak was observed within the emission spectra at the shorter excitation wavelengths (Fig 4.12). This peak centred on half the excitation wavelength; indicative of an SHG signal. This peak was seen when the sample was excited at 840nm, 870nm and 900nm, with no evidence of a stronger TPEF signal 'swamping' the SHG signal.

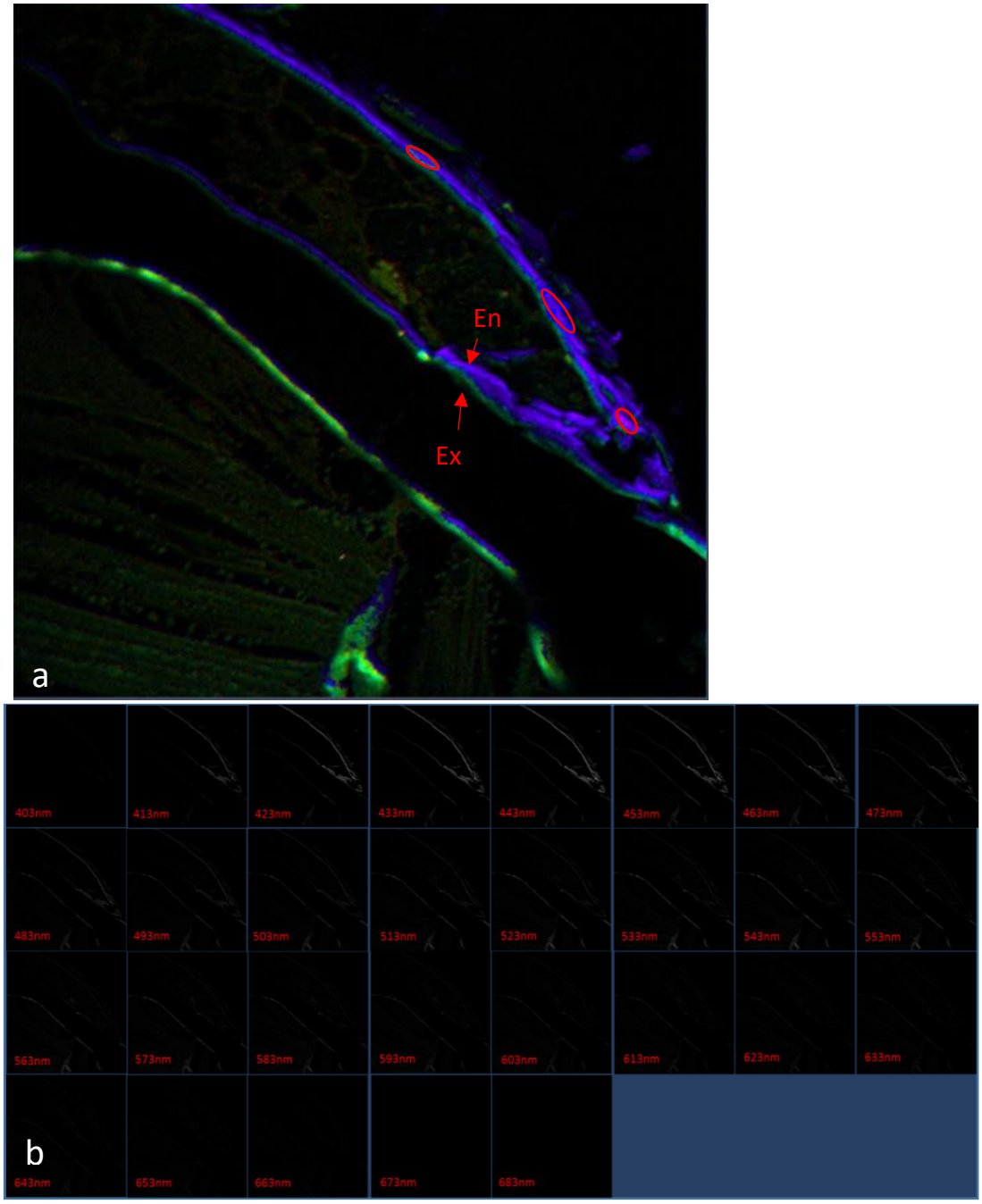

Figure 4.11: a) Lambda stack of emission spectra emitted at 840nm excitation, acquired using 40x objective. The purple coloured signal is representative of the wavelength band SHG would be produced from. Values for the intensities were taken from three ROI from the carapace. Ex stands for exocuticle and is the layer showing in mostly green, En stands for endocuticle and is the layer shown in purple (SHG signal emission) **b)** Montage of individual emission scans at set 10nm wavelengths that combine to form the lambda scan for one excitation wavelength.

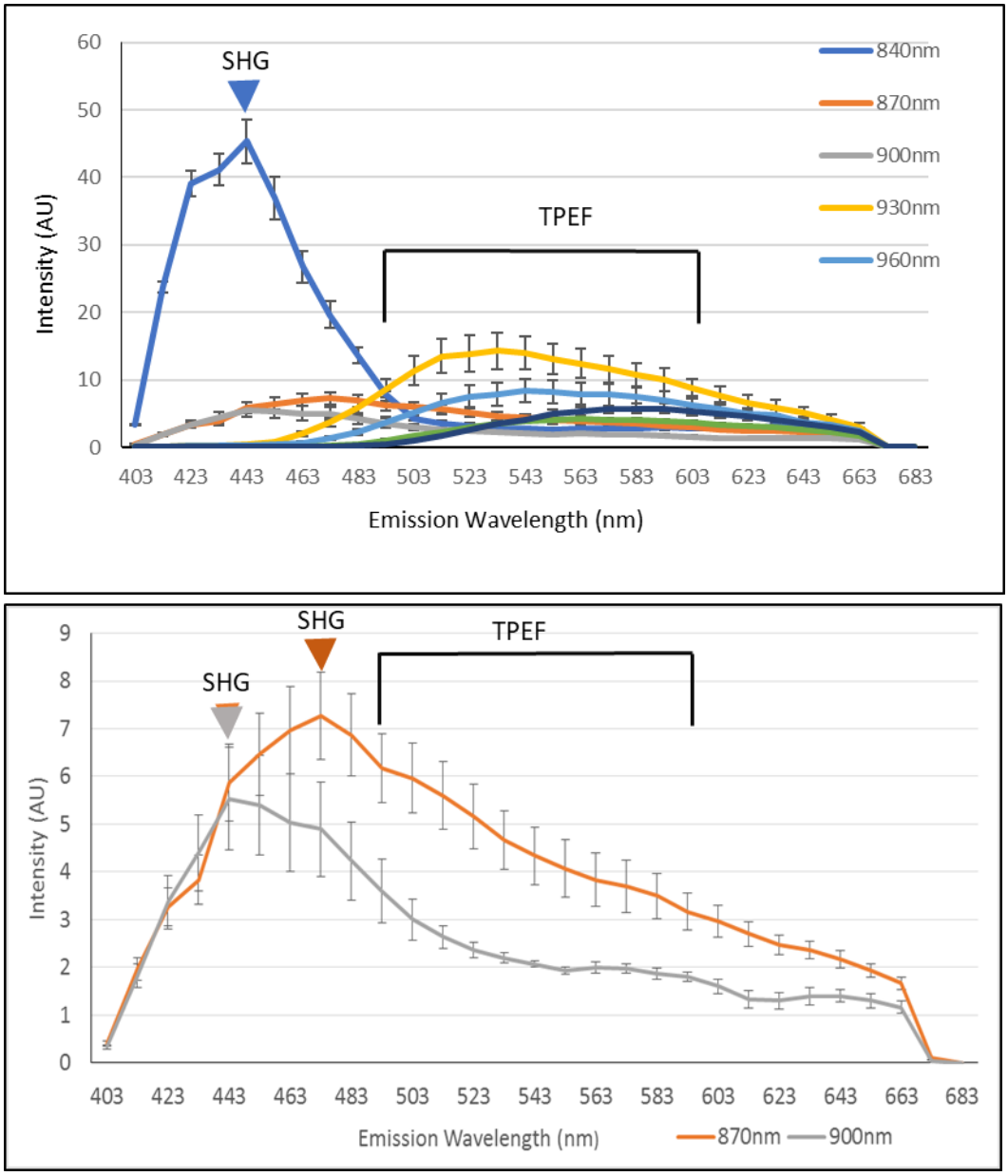

Fig 4.12) a) The expression intensity of each emission spectrum at laser excitation wavelengths 840nm to 1020nm. All curves show a broad TPEF curve however the signals between 840 and 900 show a shorter wavelength, SHG peak. **b)** The curves for 870nm and 900nm to show in better detail the expression at the SHG peak. Arrowheads point towards the range of the SHG peak and brackets show the range expected for the SHG curve.

4.3.7 Further Identification of Second-Order Signal via Powermeter measurement

An additional validation of second-order signals is an analysis of the rate of the signal to power increase. So to fully ascertain that the emission signals given by the carapace samples were second-order reactions, in addition to the checking the shape

of the peak and the range of the emission wavelengths, the signal order can be determined from the gradient of a log-log plot of the excitation power against the emission signal strength (Theodossiou *et al*. 2006).

Power levels at the sample position (at-sample) were found to be higher after 5 hours of use than the initial point, despite the laser being set to an identical power level throughout (Fig 4.13). Not only was there a difference in the at-sample power, but this difference increased with higher laser power levels. The difference is lowest at 1%, with a change of 0.71mW, and increased to 1.93mW at 2%, 2.97mW at 3%, 4.07mW at 4%, 4.88mW at 5% and finally 5.94mW at 6%. All changes were statistically significant at p>0.001.

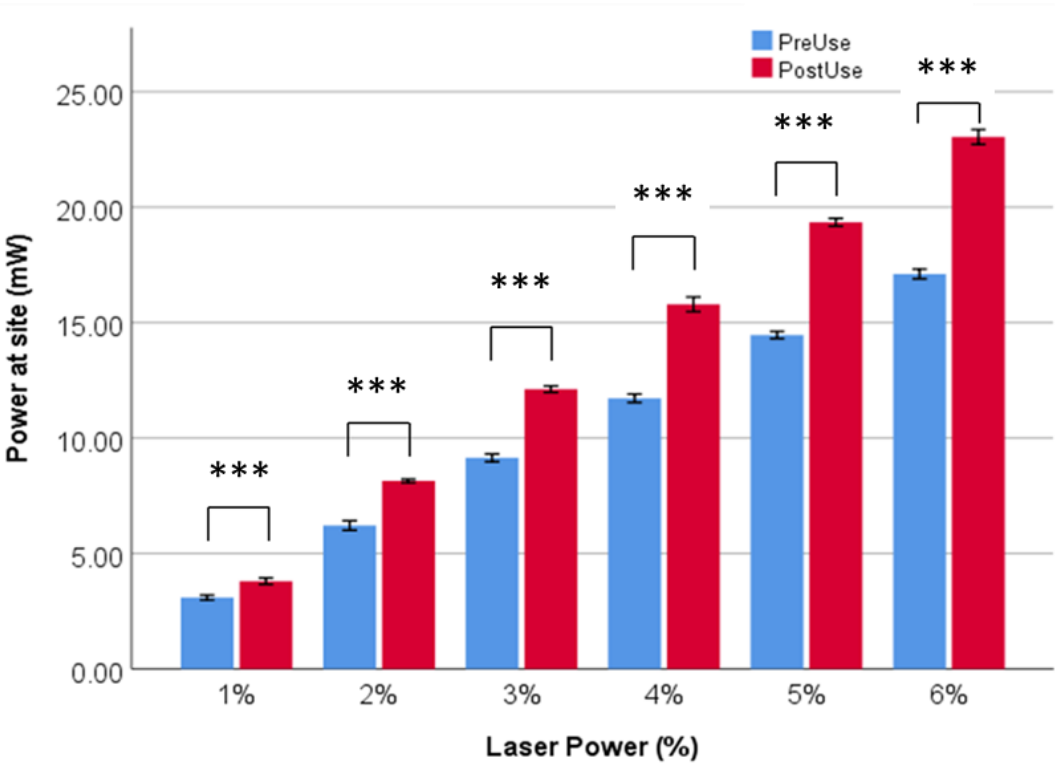

Figure 4.13) The at-site power level readings of the laser at different percentages both pre and post 5 hours of use. All readings post-use are significantly higher than pre-use, *** represents (p<0.001)

The relationship between log Power at the specimen versus the log laser power was linear (Fig. 4.14), with a gradient of almost 1 (0.9981), meaning the energy reaching the site was linearly related to the energy at the laser, with no higher-order effects.

The collagen sample gave a linear equation of y=1.857x+0.236, showing a gradient of near 2. The combined non-linear signal derived from the chitin within the carapace in the ostracod sections generated a linear equation with a gradient of 1.2379 (fig. 4.15).

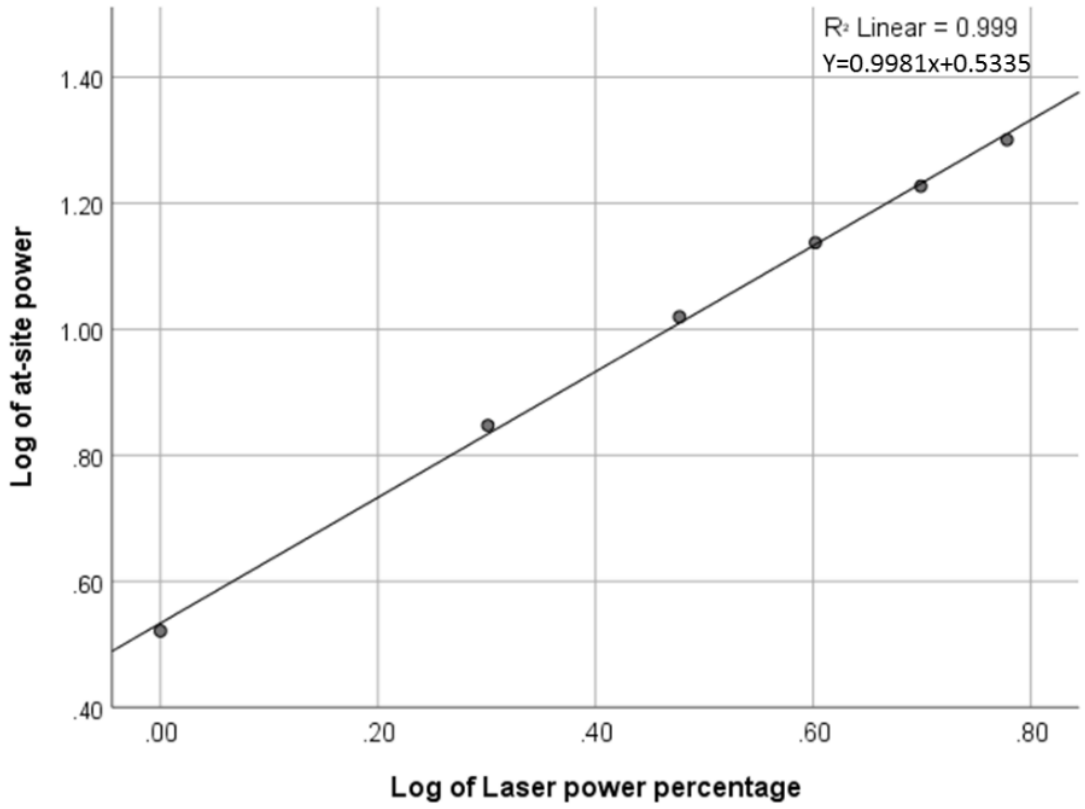

Figure 4.14 The linear relationship between the log of the power measure at site and the log of the laser power (as a percentage of the maximum laser power).

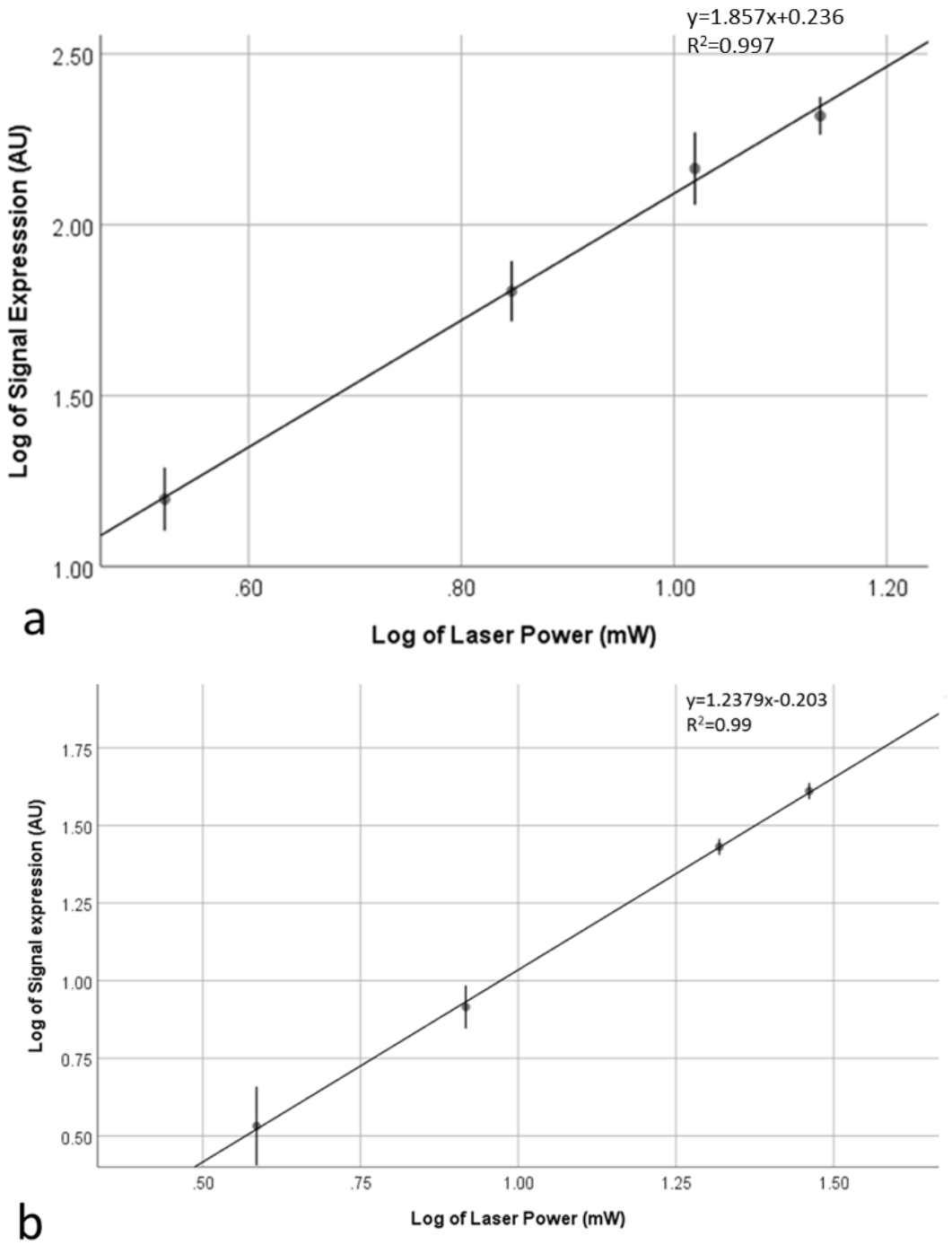

Figure 4.15: Log-log plots showing the log of the laser power against the log of signal expression showing the dependence of **a)** rat tail collagen signals and **b)** adult ostracod carapace signals as a function of laser power.

4.3.8 Identification of differences in nonlinear signals during ostracod instar development

To test whether there were any changes in the chitin distribution along the carapace during the lifetime of the ostracod, additional emission spectral analyses were carried out at 840nm excitation (Fig 4.16). This seemed to be the optimal SHG emission from previous emission spectral analysis done on the adult carapace. Regions of interest (ROI) were taken from all developmental stages. Analysis of the emission values shows that the samples all contain the specific SHG peak.

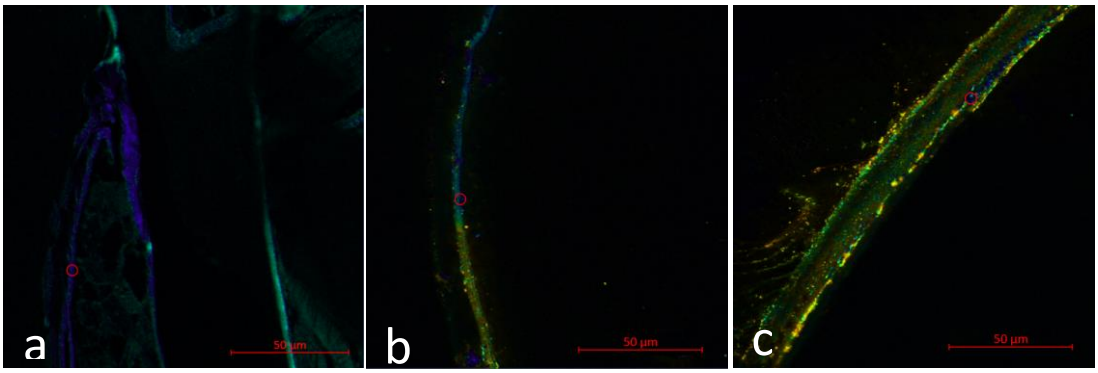

Figure 4.16: Lambda stack images of example emissions spectra at 840nm excitation for **a)** instar 1 **b)** instar 4 and **c)** adult instars using a 40x magnification objective lens. Pixel values for intensities were taken from each ROI, identified by the red circle.

The shapes of the curves showed a difference between the mean ranks and so a difference in the shape of the curves (p=0.003) (Fig 4.19). Dunn's pairwise tests were carried out for comparison between the instars at all wavelengths. A significant difference was seen between instar 4 and instar 3, instar 4 and the adult and instar 5 and the adult (p=0.029, p=0.002 and p=0.027) respectively, adjusted using the Bonferroni correction).

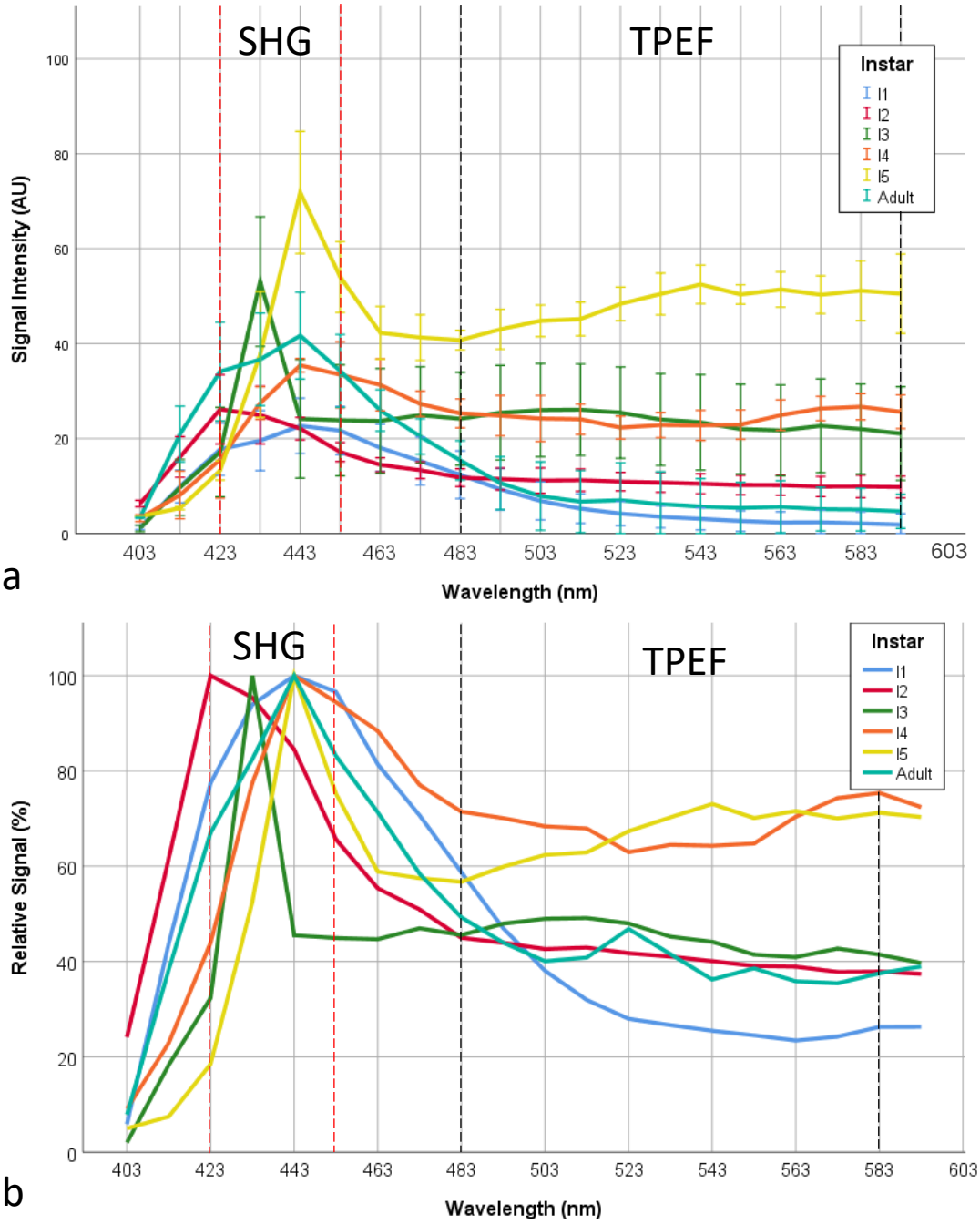

Figure 4.17: a) Expression intensity for emission spectra at 840nm excitation for all developmental stages. **b)** The relative intensity for each instar when normalised. The dotted lines represent the area selected for SHG (423-453nm) and TPEF (483-593nm) expression for comparison between the samples.

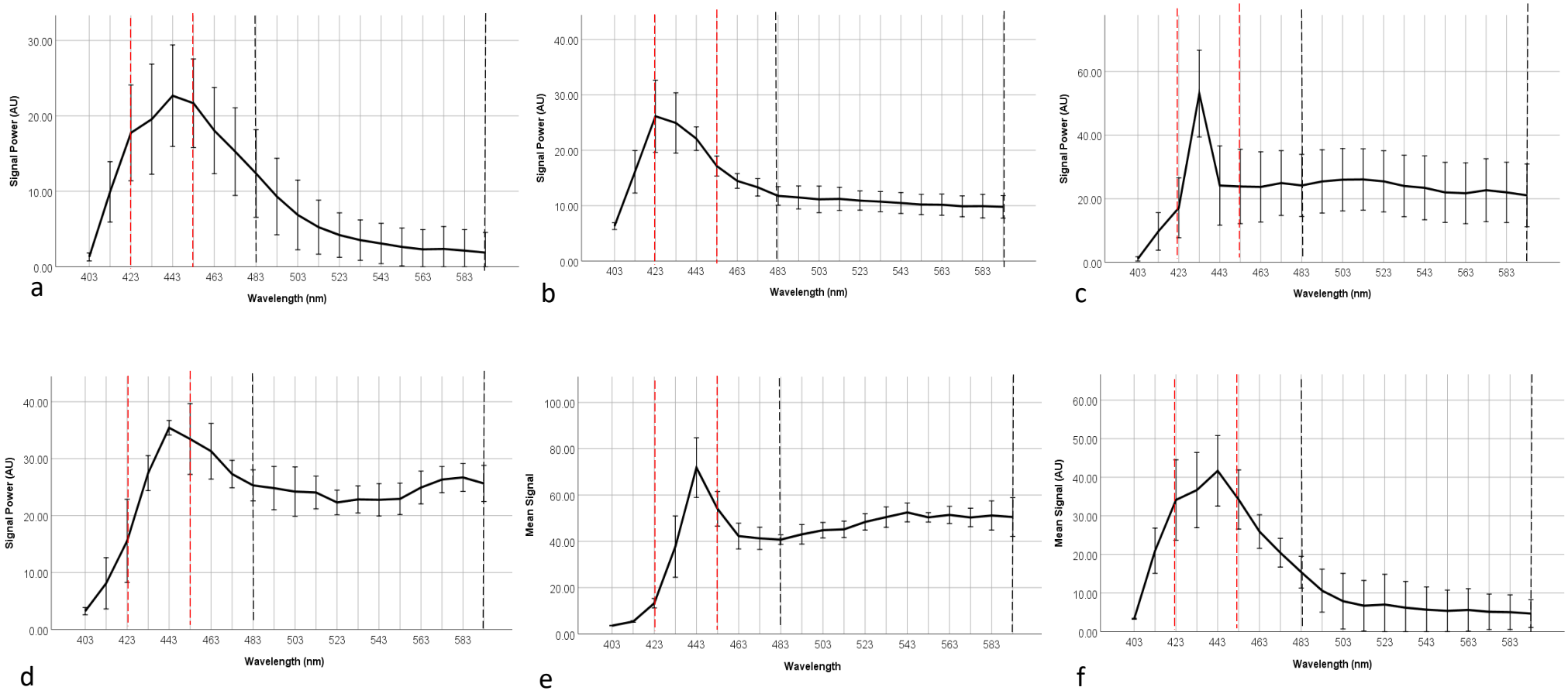

Figure 4.18) Emission spectra at 840nm excitation for **a)** instar 1, **b)** instar 2, **c)** instar 3, **d)** instar 4, **e)** instar 5, **f)** adult. The dotted lines represent the area selected for SHG (423-453nm) and TPEF (483-593nm) expression for comparison between the samples.

Kruskal-Wallis analysis with Dunn's tests between the samples within each instar showed a small amount of deviation. Instar 1 showed one significant difference, instar 2 showed two, instar 3 showed three, instar 4 showed one, instar 5 showed two and the adult showed two.

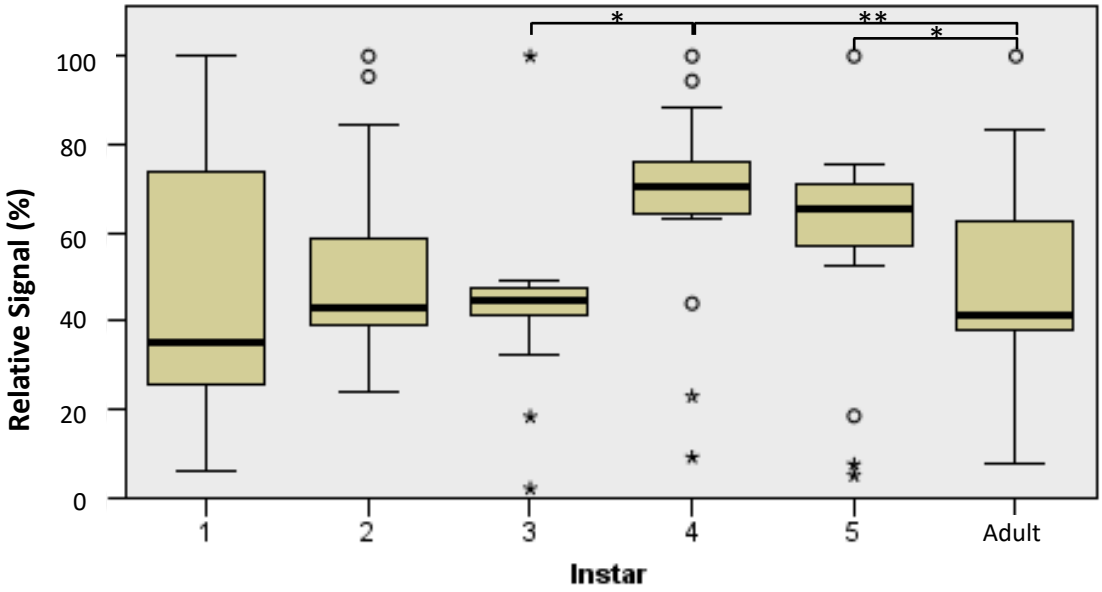

Figure 4.19: Distribution of the normalised spectrum values across each instar. Instar 4 showed a significantly different distribution to instar 3 and the adult, instar 5 was significantly different to the adult. ° represents an outlier greater than 1.5x the height of the box, ★ represents an outlier greater than 3x the height. * represents $p<0.05$ and ** represents $p<0.01$.

The spectra were split into their SHG and TPEF wavelength sections to judge where the significant difference between the instars was located. Kruskal-Wallis analysis with Dunn's pairwise tests carried out on the SHG wavelength range (420-450nm) (Fig 4.20a) showed no significant difference between the instars ($p=0.582$). Identical analysis carried out at the TPEF range (483-583nm) (Fig 4.21b) showed strong significant deviation between the instars ($p<0.001$).

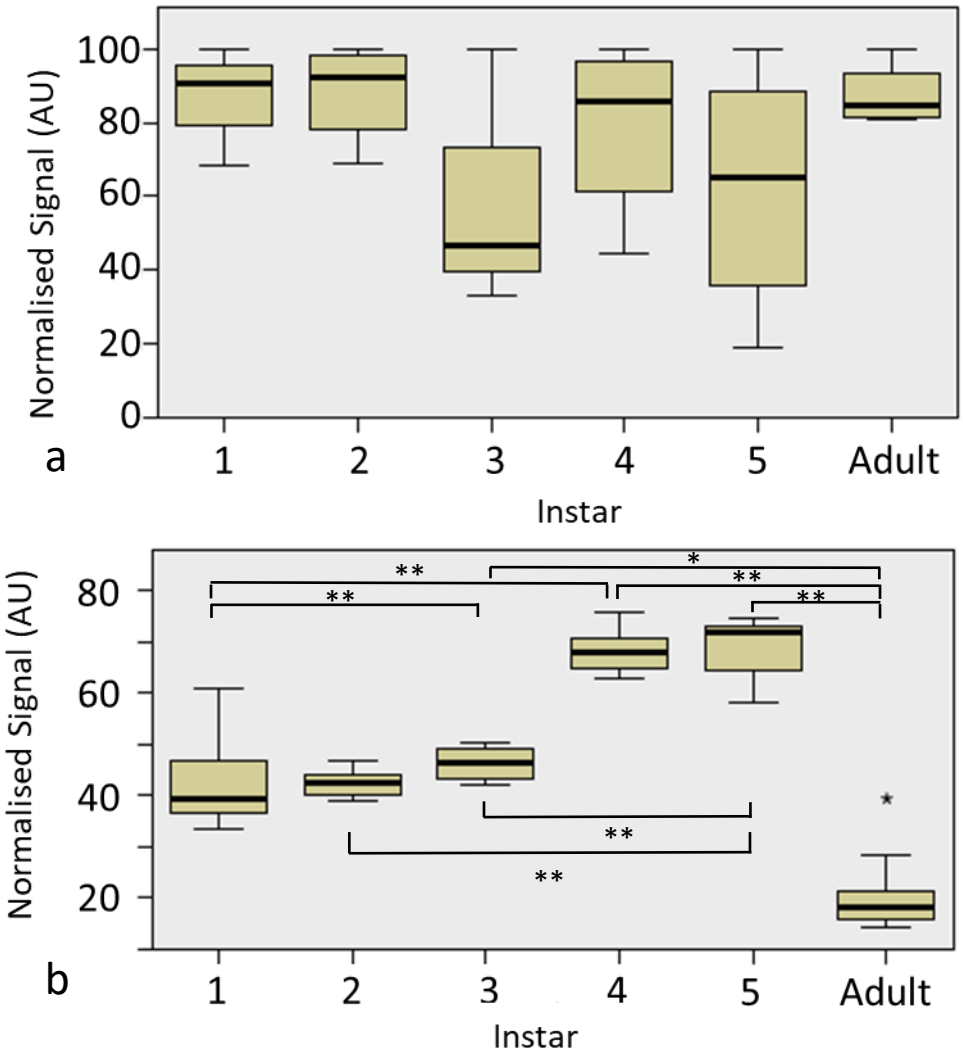

Figure 4.20: Distribution of the normalised spectra values across each instar **a)** at the SHG section (420-450nm), which showed no differences and **b)** the TPEF section (483-583nm) that showed numerous significant differences between the instars. ° represents an outlier greater than 1.5x the height of the box, ★ represents an outlier greater than 3x the height. * represents p<0.05, ** represents p<0.01 and *** represents p<0.001.

Chitin derived signals were strongly expressed in every instar (Fig 4.21), it can be seen that instar 4 and 5 do not show any signal within the centre. From figure 4.22 it can be seen that instar 1 had a significantly higher pixel percentage of chitin derived signal at 85.5±10% compared to instar 4 at 66.8±7.6% (p=0.03). No significant difference was seen between any of the other instars. Instar 2 had a pixel percentage of 78.3±4.2%, instar 3 69.9±4.2%, instar 5 67.5±8.6% and the adult showed 79.7±8.2%.

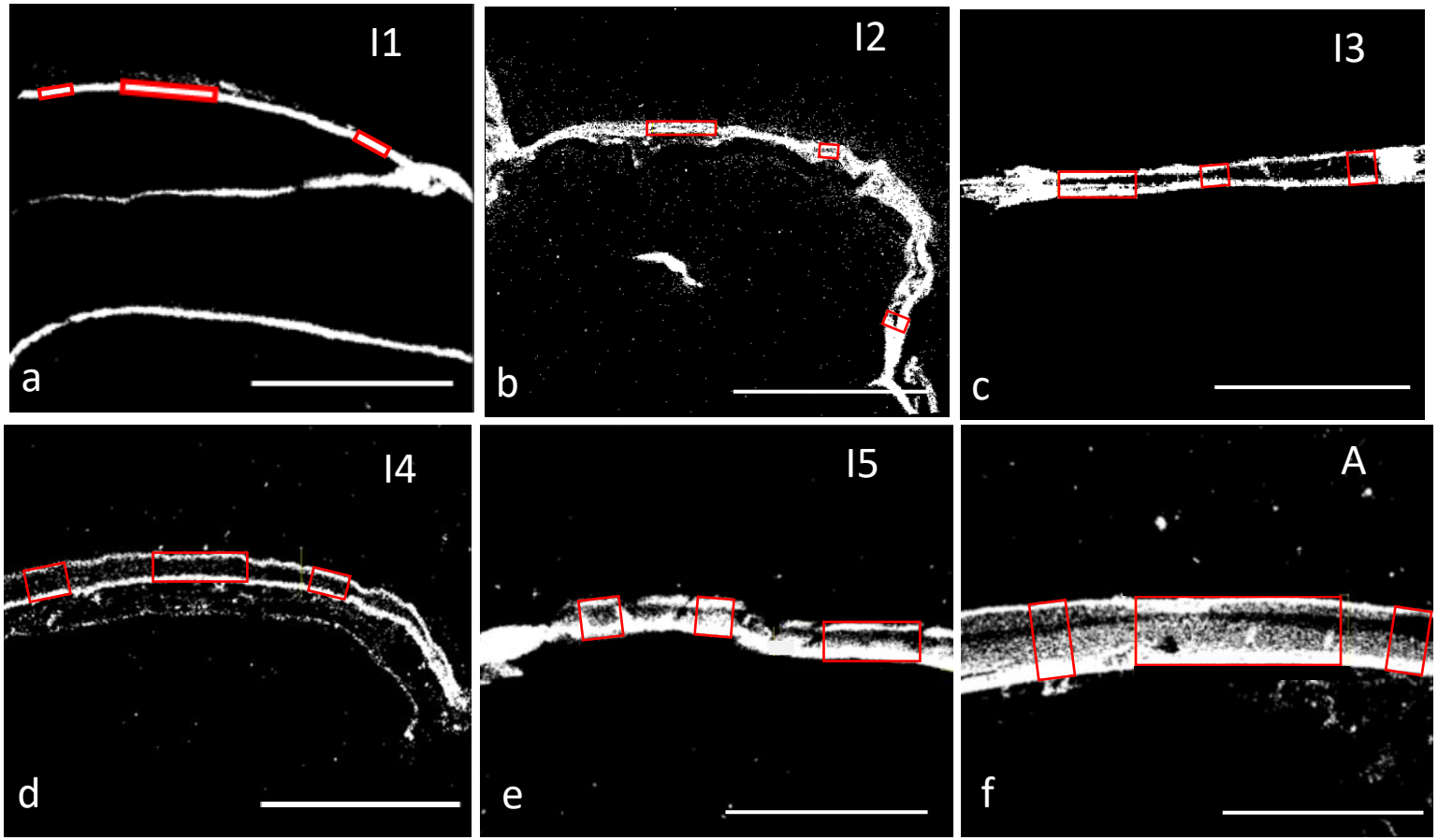

Figure 4.21: ROI selected from an instar carapace samples at the 430nm emission window, **a-f)** showing proportional chitin expression, ROI are based on the width of each individual carapace. All pixels that are white are from SHG signal given off at 430nm emission from the chitin. Scale bars are 50µm

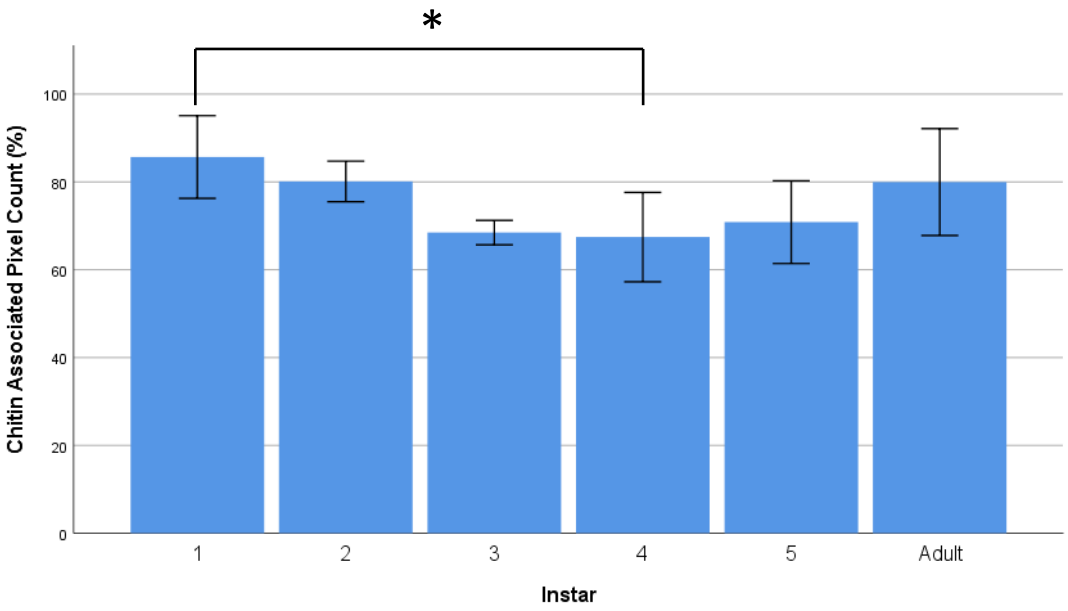

Figure 4.22: Percentage chitin contribution to carapace in different developmental stages. A decrease in percentage chitin contribution was seen from instars 4. Error bars were generated with ± SD and * represents $p<0.05$.

4.4 Discussion

To this author's knowledge, there is no previously described research data concerning the emission of nonlinear signals from chitin in crustaceans, and only a few reports in arthropods (Nie *et al*. 2012; Rabasovic *et al*. 2015; Reinhardt *et al*. 2017). The distinction between crustacean and arthropods is important to make as there are numerous differences between the exoskeletons of these two sub-phyla, particularly in the level of cuticle mineralisation (Willis 1999; Hild *et al*. 2009; Fabritius *et al*. 2016b).

Calcium especially is an integral part of the make-up of the crustacean cuticle, in which it completely encloses the chitin fibrils on multiple hierarchical orders (Seidl *et al*. 2011; Ruangchai *et al*. 2013). This high level of calcium is known to affect the density and orientation of chitin fibrils (Seidl *et al*. 2011; Huber *et al*. 2015). By contrast, calcification is extremely rare in insects and would be unlikely to be seen in

the *Plusiocampa christiani* Condé and Bareth, 1996 described by in Rabasovic *et al*. (2015), the bedbug *Cimex* lectularius from Reinhardt *et al*. (2017), or in the wings of the flies studied by Nie *et al*. (2012). While the calcium does not bind to the chitin at a molecular level and so would not affect its symmetry (or lack thereof), it does cause chitin to be more dispersed and potentially less organised, therefore may affect the amount of SHG signal generated. Combined with this is the fact that, to this author's knowledge, this is the first case of nonlinear imaging of cuticle tissue sections, rather than of the entire animal. This will significantly reduce the available amount of chitin within the sample and the area from which the signal can be generated. However, it will enable easier identification of signal emission, and also a more accurate mapping of signal location. Fortunately, the consequently lower levels of chitin did not have a negative impact on signal emission, as can be seen from the results above. An SHG peak was seen with spectral curves, as a separate peak at an emission wavelength half that of the excitation within a very narrow band, and also qualitatively expressed within the inner layers of the carapace in emission spectra lambda stacks. This narrow, steep band is attributed to the SHG's maintenance of coherence (Reinhardt *et al*. 2017).

Initial sectioning was carried out via cryosectioning with the samples embedded in Optimal Cutting Temperature (OCT) compound and then analysed with nonlinear microscopy. However, because of the hardness of our material and the relative softness of the OCT compound, the sectioning of the samples led to a 'smearing' effect, leading to an inability to generate suitable tissue sections for imaging. Instead, a resin known as butyl-methylmethacrylate (BMMA) was utilised as the embedding medium, as BMMA has been previously used for nonlinear imaging (Parfitt *et al*. 2012). However, when previously used, SHG signals were generated from the samples prior to deplasticising as the BMMA did not block the signal. However, in this current study BMMA appeared to affect signal generation, although it is not understood why this was the case. In the study by Parfitt *et al* (2012), SHG was emitted from collagen in the mouse eyelid and tarsal plate and it is likely that the amount of collagen was significantly higher than the amount of chitin within the ostracod carapace. If this was the case it could mean the BMMA diminishes the

amount of SHG signal from the chitin enough to cover it by background noise. Another potential possibility could be that the BMMA resin reacts in some way with the chitin to affect its non-symmetrical centre but does not do so with collagen. As the signal was observed once the BMMA had been removed, any potential reaction between the two is reversible to some extent and so should not affect these results.

Identifying a weak SHG signal from a strong TPEF one can be problematic. Stokes' shift should theoretically prevent the signals from overlapping and should allow for easy separation of the two signals, however problems can arise from practical issues of the equipment. The beam passes through the microscope, including the focusing lens, and interactions with this and the environment could cause a potential drift from the set signal ranges. This means it is possible for signal seen within the predicted SHG range to instead be TPEF signal and for there to be no actual SHG signal at all. Ideally, a strong SHG signal would be seen in a very narrow excitation band and no signal would be seen elsewhere. If the SHG signal was stronger than the TPEF, it would be easily identifiable as one of the TPEF images would be much brighter than the others. However, if the SHG is a weaker signal than the TPEF, any potential signal would be 'swamped' by the much more powerful TPEF signal. If this were the case it would be impossible to know whether the signal was SHG or TPEF purely from its excitation wavelength. This can cause significant confusion and so the SHG signal validation required multiple stages; including the shape of the signal to wavelength curve and the log-log response of the signal to power relationship.

More importantly for the TPEF signal is the cuticle composition. Due to the potential multiple origins of the TPEF signal, this cannot be as clear cut as the SHG signal. Rabasovic *et al*. (2015) analysed the insect *P. christiani* carapace because its low levels of pigment, protein and minerals would prevent interference (Rabasovic *et al*. 2015). Previous literature has reported on the numerous components that autofluoresce within the crustacean cuticle, with the main factors including chitin, resilin and potentially melanin (Reinhardt *et al*. 2017). Not only this but both the amount of resilin and the degree of resilin crosslinking, which greatly impacts on the autofluorescence, varies between cuticles (Neville 1975). As such it is difficult to ascertain whether the entire TPEF signal is derived from chitin, even if the

parameters are optimal for chitin autofluorescence. However, the resilin autofluorescence is emitted from two amino acids, dityrosine and trityrosine (Andersen 1964), following ultraviolet excitation (Burrows *et al*. 2008). In this current study, excitation wavelengths were too long (minimum 800nm) to excite resilin, and therefore resilin is unlikely to contribute to a potential signal. Furthermore, melanin, another endogenous fluorophore in crustaceans (Needham 1949; Horst and Freeman 1993), is unlikely to present (or will be at extremely low levels) in the carapace of *Skogsbergia lerneri* due to its transparency.

Since an SHG signal emitted from chitin was successfully identified in this study, the derivation of the TPEF signal (even though most likely to be from chitin as discussed previously) was not further investigated. SHG signal analysis was determined to be an effective tool for quantifying relative chitin content within the carapace at the different developmental stages.

However, It is worth noting that TPEF requires further investigation and if a better method of chitin isolation could be utilised TPEF could be an important tool for assessing carapace development and could prove useful in future experiments.

From the spectral imaging of ostracod carapaces, the SHG signal follows a pattern of expression which encompasses the outermost parts of the ostracod body matching to the carapace and so can be said to be emitted from the carapace. It can be seen that the majority of this signal was identified as being emitted specifically from the endocuticle, the inner layer of the carapace, which is almost entirely comprised of chitin (Vincent and Wegst 2004). Therefore, the carapace signal was determined to be derived from chitin.

Additionally, concerning the SHG signal, it is worth noting that the log laser power-log signal power plot of the SHG signal derived from the ostracod carapace had a gradient of 1.24, versus 1.85 from rat tail tendon collagen. This may be a result of rat tail tendon predominantly consisting of collagen I, (known to generate an intense SHG signal as a result of its non-centrosymmetric nature (Theodossiou *et al*. 2006). Therefore collagen type I generates a very strong second-order response. In contrast,

chitin is not distributed throughout the entirety of the ostracod carapace, and so may give a weaker signal.

What is more interesting is the results from the pixel analysis, which shows no significant pixel percentage difference except the decrease from instar 1 to 4. As the ROI of these was modified to accommodate the change in size of the carapaces, what is shown can be interpreted as the change of chitin proportion within each instar's carapace. No significant change implies that most instars have chitin cover a very similar proportion of the carapace, which grows and maintains around 60-80% coverage throughout the ostracod's lifetime. The decrease seen at instar 4 may be due to its middle stage of development. The smaller size of the earlier instars means that the chitin shows a high proportion of the overall carapace, whereas the larger carapaces have thicker chitin containing layers (as seen in chapter 3) which would show more signal. Instar 4 might be in a compromised middle point, where it is not developed enough to gain significantly more chitin but is large enough that the smaller chitin levels are no longer significant. Instar 3 seems to follow the same trend as instar 4 on the bar chart, although it was not significantly lower than instar 1 ($p=0.09$) and as the other middle instar (*S. lerneri* has 6 instars) (Cohen 1983) it would be the other carapace to show a reduced signal if this central developmental stage reduction was true. Further research from larger sample sizes and a higher resolution (for more accurate pixel distribution) would help increase the statistical power and help to see if there is this trend that is implied by the shape of the graph is valid.

Despite the large changes in the size of the ostracod towards the end of its development, significant changes in total chitin or chitin content as a percentage of total carpace were not identified. The only significant difference between developmental stages observed was lower percentage chitin at instar 4, compared to that at instar 1. This decrease in chitin contribution could be due to the fact that the younger, smaller ostracods merely do not have the space to store enough components to make a thicker carapace immediately. It is known that for some components of the carapace, for example calcium, crustaceans will only use internal stores (Glotzner and Ziegler 2000) immediately before moulting. Ostracod mothers keep their eggs inside their carapace for protection and fertilisation, however, this

protection is removed once the eggs are laid and the new ostracods hatch. So an immediate priority of the young ostracods could be collecting as many resources as they can for moulting until they have reached a perceived 'safe' thickness of carapace before slowing down towards adulthood. This would tie in with defences against predation, as if the ostracod developed chitin at a linear rate, it would mean having a weaker carapace for longer. As has been previously described chitin is influential in increasing the protection of the carapace (Raabe *et al*. 2005a; Raabe *et al*. 2005b) and so it would seem appropriate that the ostracod would attempt to reach a 'safe' level of chitin as soon as possible.

Unfortunately, at this point it is unknown what exact concentration of chitin exists within the ostracod samples, however the pixel analysis showed the % chitin contribution. Future work will include the development of techniques to quantify the exact levels and organisation of chitin within the carapace layers to determine how this alters over the six developmental stages.

In conclusion, an SHG signal derived from chitin has been established, that demonstrated chitin distribution within the ostracod carapace over a number of developmental stages. Since this work provided a two-dimensional view of the ostracod carapace, future work will be focussed on 3D analysis to complement the SBFSEM imaging already done. Image stacks can be utilised to generate a three dimensional model of chitin distribution throughout the entirety of the carapace, at different development stages. To accommodate this 3D imaging, thicker sections will need to be taken to process tissue faster, which cant be taken on an ultramicrotome and so a different cutting method will need to be established. Additionally, it is anticipated that the evaluation of such models at different stages of moulting will provide a greater understanding of how new carapace is formed at each instar.

Chapter Five

Elemental Analysis of the Carapace

5. Elemental Analysis of the Carapace

5.1 Introduction

5.1.1 Elements within the Carapace

As has been previously mentioned, calcium is a major component of the crustacean carapace and has a protective function, with magnesium and potassium playing a role in the expression of specific forms of calcium (Reddy 1977; Addadi *et al*. 2003; Al-Sawalmih *et al*. 2008; Fabritius *et al*. 2016b). However, the specific composition and distribution of the minerals within the carapace could be as important to the eventual strength of the exoskeleton as the architecture itself. All layers within the carapace contain varying levels of calcium carbonate in various forms (known as polymorphs) (Al-Sawalmih *et al*. 2008) but the compound is especially prominent in the crystalline endocuticle layer (Kesling 1951b). De Deckker states that Podocopida ostracod valves are low-Mg, having <5% Mg within their calcite matrix (De Deckker 2017).

It is important to bear in mind when discussing mineral levels within ostracod valves that the mineral concentration for ostracods varies wildly, and that numerous factors can change values between individual members of the same species or even between the valves of different instars of the same ostracod (Morishita *et al*. 2007). Rather than just being a pre-set of inflexible conditions based purely on an ostracod's genetic factors, it is instead a highly adaptive template that is influenced by numerous environmental factors. The most obvious of these is the availability of the minerals themselves and for this reason, marine arthropods are more mineral heavy than their non-marine counterparts (Holmes and Chivas 2002; Hild *et al*. 2009; Fabritius *et al*. 2016b). Other factors also play a role however, including reactionary influences that can affect the degree of crystallisation, which can in turn influence mechanical properties on an individual level (Huber *et al*. 2015). There has been evidence to suggest that, unlike with other biological $CaCO_3$-containing tissue (Seidl *et al*. 2012; Huber *et al*. 2015), crustaceans can exert a degree of control over the

orientation of their crystals and conversion between amorphous calcium carbonate (ACC) and other polymorphs (Addadi *et al*. 2003).

Mineral distribution is another important factor to discuss, and it has been shown that marine ostracod valves do not display a homogenous distribution of Ca or Mg throughout the valves (De Deckker 2017). Instead, electron microprobe analysis has shown three bands throughout the thickness of the carapace (Morishita *et al*. 2007): a high-Mg, Sr-rich outer band; a heterogeneous low-Mg, low-Sr middle band and a high-Mg, high-Sr inner band. The differences in this distribution of Mg was suggested to be due to the shape of the carbonate grains. In the *Neonesidea oligodentata* Kajiyama*,* 1913, the carbonate grains in the inner Mg-rich layer were coarser than other layers indicating a relationship between the kinetics of carbonate formation and the carapace chemistry (Morishita *et al*. 2007).

The distribution of the forms of calcium carbonate is also heterogeneous, calcite is almost only found in the exocuticle, whereas ACC can be found throughout the valve (Fabritius *et al*. 2016b). Amorphous calcium phosphate (ACP) has been found previously to occur in the mineral phase of the valve and has been shown to stabilise ACC (Reddy 1977; Fabritius *et al*. 2016b). The amount of ACP was seen to widely vary across different species, ranging from 7.5%-18% (Hild *et al*. 2009; Seidl *et al*. 2011; Fabritius *et al*. 2016b). However, while phosphorus is a commonly used stabiliser of ACC, it is not essential. There are numerous other compounds that have been suggested to fulfil the same role such as citrate or phosphoenolpyruvate (Habraken *et al*. 2015) and so it not guaranteed that ACP will be found near ACC.

Calcite is not only found solely in the exocuticle and it is also not smoothly distributed within the layer, instead usually being found in a few ‘clusters’ (Al-Sawalmih *et al*. 2008). Previously studied myodocopid species have been shown to differ in composition compared to all other orders of ostracods as they have replaced crystalline calcium carbonate, such as calcite, with ACC (Sohn 1969).

5.1.2 X-ray Analysis

X-ray radiation can be used as a structural probe in a number of different ways; either the x-ray beam is scattered as in x-ray diffraction or the atom absorbs the beam and

ejects one of its own electrons leading to another x-ray being emitted that is characteristic of the sample composition (Warren 1990).

X-ray diffraction follows a similar principle to that of WAXS and is based on the angle of the scattered x-ray beam after its interaction with repeating patterns of either individual atoms or molecules within the sample as described in chapter 3.

X-ray fluorescence (XRF) utilises the second category of x-ray analysis, the absorption of the x-ray energy by the material and the generation of characteristic x-rays from this interaction. When the beam hits the sample, part of the energy is transferred to the sample atoms, allowing a 'core' electron to jump to a higher energy orbital, a core electron being a non-valence electron which does not undergo interaction with external electrons (Rassolov *et al*. 2001). To excite these core electrons to this empty state the energy from the x-ray has to be equal or greater than that of the binding energy of the core-level state of the electron (Henderson *et al*. 2014). This leaves a positively charged, highly unstable 'core hole' which is filled by an electron from a higher orbital (Zhang *et al*. 2018). To move to this lower energy shell, the electron has to give off the energy difference in the form of an x-ray. The energy of these secondary x-rays is equal to the difference in energy between the original inner orbital and higher energy orbital and is proportional to the squared nuclear charge of the element (Chen *et al*. 2012). These specific characteristics allow for the identification of the element that the photon was emitted from.

X-ray absorption near-edge spectra (XANES) is similar in theory to the previous techniques however it is focused more on the initial absorption energy as a function of incident x-ray energy. When the x-ray energy reaches the binding energy regime of a core-shell, before the core electron is ejected, a sudden increase in absorption occurs. This increase in absorption energy is sharp and significant, which when plotted in a graph of energy against absorption shows an extremely steep increase, known as the rising edge. This gives rise to the name 'near-edge spectra'. XANES comes under the theory known as x-ray absorption fine structure (XAFS) which refers to the structure in the x-ray absorption coefficient near an x-ray absorption edge (Rehr and Albers 2000). An oscillation is caused by the electric field of an x-ray passing through an electron, which pushes the electron sequentially in opposite directions,

allowing the electron to capture the energy due to the field's oscillation in direction and strength (Henderson *et al*. 2014). Specifically, XANES relates to the readings close to the absorption edge, within around 30eV (Rehr and Ankudinov 2005), instead of extended XAFS (EXAFS) which measures absorption much further from the edge. Study of the characteristic shape of the edge allows it to discern not only between elements but also between the different isoforms within these elements. Three main identifying areas exist which are used to ascertain the correct elements, compounds and isoform. First, are the weak transitions seen before the edge known as the pre-edge transitions, second is the transitions upon the curve itself and finally the transitions seen after the curve known as the post-edge transitions (Brinza *et al*. 2013). Signals from elements can have different edges dependent upon which orbital the electron that absorbs the x-ray energy is from. Biological material, such as ostracod carapaces, is made up of lighter elements and so the k-edge is used because this edge is the most sensitive as it takes into account electrons from the 1s orbital onwards. XANES is able to identify different isoforms of the same compounds by identifying the geometrical differences in the absorption sites that alter various scattering pathways which modifies the absorption edge.

Energy-dispersive x-ray spectrometry (EDS), is similar in theory to XRF however instead of using x-ray radiation to excite the sample it uses instead an electron beam. Specifically, EDS involves inelastic scattering where electrons from the electron beam interact with the sample and lose energy without a noticeable change in direction (Scimeca *et al*. 2018). When the inelastically scattered electron hits the sample it transfers energy to the sample in the same way as stated for XRF. EDS can be carried out without the use of a synchrotron and instead, can be achieved with an electron microscope. This EDS research was specifically SEM-based, where the elemental map is projected over the 3D sample, instead of 2D TEM images.

5.1.3 Hypothesis

The elemental composition and calcium carbonate polymorphs of the *Skogsbergia lerneri* carapace is hypothesised to be similar to that of other ostracods but that

specific differences will be seen that support transparency. Additionally, we hypothesise that there will be changes throughout development, that will not substantially alter the carapace composition at different developmental stages, so that a consistent transparency is maintained throughout its lifetime.

5.1.3.1 Aims and Objectives

i. Identify the elemental distribution (using XRF) throughout the carapace valve and determine if this varies between developmental stages.
ii. Identify the elemental distribution and proportion throughout the different structural carapace layers (using EDS) within transverse tissue sections at different developmental stages.
iii. Identify the proportion of calcium carbonate polymorphs in the carapace (using XANES) and if these vary throughout developmental stages.

5.2 Experimental Design

i. Analysis of carapace elemental distribution and quantity at different developmental stages.

Elemental analysis was performed following XRF measuring levels of Mg, P, S and Cl in instar 1, 3, 4, 5 and adult valves, in triplicate (except n=1 for instar 4), on station i18 at Diamond synchrotron, as described in chapter 2.8.3. Due to the strict time constraints of awarded experimental beam-time at the Diamond synchrotron, additional repeats could not be carried out.

ii. Analysis of elemental distribution and proportion within the different carapace layers at different developmental stages.

Transversely bisected ostracod valves of instar (I1), early-mid (I2-3), late-mid (I4-5) and adult ostracods (n=3 per stage minimum) were subjected to EDS as described in

section 2.8.1. Each valve was analysed at multiple points, with a minimum of 3 points per n number, and the mean of the elemental signal data generated was presented.

iii. Determination of calcium carbonate polymorphs in the ostracod carapace throughout development.

The EM imaging seen in chapter 3 showed *S. lerneri* to contain the additional crystalline layer that is seen in certain other ostracods. The focus was thus on the elemental distribution within the internal layers of the carapace which could not be identified via XRF. Carapace valves at instars 1, 3, 5 and adult (in triplicate), and one instar 4 were subjected to XANES analysis carried out on the Diamond beamline i18 as described in section 2.8.4. Across all samples of each time point, a mean weight percentage was calculated for all major elements, any elements with a minor expression (*i.e*. <0.5%) were ignored.

iv. *Statistical Analysis*

All analysis of elemental values compared between instars was carried out via one-way ANOVA testing with Tukeys post-hoc, calculated with SPSS, showing significance at $p<0.05$.

Following Kolmogorov-Smirnov testing, all data were assumed to be normally distributed. Kurtosis and skewness were seen to be between ±1.5 for all data sets. All data generated from these sample populations were assumed to be done via random independent sampling as samples were chosen at random from their groups and no emphasis was put on elemental composition for image analysis. Equal variance between the populations was also assumed due to equally sized testing groups (for XRF and XANES testing, instar 4 had an n=1 but was not included in the analysis due to this small n number).

5.3 Results

5.3.1 XRF

XRF analysis revealed the carapaces included strong levels of chlorine, medium levels of sulphur and phosphorus and low levels of magnesium, throughout the valve (Figure 5.1). Silicon readings were taken but not included due to an extremely high background signal from the sample holders and sample images were normalised for size. Specific areas that show strong and localised signal levels are most likely a result of damaged regions. This could compact areas or allow the collection of saltwater deposits that remained after being washed in distilled water, rather than the actual carapace composition.

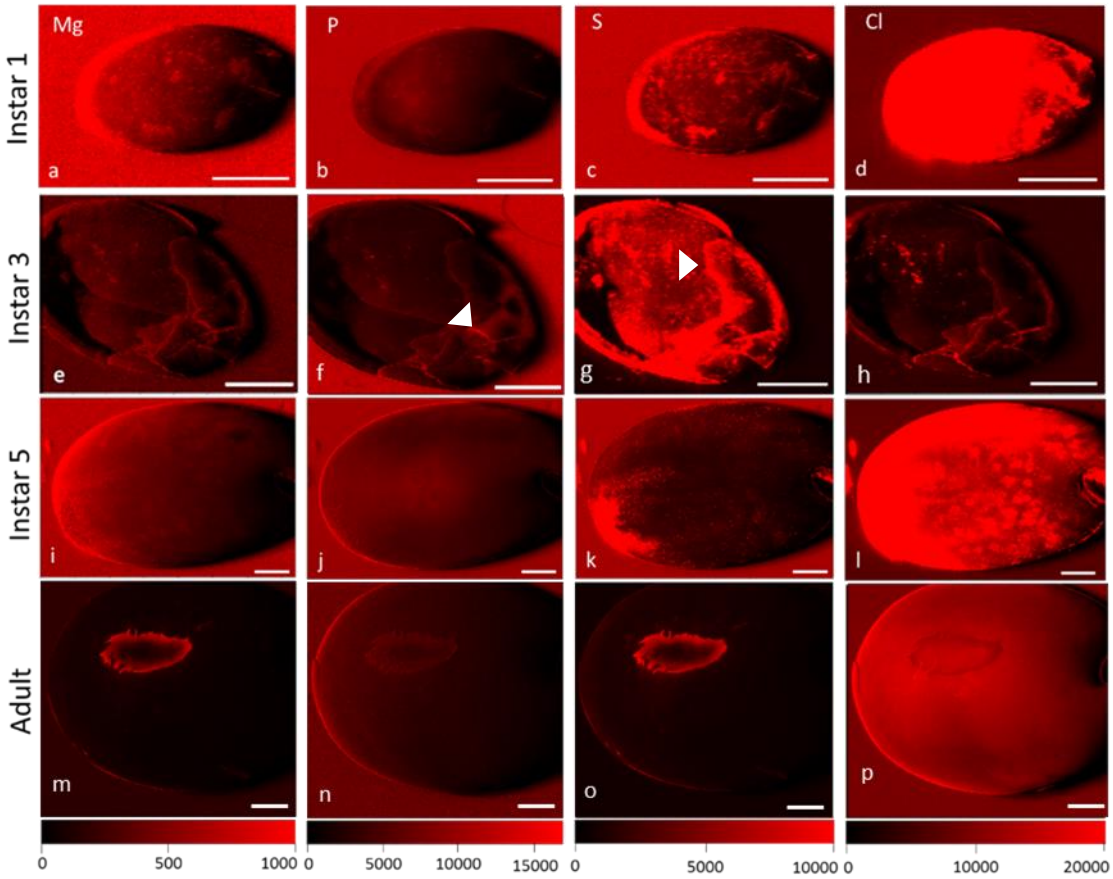

Figure 5.1: Signal expression of carapaces across developmental stages, showing Mg, P, S, Cl, stage 1 **(a-d),** stage 3 **(e-h)**, stage 5 **(i-l)** and adult **(m-p)** ostracods. Arrowheads show examples of damaged areas creating localised areas of high signal intensity. Scale bars represent 250µm.

Significant differences in elemental expression were seen across the developmental

stages (Fig 5.2). Magnesium signals were lower by 554.71 counts between instar 1

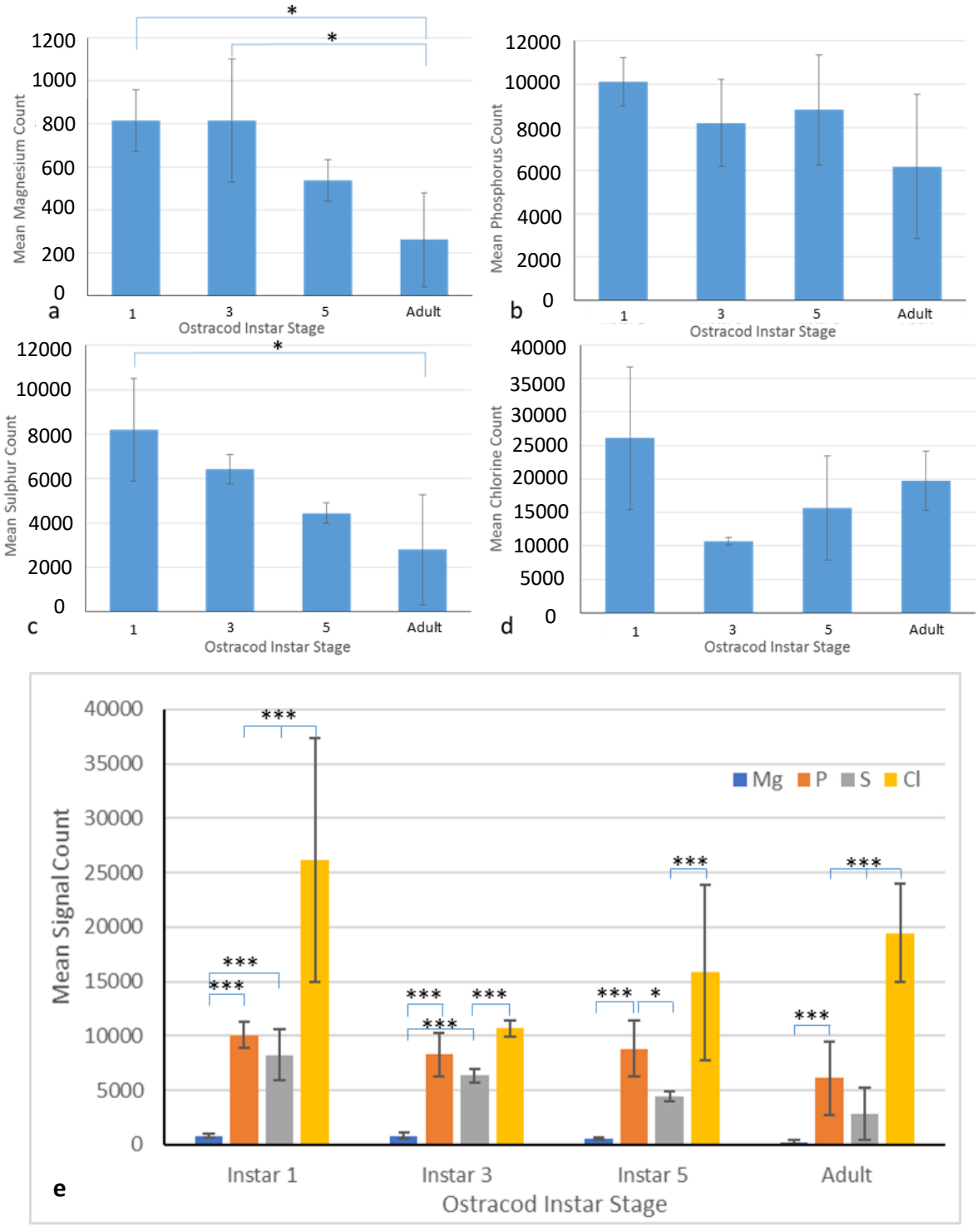

Figure 5.2: Comparison of the element levels throughout the developmental stages: **a)** Magnesium counts were lower in instar 1 and instar 3, when compared to adults. **b)** Phosphorus showed no changes. **c)** Sulphur count were lower in the adult valve, compared to that of instar 1. **d)** Chlorine showed no differences between instars. **e)** Comparison of the signals for each instar * represents $p<0.05$, *** represents $p<0.001$, error bars are ±SD.

and adult (p=0.011) and 555.82 counts from instar 3 to adult (p=0.019). Sulphur signal analysis showed a significant decrease of 5398.5 between instar 1 and adult (p=0.018). No significant differences were seen between the phosphorous or chlorine signals between any of the instars.

5.3.2 EDS

Elemental signals from ostracod cross-sections were identified via scanning electron microscopy EDS. Elemental maps were generated from the adult, instar 5, instar 4, instar 3, instar 2 and instar 1. A scanning electron micrograph of an adult carapace tissue section, with superimposed elemental maps, representative of carbon, calcium, oxygen, magnesium and phosphorous are shown in Figs 5.3a-f. distribution.

Oxygen was expressed specifically within the nodes of the crystalline layer at a higher level than outside of them (Fig 5.3d), which, in combination with strong calcium (Fig 5.3c) and magnesium signals (Fig 5.3e) also identified in this layer, suggests the formation of calcium and magnesium carbonate. Calcium and magnesium were also seen to be present across the entire cross section, however calcium showed a strong

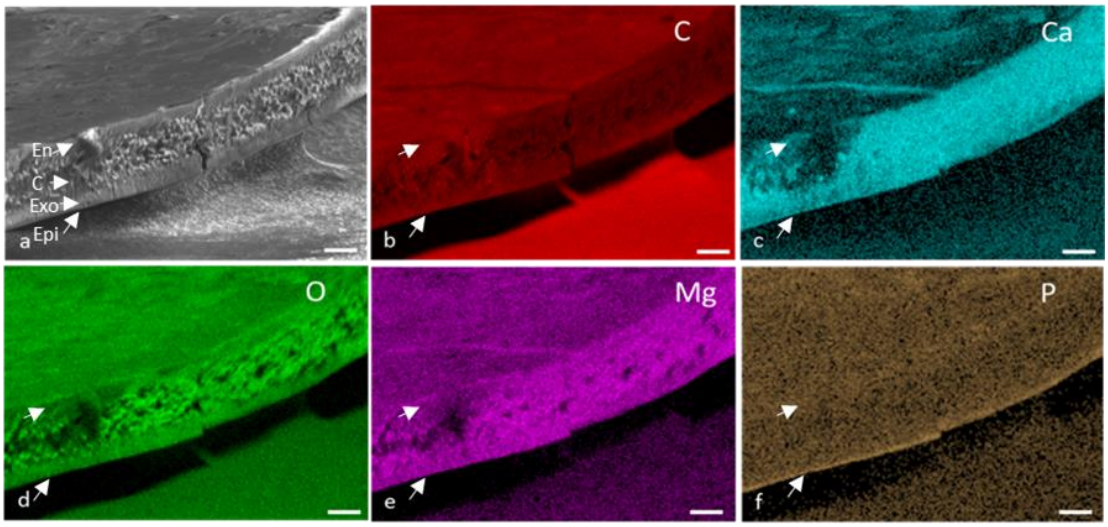

Figure 5.3: SEM images and elemental maps of the **a)** adult valve, with the following elemental distributions: **b)** carbon, **c)** calcium, **d)** oxygen, **e)** magnesium, **f)** phosphorous. Scale bars are 10µm. En = Endocuticle, C=Crystalline layer, Exo=Exocuticle, Epi=Epicuticle, En and Epi arrows are carried on through all images to help orientation.

homogenous signal expression throughout the entire cross section suggesting heavy calcium distribution throughout all layers of the carapace. A strong band of phosphorus was observed outlining the epicuticle at the edge of the valve (Fig 5.3f). Carbon was present throughout the entire sample (Fig 5.3b), consistent with general biological tissue.

The elemental distribution through the carapace layers within the instar 5 valves (Fig 5.4) followed a similar pattern to that in the adult, however, the signal was not as defined. The overall levels of oxygen and magnesium are lower within the tissue section, and oxygen shows comparatively less definition in the crystalline layer. Calcium still shows homogenous expression throughout the carapace cross-section. The phosphorus band on the epicuticle can still be seen although, unlike in figure 5.3, a broad signal was seen throughout the rest of the cross-section except for the exocuticle.

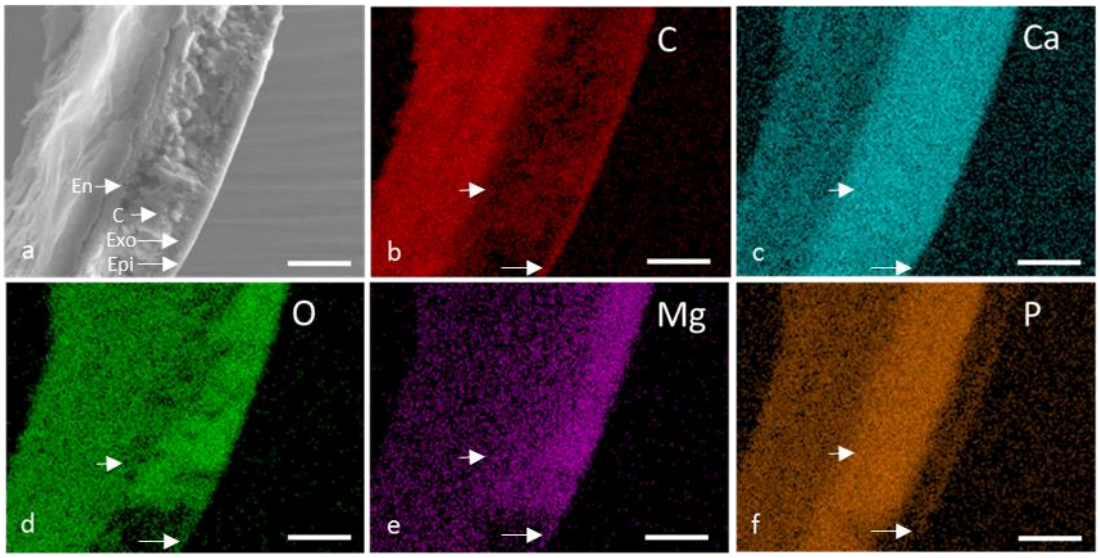

Figure 5.4: SEM images and elemental maps of the **a)** instar 5 valve, with the following elemental distributions: **b)** carbon, **c)** calcium, **d)** oxygen, **e)** magnesium, **f)** phosphorous. Scale bars are 10µm. En = Endocuticle, C=Crystalline layer, Exo=Exocuticle, Epi=Epicuticle, En and Epi arrows are carried on through all images to help orientation.

The instar 4 valve was substantially different from the other stages (Fig 5.5), although only one sample was able to be analysed which may have led to an anomalous result. The overall signal was both weak and ill-defined with very little distinction between the different layers, particularly observed with the oxygen and magnesium signals. However, calcium had a consistent signal within the cross-section. Phosphorus showed a stronger signal along the cross-section, not seen in other instars although no distinguishable epicuticle-associated signal.

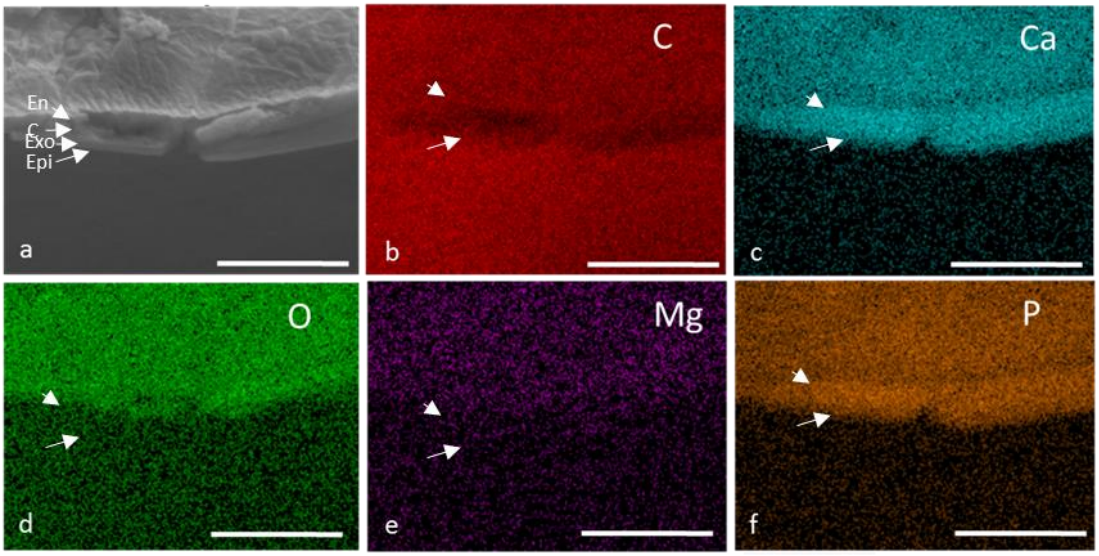

Figure 5.5: SEM images and elemental maps of the **a)** instar 4 valve, with the following elemental distributions: **b)** carbon, **c)** calcium, **d)** oxygen, **e)** magnesium, **f)** phosphorous. Scale bars are 10µm. En = Endocuticle, C=Crystalline layer, Exo=Exocuticle, Epi=Epicuticle, En and Epi arrows are carried on through all images to help orientation.

The instar 3 valve signals (Fig 5.6) were similar to instar 5 for the elemental distribution, however the localisation and strength of the signals continued to decrease, making the images appear fuzzy. Calcium and magnesium were distributed in a similar pattern as seen in the instar 5. Oxygen signal expression appeared to show areas of localisation as seen previously, however the reduced signal strength prevents accurate mapping to the crystals. There was a lack of the epicuticle-specific phosphorus signal previously seen in Fig 5.3 and 5.4f.

The instar 2 valve (Fig 5.7) was in line with what was observed at instars 5 and the adult, calcium, magnesium were seen in high levels within the cross-section, whilst

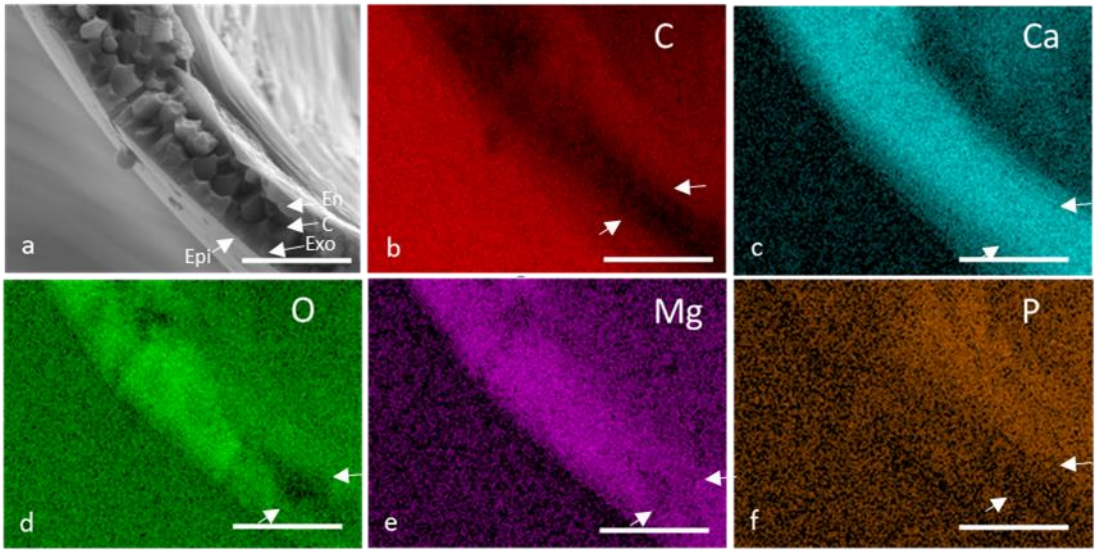

Figure 5.6: SEM images and elemental maps of the **a)** instar 3 valve, with the following elemental distributions: **b)** carbon, **c)** calcium, **d)** oxygen, **e)** magnesium, **f)** phosphorous. Scale bars are 10µm. En = Endocuticle, C=Crystalline layer, Exo=Exocuticle, Epi=Epicuticle, En and Epi arrows are carried on through all images to help orientation.

oxygen signal expression was higher within the crystals. Phosphorus showed a strong epicuticle band.

Instar 1 valves (Fig 5.8) were again very similar to the previous instars, however, the magnesium was actually seen to be lower within the main part of the cross-section.

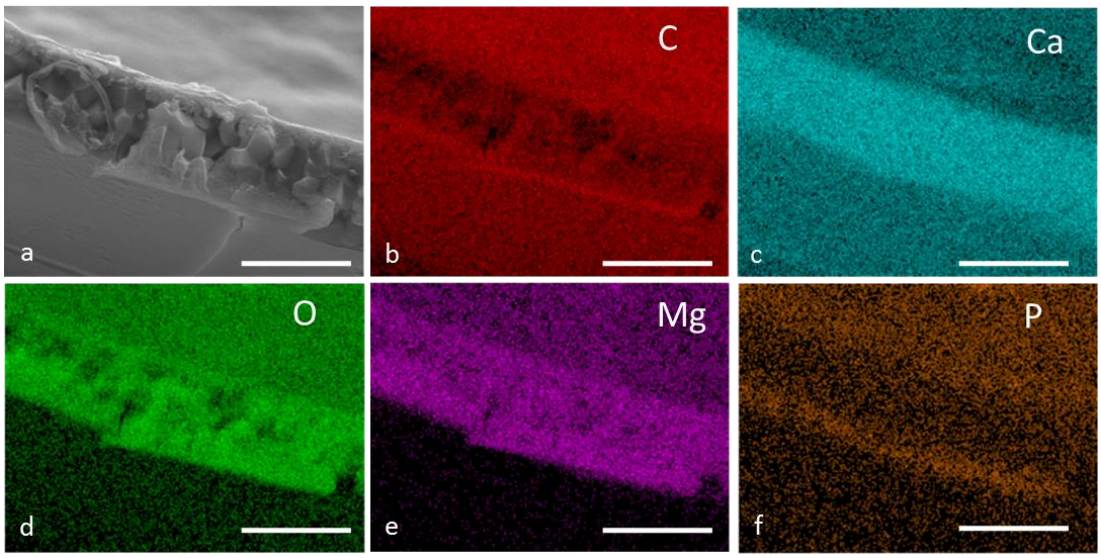

Figure 5.7: SEM images and elemental maps of the **a)** instar 2 valve, with the following elemental distributions: **b)** carbon, **c)** calcium, **d)** oxygen, **e)** magnesium, **f)** phosphorous. Scale bars are 10µm. En = Endocuticle, C=Crystalline layer, Exo=Exocuticle, Epi=Epicuticle, En and Epi arrows are carried on through all images to help orientation.

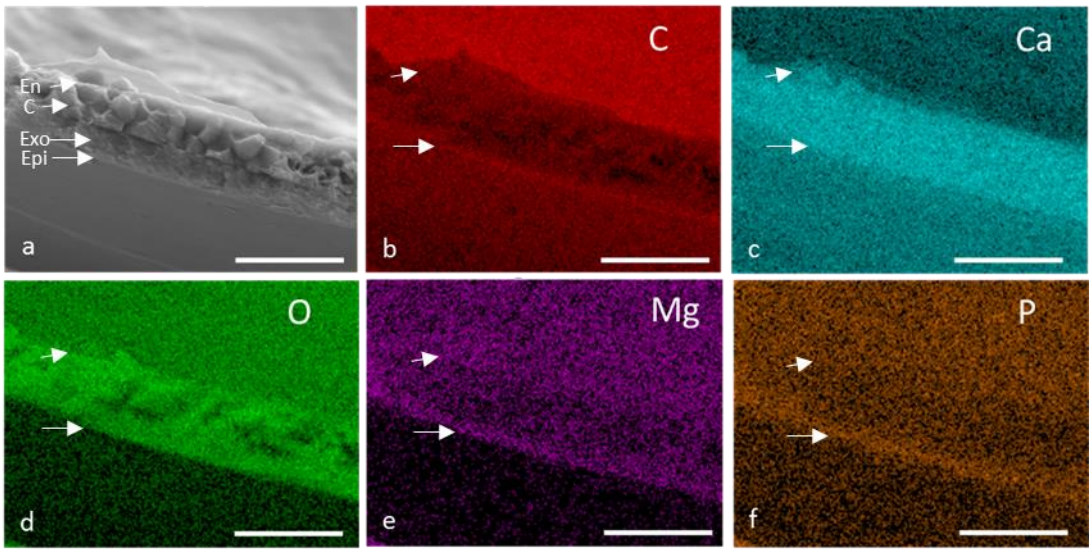

Figure 5.8: SEM images and elemental maps of the **a)** instar 1 valve, with the following elemental distributions: **b)** carbon, **c)** calcium, **d)** oxygen, **e)** magnesium, **f)** phosphorous. Scale bars are 10µm. En = Endocuticle, C=Crystalline layer, Exo=Exocuticle, Epi=Epicuticle, En and Epi arrows are carried on through all images to help orientation.

With each elemental map, an emission spectrum was also generated (Figure 5.9), from which a proportional weight percentage of each element's contribution to the total mass from the signal collected by the probe was calculated. The mean breakdown across all time points was: carbon 45.5%, oxygen 27.6%, calcium 20.3%, phosphorus 3.5%, magnesium 1.89%, silicon 0.6% and sulphur 0.42% (Fig 5.10a). The carbon signal was significantly higher than all other elements ($p<0.001$). Oxygen was the next highest and was significantly higher than all lower elements at $p=0.02$ for calcium and $p<0.001$ for the other elements. Calcium was the next highest and was significantly higher than all other elements (excluding carbon and oxygen) at $p>0.001$. No other elements showed a significant difference in signal strength.

As mentioned in the experimental design, samples were separated into four developmental stages, the initial stage (instar 1), the early to mid-stage (instar 2 and 3), the mid to late-stage (instar 4 and 5) and the final, adult stage. Very little difference in the percentage weight of the elements detected in the sample (Figure 5.10b). A significantly higher phosphorous level was observed in the late to mid-stage

(p>0.001), compared to other stages; whilst oxygen levels were significantly lower at this stage, compared to instar 1 (p>0.05).

a

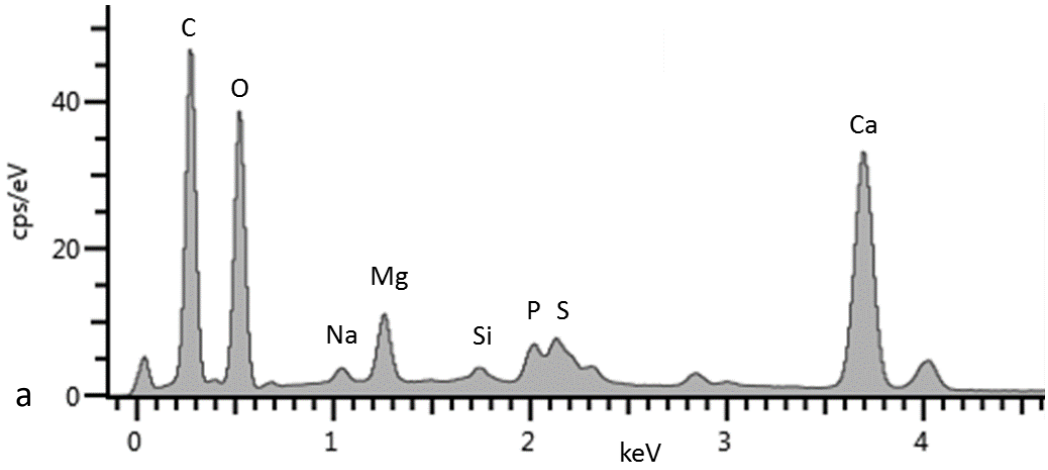

b

Element	k Ratio	Wt%
O	0.02991	56.99
Na	0.00117	1.00
Mg	0.00623	3.83
Al	0.00017	0.09
Si	0.00148	0.66
P	0.00563	2.38
S	0.00306	1.36
Ca	0.07768	30.75
Cu	0.00000	0.00
Pd	0.00602	2.91
Total:		100.00

Figure 5.9: a) Representative spectra of the adult valve, showing the peaks for each element **b)** A semi-quantitative breakdown of the elemental composition from the valve shown in **a**. The Cu and Pd seen is contamination and can be ignored.

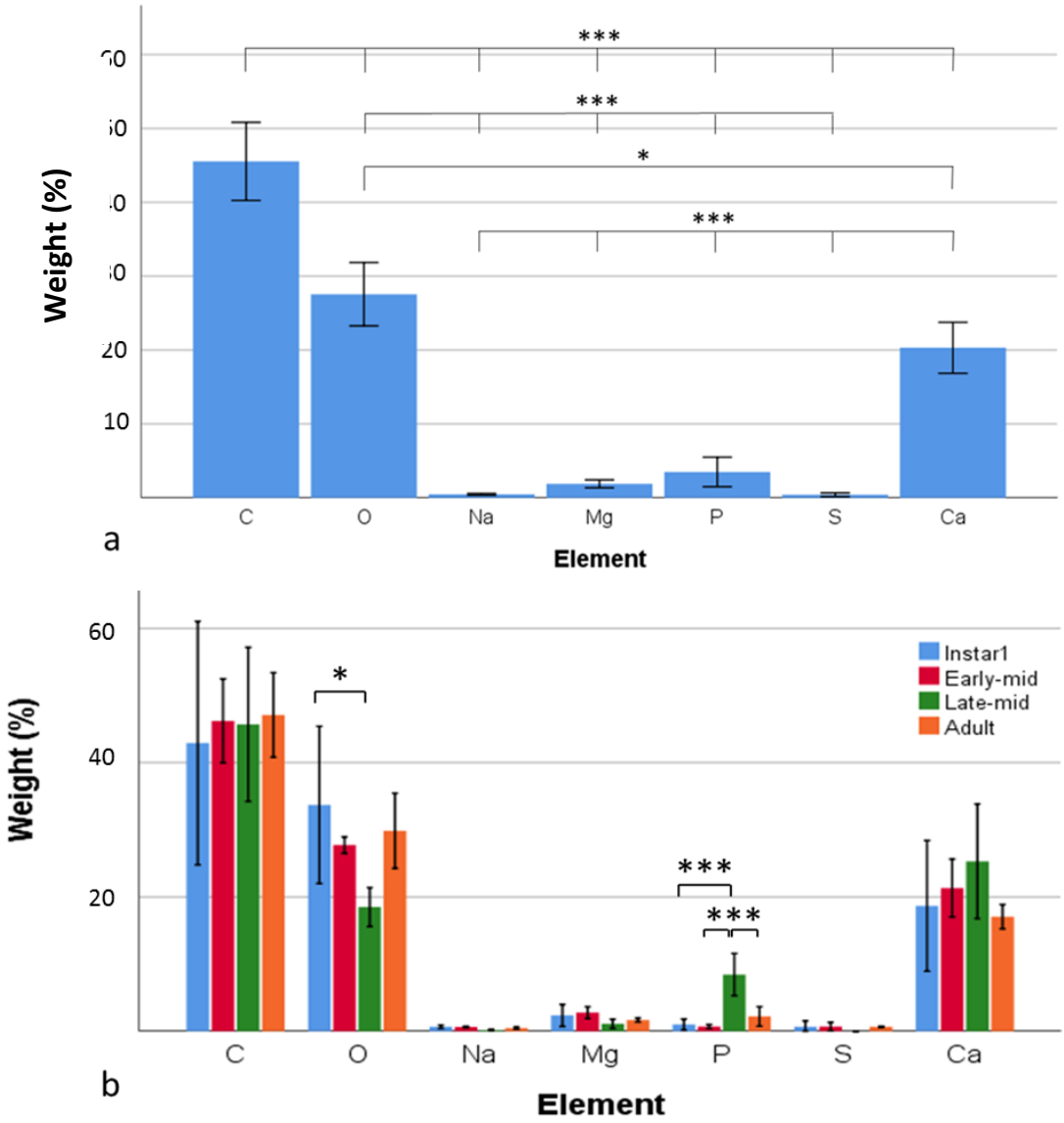

Figure 5.10: a) Mean percentage weight contribution of elements in the ostracod carapace **b)** Percentage weight value of each element as a function of developmental stage. * represents p<0.05 and *** represents p<0.001.

5.3.3 XANES

XANES analysis identified amorphous calcium carbonate (ACC) and aragonite within the carapaces as identified by their characteristic absorption spectra (Fig 5.11).

The analysis shows ACC was the only polymorph identified in all carapaces at all stages of development (Figure 5.12). In fact, ACC was the only polymorph observed instars 2 and 3, two of the three instar 5 samples and three of the adult samples. Aragonite was the other polymorph identified, but was only found in the later stages of development, instars 5 and adult. No significant difference was seen between the amount of aragonite between instar 5 and the adult (p=0.9).

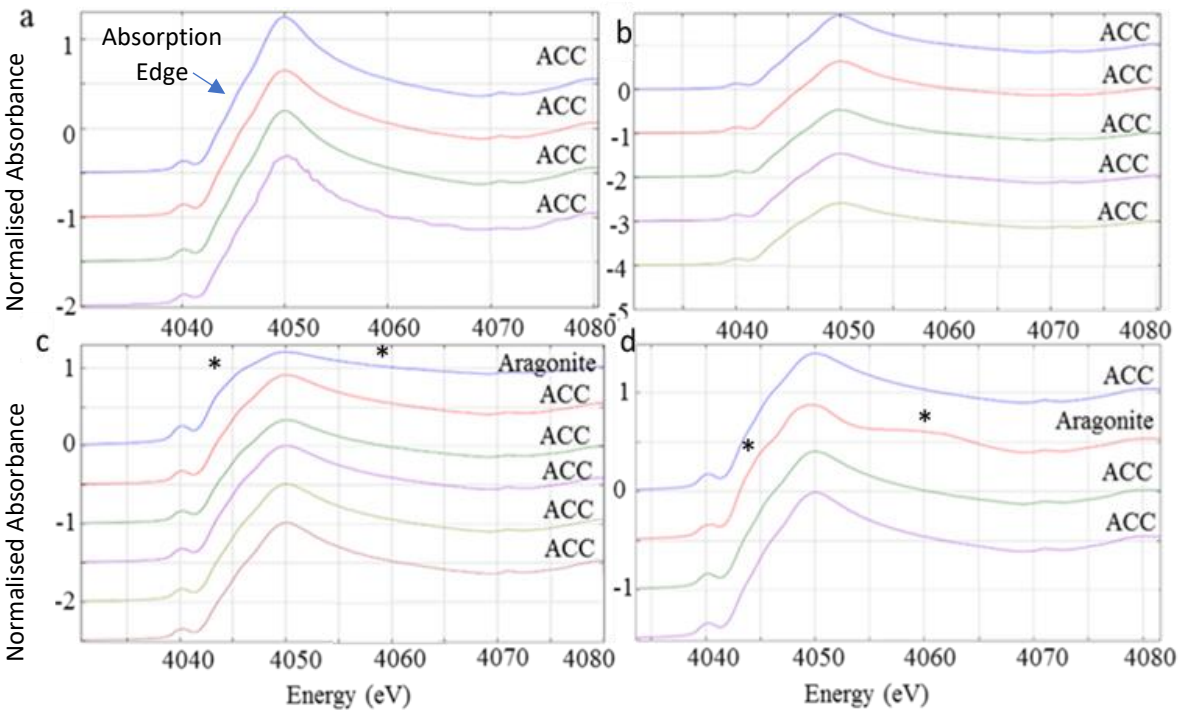

Figure 5.11: Representative Ca K-edge XANES spectra generated from four or six scan points along the long axis of the carapace valves of **a)** instar 1, **b)** instar 3, **c)** instar 5, **d)** adult, showing the internal absorption energy of the samples. Each spectrum denotes a form (polymorph) of $CaCo_3$ which was identified; ACC (amorphous calcium carbonate) or aragonite. * indicates the two distinguishing curve shapes (the pre-edge and post-edge) between Aragonite and ACC.

As well as not being seen in every sample, the aragonite polymorph was not consistently expressed across the samples. Aragonite observation was rare; being seen only once per 4-6 points making up the line scans in the majority of cases. No specific area of distribution was identified for aragonite expression, with it being seen at random scan points along the samples.

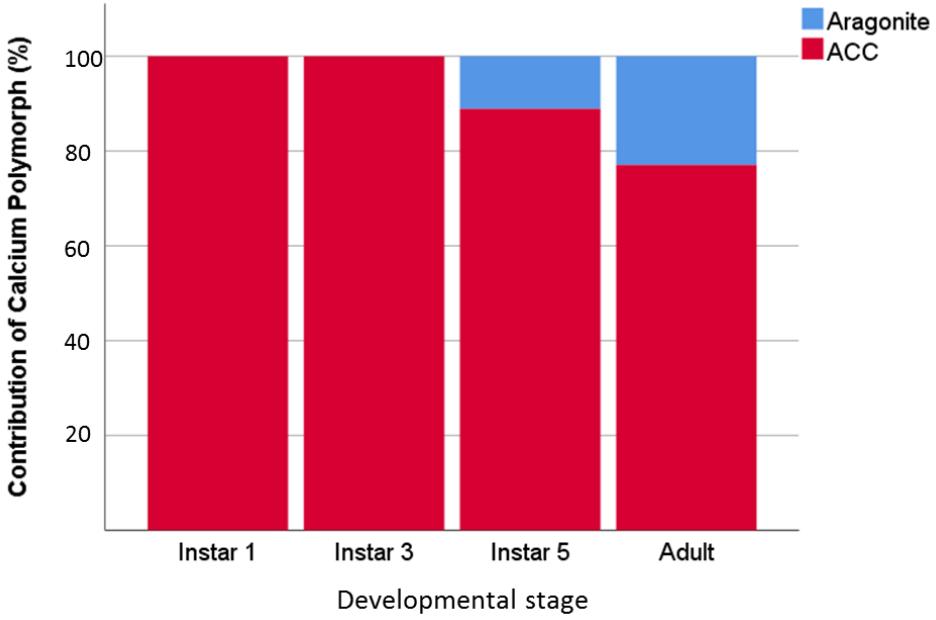

Figure 5.12: Calcium carbonate polymorphs in the ostracod valve. ACC and aragonite were quantified as a mean percentage per scan point across all valves at each instar. Aragonite is only seen in the later instars, instar 5 and the adult and no difference were seen in the amount of aragonite between the two.

5.4 Discussion

The analysis of *Skogsbergia lerneri* valves showed high levels of calcium and oxygen seen throughout the valve. XANES analysis also confirmed the presence of two $CaCO_3$ polymorphs, the most common of which was ACC. In combination with the EDS, that showed these levels are especially concentrated within the medial layer, reinforces the idea that this medial cross-section is mainly composed of calcium carbonate polymorphs. This is consistent with previous literature, the mineral component of the ostracod carapace is comprised of mainly calcium and some magnesium carbonates exemplified by *Cypridopsis vidua* and *Vargula hilgendorfii* (Kesling 1951a; Sohn 1969; Yamada 2019) which is consistent with what is seen in general crustacean species such as the lobster *Homarus americanus* and the woodlouse *Porcellio scaber* Latreille, 1804 (Becker *et al*. 2005; Al-Sawalmih *et al*. 2008), which is found throughout all the layers of the carapace. The majority of this $CaCO_3$ found in the general crustacean carapace is in a stable ACC state (Addadi *et al*. 2003).

When analysing the proportions of $CaCO_3$ polymorphs comprising the carapace, it is essential to consider their different respective mechanical properties in order to understand their overall influence on the carapace. Aragonite in its pure form has a significantly lower stiffness and hardness in comparison to calcite or vaterite when tested via nanoindentation (Sevcik *et al*. 2018). Aragonite was shown to be approximately three times less hard than that of vaterite (0.3GPa to 0.9GPa) with an elastic modulus roughly six times lower (5GPa compared to 31GPa). However, there is a large difference between the properties of minerals in their pure form and when incorporated in a biological matrix, so it is difficult to fully predict physical properties based on pure form testing alone.

Measurements within a biological matrix were carried out on similar structures, comprised of aragonite and vaterite within an organic matrix, isolated from freshwater carp, (Ren *et al*. 2013). Both structures (otoliths, structures found in the inner ear) had a substantial increase in hardness and stiffness compared to their pure forms. What was interesting however, was compared to vaterite, aragonite had a substantially higher level of both hardness (4.9GPa to 3.2GPa) and elastic modulus (67GPa to 57GPa). Therefore while aragonite initially seems like a less suitable protective material due to its pure form mechanics, it may actually be harder and tougher than the other polymorphs in biological materials. Another beneficial property of aragonite is its resistance to crack propagation, caused by the 'needle-like' (Sevcik *et al*. 2018) shape of the aragonite crystal. The direction and extent of the crack might be controlled by the degree of aragonite orientation (Ren *et al*. 2013). By increasing the orientation of aragonite crystals in one direction, there is a higher likelihood that a crack would propagate in that and vice versa. This could have significant advantages for the ostracod carapace, through control of the degree of orientation across the carapace, crack damage can be guided to areas of less importance.

Elemental composition would not only be important for protection as a function of age of the carapace, but would also have an influence on its transparency. Calcium carbonate has been seen in biological transparent material previously, a genus of mollusc called a chiton has an eye lens not made from proteins but instead from

either entirely aragonite or an aragonite/ACC composite (Speiser *et al*. 2011). However as the $CaCO_3$ in this structure is in its pure form instead of a mineral/protein composite, the lens is less applicable for mechanical comparisons with the ostracod carapace. However the chiton eye lens is a large structure containing aragonite and potentially ACC, and in combination, these contribute to maintaining transparency. Therefore it is likely that smaller structures containing the same materials, such as found in the *Skogsbergia lerneri* carapace, likely also maintain transparency. The ostracod carapace may comprise aragonite and ACC, instead of other polymorphs, to both strengthen the tissue, in the way all $CaCO_3$ polymorphs would, and also enable light transmission.

The ACC polymorph is proposed to have a unique role in crustaceans. Its thermochemical and kinetic instability at ambient conditions (Clarkson *et al*. 1992) means it has a much higher solubility than the other polymorphs (Weiner *et al*. 2003). This is important as crustaceans have the ability to reabsorb calcium into the body before moulting (Glotzner and Ziegler 2000). ACC is hypothesised to be utilised for easier transfer between the old and new carapaces, although the amount of $CaCO_3$ retained varies between crustaceans, from 24% in the crab *carcinus maeras* (Linnaeus, 1758) and 96% in the amphipod *Gammarus pulex* (Linnaeus, 1758) (Greenaway 1985; Weiner *et al*. 2003). ACC also maintains an important structural role and so, because of this previously stated instability, mechanisms to stabilise it when required must be present (Aizenberg *et al*. 2003). Such stabilisation is thought to be attributed to high proportions of glycosylated proteins and the creation of sophisticated microstructures in association with another $CaCO_3$ polymorph (Aizenberg *et al*. 2003). The ability of the carapace to transform between a major structural feature for the majority of its lifetime and an easily transportable material for reabsorption, just before moulting, would be very useful to the ostracod. ACC is also a precursor stage to numerous polymorphs of $CaCO_3$, including calcite and aragonite (Addadi *et al*. 2003). Therefore it might be produced for the purpose of turning into specific polymorphs dependent on environmental conditions, such as defence from predation (Reddy 1977; Holmes and Chivas 2002; Addadi *et al*. 2003; Seidl *et al*. 2012; Huber *et al*. 2015).

Additionally, ACC's protective function within a carapace includes that it is an isotropic material permitting equal resistance to mechanical force in all orientations (Weiner *et al*. 2003). Reinforcement by ACC at structures at their weakest orientations structural weakness can be minimised without a reduction to the maximum structural integrity. ACC has also been suggested to act as the final step in a protective material; once the actual penetration causing damage has stopped, the more elastic ACC-reinforced sections of the carapace can dissipate the impact energy (Al-Sawalmih *et al*. 2008).

One of the most significant results from the XANES analysis was the apparent absence of any calcite. The majority of crustaceans, including ostracods, contain calcite within their carapace (Kesling 1951a; Xia *et al*. 1997; Caporaletti 2011). Calcite would be expected to be present as it is both stiffer and harder than the other commonly-occurring polymorphs (Lee *et al*. 2016), as well as its use in other transparent materials (Alagboso *et al*. 2014), so its absence in the *S. lerneri* carapace was surprising. It could be that the central vertical line scan missed a significant amount of calcite within the carapace due to a specific distribution pattern. The edges of the valve would be the most likely position for calcite expression due to its more protective function. Crustacean morphological elements which are exposed to different mechanical loads have different levels of biomineralisation (Al-Sawalmih *et al*. 2008; Vittori *et al*. 2016). It has also been previously shown that calcite can form heterogeneously distributed "clusters" that might have been missed by the scan (Al-Sawalmih *et al*. 2008).

The lack of calcite may be a result of the animals' stage of moulting. While care was taken to ensure that no ostracods were not visibly transferring between two instars (identifiable by a "cloudy" hue to the valve) (Cohen 1983), no distinction was able to be made between the other, less obvious, moulting stages. There is a strong possibility that different moulting stages could have different degrees of mineral or crystalline formation. In some benthic ostracods, ambient water temperature immediately after moulting can directly affect calcite levels in the carapace (Cadot and Kaesler 1977). Valves are uncalcified initially after moulting and slowly re-calcify (Turpen and Angell 1971), so it is possible that it takes time to reconstruct specific

$CaCO_3$ polymorphs. However, to see no calcite in any of the samples means it is highly unlikely that they all were immediately post-moult.

The magnesium, as detected using EDS spectroscopy, may contribute to the absence of calcite. While magnesium is present in a wide range of biological calcite, too high a concentration of it actually inhibits calcite formation (Raz *et al*. 2000). This is because Mg^{2+} ions are readily adsorbed onto the surface of calcite, but not aragonite. The Mg^{2+} is then incorporated into the calcite structure and substantially increases the solubility, making it unstable (Berner 1975). It is important to note that in many crustaceans, calcite is only a minor part of the overall $CaCO_3$ composition (Al-Sawalmih *et al*. 2008). So perhaps the apparent lack of calcite within *Skogsbergia lerneri* may not cause major, widespread changes to the physical properties of the carapace compared to studies on other crustaceans.

Qualitatively higher levels of phosphorous were seen on the epicuticle compared to the rest of the carapace. This may suggest the formation of amorphous calcium phosphate which has been seen in crustacean carapaces (Luquet 2012) or could be evidence of higher levels of phosphorylated proteins (Becker *et al*. 2005). The epicuticle consists primarily of various proteins and lipids (Stevenson 1985) and so will have high levels of phosphorus-containing components.

Several changes were seen throughout the different developmental stages of the ostracod, both in elemental analysis and in the $CaCO_3$ polymorph composition. Aragonite was only seen within the later developmental instars (I5 and adult), which implies this change allows for a more permanent reinforcement and a greater level of structural strength required to maintain structural integrity over a larger area. Unfortunately to the author's knowledge, no direct comparisons exist between biological aragonite and ACC, however from the previous information about the physical properties of each polymorph mentioned earlier, it would be likely that aragonite has a higher hardness and elastic modulus. Total calcium concentrations did not significantly alter from instar to instar, but remained one of the higher contributors amongst other elements (excluding C and O which are essential to all biological life), showing that it remains as important within *S. lerneri* as it is in other crustaceans.

XRF data showed significant decreases in both Mg and S levels within the adult, compared to instar 1 (and instar 3 for Mg). This implies either a higher importance for the earlier instars or that the elements are rare/inefficient to incorporate and so the carapace never increases beyond its initial stockpile of Mg and S. Sulphur is especially important for crustaceans as it is involved with protein stability (Gomez-Tamayo et al. 2016) which affects the physical properties of the carapace. This stockpiling would lead to the signal count becoming more dispersed as the carapace grows larger. The late-mid stage (I4 and I5) showed a higher level of P compared to all other instars, as well as the lowest level of O; significantly lower than instar 1. The most likely explanation is that this stage, as the penultimate stage, is leading towards the transition to the final adult stage. As the carapace reabsorbs the C, the proportion of carbonates would shift, which could lead to a lower O signal. The increased P levels would also be explained as it would be the total amount of P for the adult carapace but still within the smaller carapace, leading to a higher signal.

It is interesting to note that there are significant disparities between the EDS and the XRF results. The former showing a change in P, not seen in XRF, with XRF detecting changes within Mg and S, not seen in EDS. There are two main possibilities to explain this, firstly that it could merely be a lack of statistical power due to small sample sizes. Unfortunately, due to the high demand on synchrotron time, and that this was performed in the last year of study (hence no time to submit another application), an increased sample size was not possible. Further experiments would either solve the problem or reinforce the second possibility, that they are both correctly representing different aspects of the carapace. EDS studies a transverse cross-section of the valve, which while very useful to see contribution to different layers, does not account for the entire valve. On the larger instars, only part of the full cross-section of the valve is analysed, so changes seen in the non-studied area (*i.e*. the extreme edges of the valve) could have been ignored. XRF however, detected signal from the surface view of the entire carapace, therefore any changes that happen in the carapace along an x- or y-axis would be seen by XRF and not EDS and vice versa for the z-axis. However, both techniques are likely showing true data results, and the differences in signal expression are likely due to differences in the localisation of elemental expression.

Chapter Six

Optical Properties of the Carapace

6. Optical Properties of the Carapace

6.1 Introduction

6.1.1 The Mechanisms of Transparency

The mechanisms of transparency are complex; however, they can be broken down into three basic properties: the level of scattering, the level of absorption and the thickness of the sample. This can be summarised the Beer-Lambert law (Swinehart 1962) modified for light transmission through solids (Fox 2010):

$$I = I_0 e^{-\mu x} \tag{6.1}$$

where I is transmitted light, I_0 is incident light, μ is the linear attenuation/extinction coefficient and x is the thickness. The linear attenuation coefficient μ depends on the absorbance and scattering in the material and can be defined as:

$$\mu = \frac{\mu_a + \mu_s}{\rho} \tag{6.2}$$

where μ_a is the absorbance coefficient, μ_s is the scattering coefficient and ρ is the density of the material. Therefore, thickness, scattering and absorbance all contribute to the transparency of a material. Thickness is a property that has a practical limitation within biological materials, the theoretical ideal would be a thickness as close to zero as possible however the material may be required to be much thicker to carry out its role in the organism. Scattering and absorbance can have much more complex interactions and materials can be created to display specific structural formations or compositions to minimise these properties in materials that would otherwise not be transparent.

6.1.1.1 Scattering

The scattering coefficient of a material depends on the difference in the refractive index (RI) between the sample and that of the surrounding medium (Jacques 2013). The refractive index of a material is defined as the ratio of the velocity of light in a vacuum to that within the specified material. The differences between the transmission of light in two materials (as represented by their respective RI), means that the when light progresses from one material to the other, a specified amount of light will be not be transmitted into the new material and will instead be scattered. Scattering is created any time there is a change in refractive indices, either within a material or at the surface of a material, and so materials with numerous components, such as most biological tissue will include numerous scattering events, whereas structurally consistent materials (such as glass) only scatter at their surfaces. The discussion of chapter 3.4 has previously covered how structurally, ostracods have both reduced changes to internal RI between layers and potentially use destructive interference to maintain transparency.

A specific form of scattering can occur at smooth boundaries such as the surface of the ostracod carapace; the light scattered backwards interferes to produce a reflection at a specific angle. From a material's refractive index, predicted light transmission at such a boundary can be calculated from the Fresnel equation (Born and Wolf 1980; Gupta *et al*. 2019) (assuming θ, the angle of the incident light, is 0):

$$R = \left(\frac{n_{t-}n_i}{n_t + n_i}\right)^2 \tag{6.3}$$

where R is Reflection, n_t is the RI of sample and n_i is the RI of the surrounding medium, in this case a saline solution – similar to that of seawater which has an RI of 1.339 at 577nm (Austin and Halikas 1976). The transmission of light (T) can be calculated as:

$$T = 1 - R \tag{6.4}$$

6.1.1.2 Absorption

Any light-absorbing material will absorb a fraction of the incident light per unit of travelled distance within the material and convert this into heat energy. The lower the level of absorption, the thicker the material can be while maintaining a negligible effect on the overall transparency. Absorption occurs when specific wavelengths of light possess the exact amount of energy to excite an electron within an atom interacting with the light, to a higher energy state (Nobel 2005). If the energy and the energy requirements do not match, then absorption does not occur. For a material to be transparent for humans, the only wavelengths important for absorption are those in the visible spectrum (*i.e*. 400-700nm), for example glass absorbs some UV wavelengths (Sackey *et al*. 2015) but is transparent at all visible wavelengths.

The main areas within the ostracod that would be responsible for light absorption would be cells related to pigmentation. The most obvious of these are the pigments that are contained in non-transparent ostracod carapaces that give the animal its colour. The *Heterocypris incongruens* (Ramdohr, 1808) ostracod, of the podocopid order, has an orange-yellow appearance with specific pigments seen in high densities in the epidermal cells of the valves (Green 1959) with this colour becoming stronger later in development. This presents the possibility that the optical properties of an ostracod carapace (in *S. lerneri*'s case, its transparency), may be affected by its developmental stage. Analysis of this pigmentation showed it to be comprised of the carotenoid β-carotene. While a transparent carapace is not going to contain any pigmentation granules it is interesting to note that the majority of the carotenoids within the food given to *H. incongruens* were not β-carotene (Goodwin 1954) and were not found anywhere within the carapace at all (Green 1959). This suggests that the diet of the ostracod has little effect on the colouring of the carapace, which otherwise could have an impact on *S. lerneri* as it is a scavenger and would consume a large variety of foods.

6.1.2 Refractometry

A refractometer is a tool which used for measuring the refractive index of transparent liquid or solid samples, an Abbé refractometer was used for this experiment so it will be the one explained. A refractometer works on the principle of the critical angle which is the largest

angle the incident light can approach without total internal reflection. Incident light approaching at angles below the critical angle will continue through the sample and the measuring prism to illuminate an optical image further in the instrument (Rheims *et al*. 1997). Light approaching at angles above the critical angle will not pass through, leaving part of the optical image dark (Fig 6.1). By altering the viewing angle, the exact middle between light and dark can be found, which then allows for the critical angle to be revealed and subsequently the RI to be calculated from Snell's Law. Abbé refractometers have compensating Amici prisms added to allow the use of non-monochromatic light, which would normally create a blurry border between the illuminated and non-illuminated areas. By adjusting these prisms light can be focused into a single white beam and a clearer image can be generated.

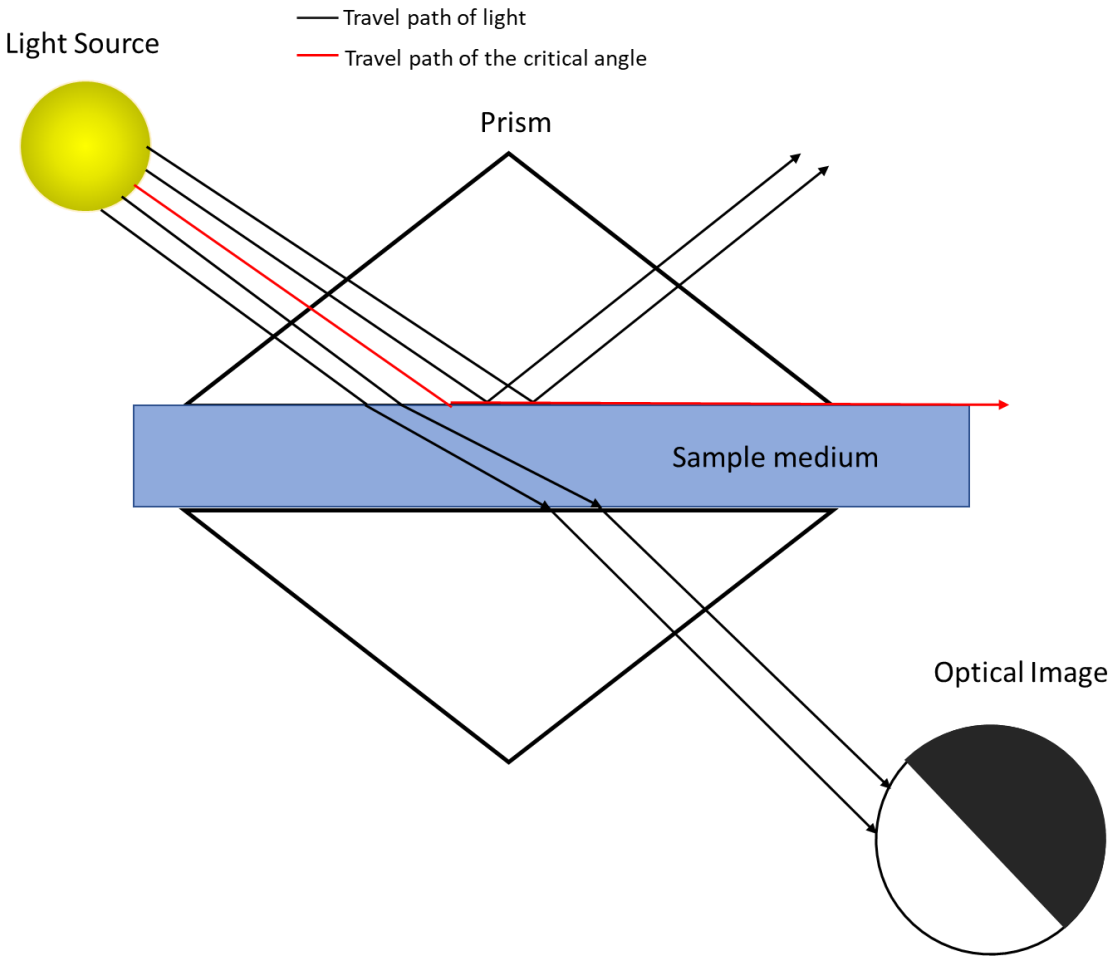

Figure 6.1: A simplified diagram of an Abbé refractometer. By using the boundary between the illuminated and non-illuminated sections of the optical image, the critical angle and subsequently the refractive index can be determined.

6.1.3 Spectrophotometry

Spectrophotometry is a technique used to measure the intensity of light after being passed through a sample, compared to the original intensity, as a function of its wavelength (Skoog *et al*. 2007) (Fig 6.2).

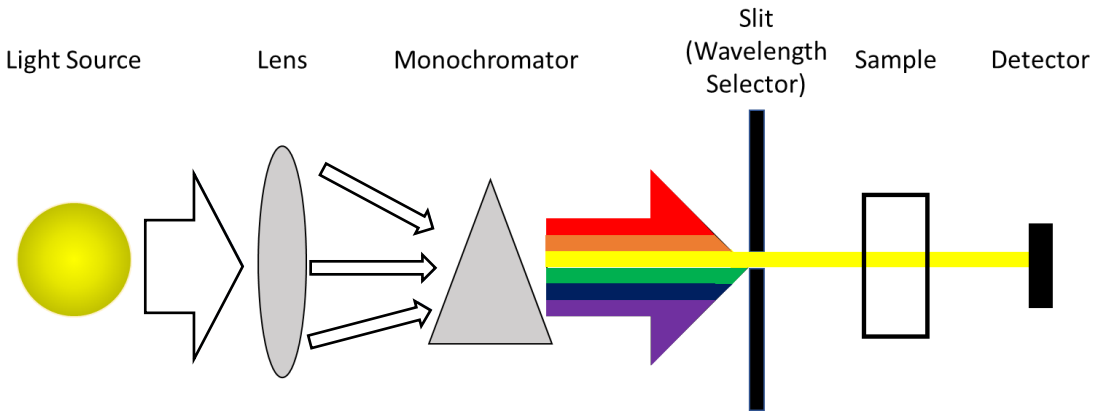

Figure 6.2: The inner mechanism of a spectrophotometer, the light source is focused and split into the wanted wavelength before been sent through the sample. The total light detected after the sample is compared to the amount before and the absorbance is calculated.

The difference between these two intensity values is labelled as absorbance, as the sample is compared to a 'zero' or a baseline measurement of a similar sample therefore differences in reflection should be minimal. This is especially relevant as commonly most spectrophotometry is carried out with liquids so the difference in light scatter between the sample and the control would be insignificant. While the most basic form of spectrophotometer analyses a sample at a single wavelength, more advanced models can measure the absorbance at multiple wavelengths in one session. While the absorbance is still measured at a single wavelength at a time, advanced spectrophotometers can quickly cycle through any range of wavelengths, from the standard visible spectrum (400-700nm) to ultraviolet (<400nm) and infrared (>700nm). This is useful for analysing the properties of a sample throughout the spectrum of light rather than using the values of the absorbance of a sample as an indicator of development (*e.g*. studying changes in metabolic processes).

6.1.4 Aims and Hypothesis

Hypothesis:

The carapace of the *Skogsbergia lerneri* will have optical properties (RI and optical transmission) consistent with general transparent materials across the visible spectrum, especially other biological examples. This transparency will not significantly alter throughout the organism's lifespan, keeping consistent optical properties during their development.

Aims:

I. Measure the refractive index of the *Skogsbergia lerneri* carapace for the final, adult stage and the previous developmental stages.
II. Develop a method for measuring the optical transmission of the *Skogsbergia lerneri* carapace and record the results for the final, adult stage and the previous developmental stages, in both a medium with a similar RI and in the medium close to their natural habitat.

6.2 Experimental Design

I. *Measure the refractive index at both the adult stages and the previous developmental stages*

Ostracod valves were measured via refractive index testing as described in chapter 2.9.3 at every instar (n=3 per developmental stage).

II. *Develop a method for measuring the optical transmission*

The spectrophotometer used was outfitted for analysis of liquids within cuvettes (See section 2.9.1 for details) and so modifications had to be made to allow for the successful completion of the experiment. Due to their small size, the sample would freely move around if merely placed into a cuvette filled with a medium. This would mean that it could not be guaranteed that the entire beam would always be travelling through the sample. Therefore, sample holders had to be created to allow constant and accurate absorbance readings of the carapace.

Initially, quartz cuvettes were used as sample holders, wrapped in black PVC tape with a 1.5mm hole, created by a biopsy punch, at the front and back of the cuvette to prevent

light reaching the detector that had not passed through the sample. This would create an easily identifiable section that would clearly show a change in absorption when compared to a positive control. Without this blackout the changes in absorbance would be washed out by the lack of absorbance seen by the majority of the sample-free cuvette. The sample was glued to the end of a cocktail stick and immersed into the suspension fluid at a fixed height, level with the hole (Fig 6.3). Unfortunately, with the suspension fluid tested (silicon oil) the sample would not stay attached to the cocktail stick. There was also the risk that movement or accidental bumps to the holder could unknowingly move the sample away from the hole and so the cuvettes were deemed not usable.

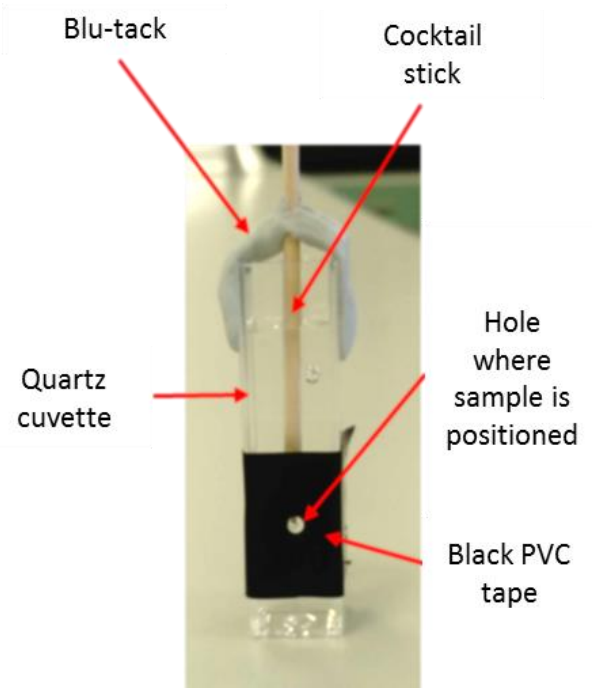

Figure 6.3: Initial cuvette-based sample holder created to replace the standard cuvette used in spectrophotometry.

An alternative sample holder was developed based on a quartz slide wrapped in black PVC tape with a 1.5mm hole created identically to last time. These solved issues occurring with the previous holders and prevented the sample from moving away from the target circle. To prevent the sample from being crushed and to hold it in place, a spacer was created out of waterproof epoxy resin and the base was coated with nail varnish to prevent leaks. This prevented any noticeable leaks, however it was difficult to judge whether it had reliably prevented very minor leakages. Tape was added on either side and a second quartz slide was placed on top of the spacer (Fig 6.4a). The slides were then taped together with the sample

and the suspension fluid inside the epoxy resin spacer to prevent leakage. Initial testing suggested that these new holders could reliably contain the sample and prevent any significant leaking. As the sample holder can no longer fit within the cuvette holder of the spectrophotometer, it is attached to the side of the cuvette holder so that it is still in the pathway of light and all light transmitted through the sample can be received by the detector(Fig 6.4b).

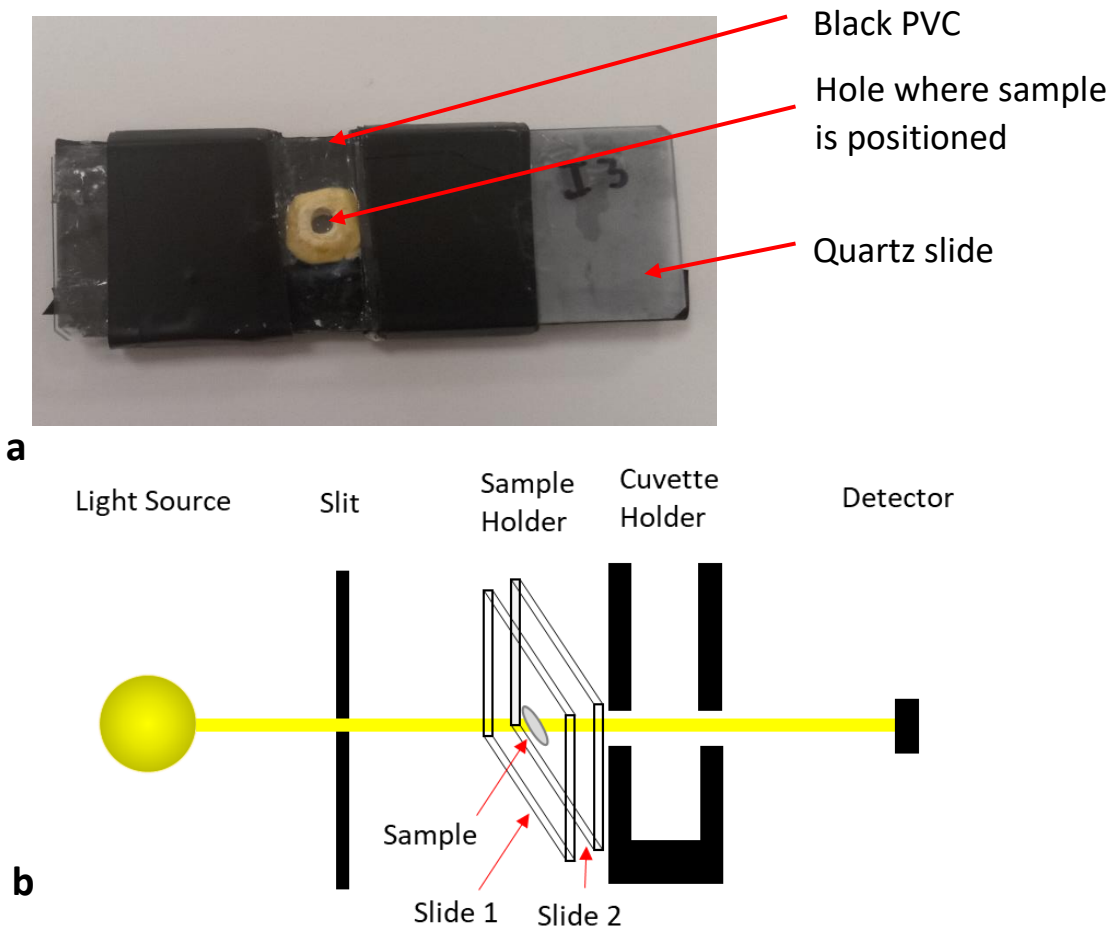

Figure 6.4: a) Finalised slide-based sample holder created to securely hold the sample in place while allowing maximum transmission. **b)** Pathway of light through modified spectrophotometer layout. The sample holder is attached to the front side of the cuvette holder to allow maximum transmission.

III. *Measure the optical transmission at both the adult stage and the previous developmental stages*

Ostracod valves were analysed for optical transmission via spectrophotometry as described in chapter 2.9.2 at every instar. Samples were initially tested with a medium of a similar RI, silicone oil (n=1 at every instar), however silicone oil caused issues with the sample holders leading to leakage and unreliable results (see 6.3.2.1). Due to this leakage and saline being much closer to the animal's natural habitat, testing was mainly carried out with a saline medium with an identical ppt as seawater (n=3 at every instar).

iv. *Statistical Analysis*

Refractive index testing was analysed via one-way ANOVA testing across the instars. Normal distribution of data was confirmed using the Kolmogorov-Smirnov test. Kurtosis and skewness were seen to be between ±1.5 for all data sets. All data generated from these sample populations is assumed to be done via random independent sampling as samples were chosen at random from their groups and no emphasis was put on apparent transparency. Equal variance between the populations was also assumed due to equally sized testing groups

6.3 Results

6.3.1 Refractive Index Testing

Refractive Index testing showed a mean RI of 1.406±0.002 for instar 1, 1.404±0.001 for instar 2, 1.401±0.001 for instar 3, 1.401±0.003 for instar 4, 1.406±0.001 for instar 5 and 1.406±0.002 for the adult. When analysed via one-way ANOVA testing, no significant differences were seen between the RI of the instars (Table 6.1) and an overall mean RI for the *S. lerneri* carapace can be given at 1.404±0.003.

Using the refractive index values, the transmission and reflection of the carapaces within saltwater can be calculated from the Fresnel equations (assuming θ is 0), using a RI of saltwater as 1.339 at 577nm (Austin and Halikas 1976) (Table 6.1).

Instar	Refractive Index	Reflection	Surface Transmission
1	1.406	0.060%	99.940%
2	1.404	0.056%	99.944%
3	1.401	0.051%	99.949%
4	1.401	0.051%	99.949%
5	1.406	0.060%	99.940%
Adult	1.406	0.060%	99.940%

Table 6.1: The mean refractive indices of the different *S. lerneri* developmental stages and their calculated reflection and transmission values.

6.3.2 Optical Transmission

6.3.2.1 Silicone Oil

Optical transmission measurements with carapaces in silicone oil showed a lack of conformity throughout the developmental stages (Fig 6.3). Instar 1 showed a general increase in transmission from 400nm to 700nm, Instar 2 showed almost no transmission at 400nm until 565nm where it rapidly increases at 602nm and then gradually increases to 700nm. Instar 3 showed a general increase in transmission from throughout the entire spectrum, instar 4 showed a minor decrease in transmission from 400nm to 700nm. Instar 5 showed a very minor increase in transmission across the spectra. The adult showed a decrease in transmission similar to instar 4.

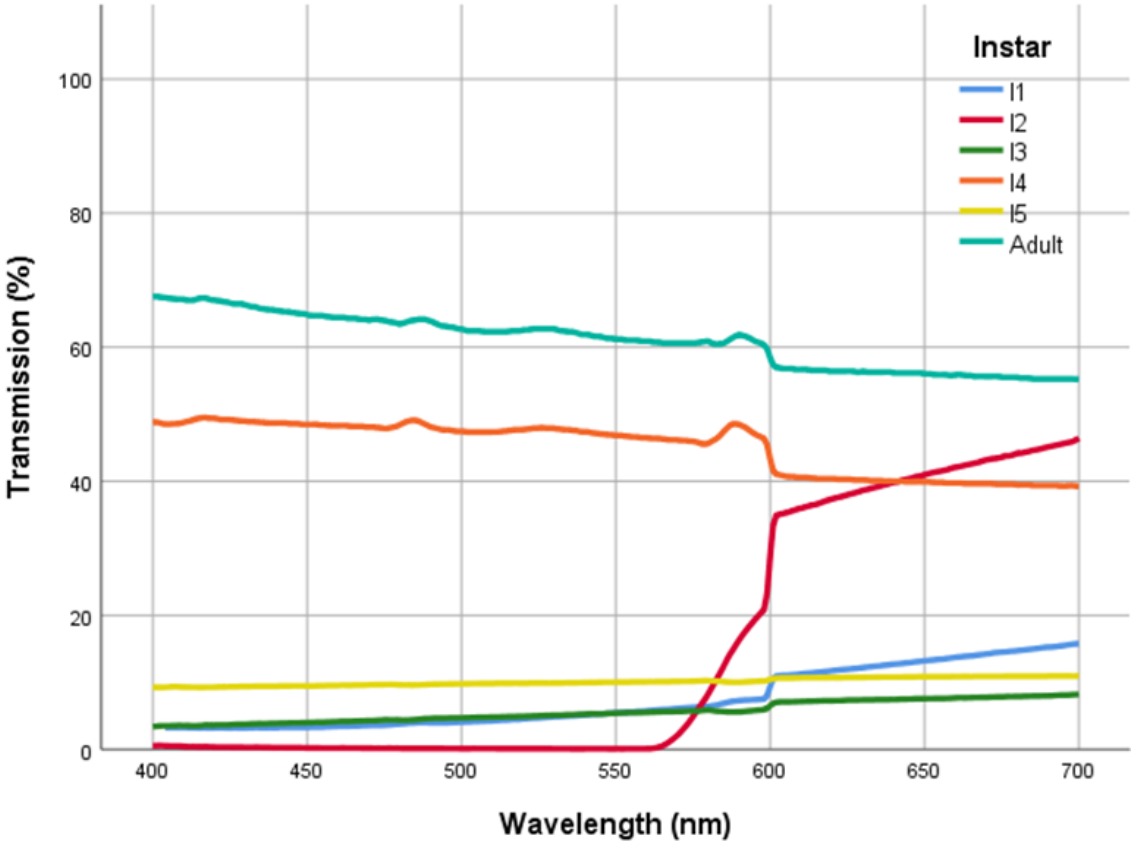

Figure 6.5: Light transmission from ostracod valves from each developmental stage, within a silicone oil medium in the visible spectrum of light.

6.3.2.2 Saline

Spectrophometric measurements showed an increase in optical transmission at longer wavelengths except for instar 5 and the adult which showed decreases (Fig 6.4). The mean Instar 1 value showed an increase in transmission from 400nm to 700nm, with a steeper increase being seen between the smallest wavelengths (400-475nm). Instar 2 showed an increase in transmission along the spectrum. A similar rate of transmission increase was seen with both instar 3 and 4. Instar 5 differed from the previous instars by showing a significant decrease in transmission throughout the wavelengths,. The adult samples also showed a decrease, however this change is minimal, unlike instar 5. One characteristic shared between all stages except instar 5 was a sharp, if minor, increase in transmission at 600nm.

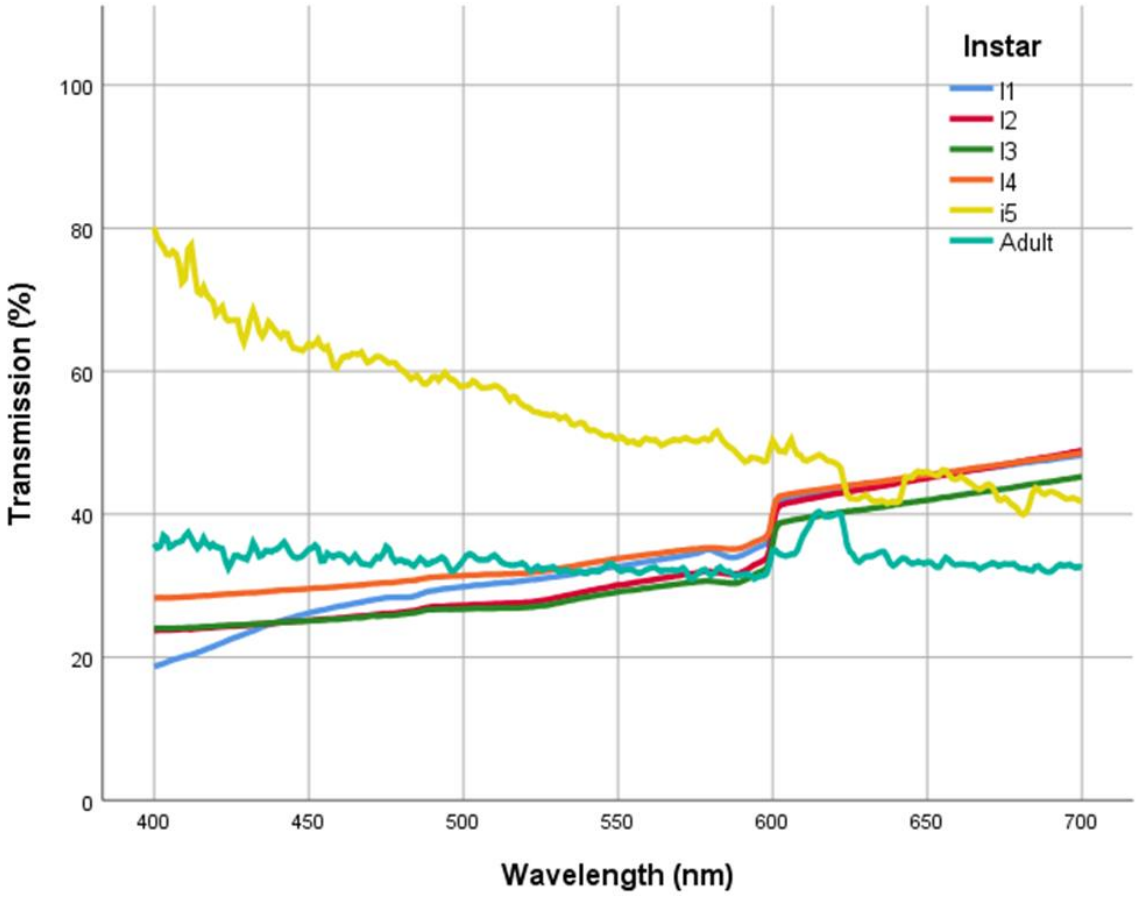

Figure 6.6: The graph of light transmission seen in from the ostracod valves within a saline medium

The proportional change in transmission was measured in each instar and compared to each other. Instars 2-4 show the most common pattern across the instars. These values showed around half of their maximum transparency at the lowest wavelengths (48.6%, 53.1% and 58.2% for instars 2, 3 and 4 respectively) and steadily increased until 600nm. The sharp transmission spike noticed previously at 600nm, while being a small increase for total transmission, was much larger proportion of their total transmission being a mean increase of 13.7%. Instars 2-4 reached their maximum transparency at the longest wavelength measured, 700nm. Instar 1 followed a very similar pattern as previously mentioned except the transmission between 400-450nm was lower than that of instars 2-4 (38.8%) and increased sharply to return to parity. Instar 5 showed a reverse of the younger developmental stages, with maximum transmission at the lowest wavelength (400nm) and half maximum transparency (52.2%) at the largest (700nm). The adult instar was unique in that it maintained a constantly high level of its maximum transmission varying between 92.7% and 76.6%

throughout all wavelengths except for a spike to its maximum transparency between 600-625.

6.4 Discussion

While previous refractive index testing has been carried out on ostracod eyes, this is to the author's knowledge the first example of analysis within the order myodocopida as well as the first analysis on transparent, full carapaces. Andersson and Nilsson measured the RI of cells within the eye and the cuticular lens (which doubles as the protective carapace) in *Notodromas monachus* (O.F. Müller, 1776) (Andersson and Nilsson 1981). Here it was shown that within the eye that the refractive index ranged between 1.351-1.371, dependant on the specific part of the eye. While this is lower than the value found for *S. lerneri* carapace this is due to the internal nature and limited function of these eye cells. These eye cells carry out no protective role and only exist for the purpose of maintaining vision. What it is of interest is that the refractive index of the cuticular lens, which would carry out the same function as the *S. lerneri* carapace in both transparency and protection, is actually 1.62 (close to that of pure calcite). This is substantially higher than the mean RI of 1.404 seen in the *S. lerneri* and leads to over ten times higher light reflection in saltwater. While the transparency of the *N. monachus* cuticular lens is still high, the fact that *S. lerneri* maintains a lower refractive across its entire carapace than *N. monachus* does over its eye window shows how adapted the *S. lerneri* is for its transparent function.

This is also the first set of results to test if the development of the ostracod affects the refractive index of its transparent biological materials. The carapace shows no significant change in RI throughout the developmental stages, maintaining a constantly high transmission of light (in its marine environment). This allows the ostracod to maintain both the highest level of visual performance and environmental camouflage throughout its lifetime.

The values given for the optical transparency were greatly different from what would be expected. While the conversions predicted by the Fresnel equations only show the transmission at the surface, the scattering caused by refractive index changes between the

carapace layers and absorption from the materials should not reduce transmission to the level seen. This could be caused by several reasons. The first possibility is that the readings were correct, and this difference is accounted for by absorbance, which is not considered with refractive index testing via a refractometer. It is immediately apparent that the spectrophotometer transmission values were too low, as a basic qualitative appraisal with the human eye shows that all carapaces appear transparent, which would not be the case if optical transmission really was approximately 30%. This implies firstly that the minimum optical transmission should be higher than any found from this analysis and secondly that the instars should not have such a disparity between their optical transmission values.

The most likely explanation is that there was an issue with measuring the samples correctly. As stated previously, analysis with the silicone oil samples was quickly stopped due to its extremely low viscosity causing it to leak from between the sample holder and the quartz slide. This means that the actual medium surrounding those valves was air and the remaining droplets of oil, which would cause numerous scattering issues as the light passed through multiple different media. However, this does not explain the results seen within the saline medium samples, where no leaking occurred. While the sample holders were improved upon several times during experimentation, they were not a professional product and minor defects may have been present. For example, an uneven surface of the epoxy resin spacer would create an imperfect seal with the slide which could allow small amounts of air/water transferal. This would lead to the creation of bubbles which would cause significant scattering.

The final cause could be an issue created by the non-standard use of the spectrophotometer. The model used was a standard spectrophotometer that requires cuvettes to measure liquids, however as mentioned in the experimental design (section 6.2) cuvettes could not be used. Instead, sample holders were created that were attached in front of the cuvette holder. While adjustments were made to accommodate this (*e.g*. increasing the assumed travel distance of the light through the sample) certain issues were unavoidable. Multiple sample holders were created to analyse the samples quickly and efficiently however this could have caused issues in reliability between samples. Every cuvette placed within a cuvette holder will have a face completely perpendicular to the incident light. However, the slight differences between each sample holder and the attachment to the side of the cuvette holder (lacking a specific, standardised slot) meant that incident light hitting the quartz slide at the front of the sample

holder may have not have been at the same angle every time. This would cause significant variability in the results for each reading, although as the readings were zeroed against a similar sample holder, this would account only for a large variability between the readings, not the overall low transmission seen.

Although the issues mentioned above make the absolute transmission readings unreliable, none of these issues should impact the wavelength dependencies measured. Therefore the trends of the instar spectra can be analysed. The fact that the transmission of light through the carapace for the majority of the instars almost doubles at the longer wavelengths compared to the shortest within the visible spectrum is the opposite to what would be expected. Due to longer wavelengths having lower frequencies they are attenuated more quickly in sea water than the shorter wavelengths (Schechner and Karpel 2004). As such they do not penetrate as deeply into the ocean and so are not as influential in the visibility of marine organisms. There might however be a simple solution to this confusing implication, the longer wavelengths are not immediately attenuated and so penetrate a certain distance (Chiang *et al*. 2011). While *S. lerneri* are benthic, they were not collected from a great depth, being within 10 metres of the surface, as such the majority of the wavelengths would reach their habitats. As long as *S. lerneri* didn't move to a substantially deeper habitat, the attenuation of longer wavelengths shouldn't matter. Instar 5 showed the greatest deviation from the normal spectra, it both had a higher transmission level compared to all other instars and had the opposite progression of light transmission across the wavelengths. This result could in part be be due to the development of the ostracod as the adult shows a similar deviation from the other instars. While the adult does not see this decrease throughout the wavelengths, it does not show the increase seen in instars 1-4 either. In fact the adult shows the most optimal distribution out of all developmental stages, staying relatively similar across all wavelengths. As the adult is the largest and longest developmental stage, it would be reasonable to assume their carapaces would be the most highly adapted to light transmission.

The spectrophotometry used in these experiments could in future be improved by improving the sample holder to avoid some of the difficulties encountered here. Creating thicker walls for the epoxy resin spacer with a specifically flattened epoxy/slide interface would remove the chance of air/water exchange and the use of a spirit level to create a flat surface that would interact with the incident light would remove any issues caused by angling of the

sample holders. Alternatively, more specific experimentation could be carried out to calculate quantitative values for the different optical properties of the carapace such as μ_a and μ_s - (Cheong *et al*. 1990), which could then be combined to generate highly accurate optical transmission values. However, to generate these values, equipment specialised for biological tissue or techniques are required, such as photothermal radiometry (Long *et al*. 1987) or time-of-flight studies (Patterson *et al*. 1989).

Overall it seems safe to judge that the predicted transmission calculated from the RI readings are much closer to the actual readings rather than the spectrophotometry data. While there is most likely some minor absorption that is ignored from the RI readings, and there is a lack of experimental data to reinforce the theoretical transmission predictions, it can be suggested that the *S. lerneri* carapace is at least as optically transparent as other transparent biological materials.

Chapter Seven

Discussion

7. Discussion

7.1 The transparent carapace of the *S. lerneri*

Skogsbergia lerneri is a rare type of crustacean; it possesses the protective exoskeleton which is a characteristic of all crustaceans, but its carapace maintains a transparency similar to that only found in the protective covering commonly seen in many crustaceans' eyes. The transparency of the *S. lerneri* carapace is not only fascinating from a purely biological perspective but also has promising potential for biotechnical applications.

Like other myodocopid ostracods, the calcified carapace consists of four main layers, namely the epicuticle - a thin outer layer, the exocuticle –comprising loosely organised chitin fibrils, a calcified endocuticle containing crystalline calcium carbonates within an organic matrix and the laminate endocuticle with densely packed chitin lamellae. This structure, together with its overall composition, allows the *S. lerneri* to maintain both its transparency and physical properties.

Until now, a comprehensive analysis of structure has not been undertaken on transparent ostracod carapaces and indeed, there have been very few studies on transparent crustacean carapaces in general, especially throughout development. Research on transparency has been carried out in one of two ways, the first has been through limited electron microscopy, such as TEM of adult transparent ostracods (Yamada 2019) or SEM of the outer carapace of transparent amphipods (Bagge *et al*. 2016). While these give a good insight into the specific area the authors were interested in (*e.g*. carapace comparison to other myodocopids or analysis of a specific anti-reflective structural feature), they lack detail and context of the carapace as a whole. They also do not probe how these structures change throughout development, which can be important when analysing an organism. This is especially important in crustaceans which completely replace their carapaces via moulting numerous times. The second area of research is in certain species where carapace transparency is only maintained over a crustacean's eyes, but not elsewhere (Alagboso *et al*. 2014; Parker *et al*. 2018). While specific transparent areas may employ similar structural features to entirely transparent carapaces, they have greater flexibility as any issues created by their structure

can be compensated for by the much larger non-transparent portion. This can be seen by the cornea cuticles of studied isopods, which contain no pore canals across the transparent section (Alagboso *et al*. 2014; Fabritius *et al*. 2016a), a feat obviously impossible to maintain across the entire carapace. This makes analysis of these areas limited for understanding how a fully transparent carapace such as *S. lerneri* can be maintained.

7.2 Instar Development

While there are many similarities between the instars, this thesis has identified substantial changes in physiology over different developmental stages (summarised in Table 7.1). The instar 1 carapace has some of the most distinctive features as it lacks crystals formed within the endocuticle. This makes the carapace significantly thinner than in other instars, with a higher proportion allocated to the exocuticle and laminar endocuticle layers, and also less specific magnesium distribution within what would normally be the crystalline endocuticle. This is not due to a lack of magnesium within the instar 1 carapace as XRF analysis (section 5.3.1) showed high magnesium counts. As magnesium is involved in the stabilisation of calcium carbonate polymorphs (Addadi *et al*. 2003; Fabritius *et al*. 2016a), it would be reasonable to assume that the crystalline $CaCO_3$ polymorphs have not fully formed into an established layer and so magnesium would not yet need to be present. Chitin inclusion (section 4.4.7) measured as percentage chitin-derived signal within the carapace, however, was at its highest in instar 1, compared to all other developmental stages. This is not surprising, as without a properly developed crystalline endocuticle layer, a greater proportion of the carapace will be either exo- or endocuticle, and so chitin based. The rate of growth from instar 1 to instar 2 was the highest throughout instar development. The change showed the highest proportional rate and the second-highest actual rate of development in the ultrastructure, even though the literature as shown it has the smallest increase in animal size (Cohen 1983). The ultrastructural data (section 3.3) showed that between these two instars, the carapace increased over 4 times in overall thickness. This consisted of an approximate 2-3 times increase with each layer and 9-fold with the calcified endocuticle layer, as well as the complete formation of this layer. However, there was no significant change in percentage

chitin contribution (section 4.4.7) or elemental composition (chapter 5) between these two instars. Therefore, the changes observed were purely related to ultrastructural differences. Instar 2 establishes the basic carapace structure that was seen in all subsequent instars; the crystalline endocuticle is formed and total carapace thickness increased, compared to instar 1. A stronger and broader magnesium signal was also seen throughout the cross-section compared to instar 1. However, analysis showed no differences in chitin distribution or $CaCO_3$ polymorph proportions, with all $CaCO_3$ structured as amorphous calcium carbonate (ACC).

The instar 3 carapace was significantly thicker than that of instar 2, while maintaining similar layer proportions. An elemental difference was present; the carapace lacked the previously identified phosphorous signal within the epicuticle. No change in epicuticle thickness was seen between instar 2 and 3, indicating that this change was attributed to compositional differences.

As well as instar 1, instar 4 showed substantial differences compared to the other stages. Instar 4 was not significantly larger than instar 3, had a lower percentage chitin contribution than instar 1 and had a reduced crystalline endocuticle thickness. This was seen in both the quantitative change in the ultrastructure measurements and the reduced calcium, magnesium and oxygen distribution, generated from the EDS analysis, which is indicative of the calcified layer. Although the instar 4 samples used in chapter 3 or chapter 5 could individually be suggested to have experimental issues, the fact that these instar 4 samples (different samples and using different techniques) were anomalies in both experiments suggests that the instar 4 carapace is unique amongst developmental stages. Chapter 5 did have a smaller sample size for instar 4 (n=1), however the additional samples were not analysed due to what appeared to be damage caused by their processing, which prevented experimentation. In retrospect these could have merely been the abnormal structure seen at this instar, the lack of the calcified endocuticle made the structure of these repeats too thin to correctly maintain its structure after processing. This uniqueness is additionally supported by the decrease in chitin-associated pixel percentage, with instar 4 being the only stage with a significantly lower chitin distribution. However, as the changes in instar 4 structure are mainly based in the crystalline endocuticle, the overall changes to chitin would be reduced. Therefore, if this structural change does have an effect it is likely in combination with the

effect caused by its position as one of the middle stages of development as mentioned in the discussion of chapter 4 (Section 4.5).

In instar 5, development-related carapace structural changes are re-established, with the carapace significantly thickened, compared to that in instar 4, with bigger epicuticle, exocuticle and crystalline endocuticle layers. While this increase of size is substantial, it is mainly relative to the abnormal structure of instar 4, as the ultrastructural thicknesses of instar 5 are in line with what would be expected compared to the progressive changes observed in all other instars. In instar 5 carapaces, calcium, magnesium and oxygen were again expressed throughout its depth (observed in tissue cross-sections) and the phosphorus band was present in the epicuticle. Percentage chitin significantly increased from instar 4 (*i.e*. no longer significantly lower than instar 1). The most significant change at instar 5 of the *S. lerneri* development was the presence of the $CaCO_3$ polymorph aragonite within the crystalline layer, as opposed to ACC, solely seen in all previous instars.

The adult carapace showed a significant increase in thickness by approximately 8 microns, compared to instar 5, indicating the largest change in size between instars. This was consistent with the rate of growth of the entire ostracod, which also showed the largest increase in body size at this stage. The carapace maintained the elemental localisation seen within instar 5, however it had significantly reduced levels of magnesium and sulphur counts compared to the early instars (Section 5.3.1, measured by XRF). The number of endocuticle lamellae and overall thickness significantly increased, as did the percentage chitin level.

Functionally, no significant difference was seen between any of the instars when it came to refractive index values. Even with all the compositional and structural changes stated above, no changes to the optical properties of *S. lerneri* appeared to occur throughout its lifetime. Although it should be noted that the RI values were measured at the surface (epicuticle) of the carapace and so no values have been measured for the deeper layers.

	Properties of the *S. lerneri* Carapace and changes over development	
Ultra-structure	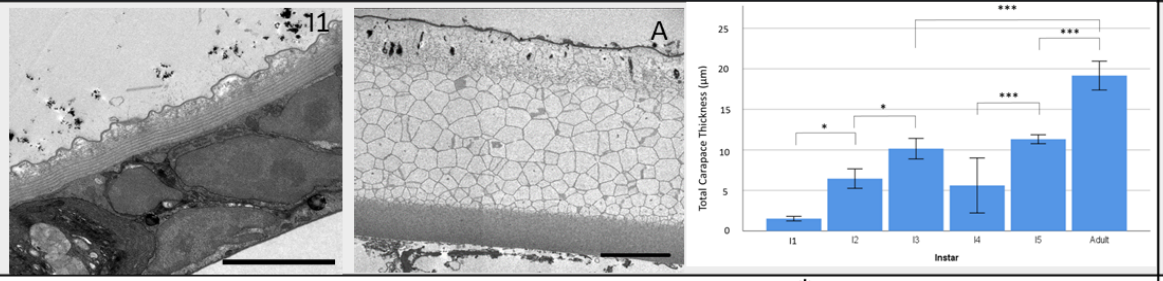	The carapace thickness increased across development, from 1.5µm to 19.2µm. The layers generally increased in proportion with overall thickness. Major deviations are seen at I1, which lacked a developed calcified endocuticle, and I4 which was thinner than was expected.
Micro-structure	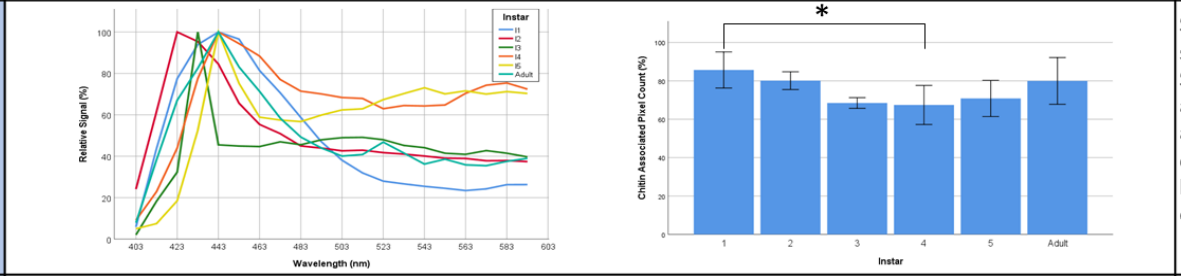	Signal expression showed a strong, statistically similar peak at SHG emission wavelengths across all instars. Chitin associated pixel analysis showed a decrease in chitin proportion from I1 and 4 but a consistent expression at all other instars (~60-80%).
Composition	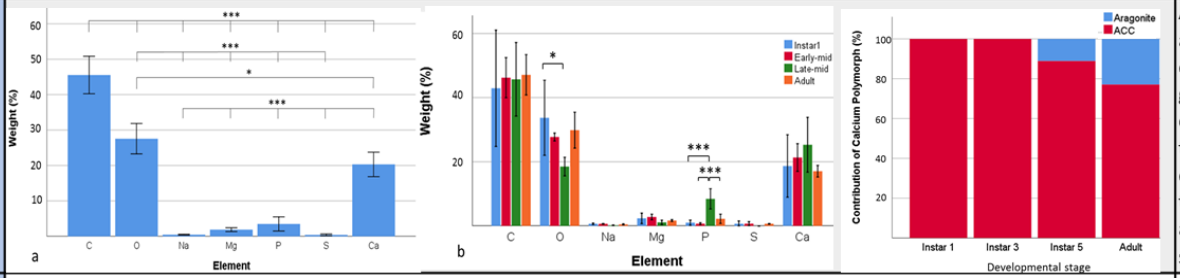	All carapaces showed higher amounts of C, O and Ca than other elements. These were generally consistent but with changes in P and O proportions in the late-mid stage. XRF showed a decreased amount of Mg and S in the adult and XANES revealed aragonite presence in the last two stages.
Optical Properties	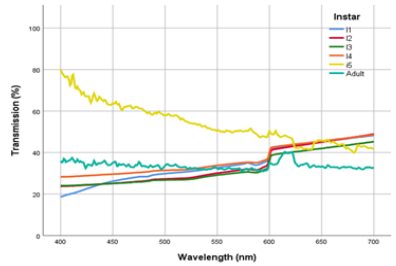 RI = 1.401-1.406 Surface transmission = 99.94-99.95%	I1-4 showed an increase in optical transmission across the wavelengths. I5 decreased in transmission in the longer wavelengths. The adult showed a consistent level of transmission at all points. RI and calculated surface transmission varied little across all stages.

Figure 7.1: Summary of various structures and properties of the *S. lerneri* carapace throughout development. Scale bars represent 5µm. * represents p<0.05, ** p<0.01, ***p<0.001

7.3 The Effect of Structure and Composition on the Physical Properties of the Carapace

Although attempts were made to test the mechanical properties of the *S. lerneri* ostracod carapace, failure of equipment meant that data could not be acquired within the timeframe of this thesis. However, through an analysis of their structural features and composition some predictions can be made. Firstly, the chitin fibrils in both the exo- and the endocuticle demonstrated the presence of twisted plywood structures (Section 3.3.1.2 and 3.3.1.4). These structures are characteristic of the crustacean carapace and have been shown to increase hardness, stiffness and potentially crack resistance (Raabe *et al*. 2005a; Raabe *et al*. 2005b). Their presence in both chitin including layers, along with the broad distribution of chitin, implies that these structures will have a widespread effect upon the carapace. The twisted plywood structures also indicate that the impressive interplay of hierarchical orders of chitin, typical of crustacean carapaces, is present in the ostracod carapace also. The synergistic effect of stiff small subunits combined into larger structures with reduced anisotropy gives a near-optimal use of the physical properties of each of the individual components available to the carapace (Nikolov *et al*. 2011). Hierarchical design and anisotropy were explained further in section 1.3.1.

The elemental composition also plays a part in the physical properties of a material and the presence of calcium carbonate polymorphs reinforces the idea that *S. lerneri* should have properties expected from a typical crustacean. Aragonite has been shown to be harder, and have a higher elastic modulus within an organic matrix than some other $CaCO_3$ polymorphs (Ren *et al*. 2013). Therefore it is possible that *S. lerneri* could exhibit even higher physical properties than expected. Aragonite has also been seen to resist and control crack propagation through its shape and orientation (Ren *et al*. 2013; Sevcik *et al*. 2018). Crack propagation is not only problematic for the carapace's protective function but also has serious negative consequences for the material's transparency. The inclusion of aragonite over other $CaCO_3$ polymorphs may impart a higher level of control over crack propagation which would minimise

the impact of damage to transparency. The presence of ACC, an isotropic material, helps remove anisotropy from within the carapace, further reinforcing the effects created by the structural chitin hierarchy (Weiner *et al*. 2003).

This analysis showed that the *S. lerneri* carapace has a high level of structural similarity to the general crustacean model and a similar composition (for instance, even differences with $CaCO_3$ polymorphs were seen). Therefore it seems highly likely that the *S. lerneri* carapace would express physical properties similar to that of the carapace of a typical, similarly sized crustacean, meaning that it would most likely maintain impressive physical properties for a transparent biological material as initially predicted.

7.4 Transparency

7.4.1 Mechanisms of transparency within the carapace

As stated within section 3.4, carapace transparency is most likely a combination of multiple different factors that work in unison, rather than a single, underlying adaptation. From an ultrastructural viewpoint, numerous transparency mechanisms can be determined, such as the potential destructive interference generated by the chitin lamellae and a thin overall carapace to reduce the impact of scattering and absorption. The ultrastructure combines with various elements within the composition of the carapace to help overcome any potential issues. The calcified endocuticle can be seen to be composed of polyhedrons of various sizes, surrounded by an organic matrix. From the elemental analysis, these polyhedrons were found to be composed mainly of calcium carbonate polymorphs. The organic matrix within this layer may impact transparency by preventing the creation of larger calcium carbonate formations. By doing so, the matrix can provide a gradient into the higher RI of the $CaCO_3$ and prevent a sharp refractive index change occurring midway through the carapace, in a similar way to the epicuticle projections. As has been

generated from the optical research, the mean refractive index of the carapace surface is 1.404, whereas the refractive index of the various calcium carbonate polymorphs is much higher, *e.g*. aragonite has a maximum RI of 1.69 and calcite 1.66 (Bragg 1924). Second, calcium carbonate crystals such as aragonite are birefringent, which would cause additional optical issues to the carapace if grouped in a large enough mass and so the maintenance of this matrix prevents this as well.

Therefore, by the placement of this organic matrix, the ultrastructure prevents two potential issues caused by the mineral composition. The chitin lamellae make up only part of the carapace ultrastructure, however, from the microstructure analysis, we can see that chitin is present consistently throughout the valve. While this consists of chitin from both the exo- and endocuticle, this still represents a substantial amount of the carapace that would be influenced by the potential destructive interference generated by the lamellae. The lack of calcite is a divergence from the majority of other ostracod or crustacean carapaces, and its absence shows a large change, even from ostracods within the same order. This means it could potentially be a direct adaptation made for maintaining transparency across the carapace. It has already been previously mentioned that the inclusion of aragonite could be due to its control and resistance to crack propagation, an issue extremely important for maintaining transparency. The high level of ACC could also have an effect, as it has been suggested to dissipate acting impact energy better, due to its more elastic properties compared to other polymorphs (Al-Sawalmih *et al*. 2008). The safer dissipation of energy would also lead to a reduced chance of cracking from the less elastic parts of the carapace. The exclusion of calcite for higher levels of ACC and aragonite could be an adaptation made to better maintain transparency after injury, at the cost of slightly lower hardness values. In addition, calcite is brittle (Huber *et al*. 2015) and its inclusion could potentially negatively impact crack resistance, so its removal could have multiple positive impacts on crack resistance.

7.4.2 Comparison with other transparent biological materials

The *Skogsbergia lerneri* carapace is structurally similar but compositionally different to the closest related examples of transparent materials. *Vargula hilgendorfii,* another myodocopid ostracod with a transparent carapace, consists of the same layers of ultrastructure, although the calcified endocuticle is less defined (Yamada 2019). The ultrastructure of the carapace covering the eye window of the ostracod *Macrocypridina castanea*, also shares similarity in the appearance and order of the layers within the carapace (Parker *et al*. 2018). While the exocuticle is more densely packed and the carapace comprises substantially more chitin lamellae, a basic homology remains. Moving away from ostracods, fully transparent amphipods have shown specific structural adaptations on the surface of the carapace (Bagge *et al*. 2016). Several species have shown monolayers of subwavelength-sized spheres on the surface of the cuticle that reduces surface reflection. No similar feature was seen on the *S. lerneri* cuticle surface, which was smooth except for pore canals, which are much too large and sparsely distributed to create the same effect.

Another previously used comparison was the corneal cuticle on non-transparent crustaceans, these show a general similarity but with distinct differences. The *Ligia oceanica* cornea shows a similar laminate endocuticle but no calcified endocuticle section is seen, the exocuticle is present, however, it is structured into lamellae much like the endocuticle (Alagboso *et al*. 2014). This exocuticle formation is closer to how the typical crustacean carapace would be, so it is interesting to note that both types of these substantially different exocuticles contribute to transparency. Specialised extensions projecting down from the epicuticle (mentioned in section 1.3.5) seen on the *L. oceanica* corneal cuticle (Alagboso *et al*. 2014) were found to be present in the *S. lerneri* carapace as well, suggesting this structural feature is a widespread adaptation and not just a hallmark from previous phylogenetics.

The major compositional difference seen between *S. lerneri* and most other ostracods is the apparent lack of calcite within the carapace. A large number of ostracods, including *V. hilgendorfii*, have been shown to include some calcite (Sohn

1969) (Xia et al. 1997), although a large amount of the literature stating the composition of the carapace is older and may be dated. As well as the ostracod carapace, the previously mentioned cornea cuticles (Alagboso *et al*. 2014) also contain calcite. It is worth noting that in both of these specific examples a large amount of amorphous calcium carbonate is also seen within the carapace, similar to *S. lerneri*, so there is some level of similarity when comparing the overall compositions.

7.5 Future work

1. One of the most exciting potential avenues for this research is the generation of a functional model for the *S. lerneri* carapace. The 3D spatial data required has already been generated in section 3.3.4 following SBFSEM . This data has also already been separated into the individual layers and each of the structural components can be identified from the images. Future testing of either optical or physical properties can be carried out on specific areas within the carapace and then assigned to these structures. This model could then simulate data for further information on carapace properties, not only for the actual carapace but also on specific sections of the carapace, which could be isolated and analysed for potential biotechnical applications.

2. The design and creation of protective transparent materials is an area in great demand for numerous different purposes (Patel *et al*. 2000; Hwang *et al*. 2003). The ability to synthetically or biomimetically create a transparent protective material such as that exhibited by *S. lerneri* is an area with exciting potential. Through the research done within this thesis, the structure and composition of the *S. lerneri* carapace has been better understood and the groundwork has been laid to expand upon the re-creation of these properties. Expansion into a synthetic re-creation of this material would require proteomic analysis to

understand how to re-create the carapace and the generation of primary cell cultures, work on which has already been started.

3. Analysis of the physical properties of the carapace would be valuable in reaffirming the implications generated from analysis of the ultrastructure. Originally this thesis was to include a section on nanoindentation within chapter 6, however, the equipment failed and had to be replaced, and this delay unfortunately prevented its inclusion. A series of nanoindentation tests would be extremely informative for revealing the hardness of the *S. lerneri* carapace and whether the inclusion of transparency came at the cost of physical properties (such as hardness). Any changes over development could be analysed and directly compared to the progression of the ultrastructure. In addition, the majority of the physical testing in crustaceans has been carried out on larger, more commonly examined examples, such as lobsters or crabs, with more complex, multi-sectioned carapaces. This makes it difficult to relate to as small and uniform a carapace as the bivalved ostracod. Analysis of hardness testing of the ostracod carapace would also be the first (to this author's knowledge) and would be impactful for any potential biotechnical applications to which the study of this carapace or that of any other ostracod could lead.

4. The absence of calcite seen within the *S. lerneri* carapace is a substantial difference from other ostracods as previously mentioned. Total calcite expression can be minimal in a lot of crustaceans and the XANES measurements carried out in chapter 5 only used a central line scan, so some ambiguity remains. Further XANES analysis, using raster scans which fully encompass the valve, can confirm this apparent lack of calcite.

5. Additional spectrophotometric research would be an area of immediate future analysis to reinforce the results generated in this thesis. As previously stated, the major problems were caused by the sample holders created to adapt the equipment for carapace analysis. The issues caused by these holders have been identified and could be remade to remove these issues and generate more valid

data. Alternatively, the use of a spectrophotometer outfitted to analyse solid materials would remove the need for sample holders to be created. With more practical optical data, the transparency values become more reliable.

6. The surface of the carapace is important in maintaining transparency and pore canal distribution could have a significant effect on these properties, therefore *S. lerneri* most likely have adapted to overcome this issue. Further examination of pore canal number or distribution on *S. lerneri* compared to non-transparent ostracods would lead to an understanding of how *S. lerneri* overcomes the problem of essential pore canals. This would give insight into how transparent biological materials can maintain essential carapace upkeep without affecting transparency.

References

Abass, A. et al. 2017. SAXS4COLL: an integrated software tool for analysing fibrous collagen-based tissues. *J Appl Crystallogr* 50(Pt 4), pp. 1235-1240. doi: 10.1107/S1600576717007877

Abe, K. and Vannier, J. 1995. Functional-Morphology and Significance of the Circulatory-System of Ostracoda, Exemplified by Vargula-Hilgendorfii (Myodocopida). *Marine Biology* 124(1), pp. 51-58. doi: Doi 10.1007/Bf00349146

Addadi, L. et al. 2003. Taking advantage of disorder: Amorphous calcium carbonate and its roles in biomineralization. *Advanced Materials* 15(12), pp. 959-970. doi: 10.1002/adma.200300381

Aizenberg, J. et al. 2003. Coexistence of amorphous and crystalline calcium carbonate in skeletal tissues. *Connective Tissue Research* 44, pp. 20-25. doi: 10.1080/03008200390152034

Al-Sawalmih, A. et al. 2008. Microtexture and Chitin/Calcite Orientation Relationship in the Mineralized Exoskeleton of the American Lobster. *Advanced Functional Materials* 18(20), pp. 3307-3314. doi: 10.1002/adfm.200800520

Alagboso, F. I. et al. 2014. Ultrastructure and mineral composition of the cornea cuticle in the compound eyes of a supralittoral and a marine isopod. *J Struct Biol* 187(2), pp. 158-173. doi: 10.1016/j.jsb.2014.06.002

Amini, S. and Miserez, A. 2013. Wear and abrasion resistance selection maps of biological materials. *Acta Biomater* 9(8), pp. 7895-7907. doi: 10.1016/j.actbio.2013.04.042

Andersen, S. O. 1964. Cross-Links in Resilin Identified as Dityrosine + Trityrosine. *Biochimica Et Biophysica Acta* 93(1), pp. 213-215. doi: Doi 10.1016/0304-4165(64)90289-2

Andersson, A. and Nilsson, D.-E. 1981. Fine Structure and Optical Properties of an Ostracode (Crustacea) Nauplius Eye. *Protoplasma* 107, pp. 361-374.

Ashby, M. F. and Jones, D. R. H. 2012. *Engineering materials 1 : an introduction to properties, applications, and design*. 4th ed. Amsterdam ; Boston: Butterworth-Heinemann.

Austin, R. W. and Halikas, G. 1976. The index of refraction of seawater. In: Agency, D.A.R.P. ed. Scripps Institution of Oceanography.

Bagge, L. E. et al. 2016. Nanostructures and Monolayers of Spheres Reduce Surface Reflections in Hyperiid Amphipods. *Current Biology* 26(22), pp. 3071-3076. doi: 10.1016/j.cub.2016.09.033

Bang, B. H. and Bang, F. B. 1957. Graphic reconstruction of the third dimension from serial electron microphotographs. *J Ultrastruct Res* 1(2), pp. 138-139. doi: 10.1016/s0022-5320(57)80002-1

Bastacky, J. et al. 1985. Quantitation of Shrinkage During Preparation for Scanning Electron Microscopy: Human Lung *SCANNING* 7, pp. 134-140.

Bate, R., H. and East, B., A. 1972. The Structure of the ostracode carapace. *Lethaia* 5, pp. 177-194.

Baur, P. S. and Stacey, T. R. 1977. Use of Pipes Buffer in Fixation of Mammalian and Marine Tissues for Electron-Microscopy. *Journal of Microscopy* 109(Apr), pp. 315-327. doi: DOI 10.1111/j.1365-2818.1977.tb01145.x

Becker, A. et al. 2005. The mineral phase in the cuticles of two species of Crustacea consists of magnesium calcite, amorphous calcium carbonate, and amorphous calcium phosphate. *Dalton Transactions* (10), pp. 1814-1820. doi: 10.1039/b412062k

Berndt, C. et al. 2019. Intraspecific Length Variation and Shell Thickness of the Ostracod Cyprideis torosa (Jones, 1850) as a Potential Tool for Palaeosalinity Characterization. *geosciences* 9(83),

Berner, R. A. 1975. Role of Magnesium in Crystal-Growth of Calcite and Aragonite from Sea-Water. *Geochimica Et Cosmochimica Acta* 39(4), pp. 489-&. doi: Doi 10.1016/0016-7037(75)90102-7

Birch-Andersen, A. 1955. Reconstruction of the nuclear sites of Salmonella typhimurium from electron micrographs of serial sections. *J Gen Microbiol* 13(2), pp. 327-329. doi: 10.1099/00221287-13-2-327

Board, W. E. 2017. World Register of Marine Species. Available from http://www.marinespecies.org at VLIZ.

Born, M. and Wolf, E. 1980. *Principles of optics : electromagnetic theory of propagation, interference and diffraction of light*. 6th ed. Oxford ; New York: Pergamon Press.

Bouligand, Y. 1972. Twisted fibrous arrangements in biological materials and cholesteric mesophases. *Tissue Cell* 4(2), pp. 189-217.

Boyd, R. W. 2008. *Nonlinear optics*. 3rd ed. Amsterdam ; Boston: Academic Press.

Bragg, W. L. 1924. The refractive indices of calcite and aragonite. *Proc. R. Soc. Lond. A.* 105, pp. 370-386. doi: http://doi.org/10.1098/rspa.1924.0026

Brinza, L. et al. 2013. Incorporation of strontium in earthworm-secreted calcium carbonate granules produced in strontium-amended and strontium-bearing soil. *Geochimica Et Cosmochimica Acta* 113, pp. 21-37. doi: 10.1016/j.gca.2013.03.011

Burrows, M. et al. 2008. Resilin and chitinous cuticle form a composite structure for energy storage in jumping by froghopper insects. *BMC Biol* 6, pp. 41-57. doi: 10.1186/1741-7007-6-41

Bursell, E. 1955. The Transpiration of Terrestrial Isopods. *Journal of Experimental Biology* 32(2), pp. 238-255.

Cadot, H. M. and Kaesler, R. L. 1977. *Magnesium content of calcite in carapaces of benthic marine Ostracoda*. Lawrence: University of Kansas Paleontological Institute, University of Kansas.

Campagnola, P. J. and Dong, C. Y. 2011. Second harmonic generation microscopy: principles and applications to disease diagnosis. *Laser & Photonics Reviews* 5(1), pp. 13-26. doi: 10.1002/lpor.200910024

Campagnola, P. J. and Loew, L. M. 2003. Second-harmonic imaging microscopy for visualizing biomolecular arrays in cells, tissues and organisms. *Nature Biotechnology* 21(11), pp. 1356-1360. doi: 10.1038/nbt894

Campagnola, P. J. et al. 1999. High-resolution nonlinear optical imaging of live cells by second harmonic generation. *Biophysical Journal* 77(6), pp. 3341-3349. doi: Doi 10.1016/S0006-3495(99)77165-1

Caporaletti, M. 2011. Ostracods and stable isotopes: proxies for palaeoenvironmental reconstructions. *Joannea Geol Palaontol* 11, pp. 345-359.

Carlstrom, D. 1957. The crystal structure of alpha-chitin (poly-N-acetyl-D-glucosamine). *J Biophys Biochem Cytol* 3(5), pp. 669-683.

Caveney, S. 1969. Muscle attachment related to cuticle architecture in Apterygota. *J Cell Sci* 4(2), pp. 541-559.

Chai, H. et al. 2009. Remarkable resilience of teeth. *Proc Natl Acad Sci U S A* 106(18), pp. 7289-7293. doi: 10.1073/pnas.0902466106

Chen, B. et al. 2014. Hole-pin joining structure with fiber-round-hole distribution of lobster cuticle and biomimetic study. *J Mech Behav Biomed Mater* 40, pp. 161-167. doi: 10.1016/j.jmbbm.2014.09.001

Chen, H. Y. et al. 2012. Advances in functional X-ray imaging techniques and contrast agents. *Physical Chemistry Chemical Physics* 14(39), pp. 13469-13486. doi: 10.1039/c2cp41858d

Chen, P. Y. et al. 2008. Structure and mechanical properties of crab exoskeletons. *Acta Biomater* 4(3), pp. 587-596. doi: 10.1016/j.actbio.2007.12.010

Cheng, L. et al. 2008. Image analyses of two crustacean exoskeletons and implications of the exoskeletal microstructure on the mechanical behavior. *Journal of Materials Research* 23(11), pp. 2854-2872. doi: 10.1557/Jmr.2008.0375

Cheong, W. et al. 1990. A review of the Optical Properties of Biological Tissues. *IEEE Journal of Quantum Electronics* 26(12), pp. 2166-2185.

Chiang, J. Y. et al. 2011. Underwater Image Enhancement: Using Wavelength Compensation and Image Dehazing (WCID). *Advanced Concepts for Intelligent Vision Systems* 6915, pp. 372-383.

Chien, C. H. et al. 2011. Label-free imaging of Drosophila in vivo by coherent anti-Stokes Raman scattering and two-photon excitation autofluorescence microscopy. *Journal of Biomedical Optics* 16(1), pp. 1-7. doi: Artn 016012

10.1117/1.3528642

Chua, C. K. et al. 2017. *Standards, quality control, and measurement sciences in 3D printing and additive manufacturing*. London ; San Diego, CA: Academic Press, an imprint of Elsevier.

Claes, J. M. et al. 2014. Iso-luminance counterillumination drove bioluminescent shark radiation. *Sci Rep* 4, p. 4328. doi: 10.1038/srep04328

Clark, B. A. and Carney, L. G. 1971. Refractive index and reflectance of the anterior surface of the cornea. *Am J Optom Arch Am Acad Optom* 48(4), pp. 333-343.

Clarkson, J. R. et al. 1992. Role of Metastable Phases in the Spontaneous Precipitation of Calcium-Carbonate. *Journal of the Chemical Society-Faraday Transactions* 88(2), pp. 243-249. doi: DOI 10.1039/ft9928800243

Cohen, A. 1983. Rearing and postembryonic development of the myodocopid osracode *Skogsbergia Lerneri* from coral reefs of belize and the bahamas. *Journal of Crustacean Biology* 3(2), pp. 235-256.

Cronin, T. W. 2016. Camouflage: Being Invisible in the Open Ocean. *Current Biology* 26(22), pp. 1179-1181. doi: https://doi.org/10.1016/j.cub.2016.09.056

Das, S. et al. 2016. Utilization of Chitinaceous Wastes for the Production of Chitinase. *Adv Food Nutr Res* 78, pp. 27-46. doi: 10.1016/bs.afnr.2016.04.001

De Deckker, P. 2017. Trace elemental distribution in ostracod valves. From solution ICPMS and laser ablation ICPMS to microprobe mapping: a tribute to Rick Forester. *Hydrobiologia* 786(1), pp. 23-39. doi: 10.1007/s10750-015-2534-4

De Deckker, P. and Martens, K. 2013. Extraordinary morphological changes in valve morphology during the ontogeny of several species of the Australian ostracod genus Bennelongia (Crustacea, Ostracoda). *European Journal of Taxonomy* 36, pp. 1-37. doi: 10.5852/ejt.2013.36

Dennell, R. 1978. Cuticle of Hoplocarid Crustacean Squilla-Desmaresti Risso. *Zoological Journal of the Linnean Society* 62(4), pp. 309-316. doi: DOI 10.1111/j.1096-3642.1978.tb01042.x

Denton, E. J. 1970. Review lecture: on the organization of reflecting surfaces in some marine animals. *Philos Trans R Soc Lond B Biol Sci* 258(824), pp. 285-313. doi: 10.1098/rstb.1970.0037

Drach, P. and Tchernigovtzeff. 1969. Sur la methode de determination des stades d'intermue et son application generale aux crustaces. *Biologie Marine* 18(3A), pp. 595-610.

Fabritius, H. et al. 2009. Influence of Structural Principles on the Mechanics of a Biological Fiber-Based Composite Material with Hierarchical Organization: The Exoskeleton of the Lobster Homarus americanus. *Adv Mater* 21, pp. 391-400. doi: 10.1002/adma.200801219

Fabritius, H. O. et al. 2012. Correlation of structure, composition and local mechanical properties in the dorsal carapace of the edible crab Cancer pagurus. *Zeitschrift Fur Kristallographie* 227(11), pp. 766-776. doi: 10.1524/zkri.2012.1532

Fabritius, H. O. et al. 2016a. Functional adaptation of crustacean exoskeletal elements through structural and compositional diversity: a combined experimental and theoretical study. *Bioinspir Biomim* 11(5), p. 055006. doi: 10.1088/1748-3190/11/5/055006

Fabritius, H. O. et al. 2016b. Functional adaptation of crustacean exoskeletal elements through structural and compositional diversity: a combined experimental and theoretical study. *Bioinspiration & Biomimetics* 11(5), pp. 1-25. doi: Artn 055006

10.1088/1748-3190/11/5/055006

Fox, M. 2010. *Optical properties of solids*. 2nd ed. Oxford ; New York: Oxford University Press.

Gerrish, G. A. and Morin, J. G. 2008. Life Cycle of a Bioluminescent Marine Ostracode, Vargula Annecohenae (Myodocopida: Cypridinidae). *Journal of Crustacean Biology* 28(4), pp. 669-674. doi: Doi 10.1651/07-2934.1

Gharagozlouvanginneken, I. D. and Bouligand, Y. 1975. Studies on Fine-Structure of Cuticle of Porcellidium, Crustacea-Copepoda. *Cell and Tissue Research* 159(3), pp. 399-412.

Giannini, C. et al. 2016. X-ray Diffraction: A Powerful Technique for the Multiple-Length-Scale Structural Analysis of Nanomaterials. *Crystals* 6(8), doi: UNSP 87

10.3390/cryst6080087

Glotzner, J. and Ziegler, A. 2000. Morphometric analysis of the calcium-transporting sternal epithelial cells of the terrestrial isopods Ligia oceanica, Ligidium hypnorum, and Porcellio scaber during molt. *Arthropod Struct Dev* 29(3), pp. 241-257.

Gluenz, E. et al. 2015. Scanning and three-dimensional electron microscopy methods for the study of Trypanosoma brucei and Leishmania mexicana flagella. *Methods in Cilia & Flagella* 127, pp. 509-542. doi: 10.1016/bs.mcb.2014.12.011

Goetz, A. J. et al. 2014. Tailored order: The mesocrystalline nature of sea urchin teeth. *Acta Biomaterialia* 10(9), pp. 3885-3898. doi: 10.1016/j.actbio.2014.06.012

Gomez-Tamayo, J. C. et al. 2016. Analysis of the interactions of sulfur-containing amino acids in membrane proteins. *Protein Sci* 25(8), pp. 1517-1524. doi: 10.1002/pro.2955

Goodwin, T. W. 1954. Some observations on carotenoid synthesis by the alga Chlorella vulgaris. *Experientia* 10(5), pp. 213-214. doi: 10.1007/bf02159276

Göppert-Mayer, M. 1931. Über Elementarakete mit zwei Quantensprüngen (Elementary Acts with Two Quantum Jumps). *Ann. Phys (Leipzig)* 9, pp. 273-294.

Green, J. 1959. Pigmentation of an Ostracod, *Heterocypris Incongruens*. *Journal of Experimental Biology* 36, pp. 572-582.

Green, J. P. and Neff, M. R. 1972. A survey of the fine structure of the integument of the fiddler crab. *Tissue Cell* 4(1), pp. 137-171.

Greenaway, P. 1985. Calcium balance and moulting in the crustacea. *Biol. Rev* 60, pp. 425-454.

Gualda, E. J. et al. 2007. In vivo imaging of anatomical features of the nematode Caenorhabditis elegans using non-linear (TPEF-SHG-THG) microscopy. *Confocal, Multiphoton, and Nonlinear Microscopic Imaging Iii* 6630,

Gupta, P. et al. 2019. Solving Fresnel equation for refractive index using reflected optical power obtained from Bessel beam interferometry. *Rev Sci Instrum* 90(1), p. 015110. doi: 10.1063/1.5043240

Habraken, W. J. et al. 2015. Layered growth of crayfish gastrolith: about the stability of amorphous calcium carbonate and role of additives. *J Struct Biol* 189(1), pp. 28-36. doi: 10.1016/j.jsb.2014.11.003

Hackman, R. H. 1987. Chitin and the fine structure of cuticles. In: Wright, J.E.a.R., A. ed. *Chitin and Benzoylphenyl Ureas*

Springer, pp. 1-32.

Hackman, R. H. and Goldberg, M. 1974. Light-Scattering and Infrared-Spectrophotometric Studies of Chitin and Chitin Derivatives. *Carbohydrate Research* 38(1), pp. 35-45. doi: Doi 10.1016/S0008-6215(00)82336-8

He, M. Y. and Hutchinson, J. W. 1989. Crack Deflection at an Interface between Dissimilar Elastic-Materials. *International Journal of Solids and Structures* 25(9), pp. 1053-1067. doi: Doi 10.1016/0020-7683(89)90021-8

Hegdahl, T. et al. 1977a. Structure and Mineralization of Carapace of Crab (Cancer-Pagurus L) .2. Exocuticle. *Zoologica Scripta* 6(2), pp. 101-105.

Hegdahl, T. et al. 1977b. Structure and Mineralization of Carapace of Crab (Cancer-Pagurus L) .3. Epicuticle. *Zoologica Scripta* 6(3), pp. 215-220.

Hegdahl, T. et al. 1977c. Structure and Mineralization of Carapace of Crab (Cancer-Pagurus L) .1. Endocuticle. *Zoologica Scripta* 6(2), pp. 89-99.

Henderson, G. S. et al. 2014. X-ray Absorption Near-Edge Structure (XANES) Spectroscopy. *Spectroscopic Methods in Mineralology and Materials Sciences* 78, pp. 75-+. doi: 10.2138/rmg.2014.78.3

Hepburn, H. R. et al. 1975. Mechanical-Properties of a Crab Shell. *Comparative Biochemistry and Physiology* 50(Na3), pp. 551-&. doi: Doi 10.1016/0300-9629(75)90313-8

Hild, S. et al. 2009. Ultrastructure and mineral distribution in the tergal cuticle of the terrestrial isopod Titanethes albus. Adaptations to a karst cave biotope. *J Struct Biol* 168(3), pp. 426-436. doi: 10.1016/j.jsb.2009.07.017

Holmes, J. and Chivas, A. R. 2002. *The ostracoda : applications in Quaternary research*. Washington, DC: American Geophysical Union.

Horst, M. N. and Freeman, J. A. 1993. *The Crustacean integument : morphology and biochemistry*. Boca Raton: CRC Press.

Huber, J. et al. 2015. Functionalization of biomineral reinforcement in crustacean cuticle: Calcite orientation in the partes incisivae of the mandibles of Porcellio scaber and the supralittoral species Tylos europaeus (Oniscidea, Isopoda). *Journal of Structural Biology* 190(2), pp. 173-191. doi: 10.1016/j.jsb.2015.03.007

Huvard, A. L. 1993. Analysis of Visual Pigment Absorbency and Luminescence Emission-Spectra in Marine Ostracodes (Crustacea, Ostracoda). *Comparative Biochemistry and Physiology a-Physiology* 104(2), pp. 333-338. doi: Doi 10.1016/0300-9629(93)90325-X

Hwang, D. K. et al. 2003. Scratch Resistant and Transparent UV-Protective Coating on Polycarbonate. *Journal of Sol-Gel Science and Technology volume* 26, pp. 783-787. doi: https://doi.org/10.1023/A:102077492777

Jackson, A. P. et al. 1988. The Mechanical Design of Nacre. *Proceedings of the Royal Society Series B-Biological Sciences* 234(1277), pp. 415-+. doi: DOI 10.1098/rspb.1988.0056

Jacques, S. L. 2013. Optical properties of biological tissues: a review. *Phys Med Biol* 58(11), pp. R37-61. doi: 10.1088/0031-9155/58/11/R37

Johnsen, S. 2001. Hidden in plain sight: The ecology and physiology of organismal transparency. *Biological Bulletin* 201(3), pp. 301-318. doi: Doi 10.2307/1543609

Jorgensen, N. 1970. Ultrastructure of some ostracods. *Bull. Geol. Soc. Denmark* 20, pp. 79-92.

Joy, D. C. 1991. The Theory and Practice of High-Resolution Scanning Electron-Microscopy. *Ultramicroscopy* 37(1-4), pp. 216-233. doi: Doi 10.1016/0304-3991(91)90020-7

Kanazawa, A. et al. 1976. Variation of Lipids and Cholesterol Contents in Tissues of Prawn, Penaeus-Japonicus, during Molting Cycle. *Bulletin of the Japanese Society of Scientific Fisheries* 42(9), pp. 1003-1007.

Kannupandi, T. 1976. Occurrence of Resilin and Its Significance in Cuticle of Pennella-Elegans, a Copepod Parasite. *Acta Histochemica* 56(1), pp. 73-79. doi: Doi 10.1016/S0065-1281(76)80028-1

Karnovsky, M. J. 1965. A Formaldehyde-Glutaraldehyde Fixative of High Osmolality for Use in Electron Microscopy. *Journal of Cell Biology* 27(2), pp. A137-+.

Kesling, R. V. 1951a. *The morphology of ostracod molt stages*. Urbana,: University of Illinois Press.

Kesling, R. V. 1951b. *Terminology of ostracod carapaces*. Ann Arbor,: University of Michigan Press.

Keyser, D. 2005. Histological peculiarities of the noding process in Cyprideis torosa (Jones) (Crustacea, Ostracoda). *Hydrobiologia* 538, pp. 95-106. doi: 10.1007/s10750-004-4940-x

Knupp, C. et al. 2009. The architecture of the cornea and structural basis of its transparency. *Adv Protein Chem Struct Biol* 78, pp. 25-49. doi: 10.1016/S1876-1623(08)78002-7

Kornicker, L. S. 1958. Ecology and taxonomy of recent marine ostracodes in the Bimini area, Great Bahama Bank. *Publications of the Institute of Marine Science, University of Texas* 5, pp. 194-300.

Kornicker, L. S. et al. 2002. *Ostracoda (Myodocopa) from Bahamian blue holes*. Washington, D.C.: Smithsonian Institution Press.

Kumar, M. N. V. R. 2000. A review of chitin and chitosan applications. *Reactive & Functional Polymers* 46(1), pp. 1-27.

Lee, S. W. et al. 2016. Behavior and characteristics of amorphous calcium carbonate and calcite using CaCO3 film synthesis. *Materials & Design* 112, pp. 367-373. doi: 10.1016/j.matdes.2016.09.099

Lindholm, M. and Hobæk, A. 2014. Stripemuslingkreps Cypridopsis vidua. Norwgian Institute for Water Research.

Long, F. H. et al. 1987. Measurement of the optical and thermal properties of biliary calculi using pulsed photothermal radiometry. *Lasers Surg Med* 7(6), pp. 461-466. doi: 10.1002/lsm.1900070604

Luquet, G. 2012. Biomineralizations: insights and prospects from crustaceans. *Zookeys* (176), pp. 103-121. doi: 10.3897/zookeys.176.2318

Maddocks, R. F. 1990. *Living and fossil Macrocyprididae (Ostracoda)*. Lawrence, Kan.: University of Kansas Paleontological Institute.

Martens, K. and Horne, D. J. 2016. Collecting and Processing Living, Non-Marine Ostracods. *Journal of Crustacean Biology* 36(6), pp. 849-854. doi: 10.1163/1937240x-00002488

Maurice, D. M. 1957. The Structure and Transparency of the Cornea. *Journal of Physiology-London* 136(2), pp. 263-&. doi: DOI 10.1113/jphysiol.1957.sp005758

Mertz, J. 2004. Nonlinear microscopy: new techniques and applications. *Current Opinion in Neurobiology* 14(5), pp. 610-616. doi: 10.1016/j.conb.2004.08.013

Michels, J. et al. 2016. Functional diversity of resilin in Arthropoda. *Beilstein J Nanotechnol* 7, pp. 1241-1259. doi: 10.3762/bjnano.7.115

Minke, R. and Blackwell, J. 1978. Structure of Alpha-Chitin. *Journal of Molecular Biology* 120(2), pp. 167-181. doi: Doi 10.1016/0022-2836(78)90063-3

Morishita, T. et al. 2007. Magnesium and strontium distributions within valves of a recent marine ostracode, Neonesidea oligodentata: Implications for paleoenvironmental reconstructions. *Geochemistry Geophysics Geosystems* 8, doi: Artn Q07009

10.1029/2007gc001585

Mosselmans, J. F. W. et al. 2009. I18-the microfocus spectroscopy beamline at the Diamond Light Source. *Journal of Synchrotron Radiation* 16, pp. 818-824. doi: 10.1107/S0909049509032282

Mrak, P. et al. 2015. Formation of the hindgut cuticular lining during embryonic development of Porcellioscaber (Crustacea, Isopoda). *Zookeys* (515), pp. 93-109. doi: 10.3897/zookeys.515.9468

Namiotko, T. et al. 2011. Soft body morphology, dissection and slide-preparation of Ostracoda: a primer. *Joannea Geol Palaontol* 11, p. 327.

Needham, A. E. 1949. Formation of Melanin in Regenerating Limbs of a Crustacean. *Nature* 164(4173), pp. 717-718. doi: DOI 10.1038/164717b0

Neville, A. C. 1969. Cuticle Ultrastructure in Relation to the Whole Insect. *Journal of Experimental Zoology* 13, pp. 17-39.

Neville, A. C. 1975. *Biology of the Arthropod Cuticle*. Zoophysiology and Ecology: Springer - Verlag.

Nie, B. et al. 2012. Multimodal microscopy with sub-30 fs Yb fiber laser oscillator. *Biomedical Optics Express* 3(7), pp. 1750-1756. doi: Doi 10.1364/Boe.3.001750

Nikolov, S. et al. 2011. Robustness and optimal use of design principles of arthropod exoskeletons studied by ab initio-based multiscale simulations. *J Mech Behav Biomed Mater* 4(2), pp. 129-145. doi: 10.1016/j.jmbbm.2010.09.015

Nikolov, S. et al. 2010. Revealing the design principles of high-performance biological composites using ab initio and multiscale simulations: the example of lobster cuticle. *Adv Mater* 22(4), pp. 519-526. doi: 10.1002/adma.200902019

Nobel, P. S. 2005. *Physicochemical and environmental plant physiology*. 3rd ed. Amsterdam ; Boston: Elsevier Academic Press.

Oakley, T. H. and Cunningham, C. W. 2002. Molecular phylogenetic evidence for the independent evolutionary origin of an arthropod compound eye. *Proc Natl Acad Sci U S A* 99(3), pp. 1426-1430. doi: 10.1073/pnas.032483599

Oakley, T. H. and Huber, D. R. 2004. Differential expression of duplicated opsin genes in two eyetypes of ostracod crustaceans. *J Mol Evol* 59(2), pp. 239-249. doi: 10.1007/s00239-004-2618-7

Oheim, M. et al. 2006. Principles of two-photon excitation fluorescence microscopy and other nonlinear imaging approaches. *Advanced Drug Delivery Reviews* 58(7), pp. 788-808. doi: 10.1016/j.addr.2006.07.005

Okada, Y. 1982. Structure and Cuticle Formation of the Reticulated Carapace of the Ostracode Bicornucythere-Bisanensis. *Lethaia* 15(1), pp. 85-101. doi: DOI 10.1111/j.1502-3931.1982.tb01124.x

Parfitt, G. J. et al. 2012. A novel immunofluorescent computed tomography (ICT) method to localise and quantify multiple antigens in large tissue volumes at high resolution. *PLoS One* 7(12), p. e53245. doi: 10.1371/journal.pone.0053245

Parker, A. R. et al. 2018. Transparenncy in the eye region of an ostracod carapce *(Macrocypridina castanea, Myodocopida)*. *Philosophical Transaction of The Royal Society A* 377(2138),

Patel, J. P. et al. 2000. Transparent ceramics for armor and EM window applications. *Inorganic Optical Materials* 4102, doi: https://doi.org/10.1117/12.405270

Patterson, M. S. et al. 1989. Time resolved reflectance and transmittance for the non-invasive measurement of tissue optical properties. *Appl Opt* 28(12), pp. 2331-2336. doi: 10.1364/AO.28.002331

Pereira, J. D. et al. 2017. Carapace ontogeny of the bromeliad dwelling ostracod Elpidium bromeliarum Muller, 1880 (Crustacea: Ostracoda). *Journal of Natural History* 51(35-36), pp. 2185-2196. doi: 10.1080/00222933.2017.1360529

Pfeiffer, F. 2018. X-ray ptychography. *Nature Photonics* 12(1), pp. 9-17. doi: 10.1038/s41566-017-0072-5

Pryor, M. G. M. 1940. On the Hardening of the Cuticle of Insects. *Royal Society* 128(852), pp. 393-407.

Raabe, D. et al. 2005a. Discovery of a honeycomb structure in the twisted plywood patterns of fibrous biological nanocomposite tissue. *Journal of Crystal Growth* 283(1-2), pp. 1-7. doi: 10.1016/j.jcrysgro.2005.05.077

Raabe, D. et al. 2005b. The crustacean exoskeleton as an example of a structurally and mechanically graded biological nanocomposite material. *Acta Materialia* 53(15), pp. 4281-4292. doi: 10.1016/j.actamat.2005.05.027

Rabasovic, M. D. et al. 2015. Nonlinear microscopy of chitin and chitinous structures: a case study of two cave-dwelling insects. *Journal of Biomedical Optics* 20(1), doi: Artn 016010

10.1117/1.Jbo.20.1.016010

Rassolov, V. A. et al. 2001. The definition of core electrons. *Chemical Physics Letters* 350(5-6), pp. 573-576. doi: Doi 10.1016/S0009-2614(01)01345-8

Raz, S. et al. 2000. Formation of high-magnesian calcites via an amorphous precursor phase: Possible biological implications. *Advanced Materials* 12(1), pp. 38-+. doi: Doi 10.1002/(Sici)1521-4095(200001)12:1<38::Aid-Adma38>3.3.Co;2-9

Reddy, M. M. 1977. Crystallization of Calcium-Carbonate in Presence of Trace Concentrations of Phosphorus-Containing Anions .1. Inhibition by Phosphate and Glycerophosphate Ions at Ph 8.8 and 25-Degrees-C. *Journal of Crystal Growth* 41(2), pp. 287-295. doi: Doi 10.1016/0022-0248(77)90057-4

Rehr, J. J. and Albers, R. C. 2000. Theoretical approaches to x-ray absorption fine structure. *Reviews of Modern Physics* 72(3), pp. 621-654. doi: DOI 10.1103/RevModPhys.72.621

Rehr, J. J. and Ankudinov, A. L. 2005. Progress in the theory and interpretation of XANES. *Coordination Chemistry Reviews* 249(1-2), pp. 131-140. doi: 10.1016/j.ccr.2004.02.014

Reinhardt, K. et al. 2017. Autofluorescence lifetime variation in the cuticle of the bedbug Cimex lectularius. *Arthropod Structure & Development* 46(1), pp. 56-62. doi: 10.1016/j.asd.2016.11.009

Ren, D. N. et al. 2013. Comparative study of carp otolith hardness: Lapillus and asteriscus. *Materials Science & Engineering C-Materials for Biological Applications* 33(4), pp. 1876-1881. doi: 10.1016/j.msec.2012.10.015

Rheims, J. et al. 1997. Refractive-index measurements in the near-IR using an Abbe refractometer. *Measurement Science and Technology* 8, pp. 601-605.

Roca, J. R. et al. 1993. Adaptive Responses in Cypridopsis-Vidua (Crustacea, Ostracoda) to Food and Shelter Offered by a Macrophyte (Chara-Fragilis). *Hydrobiologia* 262(2), pp. 127-131. doi: Doi 10.1007/Bf00007513

Rodenburg, J. and Maiden, A. 2019. Ptychography. In: Hawkes, P.W. and Spence, J.C.H. eds. *Springer Handbook of Microscopy*. Cham: Springer International Publishing, pp. 2-2.

Romano, P. et al. 2007. The exoskeleton of the lobster Homarus americanus as an example of a smart anisotropic biological material. *Acta Biomater* 3(3), pp. 301-309. doi: 10.1016/j.actbio.2006.10.003

Rosenfeld, A. 1979. Structure and Secretion of the Carapace in Some Living Ostracodes. *Lethaia* 12(4), pp. 353-360. doi: DOI 10.1111/j.1502-3931.1979.tb01021.x

Ruangchai, S. et al. 2013. The architecture of the joint head cuticle and its transition to the arthrodial membrane in the terrestrial crustacean Porcellio scaber. *J Struct Biol* 182(1), pp. 22-35. doi: 10.1016/j.jsb.2013.01.009

Rudall, K. M. and Kenchington, W. 1973. The Chitin System. *Biological Reviews* 48(4), pp. 597-633. doi: 10.1111/j.1469-185X.1973.tb01570.x

Sachs, C. et al. 2006. Hardness and elastic properties of dehydrated cuticle from the lobster Homarus americanus obtained by nanoindentation. *Journal of Materials Research* 21(8), pp. 1987-1995. doi: 10.1557/Jmr.2006.0241

Sackey, S. S. et al. 2015. Spectroscopic Study of UV Transparency of Some Materials. *Environment and Pollution* 4, pp. 1-17.

Schechner, Y. Y. and Karpel, N. 2004. Clear underwater vision. *Proceedings of the 2004 Ieee Computer Society Conference on Computer Vision and Pattern Recognition, Vol 1*, pp. 536-543.

Scimeca, M. et al. 2018. Energy Dispersive X-ray (EDX) microanalysis: A powerful tool in biomedical research and diagnosis. *European Journal of Histochemistry* 62(1), pp. 88-97. doi: 10.4081/ejh.2018.2841

Seidl, B. et al. 2011. Ultrastructure and mineral distribution in the tergite cuticle of the beach isopod Tylos europaeus Arcangeli, 1938. *J Struct Biol* 174(3), pp. 512-526. doi: 10.1016/j.jsb.2011.03.005

Seidl, B. H. M. et al. 2012. Calcite distribution and orientation in the tergite exocuticle of the isopods Porcellio scaber and Armadillidium vulgare (Oniscidea, Crustacea) - a combined FE-SEM, polarized SC mu-RSI and EBSD study. *Zeitschrift Fur Kristallographie* 227(11), pp. 777-792. doi: 10.1524/zkri.2012.1567

Serrano, C. V. et al. 2016. Ordering of protein and water molecules at their interfaces with chitin nano-crystals. *Journal of Structural Biology* 193(2), pp. 124-131. doi: 10.1016/j.jsb.2015.12.004

Sevcik, R. et al. 2018. Physical and nanomechanical properties of the synthetic anhydrous crystalline CaCO3 polymorphs: vaterite, aragonite and calcite. *Journal of Materials Science* 53(6), pp. 4022-4033. doi: 10.1007/s10853-017-1884-x

Skoog, D. A. et al. 2007. *Principles of instrumental analysis*. 6th ed. Belmont, CA: Thomson Brooks/Cole.

Smith, T. and Bate, R., H. 1983. The shell of the ostracod Halocypris infzata (Dana, 1849) examined by the ion beam etch technique. *J. micropalaeontol* 2, pp. 105-110.

Sohn, I. G. a. K., L.S. 1969. Significance of calcareous nodules in myodocopid ostracod carapaces. *The taxonomy, morphology and ecology of recent ostracoda*, pp. 99-108.

Sohn, I. G. a. K., L.S. 1988. Ultrastructure of Myodocopid Shells (Ostracoda). *Developments in Palaeontology and Stratigraphy* 11, pp. 243-253. doi: 10.1016/S0920-5446(08)70187-0

Speiser, D. I. et al. 2011. A Chiton Uses Aragonite Lenses to Form Images. *Current Biology* 21(8), pp. 665-670. doi: 10.1016/j.cub.2011.03.033

Stempfle, P. and Brendle, M. 2006. Tribological behaviour of nacre - Influence of the environment on the elementary wear processes. *Tribology International* 39(12), pp. 1485-1496. doi: 10.1016/j.triboint.2006.01.011

Stevenson, J. R. 1985. Dynamics of the Integument. In: Mantel, L.H.a.B., D. E. ed. *Inegument, Pigments, and Hormonal Processes*. Vol. 9. Biology of Crustacea: Elsevier Inc., pp. 2-32.

Suresh, S. 2001. Graded materials for resistance to contact deformation and damage. *Science* 292(5526), pp. 2447-2451. doi: 10.1126/science.1059716

Swinehart. 1962. The Beer-Lambert Law. *Journal of Chemical Education* 39(7), p. 333. doi: 10.1021/ed039p333

System, O. B. I. 1999. Distirbution Map: Skogsbergia lerneri.

Theodossiou, T. A. et al. 2006. Second harmonic generation confocal microscopy of collagen type I from rat tendon cryosections. *Biophysical Journal* 91(12), pp. 4665-4677. doi: 10.1529/biophysj.106.093740

Thorp, J. H. and Covich, A. P. 2010. *Ecology and classification of North American freshwater invertebrates*. 3rd ed. Amsterdam ; Boston: Academic Press.

Travis, D. F. 1963. Structural features of mineralization from tissue to macromolecular levels of organization in the decapod Crustacea. *Ann N Y Acad Sci* 109, pp. 177-245.

Turpen, J. B. and Angell, R. W. 1971. Aspects of Molting and Calcification in Ostracod Heterocypris. *Biological Bulletin* 140(2), pp. 331-&. doi: Doi 10.2307/1540077

Vernon-Parry, K. D. 2000. Scanning electron microscopy: an introduction. *III-Vs Review* 13(4), pp. 40-44. doi: https://doi.org/10.1016/S0961-1290(00)80006-X

Vincent, J. F. and Wegst, U. G. 2004. Design and mechanical properties of insect cuticle. *Arthropod Struct Dev* 33(3), pp. 187-199. doi: 10.1016/j.asd.2004.05.006

Vittori, M. et al. 2016. Axially aligned organic fibers and amorphous calcium phosphate form the claws of a terrestrial isopod (Crustacea). *J Struct Biol* 195(2), pp. 227-237. doi: 10.1016/j.jsb.2016.06.008

Voss-Foucart, M.-F. and Jeuniaux, C. 1978. Etude comparée de la couche principale et de la couche membraneuse de la cuticule chez six espèces de crustacés décapodes. *Archives de Zoologie Expérimentale et Générale* 119, pp. 127-142.

Walton, J. 1979. Lead Aspartate, an En-Bloc Contrast Stain Particularly Useful for Ultrastructural Enzymology. *Journal of Histochemistry & Cytochemistry* 27(10), pp. 1337-1342. doi: Doi 10.1177/27.10.512319

Warren, B. E. 1990. *X-ray diffraction*. Dover ed. New York: Dover Publications.

Weiner, S. et al. 2003. Biologically formed amorphous calcium carbonate. *Connective Tissue Research* 44, pp. 214-218. doi: 10.1080/713713619

Welinder, B. S. et al. 1976. Crustacean Cuticle .4. Isolation and Identification of Cross-Links from Cancer-Pagurus Cuticle. *Comparative Biochemistry and Physiology B-Biochemistry & Molecular Biology* 53(4), pp. 529-533. doi: Doi 10.1016/0305-0491(76)90212-1

Whitten, J. M. 1969. Coordinated Development in Foot Pad of Fly Sarcophaga Bullata during Metamorphosis - Changing Puffing Patterns of Giant Cell Chromosomes. *Chromosoma* 26(2), pp. 215-&. doi: Doi 10.1007/Bf00326457

Williams, M. et al. 2015. Ostracods: The ultimate survivors. *Geology Today* 31(5), pp. 193-200.

Willis, J. H. 1999. Cuticular proteins in insects and crustaceans. *American Zoologist* 39(3), pp. 600-609.

Xia, J. et al. 1997. Geochemistry of ostracode calcite .1. An experimental determination of oxygen isotope fractionation. *Geochimica Et Cosmochimica Acta* 61(2), pp. 377-382. doi: Doi 10.1016/S0016-7037(96)00351-1

Yamada, S. 2007a. Formation of the hinge in the podocopan ostracode Loxoconcha pulchra. *Journal of Morphology* 268(5), pp. 442-456. doi: 10.1002/jmor.10529

Yamada, S. 2007b. Ultrastructure of the carapace margin in the Ostracoda (Arthropoda : Crustacea). *Hydrobiologia* 585, pp. 201-211. doi: 10.1007/s10750-007-0638-1

Yamada, S. 2019. Ultrastructure and cuticle formation of the carapace in the myodocopan ostracod exemplified by Euphilomedes japonica (Crustacea: Ostracoda). *Journal of Morphology* 280(6), pp. 809-826. doi: 10.1002/jmor.20985

Yamada, S. and Keyser, D. 2010. Calcification of the marginal infold in podocopid ostracods. *Hydrobiologia* 638, pp. 213-222. doi: 10.1007/s10750-009-0042-0

Yumoto, M. 1994. The Shell Structure of the Carapace in *Xestoleberis Hanaii* Ishizaki (Crustacea, Ostracoda). *Trans. Proc. Palaeont. Soc. Japan, N.S.* 176, pp. 638-649.

Zhang, R. et al. 2018. X-ray fluorescence imaging of metals and metalloids in biological systems. *Am J Nucl Med Mol Imaging* 8(3), pp. 169-188.

Zhou, W. and Wang, Z. L. 2007. *Scanning microscopy for nanotechnology : techniques and applications*. New York: Springer.

Ziegler, A. 1997. Ultrastructural changes of the anterior and posterior sternal integument of the terrestrial isopod Porcellio scaber Latr. (Crustacea) during the moult cycle. *Tissue Cell* 29(1), pp. 63-76.

Zok, F. W. and Miserez, A. 2007. Property maps for abrasion resistance of materials. *Acta Materialia* 55(18), pp. 6365-6371. doi: 10.1016/j.actamat.2007.07.042

Zucker, B. B. 1966. Hydration and Transparency of Corneal Stroma. *Archives of Ophthalmology* 75(2), pp. 228-&.